Laser-cooling atoms to indistinguishability: Atomic Hong-Ou-Mandel interference and entanglement through spin-exchange

by

Adam Kaufman

B.A., Amherst College, 2009

A thesis submitted to the

Faculty of the Graduate School of the

University of Colorado in partial fulfillment

of the requirements for the degree of

Doctor of Philosophy

Department of Physics

2015

This thesis entitled:
Laser-cooling atoms to indistinguishability: Atomic Hong-Ou-Mandel interference and entanglement through spin-exchange
written by Adam Kaufman
has been approved for the Department of Physics

_____

Cindy Regal

_____

Prof. Ana Maria Rey

Date _____

The final copy of this thesis has been examined by the signatories, and we find that both the content and the form meet acceptable presentation standards of scholarly work in the above mentioned discipline.

Kaufman, Adam (Ph.D., Physics)

Laser-cooling atoms to indistinguishability: Atomic Hong-Ou-Mandel interference and entanglement through spin-exchange

Thesis directed by Prof. Cindy Regal

In this thesis, I describe the development of and scientific results from a new platform for creating ultracold atoms via single-atom control. We employ Raman-sideband cooling to isolated bosonic ^{87}Rb atoms confined within sub-micron optical tweezers, yielding single particle three-dimensional ground-state fractions of 90%. We create multiple, independent, mobile optical tweezers, which simultaneously allows multi-particle studies with single-atom microscopy and highly tunable length-scales. We employ this toolset in both of the main experiments discussed in this thesis. In one experiment, we observe Hong-Ou-Mandel interference of two bosonic atoms, each of which is independently prepared in spatially separated optical tweezers. The interference we observe is a direct consequence of the purity of the single particle quantum states produced, and the indistinguishability of the atoms. In a second experiment, we introduce a spin-degree of freedom and exploit spin-exchange dynamics, driven by the quantum-statistics of the particles, to create a spin-entangled pair of spatially separated atoms.

Dedication

Dedicated to my cute, loyal, and deeply insane border-collie husky: Maddy. No just kidding my parents.

Acknowledgements

The first time I walked into JILA B232-6 as a graduate student was in early August, 2009. The lab consisted of a chair and a phone. The arrangement was that I would call Cindy once I got there because she would be arriving later in January. She gave very direct advice: you need to figure out a laser system design for cooling and trapping, use this to make a list of what to buy, and then buy it (along with things like scissors and zipties), because we need to spend 100k in three weeks. This was terrifying, but it is also exemplary of what has been an amazing experience working for Cindy. There was clear guidance, but complete freedom to explore. She's a brilliant investigator, with super human time management skills. Always willing to make time to discuss various things and offer support where necessary, I could not imagine a better advisor over the past 6 years and I am extremely grateful to her. She is also exceptionally tolerant of neurotic graduate students; this was crucial in my case.

At JILA I benefited greatly from the network of students and professors. In particular, I would like to highlight Debbie who was my de facto advisor for my first six months at JILA. This advisor role continued from a distance while I have been at JILA, providing guidance and awesome paper edits. I have also learned a great deal from watching her ask questions in talks and presentations: specifically how to think clearly about experimental physics, to figure out what information you (probably) know and don't know.

I owe a tremendous thank you to Brian, my labmate of the past five years. Brian is a super smart, technical thinker, whose attention to detail has saved us from many snags over the past couple of years. He is also a fount of optics knowledge which has been crucial to the experiment.

Outside of lab, he has been a great friend, always willing to lend a hand, and completely and utterly always down for a beer. I also would like to thank Collin: in addition to awesome programming skills and ability to quickly pick up on a lot of things, it was great spending time with you in lab while it lasted, and so glad that it has continued outside out of lab even after you left. Outside of the single atoms lab, Tom Purdy has been an indispensible person in the Regal group: he just knows everything, which is very helpful. The rest of the lab (present and historic) – Ben, Bob, Nir, Kathrin, Niclas – have created an awesome, relaxed community.

Much of the work in this thesis emerged from a collaboration with Ana Maria Rey's group. Our meetings have been critical, and the awesome theory input from Michael "KoWally bear" Wall, Kaden *inappropriate to a thesis* Hazzard, and Mike "the entanglement tangoist" Foss-Feig indispensable. These guys in particular deserve a medal for tolerating my endless questions. I would like to highlight the Mike, who, in addition to being brilliant, has been a great, albeit permanently disparaging, friend.

My time at Amherst was pivotal in a lot of ways, and I am particularly grateful to David, Jagu and Russ. David made it clear it was OK to be a little crazy, while Jagu is the wise Dumbledore of Amherst. Russ, among many things, established my deep addiction to mathematica.

Ah, and, Jeff, with whom I have been in continuous gchat conversation for approximately the time I have had gmail, through the ups and downs of college, grad school and surely the future. More dedicated friends don't exist.

Annalise and I met approximately three years into graduate school, and I'm so glad we did because by that point I had not been motivated to do my laundry in approximately three years. Not just my hygiene, but my life got a lot better at that point, and I could not be more happy that we met. In addition, she has been intensely tolerant of mild-to-severe workaholism. Over this period I could not have imagined a better partner. Along with Annalise came a second family, in the form of Miel and Riri and the bros.

I owe a great deal to the support of my brother and parents, along with Ellie and Adie. My brother, Jake, has been a firm believer in the importance of being a nerd – this was validating

– and a supplier of endless disgusting texts. Through thick and thin, my dad has been steadfast advocate, supporter, and friend, always willing to lend an ear and defy expectations about what it means to be enthusiastic about the capabilities of a toaster. Lastly, of any person it is perhaps my mom, a science teacher (among other things), who got me started down this path: when I was 5 or so, she got out a half-covered pot of water and put it over a flame, making me watch until the water had completely evaporated. Showing the condensed water on the pot lid, she explained the parallel to rain, and I was hooked.

Contents

Chapter

Figures

Figure

Chapter 1

Introduction

1.1 Historical perspective

For nearly a century, the pursuit of ultralow temperatures in physical systems has helped reveal a variety of intriguing quantum mechanical phenomena. In the early 1900s, novel refrigeration techniques ushered in the single Kelvin regime, and along with it superfluid helium and superconductivity, both of which were understood in the context of quantum mechanics decades later [18, 19, 20, 21]. In the 1980s, similar temperatures also revealed the integer [22, 23, 24, 25] and fractional quantum hall effects [26], along with other exotic phenomena such as heavy fermion physics [27], which demand a more detailed picture of the single-particle physics [23] and underlying many-body entanglement [28]. Typically, the study of such phenomena entails putting a sample of interest in a refrigerator, and observing physics with energy scales commensurate with the thermalization temperatures. Macroscopic observables, such as conductivity and specific heat, provide a window into complex quantum mechanical many-body phenomena ascribed to the quantum states created.

Bose-Einstein Condensation and degenerate Fermi gases of neutral atoms established a new way to study low-entropy quantum systems, which rely on the ability to isolate a sample with exceptional vacuum and slowly cool the system in the absence of significant heating mechanisms [29, 30]. Due to the unique ability to tune the single-particle physics and the two-particle interactions [31, 32], ultracold atoms set the stage for studying many-body phenomena with a novel set of experimental control knobs. This toolset allowed ground-breaking observations of physical phenomena such as

the superfluid-Mott insulator transition and BEC-BCS crossover physics [32, 33]. However, while in the field of ultracold atoms and condensed matters physics tools were developed to more closely examine local properties, such as the density of states or dispersion relations [34, 35], the ability to resolve single particles was not yet developed. Recently realized in the past five years, quantum gas microscopy [11] of ultracold atoms provides single-particle resolution of interacting quantum-systems, yielding a unique perspective not possible in a traditional condensed-matter setting. So far, these microscopic studies have revealed local number bunching across the superfluid to Mott insulator quantum phase transition in the Bose-Hubbard model [36, 37], anti-ferromagnetic ordering in a quantum simulation [38], two-point correlation functions after a quantum quench in both small [39] and large systems [40], and the dynamics of interacting spin chains [41, 42]. The cooling mechanism in these experiments, historically, has been evaporative cooling [29], which is a slow form of cooling whereby iteratively the highest energy atoms in a system are ejected and the remaining sample thermalizes. Though indeed a high-fidelity mechanism for reaching low temperatures, many such systems retain small residual entropies [36, 37], particular after loading the atoms into the trapping potential of scientific interest [43, 44]. This uncontrolled entropy can preclude the measurement of quantum many-body phenomena, such as large-scale anti-ferromagnetism, due to the excessively small energy scales at play.

In a parallel frontier of atomic physics, tremendous experimental results have come out of the trapped ion community. Here, individual ions are laser cooled to their motional ground state, which is the starting point for high-fidelity quantum gates [45, 46], tests of entanglement [47], and quantum simulation of physical models of interacting spin systems [48, 49]. A confluence of large interaction energies and fast cycle times make this platform ideal to studying interacting many-body systems, with length-scales amenable to single-particle resolution. The large spin interaction energies reduce constraints on temperature, which are easily satisfied via optical pumping techniques. The experimental speed, afforded by the Raman sideband-cooling [50], results in expectation values and state tomography on realistic timescales despite an exponentially growing Hilbert space. And although the particle number in traditional ion traps has been limited, in actuality, most neutral

atom quantum dynamics experiments with analogous capabilities have been restricted to similar systems sizes [38, 40, 41, 39]. Even though a BEC provides typically 10^5 atoms, only a handful participate in a typical quantum gas microscope experiment studying quantum dynamics on the single-particle level: an experimental cycle time of 30 s with neutral atoms achieves the same studies as a 10 ms ion-based experiment, representing a serious problem when you have to run your experiment 1000 times to acquire statistics. And to make matters worse, the small interaction energy scales of neutral atoms ($10-100$ Hz) compared to ions ($10-100$ kHz), places stringent requirements on the temperatures for observing strongly correlated many-body ground-states [43, 44].

These comparisons highlight the advantages of the ion-based platform, which, from the cooling to the cycle time to the accessible many-body physics, are exclusively derived from the strong Coulomb interaction associated with the ion's charge. The comparative weakness of the neutral atom interactions, however, also allows for complementary physics, namely, wave-function overlap and coherent particle mobility via quantum tunneling. These phenomena produce physics influenced by particle indistinguishability and quantum statistics. Quantum statistics are integral to many condensed matter models, such as the Fermi and Bose-Hubbard model, and underlie fundamental behaviors like superconductivity. Therefore, in spite of the many advantages of the trapped ion approach, neutral atoms permit a whole class of studies precluded by the strong interactions between ions.

1.2 A new perspective on neutral atom control

In my thesis work we wanted to consider neutral atom control from a new perspective. We designed an experiment – rooted in ground-state laser-cooling of neutral atoms in optical tweezers, summarized in Chapter 2 and 3 – in which we could first focus on Raman-sideband cooling an isolated neutral atom to its three-dimensional ground state. Ground-state laser cooling of neutral atoms has been studied for many decades, fueled by the still unrealized goal of achieving quantum degeneracy of atomic gases via Raman-sideband cooling [51, 52, 53, 54]. While ingenious methods combining atom-atom collisions and laser-cooling have reached degeneracy [55], the final

phase-space density achieved by purely laser cooling a three-dimensional gas has been limited by rescattering effects, precluding the onset of the BEC transition [56, 57]. Our viewpoint was that by creating a lower-dimensional sample (one or two dimensional array) of individually trapped and transportable neutral atoms, laser cooling could become a formative tool for quantum gases as it has been for trapped ions. Previous work in a variety of physical systems – atoms in cavities or lattices – have demonstrated one or two-dimensional ground state cooling of single neutral atoms in lower-dimensional systems [58, 59, 60]. But three-dimensional cooling is key to the full control required to see effects of quantum statistics [61]. In our experiments, we focus on initializing a perfectly isolated set of sideband-cooled atoms in their three-dimensional ground-state. Importantly, combining this with the ability to move and tailor the positions of the atoms enables the assembly of a quantum gas to microscopic specifications [62], where the motion of the atoms is completely controlled and highly tunable spatial distributions of the particles are accessible. In the experiments that form the core of this thesis, we bring these ideas to fruition at the few-particle level by using optical tweezers and three-dimensional ground state cooling via Raman-sideband cooling.

To accomplish our goals, we created, to our knowledge, the tightest optical tweezer for single atom-trapping: it defines a mode-volume compatible with single-atom trapping [3, 5], and we aimed to explore whether the tight confinement was amenable to Raman- sideband cooling [50]. Today, the tweezers allow us isolate, detect, and place a single neutral atom in its motional ground-state in less than 200 ms. Furthermore, we have integrated the ability to make multiple tweezers, allowing parallel ground-state cooling of multiple independent atoms. We have therefore created a platform for rapid preparation of arrays of atoms in low-entropy, pure quantum-states. The work presented in this thesis describes these capabilities and the resulting new experiments we performed (Figure 1.1), and represents a starting point for a variety of explorations that harness these advances. I will discuss below particular near-term and long-term examples that are enabled by our work.

Already, optical tweezers have been used to realize Rydberg quantum-logic gates and a variety of protocols coupling atoms and photons. In such applications the thermal motion of the

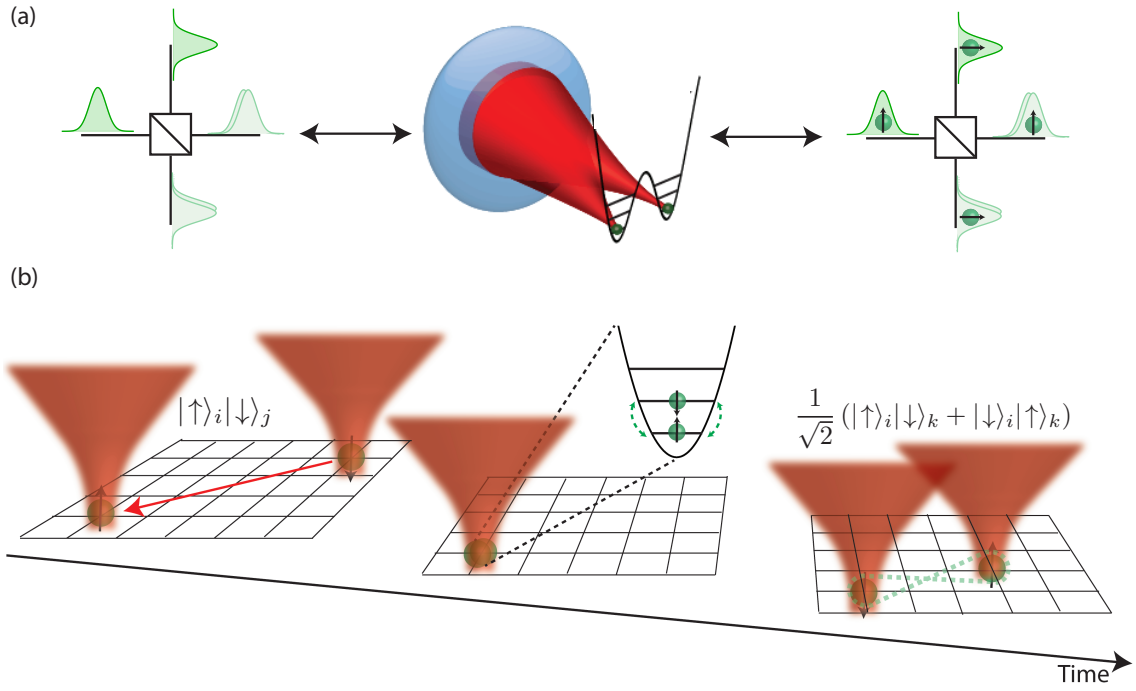

Figure 1.1: New experiments enabled by the optical-tweezer platform. (a) We create an atomic beam splitter to observe two-particle interference, thereby revealing for the first time the Hong-Ou-Mandel effect [1] with independently prepared atoms. (b) Starting with an an atom in each of two spatially separated optical tweezers, we tailor the microscopic physics to produce entangling spin-exchange collisions. Upon producing entanglement, we separate the particles and verify that the entanglement produced locally persists to create non-local quantum correlations between the atomic spins. This toolbox is crucial to using spin-exchange-based gates with neutral atoms for a quantum-computing architecture [2]. The subscripts of the states represent the atom locations over the course of the operation.

atoms has caused deleterious effects, such as dynamic light shifts, mitigated atom-photon coupling, and dephasing of high fidelity Rydberg gates [63, 64, 65, 66], all of which stand to benefit from the cooling techniques we have developed. Neutral atoms, as opposed to ions, also offer a promising avenue for interfacing atoms near material surfaces and nano-photonic devices, and such applications often require control of the atomic motion for coupling to wavelength-scale optical modes [67, 68]. Incorporating full three-dimensional motional control not only strengthens current tweezer applications [69, 70, 71], but also expands their use to experiments that are currently considered only in the context of evaporatively cooled gases. For example, one could combine two traps and realize significant wavefunction overlap for Feshbach molecule association, for the purpose of creating

single dipolar molecules [72]; indeed, this is the exact experiment underway in the Ni group at Harvard. Hence, a diversity of experimental avenues are immediately enabled by the approach we have developed.

We pursue an exciting and daunting goal of using this platform for the purpose of quantum dynamics. Pure laser-cooling approaches offer unique opportunities. Possibly the most important, and one which we regularly use in this thesis, is the ability to image the atoms more than once in an experiment: unlike evaporative cooling, we can detect an atomic spatial distribution, cool, perform, an experiment, and image again. We can therefore follow a quantum system between known initial and final conditions, removing the entropy associated with unknown initial defect positions. And, while this capability is novel in its own right, it also establishes the prospect of real-time assembly of a quantum system. This latter concept is illustrated in Figure 1.2. Here, despite the presence of a large initial entropy associated with the spatial configuration of the particles, the optical tweezers can reconfigure the positions in real-time such that a central array is free of defects [62]. Then, laser-cooling can spin-polarize and render individual atoms in their motional ground-state: a finite-sized, defect-free, ultralow entropy sample remains. Manifestations of residual entropy in evaporatively cooled systems, such a spatial defects in a Mott insulator or heating during the loading of fermions into a lattice, could be circumvented by these redistribution techniques.

1.3 Atomic Hong-Ou-Mandel effect: two-particle interference in tunnel-coupled optical tweezers

The prerequisites for quantum gas assembly – real-time manipulation of the atom positions and independent preparation of indistinguishable atoms – are exactly what we show is possible with our platform through the first observation of the atomic Hong-Ou-Mandel effect. The Hong-Ou-Mandel effect is a two-particle interference phenomenon, wherein two indistinguishable particles are interfered on a beam splitter, and the particles always emerge on the same, fluctuating output port. The effect is extremely intriguing because the final state can result through no interaction between the particles, and through no entanglement pre-existing in the two-particle state impinging

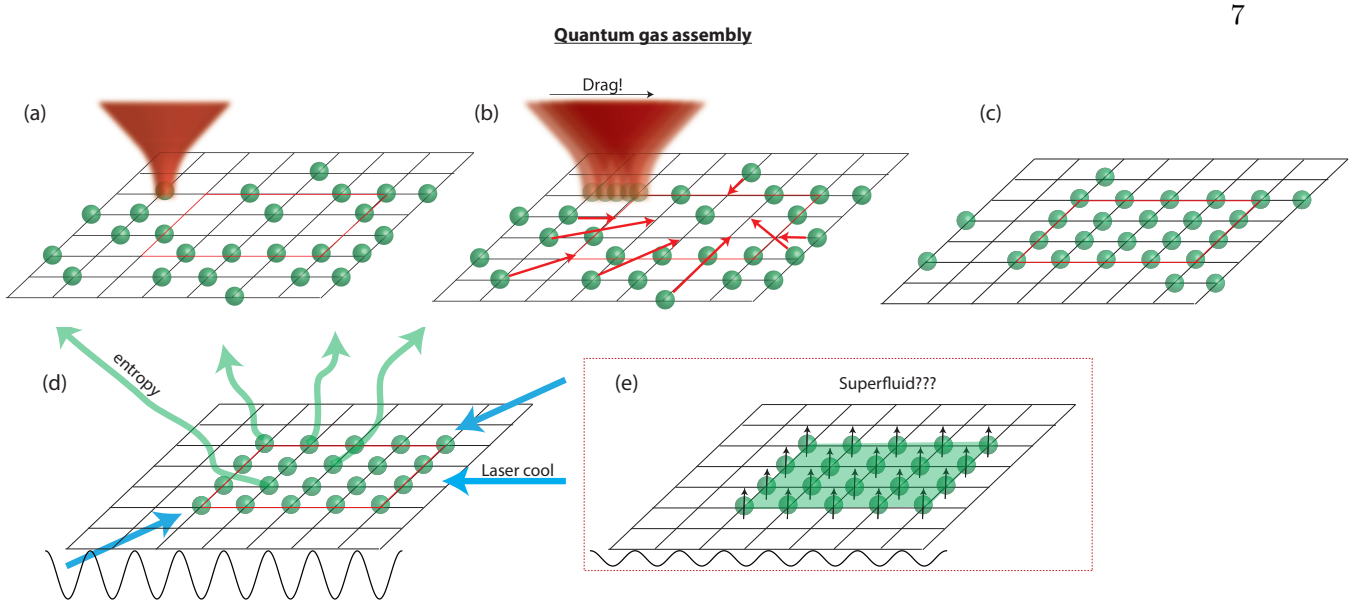

Figure 1.2: Quantum gas assembly. (a) A potential array is loaded stochastically with thermal, single atoms via light-assisted collisions [3]. (b) After imaging the random spatial distribution, an optical tweezer sequentially drags atoms (red arrows) into a central region (red square) (c) The resulting uniform array can be imaged, and the detected atoms on the edge can be removed with the optical tweezers. (d) Three-dimensional Raman sideband cooling is applied, initializing each atom independently in its motional ground-state (e) By removing spatial and motional entropy, it is possible to melt to a superfluid from a small Mott insulator via the quantum gas assembly protocol outlined in the prior steps.

on the beam splitter. In analogy to photons, we are able to observe the atomic Hong-Ou-Mandel effect by deliberately operating in a regime in which the atom interactions are negligible. We interfere the two atoms on an atomic beam splitter formed by a pair of tunnel-coupled optical tweezers, demonstrating the compatibility of our system with a variety of Hamiltonians where coherent tunneling of the atoms is integral. The two-particle interference we study contains the key physical elements of the original photonic Hong-Ou-Mandel experiment: that is, the quantum interference of the two atoms is contingent on their indistinguishability, and the interfered state exhibits mode-entanglement through the atomic beam splitter interaction. A fundamental feature of the Hong-Ou-Mandel effect is that the two-particle interference observed is independent of the origin of the bosonic particles; indistinguishability is all that is required. They can originate independently, as in radiative decay of photons [73], or they can come from nonlinear effects in

photonics systems [1], or, as was recently demonstrated, they can come from a Bose-Einstein condensate [74]. Our experiment probes the core feature of atomic Hong-Ou-Mandel interference, because the two-particle interference is the result of completely independent preparation of the atoms: its physical description is exclusively rooted in the concept of identical massive particles.

1.4 Spin-exchange between neutral atoms: realizing particle entanglement between spatially separated atoms

Our Hong-Ou-Mandel experiment relies on the ability to prepare two atoms identically in all degrees of freedom besides their position, and, as we show, the two-particle interference disappears when the atoms are deliberately prepared in different spin states through single-spin addressing. Preparing arbitrary spin-configurations of several particles opens up many experimental avenues. Quantum simulation of spinful ground-states [43, 44] and quenched systems [42, 49, 75] has been pursued with increasing interest over the past five years in both neutral-atom and ion-based platforms, but a parallel route has targeted quantum computation applications. Despite impressive progress using Rydberg blockade in neutral atoms [66, 76], here the ion platform with its robust trapping technology and the associated long-range Coulomb interaction has created a thus-far superior approach to two-qubit gates [45]. But the success engendered by these strong-long range interactions has also incurred problems: the Coulomb interaction between the ions also couples them more strongly to the environment, leading to heating and constraints on how a quantum computing architecture can be designed in the presence of ion cross-talk [50, 77, 46, 78]; an analogous statement can be made of the Rybderg blockade platform. This suggests that ideally we seek an entangling mechanism strictly between the atoms that we can switch on and off at will, to retain the ability to perform two-qubit gates while mitigating deleterious effects incurred by the qubit capacity for interaction. Although it is two-orders of magnitude slower, the spin-exchange interaction first explored with neutral atoms by the Porto group in 2007 [16], offers this exact capability: the entanglement requires overlapping the two atomic wave functions, where the quantum statistics and contact interactions cooperate to yield spin-exchange dynamics. The new challenge, therefore,

is developing the tools to bring two particles together from distant registers, overlap them for the purpose of a two-qubit gate, and separate them while retaining the entanglement created in the prior step. We demonstrate precisely this toolset in Chapter 5. Importantly, we introduce and implement a new protocol to certify the two-particle entanglement consisting of application of a local gradient and parity measurements [79], which could be applied to arbitrary spin entangled states of spatially separated neutral atoms [80, 81]

1.5 Goals and outline of thesis

For each of the experiments in this thesis, I provide a theoretical summary of the underlying physics along with a detailed discussion of the experimental protocols developed and applied. I further discuss characterizations of the various fidelities that inform our single atom preparation, as well as specific systematics associated with the quantum dynamics experiments discussed in Chapters 4 and 5. The thesis is structured as follows:

- Chapter 2 outlines the key components of the apparatus, and techniques employed for using optical tweezers for quantum dynamics experiments. The exceptionally tight focus created for atom trapping has unique associated features. Understanding precisely the created tweezer potential was crucial to our subsequent studies, and we provide a summary of these techniques.

- Chapter 3 discusses our application of Raman-sideband cooling to tweezer-trapped atoms. We explored several different approaches to this cooling, and we discuss relative advantages of each. We furthermore summarize simple theoretical models used to guide our choice of cooling parameters. The results of this chapter are the first demonstration of high-fidelity three-dimensional ground-state cooling of an isolated single neutral atom.

- Chapter 4 describes our observation of atomic two-particle interference, thereby realizing the Hong-Ou-Mandel effect with atoms. Using the cooling techniques of the prior chapter, we are able to independently prepare atoms such that their indistinguishability is manifest

when they are interfered on an atomic beam splitter. The beam splitter is achieved in a double-well potential with a tunable tunnel coupling, the characterization of which we discuss in detail. These studies constitute the first atomic demonstration of this classic experiment in quantum optics, as well as the first direct observation of indistinguishability with purely laser-cooled atoms.

- Chapter 5 presents our implementation of spin-exchange, mediated by the contact interactions between the atoms. We show how the tweezers allow coherent spatial manipulation of the particles to realize non-local entanglement through local interactions. We apply an entanglement verification protocol adapted to the entanglement produced via spin-exchange, which is also applicable to Bose-Hubbard-like systems. The results indicate the promise of interfacing tweezers with a larger quantum register for the purpose of building a quantum-computing architecture.

Chapter 2

Apparatus for single-atom preparation, manipulation, and trapping

2.1 Overview

2.1.1 Experimental design perspective

The goal in designing and building this experiment (Figure 2.1) was to create a versatile optical tweezer-based system for trapping and preparing ^{87}Rb atoms in pure quantum states. Specific performance goals included,

- A rapid cycle time for statistics acquisition
- Sufficient compactness to minimize the microscope objective working distance
- Optical access and polarization purity for all of the beams for Raman-sideband cooling
- Single atom, spatially resolved detection
- Wavelength-scale, dynamic potential generation
- Scalability to more than one atom and up to 10-20

In this chapter, I will outline capabilities that fulfill these goals, while later chapters will be devoted to the key experimental challenges and achievements.

2.1.2 Key components

The key experimental components that will be discussed in this chapter pertain to various capabilities that we regularly make use of, but are not necessarily restricted to one experiment

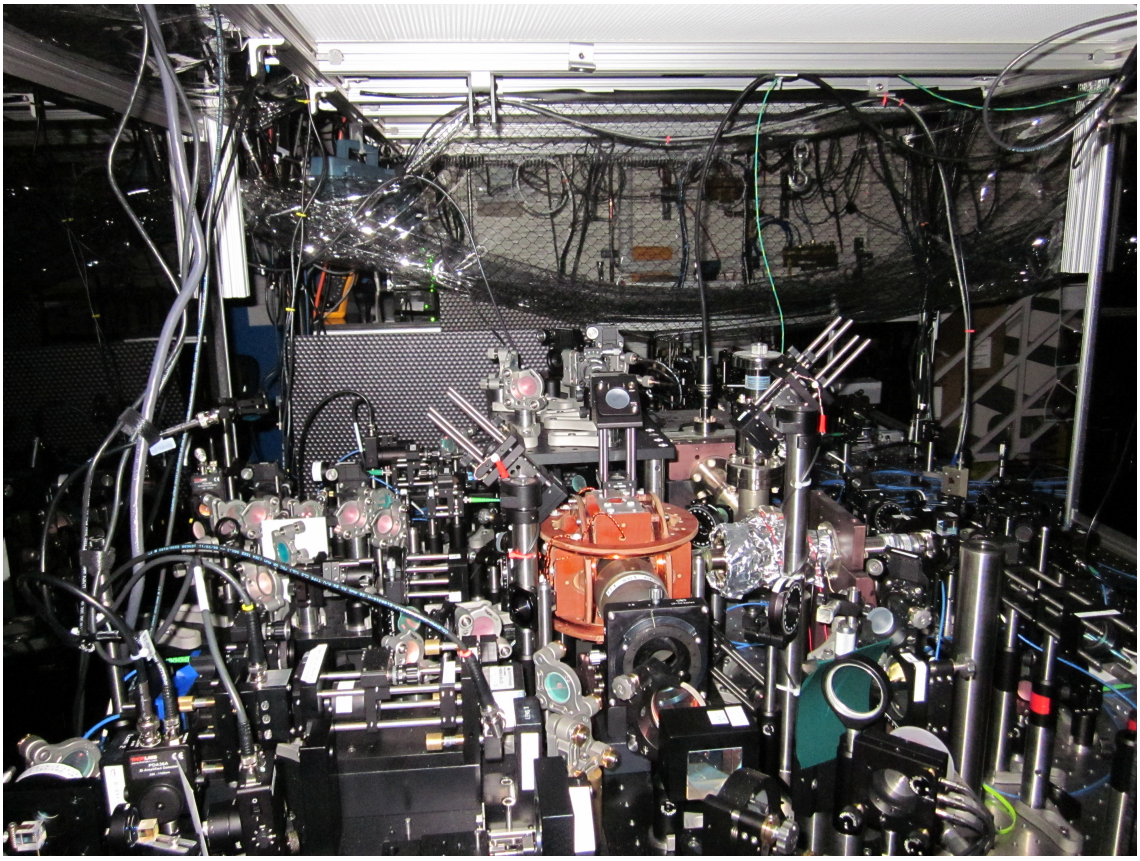

Figure 2.1: Photograph of the experiment circa 2015.

that we conducted. These components include the vacuum system and optical cell, the microscope objective, single atom loading techniques, trap characterization, single atom addressing and spatial manipulation, and preparation and coherent manipulation of the atomic spin. I will also provide a description of a typical experimental sequence, which, due to the sideband cooling and optical tweezer platform here, is distinguished in critical ways from a typical quantum gas experiment.

2.2 Vacuum chamber and cell

All of the experiments take place in a single cell from Precision Glassblowing (Fig 2.2) consisting of a quartz frame with fused-silica windows. It has a diameter of approximately 2.5 in. and a width of 1.5 in. Each window of the cell is AR-coated on both faces to minimize beam reflections (0.2% measured normal incidence) and excess background light, as well as possible trapping

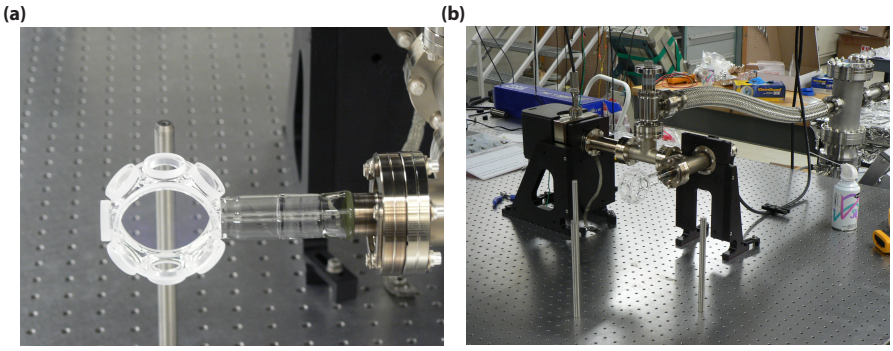

Figure 2.2: Photographs taken of the cell (a) shortly after it was affixed to the rest of the vacuum chamber (b). The cell was aligned (within 0.2^o) to the plane of the optical table by reflecting a leveled laser off of the large windows.

potential distortions. The cell width determines the working distance required for the high-NA objective, which is consequently constrained to exceed 20 mm. While we did consider a smaller cell to relax some constraints on the objective, this would have reduced the maximum possible size of the magneto-optical trap (MOT) beams, and, in turn, reduced the loading rate and increased the experiment cycle time. It was later determined that a very small MOT was sufficient for single atom loading, and a subsequent cell design uses smaller dimensions.

The vacuum system, tiny by ultracold gas standards, consists of a single ion pump. The whole system was baked out in 2010, and we reached a vacuum pressure at the ion pump (Gamma vacuum 15 L/s) of approximately $3 \cdot 10^{-11}$, though it is likely the case that the pressure in the cell is a fair bit higher given the vacuum chamber geometry. We use in-house spot-welded getters from SAES, which are daily run at 3A.

After baking, the flatness of the cell window through which we create optical tweezers and perform sub-micron imaging was measured interferometrically in a Fizeau configuration, which confirmed that it was compatible with diffraction-limited performance. The curvature was conservatively $< \lambda/4$ over a 1 in. diameter region of the window, and was consistent with it being a very weak lens likely due to the vacuum pull on the cell during its construction; we observe the opposite sign of focusing from the opposite window when each is measured in reflection. The wedge of the window was also measured to be less than 5 arc seconds. We calculated that the spherical

curvature was correctable with the collimation of the input tweezer and imaging setup, with less than 1% change in the magnification of the imaging optics calibrated out of the setup.

2.3 Laser system and beam layout

2.3.1 Lasers for the MOT and spin preparation

When we started designing the laser system, and studying various literature on Raman-sideband cooling of neutral atoms (e.g. see [51, 56, 53]), it was clear that there existed numerous sideband cooling schemes that required addressing various optical transitions. The laser system was designed so that we could address every transition on the D2 line by only flipping an AO deflection sign; this allowed us to test various cooling schemes. Furthermore, we adopted the common beatnote locking scheme at JILA [82] and elsewhere: this allows the lasers to be tuned and locked in a single experimental run over a wide frequency range to accommodate optical light shifts induced by the optical tweezers.

The laser locking scheme is illustrated in Fig. 2.3. There is a master laser locked on the weak 2-3' transition via saturated absorption spectroscopy. Two other lasers, labeled $F = 1$ laser and $F = 2$ laser, are offset-locked via phase-locking a heterodyne beatnote with the master laser, and are AO-shifted to address various transitions. Each lock can be jumped over approximately 100 MHz in under 5 ms. For example, in a single experimental run we will perform free-space polarization gradient cooling, single-atom imaging, and then resonant optical pumping on a light-shifted transition; these successive steps require jumping the laser over a 90 MHz range.

2.3.2 Beam layout at the cell

In Fig. 2.4, all of the beams used in the experiment are schematically represented with relevant optics shown. A challenge is getting all these beams in while accommodating the loss of optical access incurred by the large NA microscope objective. Here we provide a summary of beam functions, each labeled by its associated source fiber in the figure, and relevant optical components

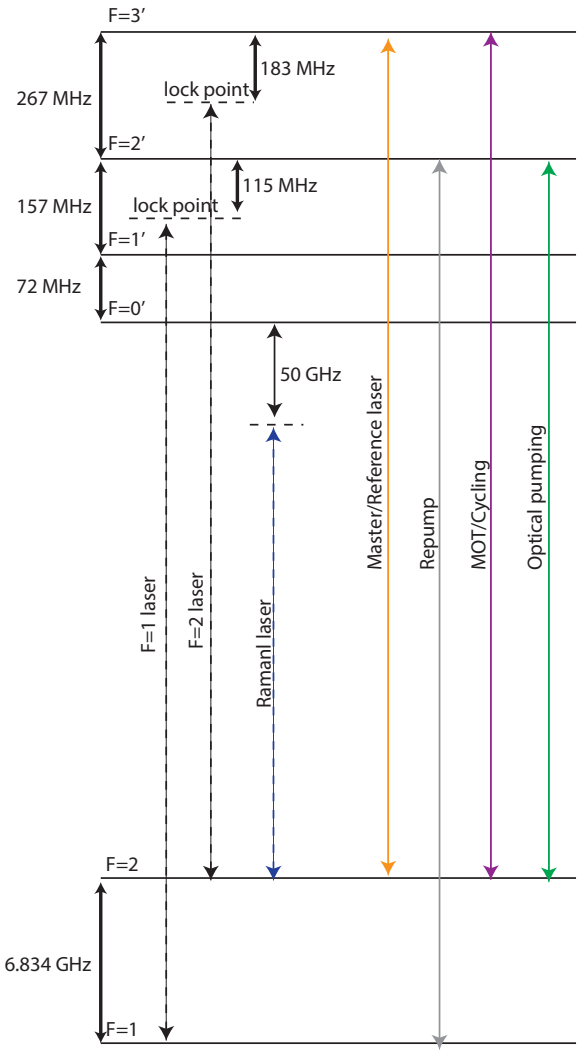

Figure 2.3: Three external-cavity diode lasers are used for the MOT and single-atom spin preparation. The optical pumping and cycling light for imaging are derived from the $F = 2$ laser and switched separately with AOMs. Two of the three MOT beams are generated via an injection locked amplifier with light from the $F = 2$ laser. The repump light is derived from the $F = 1$ laser: two separate fibers (with separate AOMs) carry repump to the experiment for the MOT and spin preparation of the atom(s), since they require different polarizations and beam vectors. Also shown is the Raman laser, which is derived from a DBR diode detuned red by approximately 50 GHz of the D2 line.The details of generation of the light used for driving Raman transitions along all three dimensions of the optical tweezer is discussed in Chapter 3. The transition splittings here are taken from Ref. [4].

used for each:

- "EO" refers to the light carrying the electro-optic modulator (EOM) generated sideband for

driving raman transitions between spin states split by 6.8 GHz. Its σ^+-polarization purity is important to suppress quantum interference of different Raman transitions pathways (however, this effect is largely eliminated by resonance conditions for this transition), and is achieved by subsequent optics also used for the optical pumping beams.

- "OP" and "RP" refer to beams on the optical-pumping and repumping transitions (see Fig. 2.3) and are used in tandem to optically pump to the $|F, m_F\rangle = |2, 2\rangle$. Their polarization is optimized to be pure σ^+; the polarization is initialized using a Glan-Taylor polarizer ("GT"), while a half-wave plate and quarter wave-plate set the polarization to circular and compensate for the birefringence of the cell window.

- "AB1" and "AB2" refer to beams used at separate times over the course of iterations on Raman cooling setups (discussed further in Chapter 3). Each beam when in use is applied with the EO beam to drive Raman transitions sensitive to the axial dimension of our trap, coincident with the z-axis.

- The "Imaging+MOT" beam is used for three purposes. It participates in creating our MOT during the loading stage of the experiment, and is at a funky angle ($\sim$ 50 degrees from z) and of smaller size (1.6 mm $1/e^2$ radius) due to the objective obscuring a large numerical aperture. Though this was not always the case, we now use this beam alone for performing in-trap sub-Doppler cooling (see Section 2.7.2 for discussion) and single atom imaging. The cylindrical symmetry of the traps allows efficient cooling via this single beam since it projects along the radial and axial dimensions of the optical tweezer, and by using a single beam we can avoid time-varying intensity gradients at the atom.

- "TOP" and "BOT" refer to Raman beams used separately to address orthogonal directions in the $x - y$ plane of the atom's (radial) motion in the optical tweezer. As with an axial beam, these Raman beams are each used in conjunction with the EO beam to drive a hyperfine-changing transition.

- The "MOT" beams in the side view refer to the two large (9 mm $1/e^2$ radius) retro-reflected beams used for loading our MOT. They nearly fill the clear aperture of the 0.9 in. side windows of the cell. Each beam contains cycling and repump light.

- "LSB" refers to the the light shift beam used to change the local effective magnetic field at one optical tweezer compared to the other, which allows for single spin addressing [2]. The light is derived from the same DBR used to generate the Raman light. The beam is introduced to the single atom imaging path via a high-quality flat glass window, and is ultimately focused upon passing through the microscope objective. A piezo-actuating mirror allows for high-resolution (10s of nm) steering of the beam to the tweezer-trapped atoms. The beam is directly collimated out of the fiber with a meniscus-achromat lens pair to reduce aberrations and to ensure a sub-micron focused spot size.

- The optical tweezer light coming from the optical rail (see Section 2.6) is transmitted by a 780nm/850nm dichroic plate, and subsequently focused by the microscope objective to form the optical tweezer(s). We have used an ECDL, DBR, tapered amplifier seeded by an ECDL, and an M^2 ti:sapphire laser as the light source, none of which exhibited significant performance differences with respect to the experiments discussed in this thesis.

- For single atom imaging, fluorescence is collected by the objective, separated by the dichroic, and magnified by a 1000 mm achromat onto the -60^o F cooled, Andor 897 CCD camera. An unshown large aperture between the dichroic and the objective sets the numerical aperture of the imaging and optical tweezer system. It is typically set between 26-27 mm for the experiments in this thesis.

2.4 Microscopic objective tests performed outside of the experiment

Our microscope objective was custom designed by ASE, a company based out of Rochester, in collaboration with us. The objective consists of a six element optical system encased in Ultem

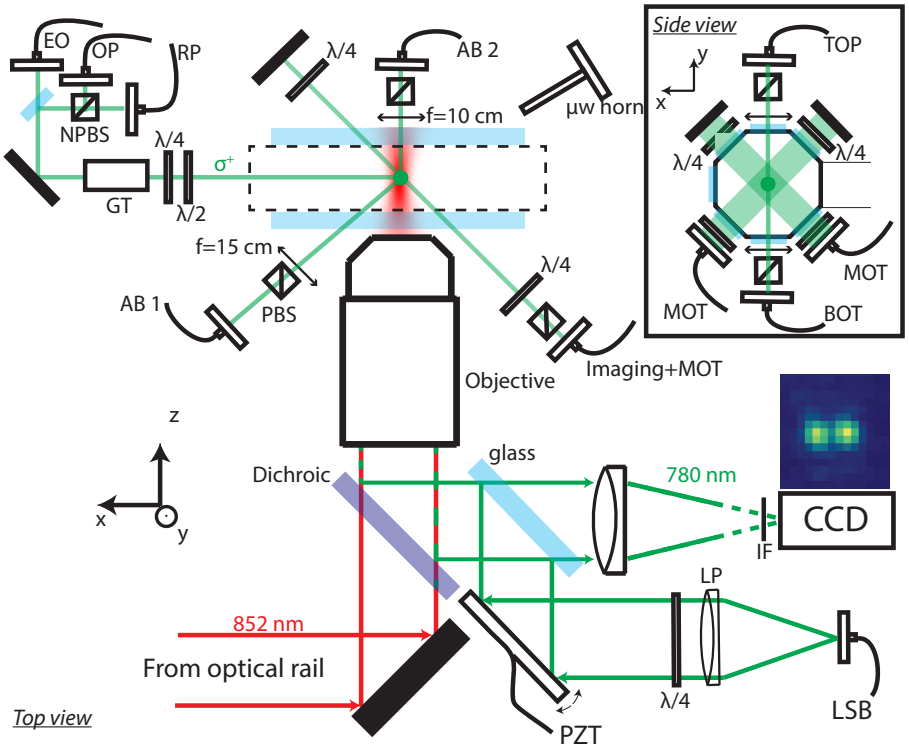

Figure 2.4: Multiple beams are used for single-atom trapping and ground-state cooling. A side and top view of the setup is provided, and a coordinate system used consistently (for the most part) throughout this thesis. In the text we elucidate abbreviations for beams and optical elements. Unless otherwise indicated, every cube is polarizing.

to minimize magnetic field eddy currents, since the front facet of the objective sits 21 mm from the atoms. The lens was corrected for the 6.35 mm thick window of our cell, and designed for 0.6 NA diffraction-limited performance at 850 nm and 780 nm. Calculations in Zemax confirmed that the 100 μm manufacturer tolerances on this thickness are compatible with diffraction-limited performance via collimation adjustment of the imaging setup and input beam, and we performed confirmatory in-situ measurements of this thickness.

When we first received the objective in September 2010, it was tested by imaging a 500 nm pinhole through a test window identical to that of our cell. At the time, measurements on the lens performance showed severe spherical aberration, which were completely correctable by increasing the cell window thickness by 1 mm (with microscope slides). The hypothesis is that one of the elements in the objective was improperly manufactured. Rather than risk damage to the optical

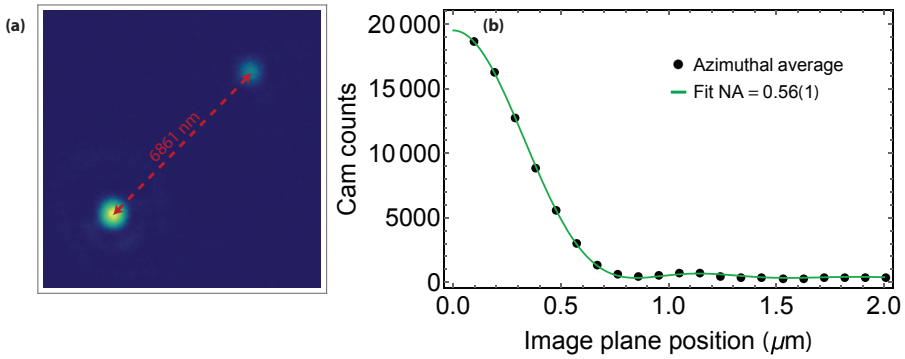

Figure 2.5: Imaging data through the ASE objective and a window similar (same manufacturer and batch) to those created for our cell. (a) We show a magnified image of a dual pinhole target for testing the objective performance and imaging magnification. The relative dimness of the upper right pinhole image is due to the inhomogeneous rear illumination of the target. (b) We show the azimuthal average of the imaged spots with a fit using the model in Eq. 2.1.

elements, we had ASE glue a cleartran plate of 1 mm thickness onto the front facet of the lens. The test data discussed below refers to times after which the plate was glued.

In Fig. 2.5a, we show an image of two 350 nm pinholes spaced by 6861 nm[1] on a DataRay WinCam, created by an optical system identical to that used for imaging single atoms. The point-spread function (PSF) of the optical system (Figure 2.5b) is derived from either of the pinhole images, while the magnification of the system is determined through their spacing.

Imaging a point-source through a finite numerical aperture (NA) system corresponds to a truncated, flat Fourier distribution in the Fourier plane, (i.e. after the source is collimated by the objective). From diffraction theory, the imaged point-spread function follows [83],

$$I(\rho) \propto \left(\frac{2J_1(\rho^*)}{\rho^*} \right)^2, \tag{2.1}$$

where $\rho^* = \rho/\rho_0$ and $\rho_0 = (2\pi \mathrm{NA}/\lambda)^{-1}$. For understanding the performance of the objective, we will use this as a model to extract the NA for which the objective is diffraction-limited; I will call this performance based number $\mathrm{NA_{DL}}$, to distinguish it from the NA associated with the aperture of the objective.

We aligned the objective in a test setup by optimizing the imaged spot size and we found

[1] The test target was created through electron etching, and came from Kapteyn and Murnane labs

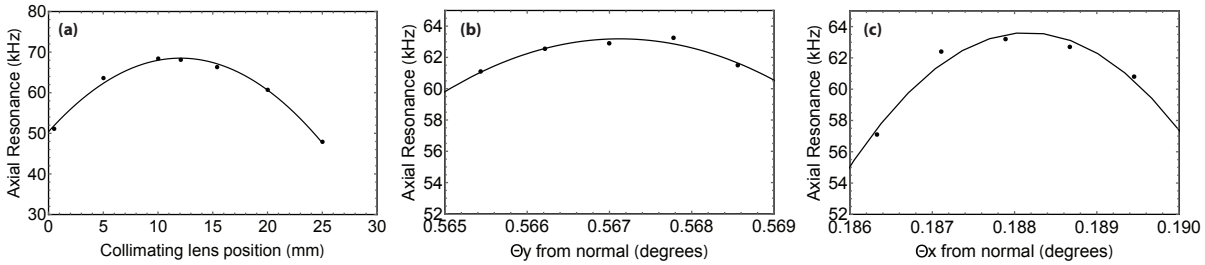

Figure 2.6: In-situ ASE lens alignment. We optimize the input beam collimation (a), and angular lens alignment in y (a) and x (c). The angles are quoted with respect to the normal of the cell window, to which the input beam is also aligned. The alignment signal is the axial trap frequency, which, in contrast to the radial frequency, is sensitive to both the spot-size and z length scale of the trap. The trap frequencies are measure with parametric excitation.

that the minimum was achieved by deliberately misaligning the lens optical axis from the cell window normal by $\{\theta_x = 0.19^o, \theta_y = 0.57^o\}$, and we observe a slight astigmatism. We determine the alignment angles by retro-reflecting a beam off the cleartran plate and observing the spatial deflection at a known distance; the angular deviations could either be from an additional aberration in the lens, or, more likely, from the cleartran plate being glued on at a slight angle. For our imaging wavelength of $\lambda = 780$ nm, we fit the imaged PSF in Fig. 2.5b to extract an $\mathrm{NA_{DL}} = 0.56(1)$, which implies that our lens is operationally diffraction-limited up to this NA. Lastly, the measured magnification from the test setup is 48.8(5).

After we placed the objective in the experiment, we optimized its alignment about these offline determined angles using the optical tweezer trap frequencies. These measurements, shown in Fig. 2.6b,c, correspond to the final alignment position of the objective. The input beam to the objective was aligned to better than 0.01 degrees to the normal of the cell window, despite the non-zero objective angle, and its collimation was also optimized on the basis of the atomic trap frequencies (Fig. 2.6a)

Further testing information and techniques will be documented in the future thesis of Brian Lester.

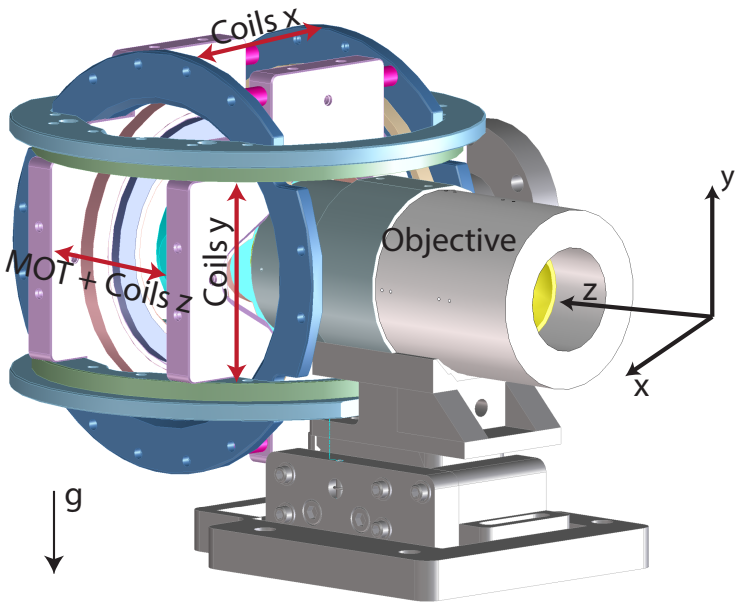

Figure 2.7: We designed and machined in-house a coil mount to fit around the cell and accommodate the spatial constraints imposed by the large objective. We performed numerical simulations in the Mathematica Radia package of the expected current to field performance for these coil pairs, which are each in the Helmholtz configuration. The created fields were consistent with the expectation at the $< 5\%$ level.

2.5 Coil mount system

We designed and machined in-house a coil mount system meant to conform to the spatial constraints of the objective and provide stable, fast magnetic field control (see Fig. 2.7). The coil frame is made from garolite phenolic for its low coefficient of thermal expansion. The mount supports eight coils, each independently wound: three coil pairs are for arbitrary three-dimensional tuning of the magnetic field quantization axis, and a fourth pair concentric with the z-axis provides the MOT gradient. Once the entire system was wound, glued and mounted, each coil was separately servo-tuned for fast switching between 0 to 5G in less than 1 ms. We did not want to have wait for the fields to settle at many times during the experiment, which motivated this low eddy-current, temperature stable, fast setup.

2.6 Optical rail system for creation of optical tweezer arrays

As discussed, we were eager to have the capability to scale to more particles/tweezers and explore quantum dynamics experiments in this platform. For the creation of multiple optical tweezers, we employ two large (3 mm, $Te0_2$ longitudinal mode) crystal AOMs with square aperture: each AOM realizes angular deflections in the Fourier plane which are converted into spatial deflections when focused by the objective. In designing the system, we were (excessively) paranoid about vibrations of the optical tweezers heating up the atoms. The primary mechanism for this to occur would be vibrations of each of the optical components that shape the tweezer beam. To combat this problem, a monolithic rail system was designed that is schematically displayed in Fig. 2.8.

The rail system was tested and shown to create aberration-free beams appropriate to be focused by the objective. As illustrated in the figure, we can create a linear array of two spots by introducing two frequencies into one of the AOMs. Due to the magnification factor (m=20) of the telescope at the end of the rail system (which is necessary to blow up the beam to exploit the high NA objective), a pair of 1:1 relays are used to avoid aberrations induced by the beam deflecting off the optical axis; the relays image each of the final deflections onto the back focal plane of the "GLC" lens in the telescope.

2.7 Tools of the trade for single atoms in optical tweezer potentials

2.7.1 Typical experimental sequence

Performing ultracold quantum dynamics experiments with sideband-cooled neutral atoms in optical tweezers is distinguished in some crucial ways from an evaporatively cooled gas of ultracold atoms. Perhaps the most significant difference is in the order in which the experiment sequence occurs, illustrated in Fig. 2.9. Initially, single atoms are stochastically loaded into optical tweezers, and are subsequently imaged to determine whether there is an atom each optical tweezer. Despite the stochasticity of the loading, the associated entropy is completely removed since we sort and analyze all of our data on the basis of this initial image. Therefore, in contrast to an evaporatively

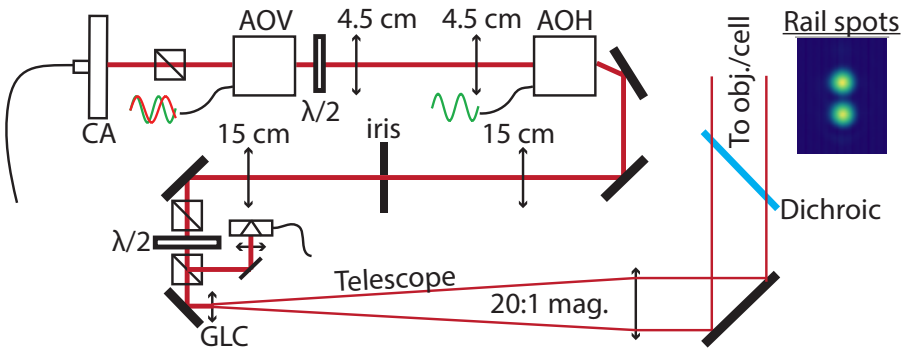

Figure 2.8: This is a schematic of the rail system used to generate the light focused by the objective to form the optical tweezers. The light emerges from an AR-coated FC-PC connectorized optical fiber and is collimated to $2w_0 \approx 1.4$ mm by an asphere "CA". It then passes through AOV, an AOM which realizes vertical (y) angular deflections. A 1:1, 4.5 cm relay images the center of AOV on to the center of AOH, an AOM which realizes horizontal (x) defections. A second 1:1, 15 cm relay images the center of AOH onto the center of the first lens in the telescope, "GLC". The beam is blown up by a factor of 20 (which commensurately demagnifies the angular deflections) once it is collimated by a 30 cm achromat. We have observed that the AOMs can rotate the polarization of the beam in a temperature dependent fashion: a pair of polarizing beamsplitters and a half-wave plate fix the fraction of light that is picked off to a photodiode for intensity stabilization. A pair of resulting spots imaged by a 1 m achromat are displayed when two RF tones of 7.5 MHz spacing are introduced to AOV.

cooled system, imaging of the spatial distribution of the particles can occur before cooling the motional degrees of freedom, and provides high-fidelity information on the initial conditions.

After this image, we subsequently initialize all uninitialized degrees of freedom of the atoms, namely their spin and motional state (the first image specifies their position) via optical pumping and ground-state cooling. The atoms are now with high fidelity in a pure quantum state, which is the starting point for a quantum dynamics experiment. The tweezer spacings and depths are modified in real-time, an experiment is performed, and then the atom(s) are separated and imaged again. We can then follow the atoms between known initial and final conditions.

2.7.2 Single atom loading

The loading of single atoms into optical tweezer is surprisingly robust once the proper parameter regime is reached. This is slightly complicated by the fact that the MOT configuration is funky for experiments in which the regions of MOT loading and tweezer formation coexist. We

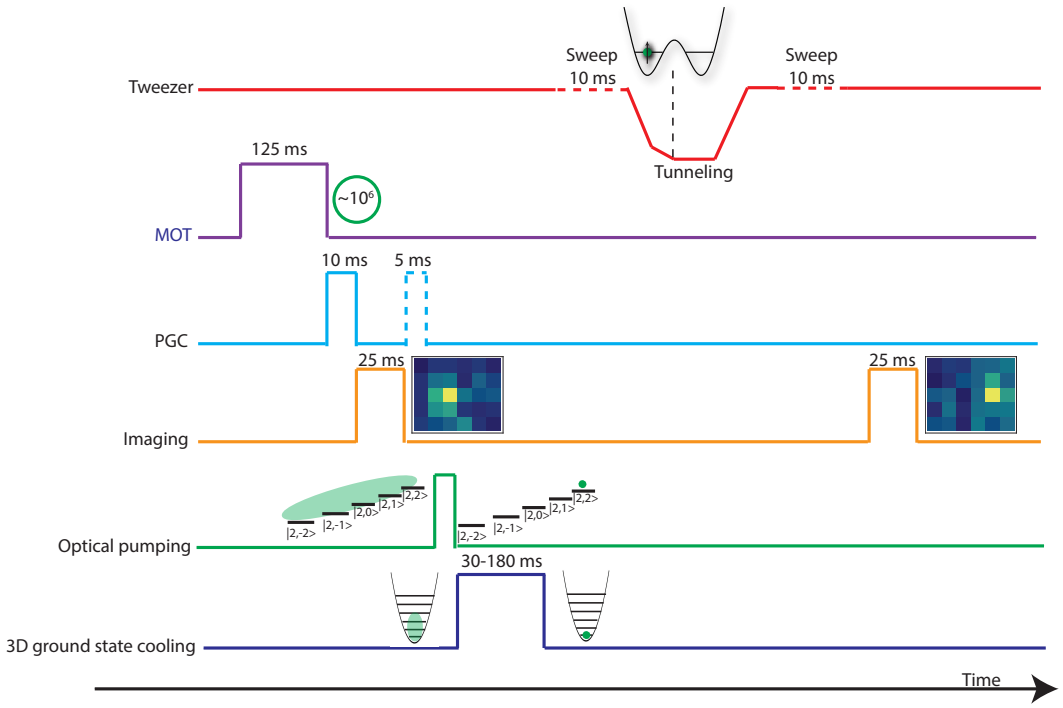

Figure 2.9: Here we illustrate a typical experimental sequence for performing a quantum dynamics experiment. A MOT of up to 10^6 atoms is formed, and free space polarization-gradient cooling (PGC: reduced intensity, -70 MHz cycling detuning, zeroed magnetic fields) cools the cloud to approximately 10 μK. At this point, some number of atoms are loaded into the tweezers and undergo light-assisted collisions [3, 5] in the presence of the red-detuned cooling light, thereby reducing the atom number in each tweezer to 0 or 1. The atom populations in each optical tweezer is imaged, and the trapped atoms are re-cooled with PGC (temperatures from which are discussed in Chapter 3). We then independently initialize the spin and three-dimensional motional state of each atom with optical pumping and Raman-sideband cooling (see Chapter 3). The optical tweezers are then adiabatically ramped to a new configuration associated with a Hamiltonian of interest; dynamics ensue. The depths and spacing of the tweezers are then varied diabatically with respect to the timescales of the aforementioned Hamiltonian, into a configuration amenable to spatially-resolved single atom detection. In the sequence shown above, the atom's position switches from the left tweezer to the right. The majority of experiments in this thesis occur in 0.5 seconds or less.

provide here a summary of the parameters for the MOT beam geometry in Fig. 2.4.

We have a stable single-atom loading probability of about 60% that has persisted now for nearly three years with little tweaking.[2] Due to the geometry, it was not obvious what was the appropriate cycling light saturation parameters $s_0 = I/I_{\text{sat}}$ for each of the beams participating

[2] As will be discussed in Chapter 4, we observe some probability that two atoms in an optical tweezer leave one atom upon undergoing light assisted collisions; this is likely responsible for the increase above 50% loading fraction.

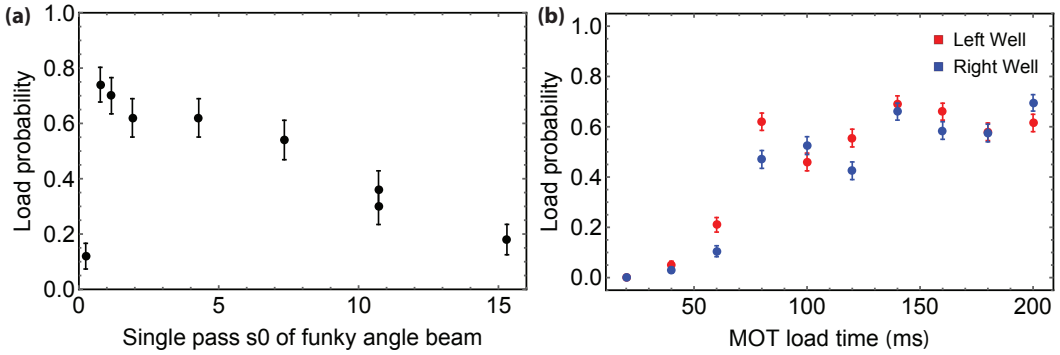

Figure 2.10: Single atom loading and imaging. (a) We set the single-pass peak intensity of each of the large MOT beams to a saturation parameter of $s_0 = 2.0$, and each of these beams delivers 1 mW of repump light; the MOT gradient was set to 9 G/cm. We then vary the cycling light saturation parameter of the funky-angle beam and measure the load probability. For each data point, the bias fields were reoptimized along all three axes, since changing the funky-angle beam intensity moves the MOT position; the plotted load probability corresponds to the peak-loading position. (b) Setting the funky-angle beam to a saturation parameter of $s_0^{Funky} = 1.12$, we measure the single atom load probability. Typically we operate the experiment with a 125 ms load time and observe 60 to 63% load probability. Other relevant parameters include the cycling light detuning of -10 MHz and the optical tweezer depth of 1.1 mK.

in the MOT ($I_{\text{sat}} = 1.67$ mW/cm^2 for circularly polarized light [4]). We study this by fixing the large MOT beam parameters as well as all other parameters of the MOT, and then vary the saturation parameter of the funky-angle beam (see Fig. 2.10). We observe that a similar (perhaps a bit smaller, the load is stable over $0.5 \leq s_0^{Funky} \leq 5$) saturation parameter is appropriate to this beam compared to the others, despite the fact that it projects onto plane defined by the large beams. We set the funky-angle beam to a saturation parameter of 1.15 and observe a rapid load rate (Fig. 2.10b), saturating to around 60% after 125 ms.

2.7.3 Single atom imaging

After loading, we allow the cooled cloud to drop (by extinguishing the PGC beams) for 25 ms and then perform molasses imaging of the atom population (0 or 1) in each optical tweezer. We have experimented with two configurations for imaging: using all of the beams used for the MOT, or using a single beam pair (indicated in Fig. 2.4). For the former configuration, we observe slow fluctuations in the atom counts, which we attribute to slow wavelength-scale variation in intensity gradients

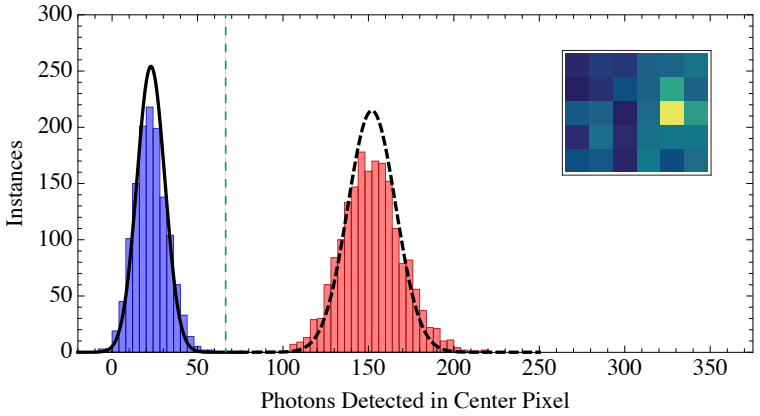

Figure 2.11: Typical imaging data observed in the experiment for a 25 ms collection. The photon counts here are computed on the basis of the brightest pixel in the camera image shown in the figure; the left peak corresponds to our background signal (blue), and the right peak corresponds to the atom signal (red). The black lines correspond to the Poissonnian expectation for the peak widths given the fitted center value of the counts for background. We find reasonable agreement, and hence are reaching the limit of imaging fidelity for a Poissoinian distribution of photon counts. The green dashed line is the threshold calculated to minimize detection errors.

arising from interferences between beams from different retro-reflected pairs. While dithering the retro-reflecting mirrors greatly mitigated this affect, using a single retro-reflected beam pair was a simpler solution, the performance of which I will discuss here. Crucially, this beam pair projects along the z and x direction allowing for three-dimensional cooling during imaging.[3]

In Fig. 2.11, we show typical imaging data acquired in the experiment for 25 ms camera exposures. The imaging beam has a fairly high saturation parameter of $s_0 = 9.3$, and a detuning of -38 MHz from the light-shifted cycling transition due to the 1.1 mK trap. We optimize the detuning and intensity by maximizing counts and minimizing any atom loss from heating; we choose parameters that are well below the regime in which we begin to see atom loss. We observe two peaks corresponding to the background and atom peak, but no two-atom peak; this is a symptom of the light-assisted collisions. The peaks are well-resolved and we can deduce the presence of an atom to much better than 1% by comparing to a threshold (dashed green line in figure) computed on the basis of the peak positions and widths. Analysis of our imaging system losses (objective

[3] Due to the degeneracy in x and y, we observe full radial cooling despite beam projection along only one radial axis. This is noted in the Chapter 3 as well.

transmission, dichroic reflection, four mirrors, interference filter transmission, quantum efficiency of the camera) and estimated atomic scattering rate show reasonable agreement (to the level of a factor of two) with the observed counts.

2.8 In-situ characterization of the optical system

In section 2.4, we discussed tests primarily addressing the performance of the ASE objective in an external setup meant to mimic that in the experiment. However, since this setup does not exactly match the experiment (e.g. though the cell window should be very similar, they are not literally the same window), and these tests primarily address the imaging as opposed to the creation of optical tweezer potentials, we performed additional in-situ tests that are summarized here.

2.8.1 Imaging performance

We can analyze the performance and PSF of our imaging system by treating a single atom as a point-source emitter. In the atom images acquired in the experiment, we do not have sufficient signal to observe the wings of the Airy-disk function, and so we fit the data (cross-sections) to a Gaussian,

$$f(x) = Ae^{-2(x-x0)^2/w^2} + o_{bg}, \tag{2.2}$$

where A is the amplitude of the atom peak, $x0$ its position, and w the (optical) Gaussian waist. The last term o_{bg} accounts for our imaging background. The goal is to determine the NA for which our system behaves diffraction-limited, which means we ultimately need to compare to an Airy-Disk pattern. To convert between the fitted Gaussians, we fit ideal Airy-disk data (Fig. 2.12a) of varying NA (Fig. 2.12c) to ascertain a conversion function (numerical interpolation) between the fitted Gaussian waist and the effective diffraction-limited NA of the system. Using the model in Eq. 2.2, we fit an atom image (Fig. 2.12b) corresponding to an accumulation image after running the experiment 1000 times. We then aperture the objective at varying diameters, and hence effective NA, and observe how the fitted Gaussian waist of the atom image varies (Fig. 2.12d). This last measurement is equivalent to what is accomplished numerically in Fig. 2.12c, and allows us to

extract the NA for which our imaging performance saturates. We observe a 780 nm minimum spot size of $w_{780} = 0.65(4)\mu$m, which corresponds to a operational diffraction-limited $\mathrm{NA_{DL}} = 0.51(4)$. Comparing to the tests done out of the setup, which showed a diffraction-limited $\mathrm{NA_{DL}} = 0.56(1)$, this is on the edge of the error bar. The imaged spot sizes in Fig. 2.12d are clearly above the expectation from Fig. 2.12c, suggesting some amount of residual aberration above 0.5 NA. If we extrapolate from these data to the expected performance for the created optical tweezer (assuming an aberration-free input beam), we expect a waist $w_{850} = 0.71(4)\mu$m. As will be discussed in section 2.8.2, in-situ measurements of the optical tweezer potential are consistent with w_{850}. This agreement, however, excludes the effect of clipping of the Gaussian input beam, which yields an input beam somewhere between uniform and Gaussian illumination; the complication associated with this, along with other unknowns, motivated the independent characterization discussed below. In conclusion, the measurements in this section suggest an in-situ performance of our imaging system between 0.5 NA and 0.6 NA with sub-wavelength spatial scales.

2.8.2 In-situ characterization of the optical tweezer

The analysis of the above section provides a good measure of the optical performance of the objective, which strongly influences the quality of the optical tweezer experienced by the atoms. However, the input beam that is focused by the objective to form the tweezer also determines the final spot realized in the experiment. Therefore, to separately assess the tweezer performance, we measure the peak intensity experienced by the atoms [84] and the radial trap frequency, with which we can back out the Gaussian waist associated with the potential. We have found that it is essential to perform a detailed characterization of the tweezer potential in order to perform theoretical comparisons with the measured tunneling and two-particle interaction energy extracted from the experiments in Chapter 4 and 5.

The radial trap frequency for a Gaussian potential is,

$$\omega_r = \left(\frac{4V}{m_{\mathrm{Rb}} w_0^2}\right)^{1/2}, \tag{2.3}$$

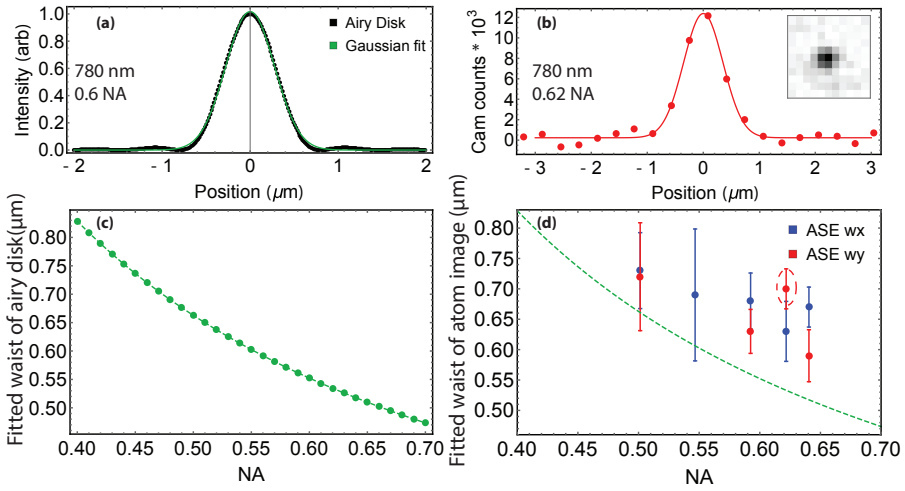

Figure 2.12: In-situ characterization of the atom imaging performance. (a) Fitting a Gaussian to an ideal Airy disk imaged by a 0.6 NA system at 780 nm. (b) A cross-section of the atom-image in the inset. For these data, the aperture of the objective was set to 26.5 mm, corresponding to a 0.62 NA. The red line is a Gaussian fit according to the fit function in the text. (c) Plot of fitted Gaussian waist v. ideal imaged Airy-disk NA, for creating an interpolation (dashed line) between Gaussian waist and Airy-disk NA for analysis of single-atom imaging data. (d) We plot the fitted atom image as we vary the objective aperture, and the corresponding NA of the imaging system. The red circled point was extracted from the data in (b). The green-dashed line is the interpolation from (c).

where V is the trap depth, m_{Rb} the mass of ^{87}Rb, and w_0 the waist we seek. In principle, this expression could be further simplified by assuming that V is determined by the peak intensity of a Gaussian of waist w_0 and with total power P. However, if there are aberrations in the resulting potential, then not all of the power that enters the objective reaches the central spot, and is instead manifest in aberrations (e.g. rings from spherical, offset lobes from coma, airy-disk character from clipping, etc). Therefore, we measure the peak intensity experienced by the atom to determine V, and measure the trap frequency to determine ω_r, which together constitute a measurement of w_0.

We measure V by probing the optical light shift on the cycling transition due to the optical tweezer light. Since the atom sits at the position of peak intensity, the light shift it experiences is a good meter of the peak intensity of the optical tweezer. On a spin-polarized atom in $|2,2\rangle$, we probe the light shift by scanning the frequency of a σ^+-polarized probe and measure the position of peak loss (insets of Fig. 2.13a) as a function of power in the telescope (Fig. 2.13a). We then calculate

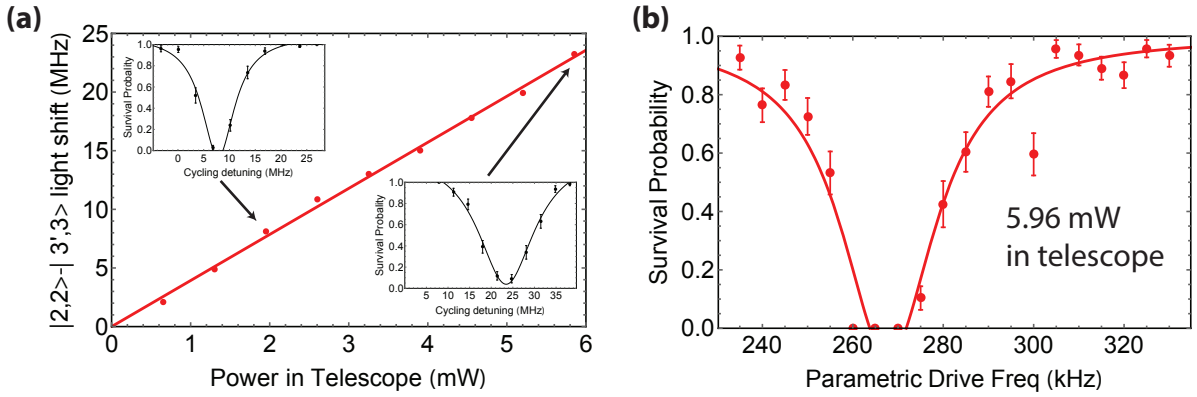

Figure 2.13: Characterization of the optical tweezer. (a) We plot the frequency position of an atomic loss resonance after exposure to σ^+-polarized cycling light as a function of the optical tweezer depth. The inset plots correspond to the indicated data points in the main plot. (b) A parametric excitation resonance from which we extract the tweezer radial trap frequency for a given input power.

the optical light shift [84, 85] on the cycling transition for a given intensity. The slope of this line provides a conversion between power in the telescope and intensity at the atoms, and, in turn, the depth V when combined with the light shift calculation. For the telescope power that yields the trap frequency measurement of $\omega_r = 134$ kHz in Fig. 2.13b, we measure a depth of 1.01(5) mK. This implies a waist of $w_0 = 0.71(1)$ μm, including a 4% correction to take into account the exact shape of the potential for an apertured Gaussian input beam.[4] This closely agrees with the measurements in Section 2.8.1, which implies that there is negligible wavefront error in the input beam.

2.9 Creation and control of a double-well potential formed by optical tweezers

A key feature of our experiment is the ability to tune the primary parameters of a double-well potential: the overall depth, the spacing of the well minima, and the relative depth ("bias") of the minima. The AOM-based control platform here (AOV and AOH in Fig 2.8) readily provides these latter control knobs. The overall depth is controlled with a standard intensity control setup via

[4] See the future thesis of Brian Lester for more details.

the photodiode in Fig. 2.8 and an AOM prior to the optical fiber that carries the tweezer light to the optical rail. For experiments performed with trap depths less than 50 kHz, we used a double-photodiode setup to increase our dynamic range at the expense of bandwidth. In this section, we discuss tests done on the bias and spacing control.

For the data discussed in this section, the amplified RF tones that create the double-well come from a dual channel Tektronix AFG3102 synthesizer. The synthesizer can perform programmable frequency sweeps that we trigger during the experiment. These sweeps allow us to dynamically reconfigure the tweezers for tunneling experiments.

2.9.1 Relative intensity control of a double-well

Here we briefly show tests performed to confirm the linearity and resolution of the double-well bias, data from which is shown in Fig. 2.14. To create the two RF tones that form the tunable double-well, we have one fixed amplitude RF tone and another tone which passes through a mixer operated in saturation. This latter RF tone is mixed with a DC control voltage that finely tunes the output. The two RF tones are then combined on a power-splitter and amplified by Mini-circuits ZHL-1-2W amplifier.

For the tunnel-coupled double-well potential, it is necessary to tune the absolute bias at the level of a fraction of the tunnel-coupling. The total intensity in the double well determines the overall depth of the potential, while the fractional bias is tuned by the relative RF power in each RF tone creating each spot of the double well. The absolute bias is the product of the fractional bias and the total depth. Therefore, for a typical tunnel-coupling of 500 Hz and tweezer depth of 100 kHz, this implies that we require fractional bias control at less than a part in thousand. The data in Fig. 2.14b corroborate this level of control; in retrospect, a finer scan might have been appropriate, but the precision with which we could extract the peak intensities of the Gaussians was also limiting.

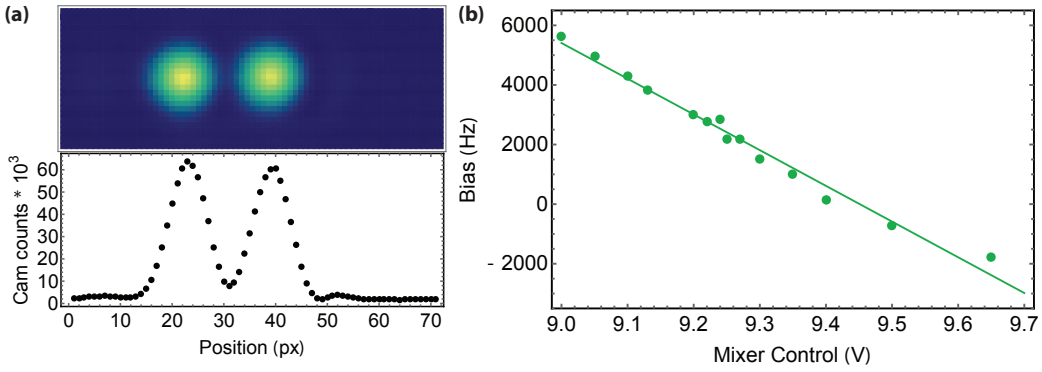

Figure 2.14: (a) Shown are two spots formed by focusing the light directly from the collimation rail with different relative intensity and the associated cross-section of these spots. The cross-section is meant to illustrate the resulting double-well potential; for red detuned light, the peaks turn into potential minima. (b) The relative well depth in units of Hz as a function of the DC control voltage discussed in the text. The absolute bias plotted is determined by the measured fractional bias from images such as those in (a) and the experimentally measured single tweezer depths for tunneling (see Sec. 2.8.2).

2.9.2 Spacing control of a double-well

The other ingredient to the double well is the spacing between the well minima. This is experimentally controlled via the frequency difference between the two RF tones comprising the double well; the resulting spacing is determined by the properties of the AO crystal, the magnification of the telescope, and the effective focal length (EFL) of the ASE lens. While we can estimate the frequency difference to spacing conversion based on these parameters, the tunnel coupling in the double well is set by the wave-function overlap between the localized wave-packets in each well, which have a spatial extent of about 100 nm in the tunneling direction. Hence, we require control much finer than this length scale, and our knowledge of this part of the optical system is not sufficiently precise.

We calibrate the spacing between the optical tweezer traps as a function of the frequency difference of the RF tones in each AO by imaging the atom locations, shown in Fig. 2.15. Given our knowledge of the imaging magnification, we can compute the spacing of the atoms. From the data displayed, and propagating error in our magnification, we measure 0.203(3) μm/MHz for the horizontal double well, and 0.209(3) μm/MHz for the vertical double well. We note that an

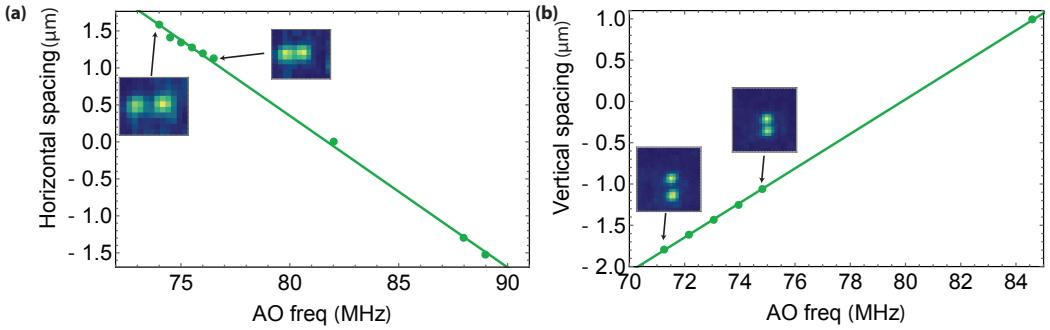

Figure 2.15: Calibrating the frequency control of the double-well spacing. Imaged atom spacing as function of varying the frequency of one tone while keeping the other fixed at 80 MHz for AOH (a) and AOV (b)

estimate of the expected dependence from the rail (based on our independent knowledge of the optical elements and properties of the AOMs) is consistent with these measurements. We also checked this calibration by imaging the spots directly out of the rail (i.e. as in the spots Fig. 2.8); while this does not test the ASE EFL, it does test the rail magnification and AO crystal properties, and this measurement is completely consistent.

2.10 Spin-sensitive detection

Through out this thesis, beginning with the sections below, we make use of spin-sensitive detection of the atom. We detect whether the atom is in $F = 2$ or $F = 1$ by applying resonant cycling light, which ejects the atom from the optical tweezer if it was in $F = 2$. Therefore, the hyperfine state is mapped onto the presence or absence of an atom in the trap. Typically the fidelity of this process is greater than 95%, especially when we drop the depth of the trap for the push-out phase. For the latter case, the fidelity is at the limit of what we can detect with our statistics, but it is on the order of 99%.

2.11 Optical pumping in an optical tweezer

One of the most important parts of our experiment is the optical pumping for spin preparation of the atom in a "dark state". Optical pumping operates by successively driving a set of transitions

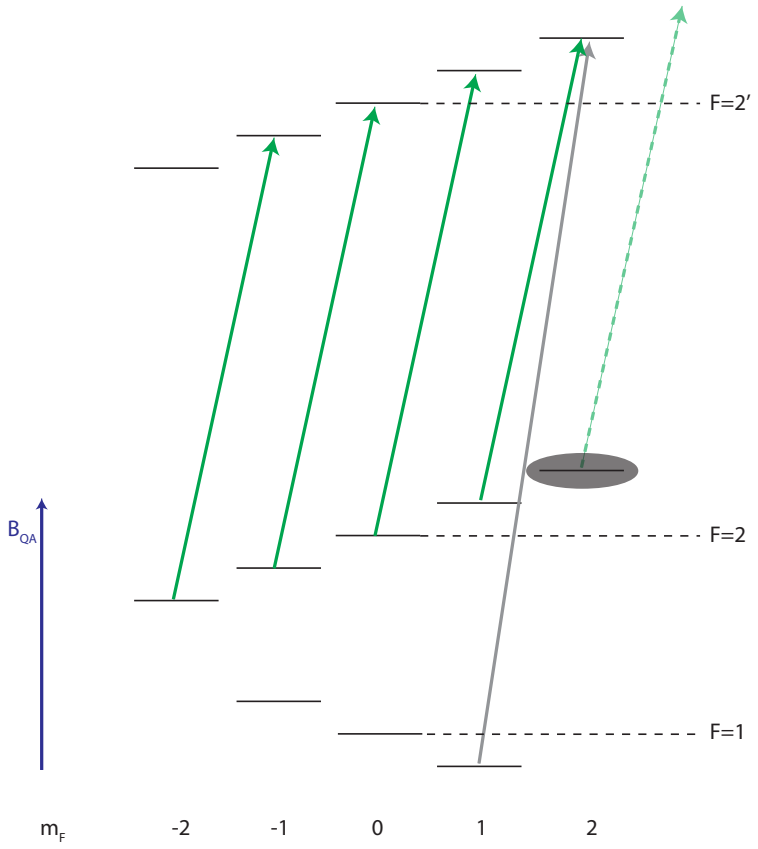

Figure 2.16: The tweezer-trapped atoms are illuminated with optical pumping and repump light, each circularly polarized. $|F, m_F\rangle = |2, 2\rangle$ (encircled by a dark blob) is decoupled from these beams because no transition exists that can be driven with these polarizations from this state. The green lines indicate σ^+ light tuned to the 2-2' transition; the gray is the σ^+ repump light on the 1-2' transition.

until the atom reaches a state, the "dark state", which is decoupled from the driving light. The dark state is crucial because its darkness is ultimately responsible for high fidelity ground-state cooling, as discussed in Chapter 3. Therefore, while preparation in a particular spin-state is significant, more important is the degree to which the dark state is decoupled from the pumping light. It turns out that these are one and the same goal, but it is worth stressing that what we ultimately seek is a high quality dark state. This section considers the various procedures and issues we confronted towards optimizing the dark state.

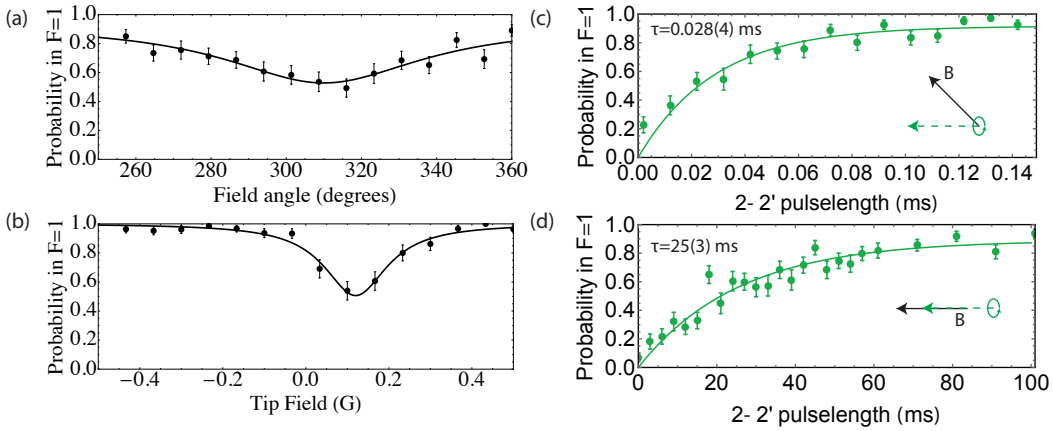

Figure 2.17: Optical pumping optimization by measuring the depumped fraction (into $F = 1$) after application of the $2 - 2'$ light. (a) Alignment of the optical pumping quantization axis by varying the angle of an added fixed size field (0.1 G); the parameters of the x coil pair are fixed to a 3 G field during this procedure. The pulse length is set to near the $1/e$-time for an initial set of quantization axis parameters. (b) Varying the amplitude of this added field at fixed angle in the $y-z$ plane for the same depumping time parameters. (c) Measurement of the scattering rate of the optical pumping beam when the quantization axis points approximately 45^o to the beam propagation direction; this largely compromises the dark state because the polarization experienced by the atom is now mixed. (d) Setting the quantization axis to the optimized parameters and measuring the depumping rate. We observe a nearly 1000-fold suppression of the depumping of the dark state between (c) and (d). We also note that this procedure both compensates angular mismatch between our coil axes and the optical pumping beam, as well as any background magnetic fields not sufficiently nulled.

2.11.1 Optimizing the optical pumping

Creating a dark state is achieved typically by using well-defined polarization light, the requirements for which are excellent preparation of the photon polarization, and precise alignment of the quantization axis to the optical pumping beam propagation direction. Fulfilling these requirements ensures that the atom experiences light with pure polarization, resulting in a very dark "dark state". Our optical pumping setup is illustrated in Figure 2.16. We use σ^+-polarized repump and optical pumping light since it minimizes the number of photons to reach the dark state of $|F, m_F\rangle = |2, 2\rangle$ (this is discussed in more detail in Chapter 3). To measure the dark state quality, we simply optically pump to $|2, 2\rangle$, and then illuminate the atom with the optical pumping light in the absence of repump. The branching coefficients from the excited $F = 2'$ manifold to the ground hyperfine levels $F = 1$ and $F = 2$ are equal and $1/2$ [4, 56]. If the light seen by the atom is pure

σ^+, then it will remain in $F = 2$. However, any fraction of the light that is π or σ^--polarized will depump the atom to $F = 1$ after, on average, two scattering events. We use this to probe and optimize our dark state.

In Figure 2.17, we display exemplary data of this optimization process. We set the depumping time to be near the $1/e$ time and vary the quantization axis direction, to optimize the alignment of the quantization axis to the optical pumping beam. We initially set a large field of 3 G in the $-x$ direction, and then add a small field in the $y-z$ plane of about 100 mG. We vary the angle of this added vector in the $y-z$ plane and observe the change in the depumping fraction (Fig. 2.17a), and set it to the minimum value. As shown in Fig. 2.17b, we then vary the magnitude of this vector, and again choose the value for which the depumping ($|2,2\rangle$ darkness) is minimized (maximized). We will typically iterate on this procedure a few times. The polarization of the light, initialized with a Glan-taylor polarizer and tuned with a half-wave plate and quarter wave plate (to compensate for the window birefringence), is optimized with this depumping signal as well in a two-dimensional walk of the wave plates.

After the above procedure, we observe the performance quantified in Fig. 2.17c,d. In Fig. 2.17d, we use the quantization axis parameters acquired through the optimization procedure, and observed a $1/e$ depumping time of $\tau_{DP} = 25(3)$ ms, which should be compared to the scattering rate of the optical pumping beam. We measure the scattering rate in-situ by rotating the quantization axis so that it is 45^o to the optical pumping beam propagation direction, and measuring the depumping time (Fig. 2.17c) of $\tau = 28(4)\mu s$. This constrains the relative intensities of $\frac{I_{\sigma-}+I_\pi}{I_{\sigma^+}} < \frac{1}{1000}$, implying that we suppress the unwanted scattering events to at least a part in a thousand.

Lastly, for the beam powers used here and with the optimized quantization axis, we can pump with the σ^+ repump and optical pumping light to $|2,2\rangle$ in a $1/e$ time of $\tau_{OP} = 50$ μs, with which we can estimate a steady-state population [86] in $|2,2\rangle$ of $P_{2,2} = 1 - \frac{\tau_{OP}}{\tau_{DP}} = 0.998$.

2.11.2 Vector light shifts and effects on the optical pumping

Vector light shifts from the optical tweezer also impose a possible limitation on the dark state quality. Here we discuss data that displays evidence of this effect, which also offers an opportunity to briefly discuss this unique feature of the optical tweezers.

For a tightly focused beam, in which the length scale associated with the spot size is comparable to the optical wavelength of the light, there is a large gradient in the electric field that occurs on a wavelength scale. Even though the input light to the tweezer is linearly polarized, an atom trapped at the focus experiences circular polarization components in a spatially dependent fashion. The mechanism for this is illustrated in Fig. 2.18a: the rotation of the electric field vector on either side of the focuses yields circularly-polarized light of opposite sense on either side of the potential. The helicity of the light couples to the atom's spin identically to a magnetic field. We numerically compute these effects by propagating the vector-diffraction integrals in Ref. [87] to compute the polarization components in the focal plane, which we then plug into expressions for the vector light shift from Ref. [56]. While we will now focus on how this informs the optical pumping, we have observed that by proper arrangement of the quantization axis we can exploit these effective fields to drive microwave transitions sensitive to the atomic motion [60].

A calculation of the effective magnetic fields is displayed in Fig. 2.18b: it points along the y-direction and varies along the x-direction. For our spot size and wavelength, this yields an effective magnetic field gradient of 1.41 G/μm. We can then estimate the spread in magnetic field experienced by a thermal atom: for an atom at 15 μK in a trap of radial trap frequency $\omega_r/(2\pi) = 140$ kHz, the wave packet size is approximately 44 nm, implying a spread in magnetic field of $\delta \mathrm{B}_{\mathrm{eff}} = 62$ mG $\hat{y}$. For a quantization axis externally applied at $B_{\mathrm{QA}} = 3\mathrm{G}\ \hat{x}$, this implies an angular variation of the quantization axis across the atoms motion of $\delta\theta = \tan^{-1}\left(|\delta \mathrm{B}_{\mathrm{eff}}|/|B_{\mathrm{QA}|}\right) = 1.2^o$. We expect this then to limit the final dark state we can achieve: it imposes the constraint $\frac{I_{\sigma^-}+I_\pi}{I_{\sigma^+}+I_{\sigma^-}+I_\pi} < \frac{0.2}{1000}$.

To test the role of the vector light shifts, we varied $|B_{QA}|$ and the trap depth and measured

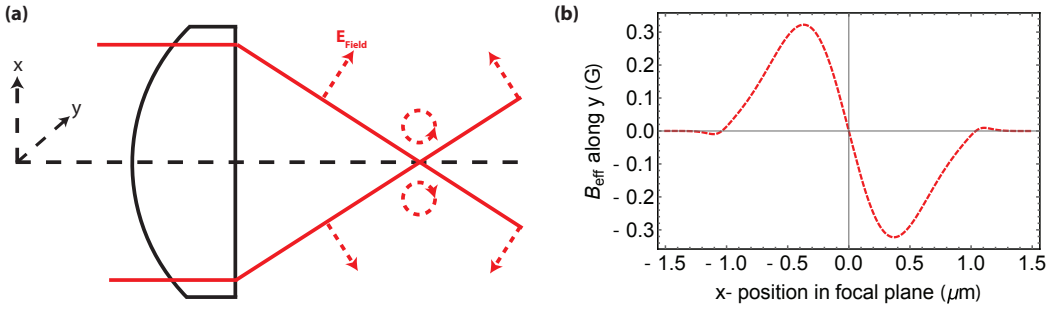

Figure 2.18: (a) Mechanism by which tightly focused linearly light couples to circularly polarized light. Because the electric field rotates on either side of the focus on the scale of a wavelength, it adds helicity to the light. (c) We numerically compute the electric field components at the focus for a 0.51 NA optical system at 852 nm, and a trap depth of 1.1 mK. Here we approximate that the tweezer beam is uniformly illuminating our objective, even though we in fact aperture the beam at its $1/e^2$ waist of 30 mm. Our calculation therefore could exceed the true gradient by 15% [6]. For the purposes of this illustration I rotated the coordinate system here because our polarization is in the horizontal plane and it is hard to illustrate the electric field gradient when it points out of the page.

the depumping time τ_{DP}, as shown in Figure 2.19.[5] The former determines the size of the angular deviation $\delta\theta$ while the depth determines the size of the effective magnetic field gradient. The blue and red data correspond to two trap depths that differ by about a factor of 20. For both cases, we see as expected that a larger quantization field suppresses depumping, and, furthermore, the deeper trap experiences a greater depumping rate (smaller τ_{DP}) for the same quantization axis. Note that for the smaller quantization axes used in Figure 2.19, the lower bound on polarization purity presented in the previous paragraph would be significantly higher. These measurements are consistent with our hypothesis that the effective magnetic fields influence the dark state purity, however, further modeling would be necessary to corroborate this with a quantitative comparison.

2.12 Two-particle spin-preparation

The ability to perform coherent spin rotations is critical in a number of the experiments discussed in this thesis. These capabilities include tweezer-resolved spin rotations, so that we can create nearly arbitrary two-particle spin states for the Hong-Ou-Mandel and spin-exchange studies.

[5] The quantization axis is 3 G for the initial optical pumping stage.

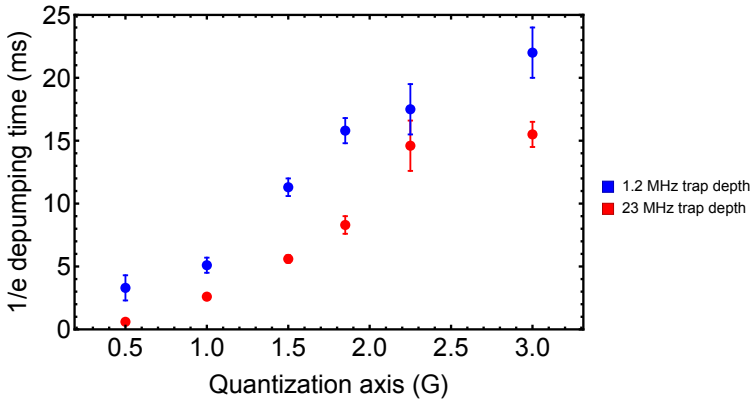

Figure 2.19: We measure the depumping lifetime τ_{DP} for two trap depths as a function of the magnitude of the quantization axis. For large quantization axis (trap depth), we observe a suppression (increase) of depumping. For each quantization axis used here, the field angle and tip field were optimized to minimize depumping; for each depth the optical pumping beam was resonant with the light-shifted transition. However, we later determined that the quarter wave plate angle could have been further optimized, which is why neither data set reaches the $\tau_{DP} = 25$ ms from the previous section. The scattering rate of the optical pumping beam (~ 100 kHz) was kept constant to $\sim 10\%$ over the entire data set presented here, including the effect of the magnetic field shifts of the optical transition (1.4 MHz).

Here I will summarize important aspects of these capabilities in our experiment.

2.12.1 Microwave rotations

While many of the spin manipulations performed in this thesis are accomplished with Raman transitions, microwave rotations are also used frequently. The microwave source is a single microwave synthesizer (Rohde-Schwartz SMF100A), which subsequently is amplitude modulated via a Miteq pin-diode for pulse-shaping. The resulting waveform passes through a 10 W Miteq amplifier, and the signal is delivered to the atoms via a sawed-off waveguide. The waveguide is outside vacuum and its tip sits approximately 5 cm from the atoms. We can reach 50 kHz Rabi rates in this fashion.

In Fig. 2.20, we show typical microwave spectra and Rabi oscillations after spin-polarizing the atom in the $|2,2\rangle$ spin state and driving the $|2,2\rangle \leftrightarrow |1,1\rangle$ transition. In Fig. 2.20a, we fix a square pulse area to π and scan the frequency of the microwave across the resonance in 3 G magnetic field. We typically observe up to 99% contrast when correcting for atom loss, and we observe increasing

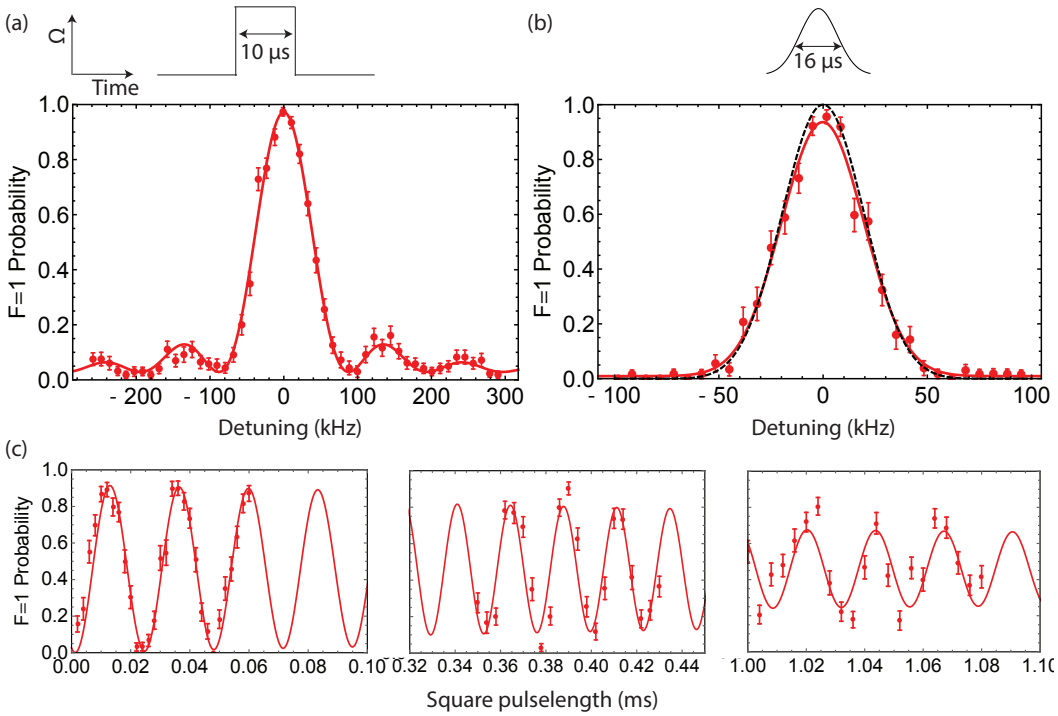

Figure 2.20: Microwave spectroscopy on single atoms (a) A square pulse is applied to a spin-polarized atom in $|2,2\rangle$ in a 3 G field. The Rabi rate is 50 kHz, and the fit is the expected response for a driven two-level system on resonance with a 10 μs pulse. (b) A temporally Gaussian pulse is applied with the profile indicated in the figure. The red line is a fit to a spectral Gaussian, while the black line is the response expected via numerical evolution of the Schrodinger equation for this pulse profile and the measured Rabi rate of 36.9 kHz. (c) Typical Rabi oscillations after application of a resonant square-pulse of varied pulse area.

loss of contrast as we reduce the Rabi rate; we also observe a 100 μs free-precession time, which implies 1 mG fluctuations of the magnetic field assuming a Gaussian distribution of noise. When we perform ground-state cooling these mitigating features persist, which largely rules out trap light shifts and vector light shifts ($\pm$0.65 mG for a 3 G quantization axis) as the exclusive contributors. In Fig. 2.20c, we show Rabi oscillations for a square pulse of varied area: for this Rabi rate we observe a damping time of 1.5 ms.

In Fig. 2.20b, we perform Gaussian pulse-shaped spectroscopy. An arbitrary waveform generator provides a Gaussian modulation of the power ($P(t) \propto e^{\frac{t^2}{2\tau^2}}$) to the pin-diode with $\tau = 3.85$ μs: the exact waveform supplied is not Gaussian, but calibrated to produce a Gaussian modulation of the microwave power. This yields a $2\tau = 16$ μs in the Rabi rate (as in the figure) and with a total

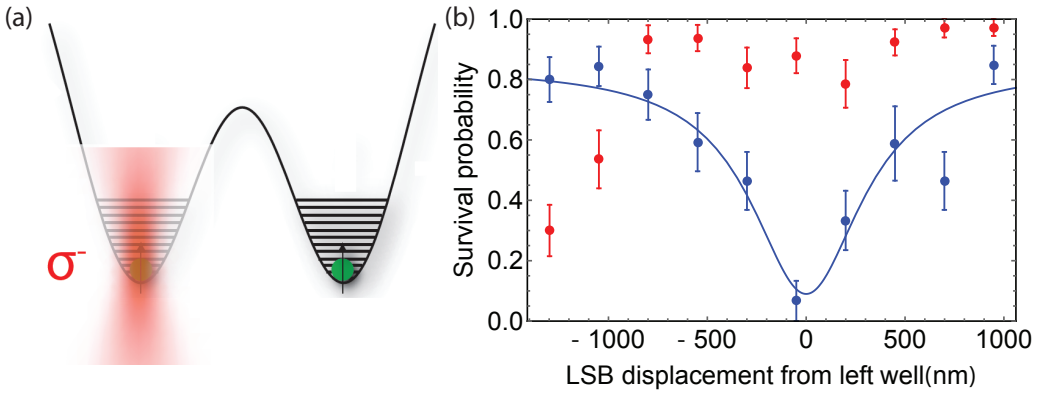

Figure 2.21: (a) Schematic of applying the light-shift beam to the left optical tweezer; the wells are spaced by 1.57 μm and 1.1 mK deep. (b) Scan of the position of the light-shift beam when placing resonant cycling light on the fiber. Typically we use a $4\mu s$ pulse with less than 1nW of power in the beam. The blue (red) points correspond to the likelihood that an atom in the left (right) well survives the pulse application.

pulse length of 30 μs. These parameters were numerically optimized based on our measured Rabi rate; the black line in the figure corresponds to a parameter free model via numerical evolution of the Schrodinger equation. The main purpose of the Gaussian pulses is that they allow for larger Rabi rates while retaining spectral resolution because the Gaussian spectral response has a sharper drop off and no wings (compared to those in Fig. 2.20a). We make use of this feature in Chapter 3 for driving narrow Raman transitions, and below for tweezer-resolved spin flips.

2.12.2 Spin addressing of single atoms in optical tweezers

We perform tweezer-resolved spin flips by changing the local magnetic field experienced by one atom with respect to the other. We align a beam (the "light shift beam") through the objective and onto one of the optical tweezers (Fig. 2.21a); it is the same wavelength as the Raman light and σ^- −polarized. Typically, a couple 100 nW is sufficient to realize up to a 200 kHz relative shift on the $|2,2\rangle \leftrightarrow |1,1\rangle$ transition. This compares favorably with the expected light shift for a 0.65 μm spot, but we cannot perform an exact comparison since the polarization is mixed due to the two 45^o reflections on the glass and dichroic.

The light shift beam is initially aligned by placing a retro-reflecting mirror in front of the

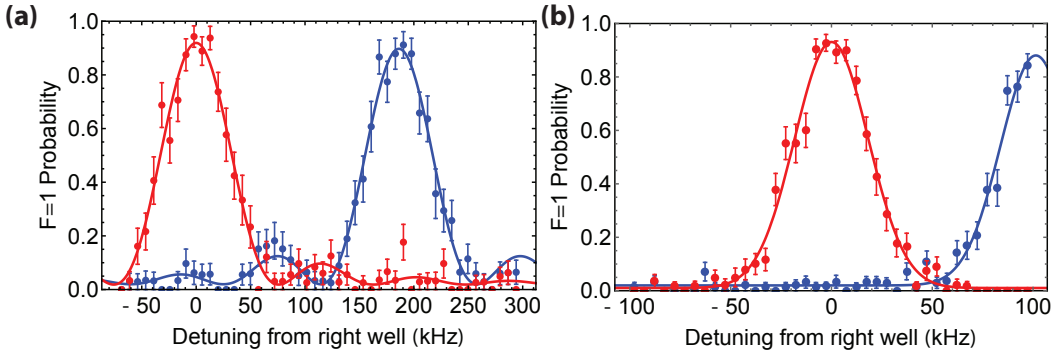

Figure 2.22: Performing microwave spectra with the light-shift beam aligned to the left optical tweezer using square (a) and Gaussian (b) pulses. The blue (red) points corresponds to the likelihood that an atom in the left (right) well is spin-flipped into $F = 1$.

objective, and overlapping the beam with the tweezer beam. We also initially set the collimation in this fashion, by ensuring they both focus to the same location along the optical axis. We then perform a fine alignment by putting resonant cycling light on the optical fiber that carries the light to the experiment. With a two-axis piezo mirror we scan the x and y position in the objective focal plane; we iterate on this alignment and the collimation of the beam. In the end, we can see a loss resonance as a function of position that only affects one of the wells, as shown in Fig. 2.21b. We realign the x and y piezo positions on a daily basis and observe slow drift on the 100 nm scale.

Using the far red-detuned light, we can then finely adjust the relative position of the spin flip resonances for each trap. Two representative spectra are shown in Fig. 2.22, one using square pulses and the other Gaussian. We typically observe no shift on the non-targeted tweezer with respect to the case of the beam off, suggesting that we are making a tight spot with this setup. One concern is that the diabatic switching of these beams, which is necessitated by their scattering rate, could cause motional heating of the atoms. The beam is applied with a 30 μs square temporal profile, and the depth potential it applies (< 500 kHz) is only about 2.5% of the tweezer trap depth of 1.1 mK. A calculation of the perturbation to the oscillator states shows that heating is expected to be less than 1%, which was also experimentally verified with sideband spectroscopy.

To maximize the preparation, we need to balance a number of concerns: (1) minimizing the

light shift beam power due to spontaneous emission, (2) maximizing the microwave Rabi rate to maintain the fidelity of the π pulses, and (3) minimizing the ratio of the peak widths to peak separation. We care about (1) since it mitigates the spin preparation and causes heating, and (3) to prevent off-resonantly driving spin flips. By eliminating the sinc-function wings from a square pulse, and furthermore, by having a narrower spectral profile for the same Rabi rate (Lorentzian vs. Gaussian), Gaussian pulse-shaping is advantageous for creating arbitrary two-particle spin states with the light-shifting technique. We can create arbitrary states with above 90% fidelity. This likely could be improved by switching to frequency and amplitude modulated pulses (e.g. HS1 pulse [2]), but at the expense of interrogation time: this would require going to a farther detuned light-shift beam because these require millisecond pulse lengths.

Chapter 3

Cooling a single atom in an optical tweezer to its motional ground-state

In this chapter, I will present results demonstrating the first realization of three-dimensional Raman-sideband cooling of a single isolated, addressable neutral atom. In addition to exploiting key features of the optical tweezer platform itself, the results of subsequent chapters rely on the ability to prepare indistinguishable atoms in pure quantum states of spin and motion via laser-cooling techniques. The discussion in this chapter is therefore foundational to the results presented in this thesis.

Motional control of neutral atoms has a rich history, and increasingly interest has turned to the problem of single-atom control. To date, optical lattices created by standing waves of light have been the main platform for realizing motional control of collections of single neutral atoms. Approaches have included demonstrations of the Mott insulator transition of an evaporatively cooled gas [11, 2], and explorations of laser cooling collections of atoms in a lattice [51, 52, 53, 54, 58, 59, 60, 88, 61]. More recently, in spin-dependent lattices experimenters have harnessed microwave signals to cool and control atomic motion [60, 61]. Our work in an optical tweezer breaks with typical lattice experiments, and instead more closely resembles the sideband cooling and spectroscopy techniques used with atomic ions [50]. We hold a single atom in a far-detuned tweezer trap and apply near-resonant, pulsed cooling and spectroscopy light that couples two ground state hyperfine levels (Fig. 3.1a). The complete separation of the trapping and cooling beams [54, 59, 88] allows us to realize rapid cooling as well as low trap spontaneous emission rates and hence long coherence times. As subsequent chapters will discuss in detail, by approaching the cooling fidelities

achieved with evaporative cooling in this tweezer-based platform, we have established a new route to creating low-entropy arrays of neutral atoms for quantum dynamics experiment

In this chapter I will focus on ground-state laser cooling in the context of our experiment, and provide less of a completely general picture of Raman-sideband cooling (for a very general description, I highly recommend Ref. [56]). I will discuss important theoretical calculations done in order to guide our choice of cooling parameters in the experiment, as well as to gain a decent grasp of various regimes of cooling. I will discuss briefly theory for coherent Raman transitions and master equation calculations of the cooling, then experiments with three different types of sideband cooling: pulsed, continuous, and Gaussian pulsed cooling. The first pulsed cooling discussion relies heavily on material from our publication on the subject [89].

3.1 Quick summary of Raman sideband cooling in an optical tweezer

We laser cool to the ground state by employing a technique known as Raman sideband cooling [51, 52, 53, 56, 90]. Raman sideband cooling operates by iterating on a two step process that manipulates the atomic spin and motion, and resolves motional transitions even when the trap frequency is less than the electronic transition linewidth. In our scheme, we utilize two hyperfine levels of ^{87}Rb: $|F, m_F\rangle \equiv |2, 2\rangle$ and $|1, 1\rangle$ (Fig. 3.1b), where F is the hyperfine angular momentum quantum number and m_F its projection. The first step is a stimulated Raman transition on $|2, 2; n\rangle \leftrightarrow |1, 1; n-1\rangle$ that reduces the vibrational state by one quantum while also realizing a spin flip. A set of beams (RB_i), illustrated in Fig. 3.1a, operate in pairs to drive these coherent Raman transitions between spin and motional states. The second step to the cooling is the dissipative step: The atom is optically pumped back to the initial spin-state via a spontaneous Raman process, while the emitted photon carries away entropy. By repeating these steps, population accumulates in the $|2, 2; 0\rangle$ state because it is dark to the Raman beams and the optical pumping light.

For Raman cooling to be successful, the optical pumping step must preserve the reduced vibrational state. The vibrational excitation probability depends on the motional quantum number n and the Lamb-Dicke parameter, $\eta^{OP} \equiv x_0 k_{OP}$, where $x_0 = (\hbar/2m\omega)^{1/2}$ is the oscillator length

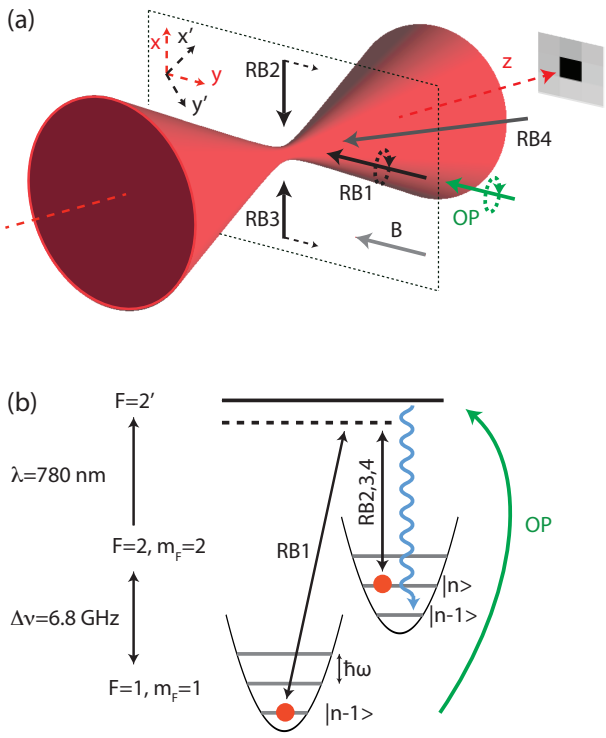

Figure 3.1: Experimental setup for tweezer trap, detection, and three-dimensional motional control. (a) Orthogonal radial axes, indicated by x' and y', are addressed by Raman beam 1 (RB1) (σ^+-polarized) and RB2 (π-polarized), or RB1 and RB3 (π-polarized). RB1 and RB4 (linearly polarized in y-z plane) address the axial direction. Note we should be able to cool all three axes with a single pair of counterpropagating beams. (b) Level diagram for ^{87}Rb with associated beams from (a). Optical pumping consists of σ^+-polarized repump light on the $F = 1 \rightarrow 2'$ transition along with optical pumping light on $F = 2 \rightarrow 2'$.

for a particle of mass m and k_{OP} is the optical pumping wave number. In our experiment, Raman cooling begins with an atom in a mixed thermal state, with a temperature corresponding to an average vibrational quantum number $\bar{n}$. The likelihood of excitation from the optical pumping depends on the size of the thermal atomic wave packet compared to the wavelength of the optical pumping light. Therefore, the excitation probability due to a single scattered photon scales as $(k\sqrt{\langle x^2 \rangle})^2 = (\eta_{\text{eff}}^{OP})^2 \equiv (2\bar{n}+1)(\eta^{OP})^2$, and hence the Raman cooling efficiency scales inversely with $(\eta_{\text{eff}}^{OP})^2$ [91]. Therefore, ground state cooling (achieving $\bar{n} = 0$) requires (1) low enough initial temperatures before starting Raman cooling, and (2) sufficient confinement, i.e. large trap frequencies. The analysis in this chapter will come back to these two key points on a number of

occasions.

3.2 Theory of coherent Raman transitions

3.2.1 Raman transition Rabi frequencies: internal degrees of freedom

The set of beams in Fig. 3.1a display the primary toolset with which we can drive Raman transitions that address all three motional degrees of freedom of an atom in the optical tweezer. The beam directions and frequencies are chosen such that RB1 ("EO beam") is paired with one of RB2-4 ("Top", "Bottom", and "Axial" beams, respectively) to impart momentum to a chosen motional axis. The details of the beam frequency generation will be discussed in a later section, and for the purposes of the discussion here of Raman transitions I will simplify the picture to what is shown in Fig. 3.2. To connect with our experiment, RB1 plays the role of beam 2, while RB2-4 plays the role of beam 1. In the presence of beams 1 and 2, the atomic eigenstates are dressed by the electric dipole interaction, and contain very small amplitudes of the excited state $|i\rangle$. By diabatically pulsing on these beams, quantum amplitude can rotate from $|s\rangle$, virtually through the excited state, and into $|f\rangle$. This is a Raman transition; it is a second-order perturbative process.

Here we provide a general description for calculating the Raman Rabi frequency, which we define as the frequency with which the measured probabilities oscillate between the Raman coupled ground-states $|s\rangle$ and $|f\rangle$; the amplitudes oscillate at half this frequency, and the off-diagonals in the Hamiltonian of the restricted two-level system of the ground states is 1/2 the Raman Rabi frequency. This definition varies in the literature, so here we explicitly define quantities necessary to calculate the Raman Rabi frequency using the atomic and Raman beam parameters. For a two-photon transition between states $|s\rangle$ and $|f\rangle$, the Raman Rabi frequency can be written simply as [92],

$$\Omega_R = \frac{\Omega_1 \Omega_2}{2\Delta}, \tag{3.1}$$

where Ω_1 and Ω_2 are the single photon couplings due to beams 1 and 2, respectively, and Δ is the intermediate state detuning from the excited state depicted in Fig. 3.2. Typically, the detuning

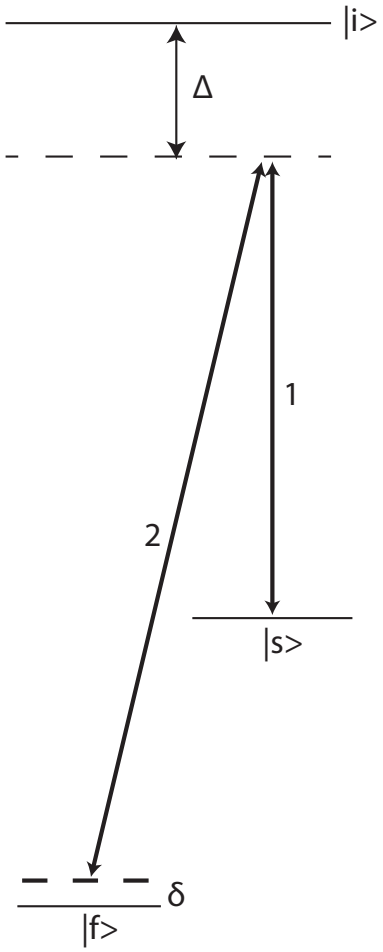

Figure 3.2: Raman transitions. In our setup, we drive transitions of $\Delta m_F = \pm 1$, necessitating one beam of π- polarization (beam 1) and another of circular (beam 2). The difference in the beam frequencies is resonant with the splitting between the states between which we hope to drive a transition, up to an amount δ (Raman detuning). Both beams are far detuned from an excited state $|i\rangle$, and each yields dressing of this state quantified by the single photon couplings Ω_1 and Ω_2, respectively. For explanatory purposes, we simplify the picture to driving a transition between two states, $|s\rangle$ and $|f\rangle$, through a single intermediate, excited state $|i\rangle$. In practice, the Raman beams couple to many excited states (see text).

is much larger than either of the single photon couplings to avoid significant populations in the excited state and hence spontaneous emission. The single photon coupling Ω_b is calculated from the dipole matrix elements of the transition in question as,

$$\Omega_b = \mathbf{d} \cdot \mathbf{E_b}/\hbar, \tag{3.2}$$

where $\mathbf{d}$ is the electric dipole operator, and $\mathbf{E_b}$ the electric field of the light driving the single

photon process (beam 1 or 2). If a single excited state existed, we could simply calculate these two single photon couplings in Eq. 3.1 to compute the Raman Rabi frequency. However, in general, many different excited states can couple to the ground states $|s\rangle$ and $|f\rangle$, and each Raman pathway contributes to the final coupling between the ground states. Therefore, a more general expression for the Raman Rabi frequency is required [93],

$$\Omega_R = \frac{1}{2\hbar^2}\sum_i \langle f|\mathbf{d}\cdot\mathbf{E}|i\rangle\langle i|\mathbf{d}\cdot\mathbf{E}|s\rangle/\Delta_i, \tag{3.3}$$

where the sum is taken over the set of all intermediate states $|i\rangle$ with associated intermediate state detunings Δ_i. We now seek a general expression for the dipole matrix elements between each of the ground-states with an excited intermediate state. We therefore require expressions for matrix elements of the form,

$$\hbar\Omega_b(F, m_F, F', m'_F) = \langle F, m_F|\mathbf{d}\cdot\mathbf{E}|F', m'_F\rangle, \tag{3.4}$$

where the primed quantum numbers denote an excited intermediate state, and the unprimed quantum numbers one of the ground-state quantum numbers. Using Ref. [4], these can computed exactly with the aid of the measured D1 and D2 excited state lifetimes τ_{D1} and τ_{D2}, respectively. Skipping some algebra, we can write (using D2 line here for τ),

$$\begin{aligned}\hbar\Omega_b(F, m_F, F', m'_F) = &\left(\frac{2I_i}{\epsilon_0 c}\right)^{1/2}\left(\frac{3\pi\epsilon_0\hbar c^3}{\tau_{D2}\omega_{FF'}^3}\right)^{1/2}(-1)^{F'+J+1+I}\sqrt{(2F'+1)(2J'+1)}\\ &\begin{Bmatrix} J & J' & 1\\ F' & F & I\end{Bmatrix}_{6j}\langle F, m_F|1, -q, F', m'_F\rangle_{CGC},\end{aligned} \tag{3.5}$$

where J and J' refer to the quantum numbers with respect to fine-structure for the ground and excited states, respectively; $\omega_{FF'}$ refers to the angular transition frequency between the hyperfine states F and F' in the matrix element[1] ; the curly brackets refer to a 6j-coefficient; the last matrix element with the CGC subscript refers to a Clebsch-Gordan coefficient; q refers to the spherical polarization component of the light driving the single-photon transition (±1 for $\sigma^{\pm}$ and 0 for π); I_i refers to the intensity of the light driving the transition (beam 1 or 2 in what follows); $I = 3/2$ is

[1] We neglect magnetic field shifts of the sub-levels, which are small compared to everything else

the nuclear spin. The Raman Rabi frequencies through the D1 and D2 line between ground-states $|F^s, m_F^s\rangle$ and $|F^f, m_F^f\rangle$ are then,

$$\Omega_{D2} = \frac{1}{2}\sum_{F'=0}^{F'=3}\sum_{m'_F=-F}^{m'_F=F'} \frac{\Omega_1(F^s, m_F^s, F', m'_F)\Omega_2(F^f, m_F^f, F', m'_F)}{\Delta_{F',\omega_{(1,2)}}}, \tag{3.6}$$

and,

$$\Omega_{D1} = \frac{1}{2}\sum_{F'=1}^{F'=2}\sum_{m'_F=-F}^{m'_F=F'} \frac{\Omega_1(F^s, m_F^s, F', m'_F)\Omega_2(F^f, m_F^f, F', m'_F)}{\Delta_{F',\omega_{(1,2)}}}, \tag{3.7}$$

where $\Delta_{F',\omega_{(1,2)}}$ is the intermediate state detuning from F' of the Raman beams, each with angular frequency ω_1 and ω_2 (one only requires knowledge of one frequency here since we are assuming the beams are on Raman resonance, i.e. $\delta = 0$ in Figure 3.2). Since in our experiment we detune -50 GHz from the D2 line, the states in this manifold primarily contribute (D1 line couplings contribute at the 1% level). However, we include both lines in performing a calculation of expected rates. The final Raman Rabi frequency is the sum of the coupling from the D1 and D2 line,

$$\Omega_R = \Omega_{D1} + \Omega_{D2}. \tag{3.8}$$

We find agreement at the 40% level with our experimentally measured Rabi frequencies and these calculations. Disparities are likely due to our lack of knowledge of the exact intensities of the focused Raman beams at the atoms.

3.2.2 Raman transitions: external degrees of freedom and full Hamiltonian

While the above calculations address how a Raman beam pair couples to the internal degrees of freedom of an atom, the pair coherently couples to the external degrees of freedom by imparting momentum. For a pair of beams with momentum vectors $\mathbf{k_1}$ and $\mathbf{k_2}$, the momentum kick an atom experiences after a transition between the spin ground-states is,

$$\hbar\mathbf{\Delta k} = \hbar(\mathbf{k_1} - \mathbf{k_2}). \tag{3.9}$$

Therefore, whenever the beam pair is not copropagating the atom will experience a momentum kick. The quantum operator that realizes this process is the momentum translation operator $e^{i\Delta k\hat{x}}$,

where $\hat{x}$ is the position operator. For an effective spin-1/2 atom (which is the case here, $|\uparrow\rangle \equiv |2,2\rangle$ and $|\downarrow\rangle \equiv |1,1\rangle$), the Hamiltonian for the Raman interaction can then be written [94],

$$H_R = \frac{\hbar\Omega_R}{2}\left(e^{i\Delta k\hat{x}}\sigma^+ + e^{-i\Delta k\hat{x}}\sigma^-\right), \tag{3.10}$$

where σ^+ and σ^- are the spin raising and lowering operators, respectively, with respect to the eigenstates of σ_z. Reaching this Hamiltonian requires going into the rotating frame and making the rotating wave approximation. For the purposes of this discussion, we have also assumed that the momentum kick is entirely along the motional axis defined by $\hat{x}$; in general, we can replace $\Delta k\hat{x}$ with $\mathbf{\Delta k}\cdot\mathbf{x}$ to treat multiple quantized dimensions. For an atom trapped deep in an optical tweezer, the atom's motion is harmonic to very good approximation, and so we decompose the position operator in terms of raising and lowering operators. After doing this, from H_R, much of the physics of Raman sideband transitions can be deduced upon making the simplification that we operate in the so-called Lamb-Dicke regime. To elucidate the meaning of this, we focus on the argument of the exponential,

$$i\Delta k\hat{x} = i\Delta k x_0\left(a + a^\dagger\right), \tag{3.11}$$

where a and $a^\dagger$ are the creation and annihilation operators for a harmonic oscillator of frequency ω and mass m, and $x_0 = \left(\frac{\hbar}{2m\omega}\right)^{1/2}$ is the ground-state extension. We now define the Lamb-Dicke parameter $\eta^R = \Delta k x_0$, which contains a ratio of the length-scales associated with the momentum kick ($2\pi/\Delta k$) and the size of the atomic wave packet x_0. Making the assumption that we are in the Lamb-Dicke regime (LDR) with respect to the Raman beams necessitates that $\eta^R\sqrt{\langle(a+a^\dagger)^2\rangle} << 1$, which relies on the assumption that the atom is sufficiently cold that its thermal wave packet is small compared to $2\pi/\Delta k$ [90]. We can then expand H_R to first order,

$$H_R^{LDR} = \frac{\hbar\Omega_R}{2}\left(\sigma^+\left(1 + i\eta^R\left(a + a^\dagger\right)\right) + h.c.\right) + \mathcal{O}((\eta^R)^2), \tag{3.12}$$

with which we can see the three lowest-order processes realized by the Raman interaction in the matrix elements of the states $|\{\uparrow,\downarrow\}; n\rangle$,

$$\langle\uparrow; n+1|H_R^{LDR}|\downarrow; n\rangle = \frac{i\hbar\Omega_R}{2}\eta^R\sqrt{n+1}, \tag{3.13}$$

$$\langle\uparrow; n-1|H_R^{LDR}|\downarrow; n\rangle = \frac{i\hbar\Omega_R}{2}\eta^R\sqrt{n}, \tag{3.14}$$

$$\langle\uparrow; n|H_R^{LDR}|\downarrow; n\rangle = \frac{\hbar\Omega_R}{2}, \tag{3.15}$$

where the first two cases correspond to the so-called blue and red sideband, respectively, and the third case refers to a carrier transition which does not influence the atomic motion. From these matrix elements, we see that in the LDR the sideband Rabi frequencies from the Fock state $|n\rangle$ are $\{\Omega_{RSB}^{LDR}, \Omega_{BSB}^{LDR}\} = \eta^R\Omega_R\{\sqrt{n}, \sqrt{n+1}\}$. Each of the transitions can be resonantly driven by appropriate choice of $\delta \approx \pm\omega$ from Fig.3.2.[2] While in the LDR, this largely summarizes the control achieved by Raman interactions on harmonically trapped atoms, and provides most of the tools necessary for discussing the data in the rest of this thesis, exact analytic expressions for each of the Rabi frequencies exist,

$$\Omega_{SB}(n,m) = \Omega_R e^{-(\eta^R)^2/2}\left(\frac{n_<!}{n_>!}\right)^{1/2}(\eta^R)^{|n-m|}L_{n_<}^{|n-m|}((\eta^R)^2), \tag{3.16}$$

$$\Omega_c(n) = \Omega_R e^{-(\eta^R)^2/2}L_n^0((\eta^R)^2), \tag{3.17}$$

where the first equation describes sideband Raman Rabi frequencies between the n and m motional states and $n_<$ ($n_>$) refers to the smaller (larger) of the two, while the second equation describes the carrier Raman Rabi frequency from state n [92]. The expressions are written in terms of the generalized Laguerre polynomials L_n^a. We use these expressions when performing analytic fits to the thermal carrier dephasing data in Section 3.4.3, and also check the numerics discussed below by comparing the Fock state evolution against these expressions.

3.2.3 Full Hamiltonian for a harmonically bound atom and coherent dynamics

The above treatment addresses the main function of the Raman beams on motional Fock states. However, the starting point for Raman cooling in our experiment is subsequent to sub-Doppler polarization gradient cooling of an atom. We approximate the atom's motion at this time

[2] There is a small shift $\delta' \approx \frac{\omega}{2}\left(\frac{\Omega_R}{\omega}\right)^2$ of the sideband position due to dressing from the carrier.

as a thermal density matrix,

$$\rho_T = \frac{1}{Z}\sum_n e^{-n\hbar\omega/k_bT}|n\rangle\langle n|. \tag{3.18}$$

It is important to stress what exactly this density matrix means for a single atom since we do not have some thermalized ensemble: the purely diagonal ρ_T quantifies the likelihood that on any given run of the experiment the atom is in the motional state $|n\rangle$ after sub-Doppler cooling. Therefore, when solving for coherent dynamics, we will implicitly be computing an incoherent sum of coherent evolutions with weights determined by this thermal distribution. With ρ_T as our initial condition, we can then solve the dynamics for a Hamiltonian H using the Von-Neumann equation $i\hbar\dot{\rho} = [H, \rho]$. The total Hamiltonian H for the atom including both the Raman interaction and the harmonic potential is,

$$H = -\frac{1}{2}\hbar\delta\sigma_z + \frac{\hbar\omega}{2}|0\rangle\langle 0| + \sum_n n\hbar\omega|n\rangle\langle n| + H_R, \tag{3.19}$$

where the kets refer to the quantized harmonic states from the motional degree of freedom, but residing in the full motional-spin Hilbert space.

In Fig. 3.3a, we show coherent dynamics for the sidebands, to illustrate the Rabi flopping on the red and blue sidebands for a spin-down atom at 15 μK in a trap of $\omega/2\pi = 140$ kHz. Due to the incoherent sum of frequency components from each motional state in the thermal density matrix, the sideband Rabi oscillations look funky. Crucially, and despite the funkiness, one can use these oscillations to show a key feature of the sidebands, namely that they carry temperature information on the atom provided the atom's motion conforms to a thermal distribution. In the Lamb-Dicke regime, one can apply the well-known [50] expression to the so-called "sideband asymmetry",

$$\frac{\bar{n}}{\bar{n}+1} = \frac{A_{RSB}}{A_{BSB}}, \tag{3.20}$$

where $A_{RSB}(A_{BSB})$ are the probabilities for a spin-flip when on the red-sideband (blue-sideband) resonance. In the limit of perfectly being in LDR, this expression is time independent [50] which we numerically investigate in Fig. 3.3b. Ultimately, the expression arises due to the different matrix elements of the raising and lowering operators, however, it is not obvious why it persists

for arbitrary times in the dynamics. We compute $\bar{n}$ as prescribed by Eq. 3.20 at each time in the coherent evolution, and we compare this to the known $\bar{n}$ from the temperature (dashed black line),

$$\bar{n} = \frac{1}{e^{\frac{\hbar\omega}{k_b T}} - 1} = \mathrm{Tr}(a^\dagger a \rho_T). \tag{3.21}$$

Due to a small amount of second-order (i.e. outside LDR) effects and off-resonant carrier transitions, there is a slight difference between the dashed line and the computed $\bar{n}$, the effect of which is enhanced when the sidebands are small. Importantly, we see that Eq. 3.20 is a tight lower bound since the plotted value never drops below the true $\bar{n}$, so that we cannot underestimate our temperature on the basis of this technique. Typically, we perform such thermometry at π-pulse on the sidebands because this maximizes signal-to-noise and yields via Eq. 3.20 a value closest to the true $\bar{n}$; we usually take a full spectrum on the red and blue-sidebands to extract high-statistics amplitudes. In contrast, when each of the peaks is small, taking the ratio becomes increasingly unreliable with respect to noise. Overall, this is a very powerful tool for performing thermometry on atoms.

I also want to point out that these simulations illustrate why it is important to start near the LDR when cooling: when the atom is very hot, sideband transitions rapidly dephase due to the broad distribution in Fock states and increased sensitivity to the motional state when expanding H_R to higher orders. This implies that the cooling process is slowed. It is also the case that for a large distribution of Rabi rates it is possible to create additional dark states for a particular sideband pulselength (see Section 3.3.2). Lastly, it is evident that, for a thermal state, the $n^{1/2}$ relationship of the sideband Rabi rate causes the increased peaking of the oscillations before a pulse area of π in the ground state sideband Rabi frequency; we exploit this property for improved cooling in Section 3.3.2.

As a comparison to the ground-state dynamics, we show the same coherent sideband simulations for an atom at temperature 1.7 μK ($\bar{n} = 0.02$): the asymmetry between the sidebands is greatly enhanced. Since the atom is in the ground state $P_{GS} \approx 1 - \bar{n} = 0.98$ fraction of the experiments, the red-sideband transition is suppressed since it is impossible to remove anymore

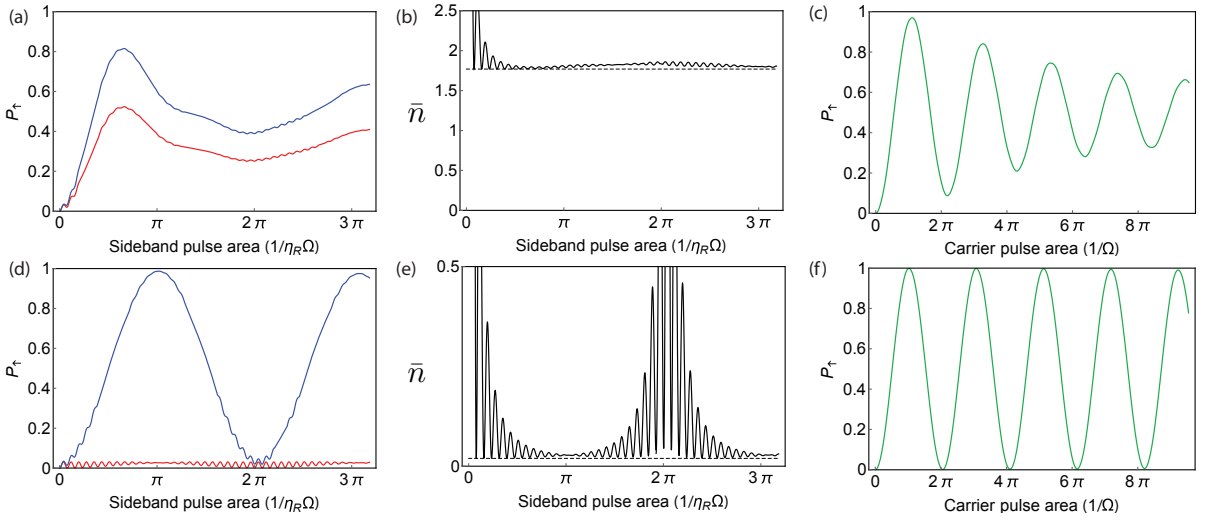

Figure 3.3: Coherent sideband and carrier oscillations, determination of $\bar{n}$, for $\eta^R = 0.22$ and $\omega/(2\pi) = 140$ kHz. Top (bottom) row for thermal state of temperature 15 μK (1.7 μK) (a,d) Coherent sideband oscillations for $\delta \approx \pm\omega$, where to hit resonance for the sideband oscillations we correct for the slight dressing of the sideband resonance by the carrier (this pulls the sidebands closer to the carrier). The red and blue-sidebands are correspondingly colored. (b,e) Computing $\bar{n}$ from the sideband oscillations using Eq. 3.20, and comparing to the dashed line whose position is the true $\bar{n}$ from Eq. 3.21. (c,f) Expected dephasing (and lack thereof) of carrier oscillations via Eq. 3.22 as a function of temperature. For (a,d,c,f) we plot the likelihood to measure the particle in spin-up, $P_\uparrow$, given that it started spin-down and in the stated motional distribution.

motional quanta once the atom is in the ground-state. This latter temperature, as will be shown, is about what we achieve along each dimension of the optical tweezer.

Lastly, in Fig. 3.3c,f, we show another thermometry technique we employ in the experiment [88]. While in the LDR the carrier Rabi frequency for a given Fock state is insensitive to the motional quantum number, beyond first order (i.e. by definition outside LDR) it becomes sensitive to the motional state as is indicated by the exact analytic expressions for the Rabi frequency. We can use this sensitivity as an additional check on our thermometry: for a thermal state, carrier Rabi oscillations should damp out at a rate directly related to the temperature. We show this numerically in the figures, and we fit our data using a thermal distribution of the Rabi evolutions,

$$P_\uparrow(t) = \sum_n = \frac{P_T(n)}{2}(1 - \cos(\Omega_c(n)t)), \tag{3.22}$$

where $P_T(n)$ is the Boltzmann weight in the Fock state $|n\rangle$ for an atom at temperature T. As shown

in later experimental sections, we find nice agreement between this approach and our sideband spectroscopy.

3.3 Raman-sideband cooling theory: adding dissipation

The key ingredient to the cooling is the addition of optical pumping, which performs an irreversible dissipative step to cool the atom. To model the cooling in our experiment, we employ a master equation calculation. The master equation is a standard tool for open quantum systems, and provides the ensemble average (i.e. many runs of the experiment) of the dynamics when quantum jumps occur due to coupling to a bath. The quantum jumps in our experiment occur when the atom spontaneous emits a photon into vacuum upon decaying from the excited state $2'$. However, because the lifetime in the excited state is so short compared to the rest of the dynamics, we can model the optical pumping as simply a quantum jump between the spin-up and spin-down state. In what follows, we will treat the down state as the dark state (it is reversed in the experiment, but this simplifies discussion and is consistent with the above discussion on coherent transitions) and summarize our master equation formalism. Furthermore, we will break up our treatment into two cases: (1) sideband cooling via continuous cooling, where the optical pumping and coherent Raman coupling are on concurrently, (2) pulsed cooling in which the optical pumping and Raman transitions are staggered. The sideband cooling has a pretty large and coupled parameter space, and the numerics discussed in this section were an extremely important guide in our choice of experimental parameters.

3.3.1 Continuous cooling

To properly account for the motional heating during optical pumping, we must calculate the number of photons absorbed to optically pump the atom. Using the known line strengths [4], this corresponds to three photons on the average for the spin-states used in the experiment, and, including the dipole emission pattern profile, correspondingly causes for x/y (z) axes three (one)

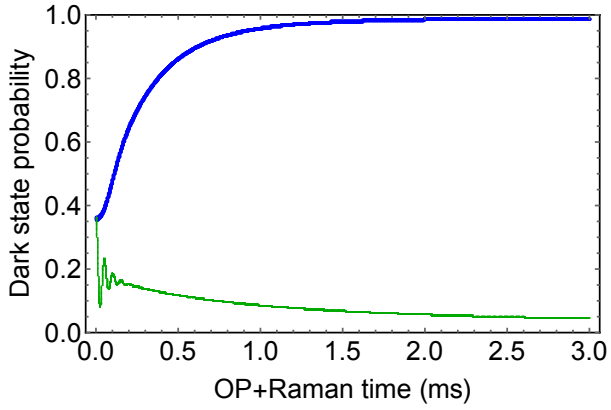

Figure 3.4: Simulation of continuous sideband cooling. We show the expected dark state population $|2,2;0\rangle$ as function of time that an atom is exposed to Raman and optical pumping beams. The blue (green) is for the case of $\delta \approx -\omega$ ($\delta = 0$). The simulation uses parameters close to the radial continuous cooling of Section 3.4.6: $\Omega_R/(2\pi) = 20$ kHz, initial $T = 15$ μK, $\eta^R = 0.22$, $\eta^{OP} = 0.16$, $\Gamma = 30$ ms^{-1}, and $\omega/(2\pi) = 140$ kHz.

momentum kick of magnitude $\hbar k_{op}$.[3] We define an optical pumping operator as follows, using a radial direction for the purpose of this discussion. Since we take the cooling state, the dark spin state, to be $|\downarrow\rangle$, we can define an optical pumping operator for a scattering rate Γ (units $1/s$),

$$\hat{O} = \Gamma^{1/2}\sigma^{-}\left(e^{ik_{OP}\hat{x}}\right)^{3}, \tag{3.23}$$

where the spin lowering operator recycles the spin state while the second terms realizes the associated heating with scattering three photons of wavenumber k_{OP}. As with H_R, the degree to which a momentum kick couples to the atom's motion depends on the Lamb-Dicke parameter, but in this case the one associated with the optical pumping $\eta^{OP} = k_{OP}x_0$. We accordingly define the Lindblad operator,

$$\mathcal{L} = \hat{O}\rho\hat{O}^{\dagger} - \frac{1}{2}\hat{O}^{\dagger}\hat{O}\rho - \frac{1}{2}\rho\hat{O}^{\dagger}\hat{O}. \tag{3.24}$$

[3] We expect on the average, in total, 6 photon momentum kicks, with 2.5/2.5 and 1 for x/y and z, respectively. However, we use 3 as an upper bound for each of the radial axes since it simplifies the discussion and 2.5 scatters is weird.

For continuous cooling, we have both the coherent Raman process, the harmonic confinement, and the dissipation term from $\mathcal{L}$. The master equation to be solved is then,

$$i\dot{\rho} = [H, \rho] + i\mathcal{L}. \tag{3.25}$$

We numerically solve Eq. 3.25 in order to guide our choice of cooling parameters and understand various possible issues associated with the cooling. In Figure 3.4, we show typical results for cooling parameters close to those used in our experiment for continuous radial sideband cooling. After 3 ms the atom is cooled to the dark-state ($|\downarrow; n = 0\rangle$) with 98% probability when we set δ to the red-sideband. To illustrate the dominant heating mechanism for this setup, I show the dynamics for the boneheaded choice of setting $\delta = 0$, i.e. to the carrier resonance (darker green). In this case, the coherent Raman process flips the spin but does not change the motional state, while the optical pumping recycles the atom and realizes three momentum kicks. Therefore, for every spin flip, the atom is heated by the optical pumping. This implies that a key concern is the spectroscopic width of the carrier during cooling, since if there is appreciable carrier transition amplitude at the position of the red-sideband then that contributes a corresponding heating rate. There are two contributions to this width: the carrier Rabi frequency sets the overall Lorentzian profile of the coherent transition (with an additional oscillating envelope when coherent), but the optical pumping reduces the lifetime of $|\uparrow; n\rangle$ and consequently also broadens the state. The frequency width of the carrier transition is therefore $(2\pi)^{-1}\sqrt{\Omega_c^2 + \Gamma^2}$. This implies that, in comparison to pulsed cooling where the optical pumping is not simultaneous with the Raman transition, the continuous cooling is necessarily slower for a similar carrier heating rate; indeed, we observe increased steady-state excitation fraction in the numerics as either of these rates is increased.

Lastly, it is important to note the sense in which this cooling simulation does not exactly map onto the experiment. Firstly, and obviously, this is one-dimensional and so we expect that all the 3D cooling should take longer due to optical pumping heating during the cooling of other dimensions. Secondly, while we account for the heating due to the three photons scattered during optical pumping, we do not account for the factor of three in spin-recycling time. This was a

deliberate choice: it is the scattering rate out of the pumped state that determines its width and hence any resulting heating. Without adding the excited state to this code (which would have increased the simulation time), the only way to reflect the factor of three slowing in the simulation would be to reduce this scattering rate Γ, which would then improperly simulate the broadening. Since we care more about the heating as opposed to the exact cooling speed (which is reduced by this increase in recycling time) in modeling the continuous cooling, we opt to have this inaccuracy. When using the cooling simulations to guide choice of experimental parameters, we always have used significantly longer cooling times (or number of cycles of continuous cooling) to reflect these physical distinctions between the theory and experiment. Thirdly, for the experimental continuous cooling of Section 3.4.6.1, it is the repumping Γ_{RP} that sets the width of the transition; this does not effect the modeling, but merely the translation between theory and experiment. Our experimental dark-state is $|2,2\rangle$, from which we drive transitions to $|1,1\rangle$. After the sideband transition, the spin is bright to the repumper, and, in combination with the $F = 2$ optical pumping beam the atom, is recycled to $|2,2\rangle$.

3.3.2 Pulsed cooling

We also perform simulations of pulsed sideband cooling, where the optical pumping and coherent sideband pulses are staggered in time. We first evolve Eq. 3.25 without the dissipative Lindblad term for an amount of time that is the sideband pulselength and for a detuning δ resonant with the red-sideband. We then pass the resulting density matrix to a new equation, Eq. 3.25 without the Hamiltonian term, and evolve the density matrix for 5 times the optical pumping τ (to fully recycle the spin state). Because we omit the Hamiltonian in the second step, we are ignoring any evolution of coherences that develop due to the motional superpositions achieved by the momentum kicks. However, since these momentum kicks are randomly distributed in time, they are completely dephased provided the optical pumping time is much longer than $1/\omega$, which is satisfied for all the simulations done here [95].

In Fig. 3.5, we show two cooling trajectories (dark state fraction versus cooling cycle; each

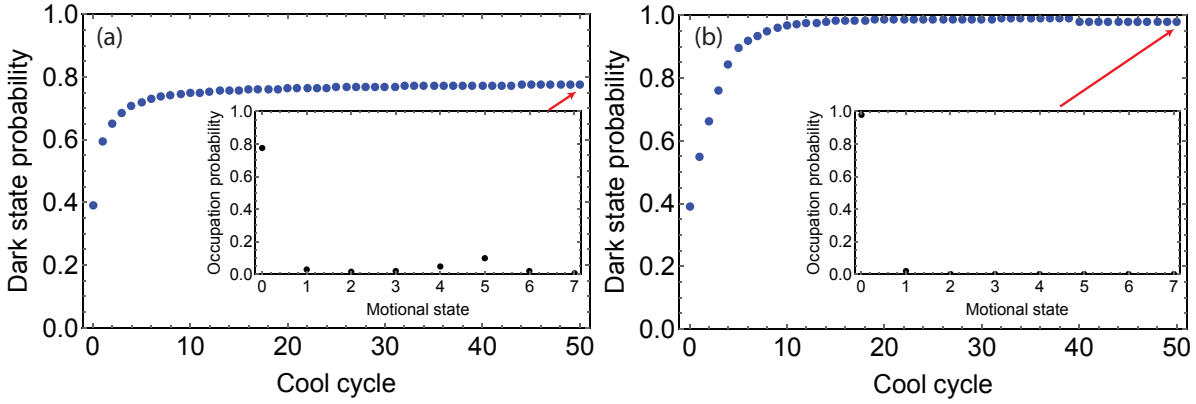

Figure 3.5: Simulation of pulsed and chirped pulsed cooling. For both simulations shown, we use $\Omega_R/(2\pi) = 31$ kHz, $\omega/(2\pi) = 150$ kHz, $\eta^R = 0.22$, $\eta^{OP} = 0.16$, $\delta \approx \omega$. (a) Pulsed sideband cooling using the same pulse length of $\Delta t = \pi/(\eta^R\Omega_R) = 73$ μs for the entire cooling routine. (b) Pulsed sideband cooling using $\Delta t = 48$ μs ($\Delta t = \pi/(\eta^R\Omega_R)$) for the first 40 (last 10) pulsed-cooling cycles. The kink at cycle 40 in the cooling trajectory comes from the change in the pulselength. It is clear that the shorter pulselength by itself would actually be sufficient for 99% cooling fidelity in ~ 0.5 ms. The insets show the motional state occupations at the end of the cooling for each protocol on the basis of the diagonals of the final density matrix.

.

cooling cycle consists of one sideband pulse then optical pumping recycling) to emphasize the main complication associated with pulsed cooling. In contrast to continuous cooling, an additional experimental parameter is manifest in the pulselength used for the Raman transition. A natural first choice for this is the sideband ground-state π-pulse, i.e. $\pi/(\eta^R\Omega_R)$. If the atom is initially very cold, this is a good choice since it should with high efficiency transfer first excited atoms into the ground state. However, we observe in the numerics (Fig. 3.5a) that the final dark-state fraction is 77% when starting from a initial thermal state of 15 μK ($\bar{n} = 1.6$, which is a typical initial temperature in the experiment). Interestingly, the staggering of the coherent and optical pumping process changes the steady-state distribution in a very pernicious fashion.

To elucidate this behavior, we show in Fig. 3.5a inset the atom motional state occupations after cooling. This is not thermal: there is not monotonic exponential drop off in the occupations, but rather drop off then a bump around motional states $4 \leq n \leq 6$. Interestingly, and annoyingly, this is because those states have red-sideband Rabi frequencies that are nearly double the ground-state

sideband Rabi frequency (for $\eta^R = 0.22$ and states $n = \{4, 5, 6\}$, $\frac{\Omega_{SB}(n,n-1)}{\Omega_{SB}(1,0)} = \{1.81, 1.97, 2.11\}$): for a choice of a π-pulse for the ground-state, this is a 2π-pulse for those motional states! It follows that these motional states are predominantly dark to the Raman drive, and tend to have appreciable steady-state populations. Even more perniciously, if an experimenter were to apply the assumption that this was a thermal state and subsequently perform sideband spectroscopy with a pulse length of $\pi/(\eta^R\Omega_R)$, they would incorrectly conclude a very high ground-state fraction since the red-sideband would be nearly zero despite the existence of an excited fraction (since this fraction is dark to this pulselength). Lastly, higher vibrational states exist that are also even multiples of the ground-state sideband Rabi frequency, however, for the initial temperatures in this thesis the discussed group of states is primarily relevant; other atomic species for which the sub-Doppler cooling is worse should likely consider this effect when performing pulsed sideband cooling.

With the above considerations in mind, for Raman-sideband cooling to work for all initial conditions in consideration, there must be only one dark-state with no others along the way as the atom is cooled from highly excited states. And the paranoid experimenter should perform spectroscopy at multiple pulselengths, since no motional state except the ground-state is dark to all pulselengths; alternatively, a frequency scan will also reveal an overdriven structure at the red-sideband if a non-thermal state of this variety has been prepared. From an experimental perspective, we in fact are less affected by this phenomenon because it presumes that we have full coherence after a 2π rotation: in fact, for Rabi frequencies typical to the sideband transitions ($1 - 10$ kHz), our magnetic field fluctuations preclude full contrast 2π rotations (this was verified by microwave spectroscopy). Nevertheless, we do address these concerns in our typical pulsed cooling protocol, which we simulate in Fig. 3.5b. The solution is to perform the cooling with two different pulselengths. The first 40 cycles of cooling use a shorter pulselength, one which the excited states see as closer to a sideband π-pulse. Afterwards, the thermal distribution is grouped in the lowest few motional states, to which we apply the ground-state sideband π-pulse for 10 cycles; it is unclear whether these last cycles even matter (in fact, according to the simulation it hurts the ground-state fraction likely due to increased carrier transitions, but only at the 0.8% level.). The

resulting ground state fraction is 98%, akin to the continuous cooling. However, the cooling really saturates on a much faster time scale: if we just assume 10 cycles are necessary, then ideally the cooling could occur in under 1 ms.

3.3.3 Optical pumping purity

The darkness of the dark state matters, and its irreversible coupling to the other states in the Hilbert space guarantees population accumulation in this state. There is the darkness that comes from the motional ground-state decoupling from the Raman drive when the red-sideband is spectrally resolved from the carrier, and there is darkness from the optical pumping polarization purity. One question I wondered about for some time is which, continuous or pulsed, is more sensitive to polarization impurity. On the one hand, continuous cooling keeps the optical pumping on continuously, yet the population that accrues in the dark-state is always steady-state as in pulsed-cooling. In the end I concluded that since the dark-state occupation will in both cases be determined by the competition of rates populating and depopulating the dark spin-state, and those rates are the same for pulsed and continuous cooling, the two protocols are equally sensitive to polarization purity in terms of the resulting spin-state. However, it is not clear how much motional heating this causes in turn: perhaps one technique is better at recovering from the motional heating caused by excess spin population in bright states. Assessing this question experimentally is a bit challenging to our setup since changes to the polarization of the OP beam would affect other beams as well. To study this question theoretically, I varied the fractional depumping and looked at the purity of the resulting density matrix for each procedure, as shown in Fig. 3.6. Interestingly, it seems the continuous cooling is much more robust against polarization impurity causing dark state depumping. I do not have a good explanation for this, but for both cases our part in a thousand relative depumping has negligible effect. I would hypothesize that this is related to the inefficiency of the pulsed sideband transitions when the distribution of motional states is broad.

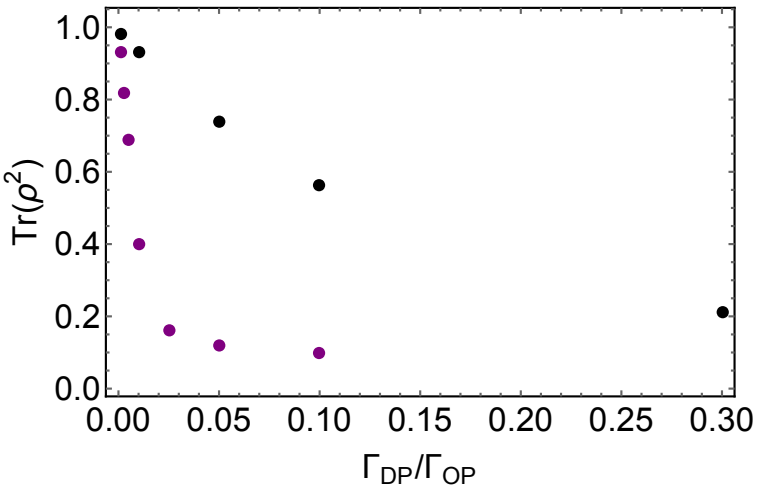

Figure 3.6: Effect of polarization impurity on different sideband cooling protocols. Using the continuous-cooling parameters of Figure 3.4 except that we now use $\omega/(2\pi) = 150$ kHz, and the pulsed-cooling of Figure 3.5b, and we model the effect of the polarization purity of the optical pumping beam. This is achieved by varying the ratio of good to bad polarization, which is equivalent to the ratio of depumping scattering rate to the good polarization scattering rate: Γ_{DP}/Γ. A term is added to Eq. 3.23 of the form $\Gamma_{DP}^{1/2}\sigma^{+}$. Since we care both about the motional and spin distribution, I plot the resulting density matrix purity on the y-axis, for the case of continuous (black) and pulsed (purple) cooling. The continuous cooling is significantly more robust against this experimental systematic.

3.3.4 Choosing between pulsed cooling and continuous: taking stock of experimental and theoretical concerns

Before discussing data, I want to briefly express my view (really, lack thereof, this is more of a summary) on choice of performing continuous or pulsed sideband cooling. From the above discussions, it is clear that continuous sideband cooling is necessarily slower than pulsed cooling, but skirts some of the complications associated with pulselength-sensitive dark-states. For the experiments in this thesis, speed is mainly relevant to the experimental cycle time; in particular, the simulations done here are all 1D, but since we cool in 3D everything is a fair bit slower. Continuous cooling typically takes 150 ms, while pulsed cooling only requires ~ 30 ms.[4] Experimentally, the beauty of continuous cooling is that you are less sensitive to the exact Rabi frequency since there is no pulse length to consider, and the scattering rate of the optical pumping means the transition

[4] The reduced confinement of the axial direction increases all the time scales significantly, as well as the heating of all directions as the atom is cooled along each dimension.

retains a width that is larger than our magnetic field noise even if the Rabi frequency droops due to, for example, beam drift. Since we found that we had to often recalibrate the sideband positions with pulsed cooling, we opted to take the hit in cycle time because the continuous cooling did not require this recalibration. It is worth noting, however, that we can afford this hit in cooling speed because the heating rate during cooling (in our case, fundamentally from the Raman beam and tweezer spontaneous emission) is orders of magnitude less than the cooling rate. The final ground-state fraction is determined by a competition of the cooling and heating rate, hence necessitating an increased cooling speed to maintain the same ground-state fraction for an increased heating rate. This is likely why ion experiments stick to pulsed cooling, because these experiments have a high heating rate when the ions are trapped near the electrodes [50, 96] and their huge trap frequencies (couple MHz, typically) allow super fast cooling without off-resonant carrier heating.

Very recently, we have experimented with an approach that is summarized in Section 3.4.7. The idea here was to first perform a quick bit of continuous sideband cooling on the radial dimension of the trap so that the atom is mostly in the first couple of motional states to remove the concern of pulselength-sensitive dark states, after which we apply pulsed cooled with temporally Gaussian pulses [60]. However, for technical reasons that are presently being addressed, we could only just do continuous or pulsed cooling, but not both. The temporally Gaussian pulses result in a Gaussian frequency response of the atom, meaning they are much flatter on the top with a steeper drop off compared to the Lorentzian profile of a square pulse: The larger Rabi frequency mitigates the effects of magnetic field noise (slow drift requiring recalibration and decoherence requiring faster Rabi frequencies) while retaining spectroscopic resolution from the carrier. At some level this captures the best of both worlds: the robustness of continuous cooling and the potential speedup of pulsed cooling. In Section 3.4.7, we show the results of the Gaussian pulsed cooling, which we find is extremely robust due to the large Rabi frequencies.

3.4 Experimental results: Raman-sideband cooling

Here I will discuss our experimental implementation of sideband cooling, and the three versions used over the course of the past 4 years. For each cooling protocol, I will provide a table of the measured Raman Rabi frequencies on the carrier used for each beam pair, the Raman Lamb-Dicke parameters, and the measured optical pumping scattering rates (OP and RP beams) when relevant to the cooling. I will also give a brief summary of how we generate the Raman beams frequencies, as well as our characterization of the initial temperature of single atoms in the tweezers. For all of the cooling data, we cooled in either a 140 kHz (29 kHz) or 150 kHz (30 kHz) radial (axial) trap, leading to the optical pumping Lamb-Dicke parameters tabulated in Table 3.1.

Optical pumping Lamb-Dicke Parameters

Dimension	η_{OP}	Photon kicks from OP
Axial z	0.35	1
Radial x	0.16	2.5
Radial y	0.16	2.5

Table 3.1: We tabulate the optical pumping Lamb-Dicke parameters for the radial and axial dimensions of the optical tweezer. We use the trap with $\omega_{\text{radial}}/(2\pi) = 150$ kHz for these calculations, and the $\omega_{\text{radial}}/(2\pi) = 140$ kHz exhibits negligible differences. We also list the number of total momentum kicks (from absorption and emission) from three photons that are absorbed for optical pumping back to $|2,2\rangle$; these numbers are determined in a master equation including all the line-strengths and optical pumping polarizations, in conjunction with a calculation of the dipole emission profile associated with our quantization axis and with the polarization of the three photons (two σ^-, one π) on average emitted by the atom during this time.

.

3.4.1 Choice of beam geometry

We chose the beam geometry indicated in Figure 3.1 for a couple reasons. Firstly, we wanted to ensure that for a range of initial temperatures for the atom, we would be in the Lamb-Dicke regime to perform reliable sideband thermometry. Therefore, we deliberately chose slightly smaller Δk, and correspondingly smaller η_R, for the Raman beams. We knew that our initial temperature for the axial dimension would not be amenable to sideband thermometry (due to the lower confine-

ment), however we still opted for a slightly smaller associated η_R to reduce dephasing from higher order contributions in H_R. In later experiments, we switched the axial beam geometry (AB2 in Figure 2.4) to increase the axial Lamb-Dicke parameter, because we decided that a broader sideband peak (due to the increase in sideband Rabi frequency) was advantageous against drifts and we were exploring using a lattice to increase the confinement along the axial direction. I will not discuss the lattice in this thesis, but the slightly larger Lamb-Dicke parameter did not seem to make an observable difference for our tweezer cooling.

Another important design choice was the direction for the optical pumping beams. We chose both of them σ^+ since this minimizes the average number of photons to reach the spin-stretched dark-state, which implies that they would need to be parallel to the quantization axis. The fact that the effective magnetic field gradients from the trap point along y necessitated a quantization axis along x or z. Since the direction of the optical pumping guarantees three photons absorbed along that axis (and subsequent scattering into the dipole emission profile defined by the quantization axis), it is optimal for 3D ground-state cooling efficiency to have this momentum imparted to the axis with the smallest η_{OP}. Hence, we chose the optical pumping beam to be along the x direction. These considerations illuminate an important feature of sideband cooling, namely that even though the sideband transitions primarily address one axis the optical pumping couples the axes; in other words, poor cooling (e.g. by sitting too close to the carrier) of the axial direction heats the radial direction as well.

Lastly, all of the cooling is performed in a 3 G field to suppress dephasing and dark state depumping.

3.4.2 Beam generation

The Raman beams are detuned approximately 50 GHz red of the D2 line, as shown in the Chapter 2. As discussed earlier, RB1 is always used in combination with one of RB2-4 to address an axis with polarizations and spot sizes listed in Table 3.2. The intensity of each of the four Raman beams is separately switched with acoustic-optic-modulators, and RB1 additionally passes

through an in-fiber electro-optic phase modulator (EOM) operating near the hyperfine splitting of 6.8 GHz. RB1, prior to passing through the EOM, is frequency shifted by +10 MHz from RB2, RB3, and RB4 (also called AB1, and later replaced by AB2). Because the EOM sidebands are not filtered, this shifting (as well as the polarization) ensure that only the upper optical sideband on RB1 is resonant with a Raman process while the lower optical sideband is 20 MHz off-resonance and can only participate in the Raman transition if σ^--polarized; the beam frequency therefore prevents quantum interference effects and transitions as a result of any residual σ^- polarization on RB1 [92].[5] The 10 MHz frequency difference between the RB1 carrier and RB2-4 is also sufficiently large so as to avoid parametric heating. The beam detunings and polarizations are such that starting in $F = 2$ the atom always stimulated emits into RB1 while absorbing a photon from the other beam in use, which determines the direction of momentum transfer effected with each beam pair. The light shift on the $|1,1\rangle \leftrightarrow |2,2\rangle$ transition is ~ 90 kHz for all of the Raman beam pairs, which is dominated by the vector light shift induced by the σ^+-polarized RB1 beam when focused. After 2012, we switched to having RB1 unfocused due to alignment sensitivity: since this beam induces the largest light-shift, its alignment affects both the Raman Rabi frequency as well as the cooling frequencies. This change reduced angular sensitivity of the path, and we also reduced the intensity so that the overall light shift was closer to 30 kHz.

3.4.3 Characterization of initial temperature before sideband-cooling

After imaging the population in the optical tweezers, we perform sub-Doppler cooling. As noted earlier, prior to 2012 we used all three beams from the MOT for performing imaging and PGC, but observed that the atom counts fluctuated and that these fluctuations were correlated with the atom temperature (as determined by release and recapture [97]). These fluctuations were tracked down to fluctuations in the interference pattern formed between beams of different beam pairs in the MOT (i.e. beams that were not counter-propagating). We address the challenging

[5] The AO-shifting scheme also ensures that for the EOM modulation frequency applied for resonant Raman transitions with RB2-4, the optical sidebands themselves cannot resonantly participate in Raman processes.

Raman beam properties

Beam	Polarization	Approximate spot size
Axial, RB4/AB1/2	$\sim \pi$	50 μm
Top, RB2	π	50 μm
Bottom, RB3	π	50 μm
EO beam, RB1	σ^+	50 μm then 405 μm

Table 3.2: We list the properties of the Raman beams used in the experiment, with also a transcription between RBi and name used here. It made the figures to busy to use these full names. We note that AB1 and 2 have similar spot sizes but, as previously noted, refer to different beam paths. AB1 is approximately π polarized because it is linearly polarized in the $x-z$-plane (axes from Figure 2.4) but comes in at an angle to the quantization axis, thereby creating σ^-/σ^+. This polarization impurity does not effect the Raman transitions from $|2,2\rangle$ since there is only $\Delta m_F = -1$ transitions from this state, however, if we tried to drive transitions from $|1,1\rangle$ this in principle could be possible though we are very far detuned from a transition.

problem of stabilizing the phase of the interference pattern with respect to the sub-wavelength extent of the atom in the tweezer trap by modulating the position of our retro-reflecting mirrors at 1 kHz. This yields a time-averaged cooling that does not exhibit shot-to-shot variations in the final PGC temperature due to slow fluctuations in the interference pattern. After 2012, we switched to using a single retro-reflected beam (the "Imaging+MOT" beam) for the sub-Doppler cooling. The parameters (detuning and intensity) for the PGC cooling were optimized on the basis of quasi-adiabatically dropping the trap to a very shallow depth ($\sim$ 1 μK) and maximizing the survival probability of single atoms in the trap, which avoids servo wind-up effects when switching the trap.

Figure 3.7a shows sideband spectra after PGC along orthogonal radial directions. The asymmetry between the $\Delta n = -1$ and the $\Delta n = +1$ peaks determines the population of the atoms in the ground state. (Because we begin in the upper hyperfine state and vary the frequency of RB1, the $\Delta n = -1$ peak is on the right in Fig. 3.7.) Applying Eq. 3.20 to the $\Delta n = -1$ and $\Delta n = +1$ sidebands we find $\bar{n}_{y'} = 1.1 \pm 0.4$ or $\mathrm{T}_{y'} = 11 \pm 3$ μK assuming a thermal population distribution; correspondingly $\bar{n}_{x'} = 1.7 \pm 0.7$. Using the dephasing of the carrier Rabi oscillations (see Eq. 3.22), the accuracy of which does not depend on being in LDR, we find from the data in Fig. 3.7b that $\mathrm{T}_{y'} \leq 16 \pm 2$ μK. For comparison, we also employ a standard thermometry technique in which the atom is quickly released, and the probability of recapturing the atom at a variable time later is

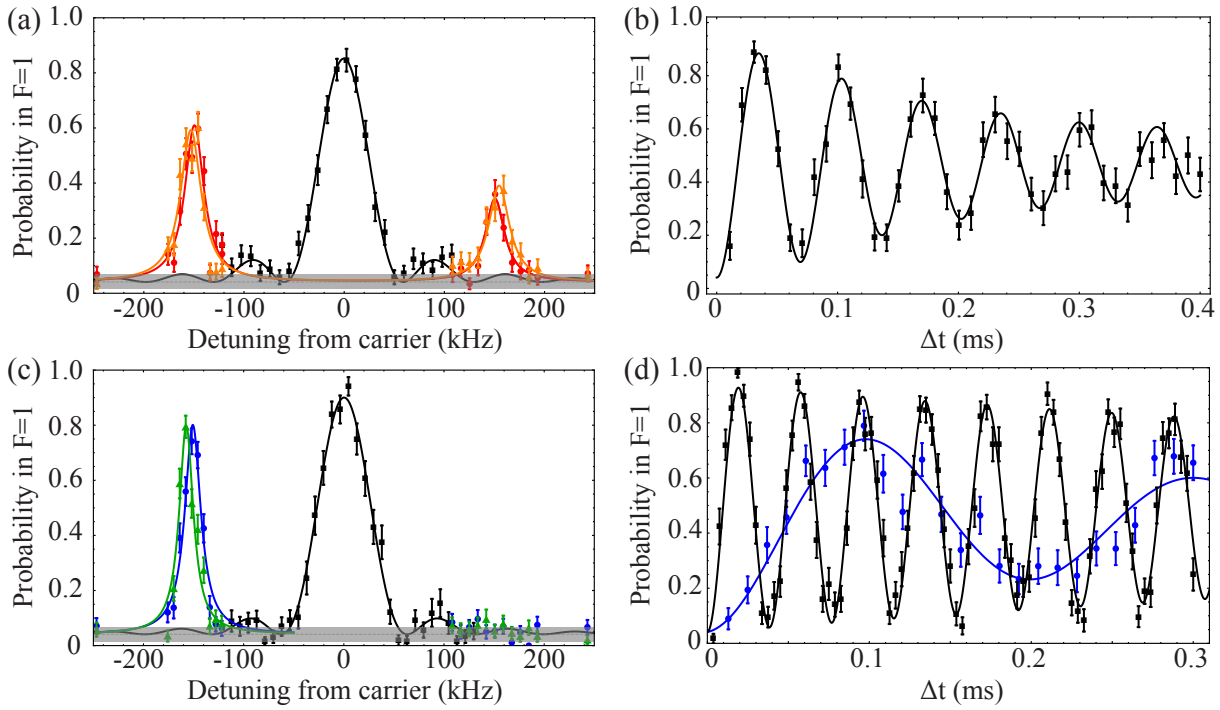

Figure 3.7: Single atom sideband spectra and Rabi oscillations in the radial dimensions before (a, b) and after (c, d) ground state cooling. (a) The black squares are a carrier peak in the y' direction using a $\Delta t = 15$ μs (near π) pulse. The red circles (orange triangles) are sidebands along the y' (x') axis for a 75 μs (near π) pulse, demonstrating an initial thermal population of vibrational states – these axes are defined in Figure 3.1. The solid lines are fits to a Rabi sinc function for the carrier and Lorentzians (an approximation) for the sidebands; each fit contains an offset at our measured background (gray shaded region centered at 0.04). (b) Carrier Rabi oscillations for the y' direction showing dephasing of a thermal state. Here the carrier Rabi frequency was set to 15 kHz, instead of 26 kHz. The solid line is a fit to the data using a thermal distribution of Rabi frequencies. (c) Raman cooled radial sidebands; no Raman cooling is applied to the axial direction for these data. The black squares are a cooled carrier peak using a 15 μs pulse. The blue circles (green triangles) are spectra along the y' (x') axis using a 75 μs pulse, displaying a significant asymmetry that is the hallmark of a large ground state population. (d) Rabi oscillations for a radial ground state cooled atom with a fit to a damped sine for the carrier (black squares) and the $\Delta n = +1$ sideband (blue circles), which demonstrates coherent control of the spin-motional states; the carrier dephasing is suppressed due to the purity of the vibrational distribution. Each data point is an average of 150 experimental runs, and hence ~ 75 atoms.

measured and compared to a classical Monte Carlo model [97] from which we estimate a temperature of 13 ± 1 μK. The agreement between our three measurements validates sideband spectroscopy as a reliable form of thermometry in an optical tweezer, and we find low PGC temperatures are possible despite the varying effective magnetic fields within the focus. Lastly, using the single beam

pair for performing in trap PGC, we optimize the parameters via the adiabatic drop down method and measure via carrier dephasing a slightly higher temperature of $T_{y'} \leq 21 \pm 3$ μK.

3.4.4 2D pulsed cooling results

For the radial dimensions, the PGC allows us to start our Raman cooling reasonably far into the Lamb-Dicke regime with $\eta_{\text{eff}}^{OP} \sim 0.3$ ($\bar{n} \sim 1.5$ and $\eta^{OP} = 0.16$). As a first demonstration of pulsed-sideband cooling, we show radial ground-state cooling with which we can contrast the thermal radial data. We apply a coherent Raman transition on the $\Delta n = -1$ sideband using an intensity corresponding to a ground state carrier Rabi frequency of $\Omega_c = 2\pi \times 26$ kHz, where the $\Delta n = -1$ sideband Rabi frequency is $\Omega_{SB} \sim \eta^R \Omega_c \sqrt{n}$. Therefore, we apply 60 μs pulses for 47 cycles and switch to 75 μs pulses for the last 3 cycles when the remaining excited state fraction is primarily in the first excited state. The pulses are applied to each radial axis by alternating Raman beam pairs. Interspersed between the Raman pulses are optical pumping pulses 90 μs long that recycle the atom back to $|2, 2\rangle$. Note we do observe cooling of both radial dimensions even if we employ a single pair of cooling beams, indicating there is coupling between the radial dimensions of our anharmonic potential. To assure and verify cooling in both dimensions, however, we cool and probe each axis separately.

After Raman cooling we see a significant asymmetry in the radial sideband spectroscopy due to a large ground state occupation (Fig. 3.7c). While the $\Delta n = -1$ sideband is suppressed, the $\Delta n = +1$ sideband has increased in height due to decreased dephasing as the thermal distribution is narrowed. Figure 3.7d shows Rabi oscillations for both the carrier (black) and $\Delta n = +1$ sideband (blue) transition, the latter of which oscillates slower by a factor of η^R. Figure 3.7d further demonstrates the coherence of our motional transitions. The carrier decays less quickly than in Fig. 3.7b, as expected for colder atoms; the sideband transition Rabi oscillations decay slightly faster than the cold carrier's due to its relative narrowness, but note that it maintains high contrast on the first oscillation. To assess our final occupation, we compare the measured signal at the position of the $\Delta n = -1$ transition peak to the measured background level due to

any atoms left in $F = 1$ and imperfect push-out efficiency. We use the data points at the very edge of the spectra to determine the offset. Since we are not able to fit the data at the position of the $\Delta n = -1$ sideband, we use the three data points closest to its calibrated position (± 8 kHz about the position of the sideband ascertained from the thermal spectra) and take the mean and standard deviation to conservatively estimate its height and associated error bar, respectively. We find $\{\bar{n}_{x'}, \bar{n}_{y'}\} = \{0.05^{+0.05}_{-0.04}, 0.02^{+0.04}_{-0.02}\}$.

3.4.5 3D pulsed cooling results

To achieve large three-dimensional ground state occupations, we must cool the weaker axial dimension of the trap where both spectroscopy and cooling are more challenging due to the smaller trap frequency. Figure 3.8a shows a thermal axial spectrum after PGC. The near equality of the $\Delta n = +1$ and $\Delta n = -1$ transitions and the presence of significant second order sidebands (given $\eta^R = 0.23$ for this dimension) are consistent with a small initial ground state population. Assuming an isotropic initial temperature of 12 μK, we would expect $\bar{n} = 8$, which corresponds to a challenging starting point of $\eta^{OP}_{\text{eff}} = 1.4$. Further, the smaller trap frequency makes it difficult to spectroscopically separate the carrier and sideband peaks while maintaining Rabi frequencies that are insensitive to technical dephasing. For the cooling, a large Rabi frequency leads to off-resonant carrier transitions that cause heating, while too small a Rabi frequency leads to smaller transfer efficiencies and slow cooling.

Despite these barriers, we are able to Raman cool in the axial dimension and achieve the significant three-dimensional ground state occupations evidenced in Fig. 3.8b after 33 ms of cooling. For the three-dimensional cooling shown in Fig. 3.8b we toggle the Raman laser pulses to address each of the axes of the trap, and between each pulse we insert 90 μs of optical pumping. The cooling process in total occurs in 75 cycles: The first 50 cycles use a Raman pulselength of $\Delta t = 48$ μs ($\Delta t = 40$ μs) for the radial (axial) directions, and then $\Delta t = 72.5$ μs ($\Delta t = 80$ μs) for the final 25 cycles. The two-stages of pulselengths is motivated by the conclusions in Section 3.3.2; we also stick to a pulselength below a ground-state sideband π-pulse (167 μs) for the axial direction to

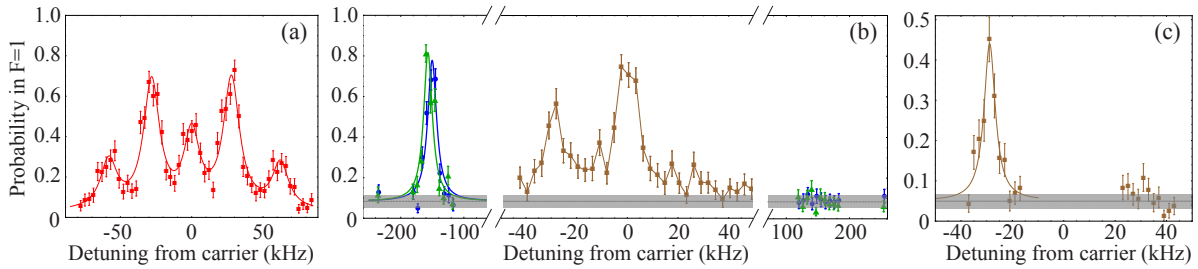

Figure 3.8: Axial spectra and 3D ground state pulsed-cooling of a single neutral atom. (a) A thermal axial spectrum (red squares) using an intensity corresponding to a cold carrier Rabi frequency of 12 kHz and a $\Delta t = 65$ μs Raman pulse. The data are fit to Lorentzians (solid line) to guide the eye. (b) Result of simultaneous sideband cooling in three-dimensions, demonstrating significant sideband asymmetries and simultaneous ground state occupations in all dimensions. The axial data (center) illustrates our cooling parameters, and is performed with a carrier Rabi frequency of 10.6 kHz and a pulse of 236 μs (near π pulse on the ground state $\Delta n = +1$ sideband, a 5π pulse on the carrier). For the radial data, the blue circles (green triangles) are spectra along the y' (x') axis using a 75 μs pulse. The solid lines on the $\Delta n = +1$ sidebands are Lorentzian fits. (c) After 3D cooling, axial spectroscopy for a halved carrier Rabi frequency of 5 kHz and a pulse of 450 μs. Better spectroscopic resolution affirms a large axial ground state occupation.

always address the first handful of motional states that are populated by a momentum kick. The cooling parameters are listed in Table 3.3. Between each of the spectroscopic scans in Fig. 3.8b, we recalibrated the position of the sidebands since we observed the presence of a few kHz shifts (1 mG) which are comparable to the width of the sideband transitions, particularly for the axial direction (during cooling $\Omega_{SB}^{\text{axial}} \approx 3$ kHz).

Unlike the radial dimensions, we use different parameters for the axial cooling than are ideal for spectroscopy. To highlight this distinction, we show two spectra of cooled atoms. The axial spectrum in Fig. 3.8b approximates the parameters used during our cooling, which balance speed with spectroscopic resolution. While there is a clear sideband asymmetry in the spectrum, the size of the Rabi frequency compared to the axial trap frequency complicates a temperature analysis because off-resonant carrier transitions occur at the frequency position of the sidebands. This is illustrated in Figure 3.9 where we show a calculated spectrum for these pulse parameters, but a full comparison to this calculation is complicated by the partial dephasing we observe.

In Fig. 3.8c, we halve the spectroscopy Rabi frequency to sacrifice coherence for spectroscopic resolution. For this Rabi frequency and pulse, the spectrum is dephased and hence we can under-

Pulsed cooling parameters

Raman beam pair	Ω_c	η^R
Axial (AB1)+EO	13 kHz	0.23
Top+EO	30 kHz	0.22
Bottom+EO	30 kHz	0.22

Table 3.3: Here we list the typical parameters used for the pulsed cooling experiments.

stand the spectrum simply as a set of multiple Lorentzians. We extract our axial temperature from the sideband asymmetry in Fig 3.8c, assuming the dephasing uniformly affects the two sideband peaks, which is consistent with magnetic field driven dephasing. Using the procedure outlined in Section 3.4.4, for both the radial and axial dimensions we analyze the data attributing all of the signal observed at the $\Delta n = -1$ position to the sideband (i.e. we are including off-resonant carrier spin flips), thus placing an upper bound on the achieved temperature. Taking this approach we extract temperatures in all three dimensions, again subtracting off a measured background and assuming a thermal distribution. The result is $\{\bar{n}_{x'}, \bar{n}_{y'}, \bar{n}_z\} = \{0.02^{+0.07}_{-0.02}, 0.01^{+0.06}_{-0.01}, 0.08^{+0.08}_{-0.06}\}$. For the axial dimension, for which a large initial thermal distribution exists, we confirmed that the sideband asymmetry is pulse length insensitive and also that there is significantly reduced dephasing of carrier Rabi oscillations.

The above occupations indicate we have cooled a single neutral atom to the ground state of an optical tweezer with $97^{+3}_{-11}\%$ probability in the radial plane, and $93^{+5}_{-7}\%$ probability in the axial direction, and hence a three-dimensional ground state population of $90^{+8}_{-16}\%$. While this estimate neglects imperfections in our spin preparation and detection, this is not a fundamental impediment to the final temperature. The limitation to our quoted temperature here is the precision of the spectroscopy measurement.

3.4.6 3D continuous sideband cooling

Once we started using the cooling to perform tunneling experiments, for which consistent high-fidelity preparation is required, we experimented with using the continuous cooling method.

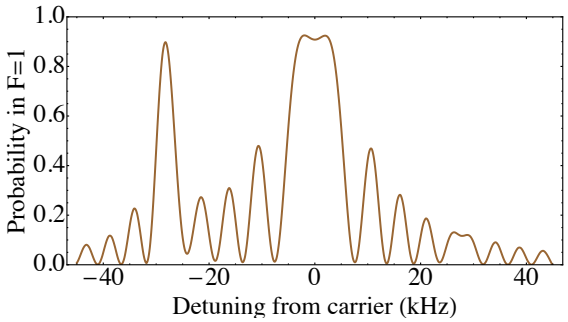

Figure 3.9: Simulated coherent axial spectrum with a square pulse. We simulate an axial spectrum for the parameters: $\bar{n} = 0.1$, $\Omega_R/2\pi = 10.6$ kHz, $\Delta t = 236$ μs, $\eta^R = 0.23$, and $\omega/2\pi = 30$ kHz. These parameters closely approximate those used for the axial spectrum in Figure 3.8b. Since we are using a π-pulse for the sidebands, this necessarily entails lots of oscillations from the carrier which is significantly overdriven. This complicates applying Eq. 3.20, which assumes that carrier transitions are not occurring at the position of the sidebands. When performing axial thermometry, we attribute all the signal at the position of the sidebands, which makes the temperature estimates conservative. Note that coherent cancellation of the spin-flips between the carrier and sideband transitions (which in principle could cause underestimating the temperature) is not possible since the states coupled in each are different: one has a change in motional state while the other does not. Such paths, therefore, always add incoherently.

The goal was to alleviate some of the constraints on the exact cooling frequencies so that recalibration of the sideband positions was not necessary, and perhaps sensitivity to the exact Rabi frequencies. The continuous cooling turned out to be very robust, particularly after we developed a frequency control setup that allows us easily to calibrate all the sideband positions in one measurement. Each morning we measure the location of the carrier resonance with a pair of Raman beams addressing the radial dimension, and all of the beam detunings are defined with respect to this frequency (see Figure 3.10). The resonance position is affected by changes in the magnetic field, as well as light shifts induced by the Raman beams; we observe less than 5 kHz drift day-to-day (in a 3 G field), which is indicative of small magnetic field drifts and the relative stability of our laser intensities.

3.4.6.1 Continuous cooling cycle

While I have harped on the differences between the continuous and pulsed-cooling, our continuous cooling protocol actually retains some features of pulsed-cooling. Unlike bulk degenerate

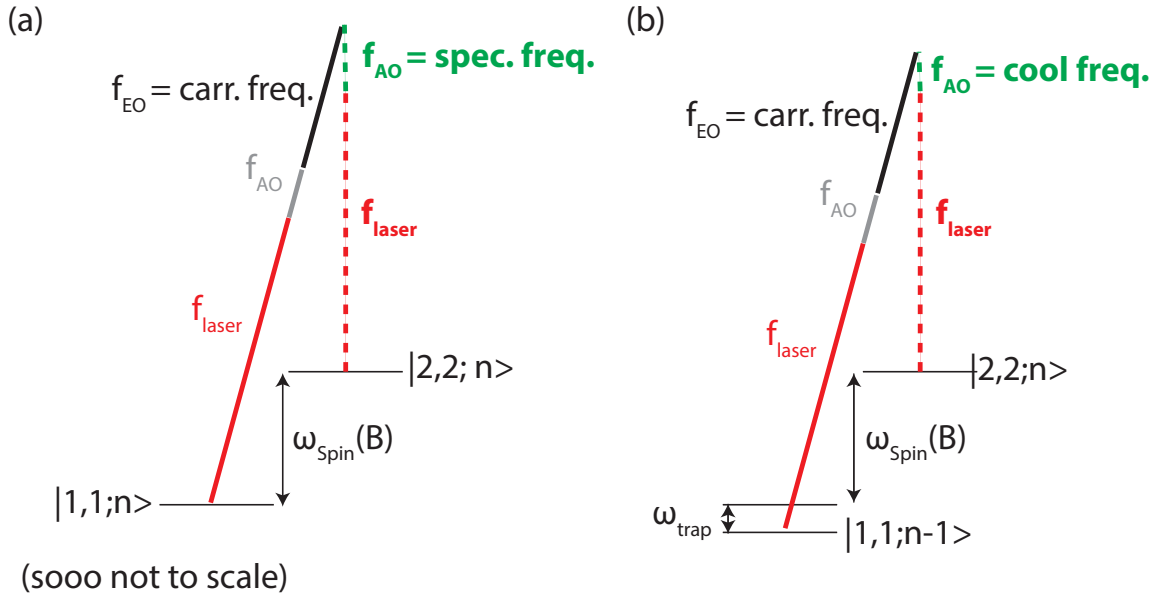

Figure 3.10: Since all the Raman beams are derived from the same DBR (with frequency f_{laser}), their final frequency is determined by the AOs through which they pass, as well as by the EO for the case of the EO beam. (a) We choose a particular AO frequency ("spectroscopy frequency") for the top beam (dashed colored lines in figure, bold frequency labels) when doing carrier calibration, while for the EO beam (solid colored lines in figure, unbold frequency labels) we scan the microwave frequency (f_{EO}) that determines the optical sideband for the Raman process (and its AO frequency is fixed). This measurement yields a microwave frequency for which we observe the carrier transition: we call this the "carrier frequency." (b) Fixing f_{EO} to the carrier frequency, we scan the frequency of the top, bottom, or axial beam to optimize the cooling and ascertain the associated "cooling frequency" for each beam. For the top and bottom beam, the difference between the spectroscopy frequency and the cooling frequency is very close to the trap frequency, as expected for cooling on the red-sideband; the axial is offset from the spectroscopy frequency by an amount which includes both the difference in the light shift from this beam compared to the top beam, as well as the trap frequency of the axial direction. Ground state cooling is performed with the microwave frequency set to the carrier location, while the top, bottom, and axial beam are set to their cooling frequencies. By measuring the carrier location each day, we can calibrate all of the magnetically field sensitive sideband resonance positions on the basis of this single measurement.

sideband cooling of neutral atoms in an optical lattice [56, 53], in which the cooling of all dimensions occurs concurrently, in our case each continuous cooling cycle addresses each radial axis and the axial axis separately. A schematic of a cooling cycle is illustrated in Fig. 3.11. The cooling is continuous since the optical pumping beams are always on concurrent with the Raman beams, but the Raman beams themselves are staggered in time. We stagger the Raman beam pulses for a couple reasons. This was partly to retain the ability to modulate the repumping scattering rate,

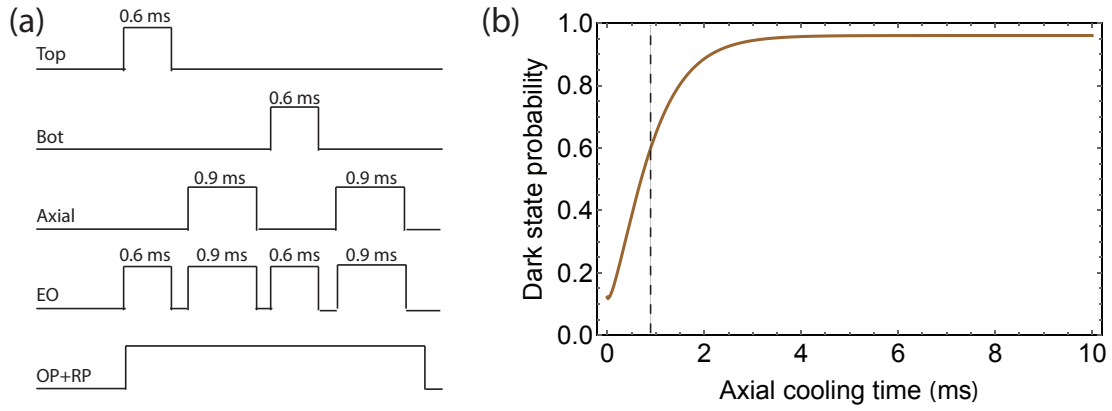

Figure 3.11: Continuous cooling cycle and axial cooling trajectory. (a) This timing diagram illustrates the sequence of Raman beams that are turned on and the corresponding times. The optical pumping beams are on for the entirety of the cooling time, during which the cycle is applied usually 50 times. The goal was to slowly cool the axial direction while repairing the heating done to the radial direction. The integrated axial cooling time is much longer than the time it would take to ground-state cool the axial direction according to the master equation numerics in (b), while the radial cooling time in just one cycle (done with top/bottom beams) is closer to what it would take to ground-state cool a radial axis since it is much faster. We therefore keep the atom close to the radial ground-state during the entirety of the three-dimensional cooling. (b) We show a simulated cooling trajectory for the axial direction using typical experimental parameters: $\Omega_R/(2\pi) = 7$ kHz, $\omega/(2\pi) = 29$ kHz, $\eta^R = 0.36$, $\eta^{OP} = 0.35$, an initial temperature of $\bar{n} = 8$, and we use the axial photon heating of 1 per optical pumping recycling.

which determines the width of the $|\downarrow\rangle$ state, depending on the axis being addressed; we have experimented with reducing this scattering rate for the axial cooling due to the reduced spectroscopic resolution of the carrier, but we determined that the same scattering rate was sufficient for all axes. Another reason to stagger the axes being addressed is that we have read about additional dark states being created when all the beams are on at the same time [54]. Lastly, dimensional staggering of the pulses decouples the cooling frequency for one beam from the alignment of another beam by ensuring that the light shift from one does not effect the location of the cooling resonance for another.

The entire cooling procedure is commenced with $10 - 15$ ms of continuous radial cooling with the EO and top beam to radially ground-state cool the atom. This ensures that once the 3D continuous cooling cycles start, the likelihood of radial motional excitation from the momentum kicks of the optical pumping is minimized (and this is at minimal expense to the axial direction,

which is already hot and scatters 1/5 the number of photons during pumping). Another added benefit is that broadening of the narrow axial sidebands due to the tweezer vector light shifts is suppressed by minimizing the radial extent of the atomic wavepacket. Experimentally we then apply 50 continuous cycles, after the last of which we have 1 ms of optical pumping to ensure the atom is spin polarized. The final temperature achieved is very consistent day-to-day. Since these times worked so consistently, we were hesitant to try to minimize them: it is possible, therefore, that the cooling time could be compressed. It is also fairly time consuming to take a set of sideband spectra for every experimental parameter (in a coupled space) involved in the cooling, so we were happy to stick with a functional cooling scheme even if its efficiency was not completely optimized.

3.4.6.2 Radial cooling resonance position

While some parameters we chose on the basis of our cooling calculations, calibration of the cooling frequencies was done experimentally. As was just mentioned, we were eager to optimize the cooling parameters without having to take 25 min spectroscopy scans for the top/bottom and axial axes each time we changed a parameter. We settled on a somewhat coarse approach inspired by the adiabatic lowering methods in Ref. [97]: we scan a parameter in the cooling and then perform an approximately adiabatic ramp of the trap depth down to ~ 1 μK and measure the atom loss. When the cooling is not working well, atoms populate higher lying bound states in the trap which subsequently couple to free-space modes during the ramp sequence. I call this measurement "coarse" because the final trap still retains many bound states, and hence does not directly probe the ground-state fraction. We optimize the exact cooling resonance locations using the ramp-sequence method, since a number of experimental factors can influence these exact frequencies.

In Figure 3.12a, we show an example of scanning the cooling frequency of the top and bottom beams while the EO beam is fixed on the carrier frequency (defined in Figure 3.10). There is a clear resonance close to the expected position of the sideband. In order to contrast the "cooling bandwidth," I show the same scan using pulsed and continuous cooling for the same Rabi frequencies. It is clear from the scan that the continuous method is significantly broader, as expected due

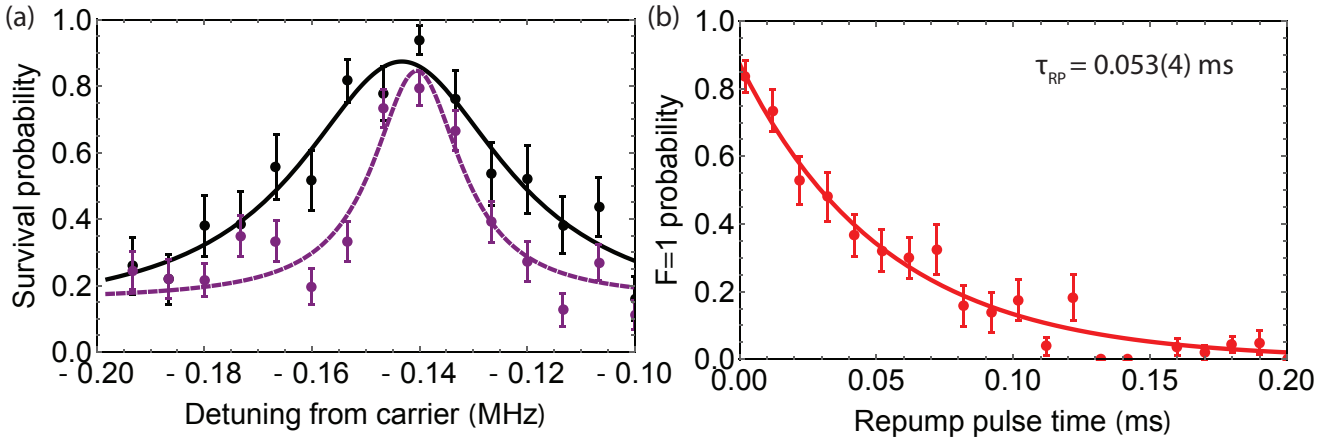

Figure 3.12: Varying radial cooling frequencies during sideband cooling, typical repump scattering rate measurement. (a) Here we vary the Raman detuning of the top and bottom beams while performing a ramp-sequence measurement after continuous (black) and pulsed (purple) cooling. Though the Raman Rabi frequencies are the same ($2\pi \cdot 20$ kHz), the pulsed cooling operates over a narrower bandwidth due to the absence of the repump broadening. The trap used here has a $\omega_{\text{radial}}/(2\pi) = 140$ kHz. The amount of loss observed at the peak of these curves is due to non-adiabaticity in this ramp; we have performed some tunneling experiments at similar depths of 1 μK and observe no loss using a slower, two stage ramp. (b) Repumping to $F = 2$ from the $|1, 1\rangle$ state. We prepare $|1, 1\rangle$ by performing sideband cooling then applying a π-pulse on the carrier. The repumping rate ($1/\tau$) is half the scattering rate Γ (photons/sec), due to the branching coefficients of 1/2 from F=2' to F=1 and F=2. We use such measurements to calibrate the repump scattering rate, which is crucial to the cooling performance.

to the scattering rate of the repump beam. We measure in Figure 3.12b the lifetime of the $|1, 1\rangle$ state in the presence of the repumping used during cooling to extract an expectation for the broadening it causes. If we calculate the expected FWHM of the red sideband for pulsed and continuous cooling (4.4 kHz and 6.9 kHz, respectively), we find that the width of the curves in Figure 3.12a are each about a factor of two larger. This is most likely because the measurement is non-linear in the ground-state fraction as the atom becomes cold: even if we have a broad motional occupation distribution of the bound-states in the shallow trap, the atom will always survive the ramp. This in turn will broaden the cooling resonance as a larger range of cooling parameters is sufficient to cool the atom to a distribution that survives the ramp down, as compared to the range that yields maximal ground state fraction.[6] Another indication of this mechanism is that we observe that

[6] This broadening effect clearly grows with the trap depth to which we ramp during the adiabatic ramp sequence: for example, if we did not ramp at all we would observe that this cooling resonance is much broader.

down to very small repump scattering rates the atom survives the ramp sequence. Therefore, as stated, this is a useful probe of the cooling performance, but one which we always confirm correlates with ground-state cooling.

3.4.6.3 Repumping and optical pumping scattering rates

Due to this insensitivity in the repumping scattering rate for the ramp-sequence measurement, the choice of repump and optical pumping scattering rates is a little tricky. Since the optical pumping beam only talks to $F = 2$, we just set its scattering rate to be a bit larger than the repump scattering rate so that it is not limiting during optical pumping but also not causing excess depumping. The choice of repump scattering rate is one which balances the broadening of the transition with the cooling speed. Assuming a single photon is required for recycling the atom, it can be shown [56] that the cooling rate saturates when the repump scattering rate $\Gamma_{RP} = \sqrt{2}\Omega_{SB}$, and so increasing the scattering rate further only increases off-resonant carrier transitions; this is directly analogous to the quantum zeno effect. For the $\tau = 0.053(3)$ measured in Figure 3.12b, this corresponds to $\Gamma_{RP} = \frac{2}{\tau} = 38(2)$ ms^{-1} since it takes two photons to repump to $F = 2$. The radial ground-state sideband Rabi frequency $\Omega_{SB} = 2\pi$ 4.4 kHz is very close to fulfilling this above criterion for $\Gamma_{RP} = 38$ ms^{-1}. It is important to point out, however, that these statements assume that it takes one photon to pump back to $|2, 2\rangle$, when in fact we know it requires three. Therefore, it is possible we could further speed up the cooling, but possibly at the expense of carrier heating. Both master equations simulations and spectroscopy confirm that this choice of repumping scattering rate yields greater than 95% ground-state fractions for each dimension with the Rabi frequencies listed in Table 3.4. Lastly, as the saturation intensity of the optical pumping and repumping beams is increased, one could become concerned about the fluctuating dipole force for an optically-dipole-trapped atom [6].

3.4.6.4 Axial cooling resonance positions

We calibrate the axial cooling resonance using the ramp-sequence technique as well, data from which is shown in Figure 3.13. From these data, we observe significant cooling is possible via the first and second sideband resonances, which are indicated in the diagrams. When using AB1 for axial cooling, we have used the second-sideband resonance for the first 75 times the axial cooling pulse is applied (there are two applications during a cycle as defined above). This resonance has the added benefit of being further resolved from the carrier so that we could use a larger Rabi frequency when driving the transition, with which we can robustly cool on a broader transition. After 75 cooling axial pulses with second-sideband cooling (and the radial cooling on the first-sideband staggered between), we observe red and blue sidebands via axial spectroscopy whose asymmetry indicates $\bar{n}_z = 1.0(5)$. We subsequently apply 25 pulses with first-sideband axial cooling, which ultimately determines our final ground-state occupation. Lastly, when we switched to using AB2, we tried using exclusively first sideband cooling and found comparable performance – it is the parameters of this cooling that are listed in Table 3.4. Nevertheless, I wanted to discuss the second sideband cooling since we employ this hybrid sideband procedure for the data discussed in Chapter 4 in order to finely tune the motional distinguishability of two atoms, and, furthermore, because this two-tiered approach could be helpful when starting from a very hot sample.

Before moving on to spectroscopy, I wanted to stress the importance of determining the cooling resonance in this fashion. We have observed small few kHz shifts of the continuous cooling resonance positions with respect to the measured sideband positions. This is because, for continuous cooling, the optical pumping and repump beams can induce small light shifts of the spin states (the former can shift $|1,1\rangle$, while the latter can shift both $|1,1\rangle$ and $|2,2\rangle$ if not exactly on resonance); these effects are not expected for pulsed cooling and the cooling resonance is observed to be at the position of the sideband. In Figure 3.12a, there is a small 3(1) kHz between the pulsed and continuous cooling resonance positions, and for the axial sideband cooling we observed a similar shift between the measured location of the sidebands and the position of maximal cooling determined

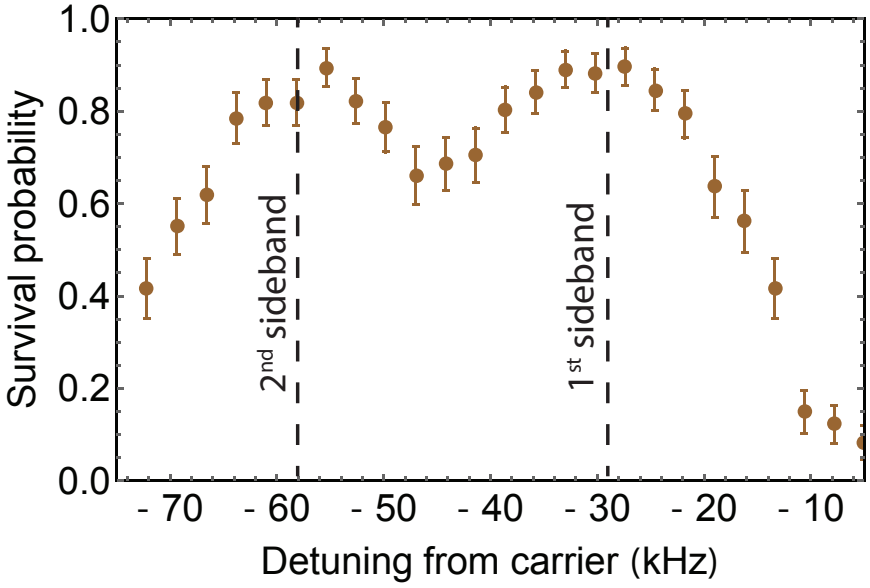

Figure 3.13: Ramp-sequence calibration of axial cooling frequency. We scan the Raman detuning of the axial beam (AB1 here) and observe the positions of maximal atom survival. These coincide with the regions in which we expect the multiples of the trap frequency to be (dashed lines), and we typically set the cooling frequency to the center of either range when performing first or second sideband cooling. The increased survival probability is likely more directly an indication of lower heating of the radial direction during cooling by cooling the axial direction to the ground-state (which, of course, is dark). As we approach the carrier at higher frequencies, the increased loss is likely from radial heating due to carrier transitions inducing optical pumping. This statement is based on the fact that the larger confinement of the radial direction implies fewer bound-states in the trap, and hence greater susceptibility to loss for a given $\bar{n}$.

via ramp-sequence methods (see Figure 3.13). Surveying similar measurements over the past while, this shift with the radial continuous cooling resonances has been between 3 and 7 kHz. Though a careful characterization of this effect and its dependence on the optical pumping beams has not been performed, the consistency of the shifts supports this procedure for choosing the cooling frequencies as opposed to just spectroscopically measuring the sideband positions of a thermal atom.

3.4.6.5 3D ground-state spectra via continuous cooling

Using the parameters listed in Table 3.4, we achieve the ground-state fractions indicated by the spectra in Figure 3.14. The final temperatures, $\{\bar{n}_{x',y'}, \bar{n}_z\} = \{0.016(13), 0.21(0.14)\}$, are consistent with the pulsed cooling results within our experimental precision; in particular, it is very

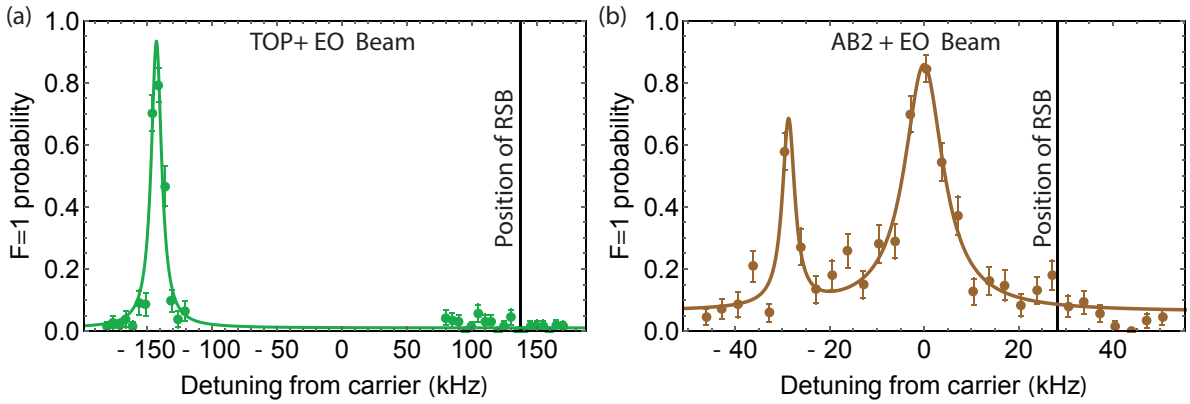

Figure 3.14: Continuous cooling sideband spectra for a radial dimension and the axial dimension. (a) Top and EO beam spectroscopy of the radial dimension of the tweezer after continuous sideband cooling. The pulselength here is near a π-pulse on the blue-sideband from the ground state. The reduced offset in these data compared to the pulsed section is due to improved push-out fidelity (we drop to a shallow depth to perform the push-out) and the reduced Rabi-frequency of $\Omega_R/(2\pi) = 20$ kHz. (b) AB2 and EO beam spectroscopy of the axial dimension of the tweezer. In both plots, the black line indicates the expected position of the associated red-sideband for the dimension probed.

difficult to discern any excited state fraction for the radial spectra. We show one radial direction here since we do not observe asymmetric temperatures for the radial directions of the trap. We consistently observe spectra of this quality using the continuous cooling regimen.

3.4.7 3D Gaussian-pulsed cooling

As was discussed earlier, we have very recently been experimenting with a Gaussian pulsed-cooling approach. Inspired by the clean spectra created using Gaussian amplitude modulation in Section 2.12, we applied this same modulation to the Raman beam powers to reduce off-resonant carrier transitions during cooling and sideband thermometry while retaining large Rabi frequencies that are less susceptible to dephasing and drift.

To achieve this control, we simply mix the RF frequency supplied to the top, bottom or axial (AB2) beam AO with a modulated voltage from an arbitrary waveform generator. The voltage to optical power is separately calibrated, and the Gaussian envelope is generated using this calibration.

Continuous cooling parameters

Raman beam pair	Ω_c	η^R	Γ_{RP}	Γ_{OP}
AB2+EO	$6-8$ kHz	0.36	33(4) 1/ms	70(10) 1/ms
Top+EO	19.5(2) kHz	0.23	33(4) 1/ms	70(10) 1/ms
Bottom+EO	19.0(3) kHz	0.23	33(4) 1/ms	70(10) 1/ms

Table 3.4: Here we tabulate the cooling parameters used for typical continuous cooling experiments. The uncertainty in the Rabi frequencies and optical pumping rates reflects the measurements of those values done closest to the spectra shown in Figure 3.14, and not the required parameter range for which the cooling is robust. These numbers are tabulated for the case of entirely first-sideband cooling of the axial direction. We typically doubled the power (40% increase in Rabi frequency) for second-sideband cooling when using AB1.

The Rabi frequency is varied as,

$$\Omega_c(t) = \Omega_{\text{peak}} \left(e^{-t^2/(2\tau^2)} \right)^{1/2}, \tag{3.26}$$

where we have retained the normal Gaussian definition of τ in order to emphasize the presence of the power of 1/2, and Ω_{peak} is the peak carrier Rabi frequency during the modulation. This square-rooting arises because we only modulate one of the beams in the Raman process (EO beam is unmodulated), and the square root of its intensity determines the single-photon coupling it contributes to the Raman Rabi frequency. The τ for each dimension is chosen such that the total pulse-area of the Gaussian is near a sideband π-pulse from the ground-state: the measured Rabi frequencies and associated τ for each dimension are displayed in Table 3.5.

The cooling protocol operates as follows. We apply pulsed cooling on all three dimensions with pulselengths of 120 μs (138 μs) for radial (axial) dimensions with optical pumping staggered between each pulse. There are 100 cycles, each including a pulse on each of the three dimensions. The larger Rabi frequencies used here significantly shift the location of the sidebands towards the carrier due to off-resonant dressing through the carrier [98] (see also Figure 3.15), and so we calibrate the position of the sidebands using the Gaussian pulses.

In Figure 3.15, we show ground-state cooled spectra using this method. The cleanness of the spectra (offset, scatter) is evidence of the suppression of carrier transitions at the position of the sidebands; the improvement is made clearer when considering that the Rabi frequency here is

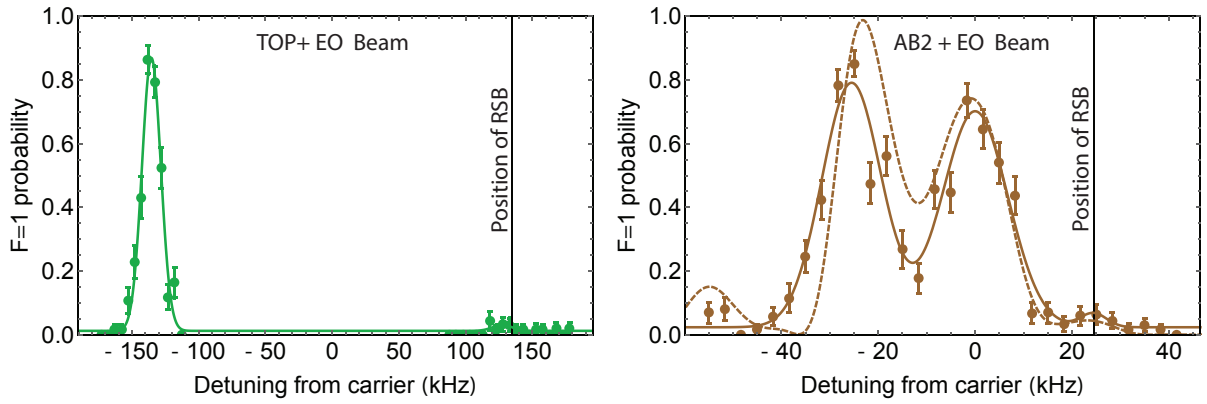

Figure 3.15: Sideband spectra after Gaussian pulsed cooling. We show spectra for the radial (a) and axial (b) directions of the tweezer. For the axial data, we compare the spectra with an numerically calculated spectrum (dashed line) using $\bar{n}_{axial} = 0.05$ ($T = 0.45$ μK, $\omega/(2\pi) = 29$ kHz, and the parameters listed in Table 3.5). The solid lines for each are fits using a sum of Gaussians. The axial spectrum exhibits significantly higher contrast and coherence compared to other axial spectra shown in this chapter, which necessarily used a lower Rabi frequency to retain spectral resolution for square-pulse spectroscopy.

50% (140%) larger than what is used in the pulsed-cooled radial (axial) spectra from Figure 3.8b and Figure 3.9. Furthermore, the significantly higher contrast of the axial blue-sideband compared to any of the axial spectra previous shown in this thesis strongly corroborates the hypothesis that the relative narrowness of these peaks is what has suppressed the contrast. To test how close we are to the full coherence, I show a calculation of the expected spectrum (dashed line) using the parameters listed in Table 3.5 for a $\bar{n}_{\text{axial}} = 0.05$. It is clear that the contrast is still not perfect, and there is slight relative shift of the measured sideband location compared to the calculation. The latter disparity could be from not perfectly creating a Gaussian, which changes the degree to which carrier shifts the location of the sidebands; it is also possible that at these large Rabi frequencies, the coupling of AB2 and the EO beam to the radial axis may induce dressing through the radial sideband, thereby pulling the axial blue sideband away from the carrier some; this effect is not accounted for in the code. Lastly, I have numerically looked at what happens to the sidebands for a 2π pulse to see if pulse-length sensitive dark-states would be spectrally concealed: while the crazy oscillatory behavior in an overdriven square pulse spectrum is not evident, there are peaks

at the 5% level which would likely be evidenced in these spectra if there were significant excited state fractions. In other words, far away from a π-pulse, the frequency response of the atom is not exactly Gaussian and these excited state populations would likely show up experimentally. We have also confirmed experimentally that the ground-state occupation achieved with this method is very similar to the continuous cooling on the basis of the spin-exchange oscillation contrast discussed in Chapter 5.

Gaussian cooling parameters

Raman beam pair	Ω_c	η^R	τ
AB2+EO	24 kHz	0.36	17.8 μs
Top+EO	41 kHz	0.23	15.3 μs
Bottom+EO	41 kHz	0.23	15.3 μs

Table 3.5: Here we list the parameters used for Gaussian shaped pulses during pulsed-sideband cooling. The length of the pulse applied is 120 μs (138 μs) for the radial (axial) beams. The τ and Ω_c for each dimension was chosen such that the pulse was near a π-pulse on the ground-state sideband Rabi frequency.

In conclusion, this last method of cooling offers further robustness by broadening the sidebands without off-resonant carrier heating, and increased cooling speed by using pulses. The cleanness of the spectra, furthermore, in principle allows more precise quantification of the temperatures achieved. For the size of red-sidebands observed in these data, however, the standard errors in the amplitudes are 100%. While we have not performed Gaussian spectroscopy after applying the cooling techniques of the previous sections, the resulting temperatures here,$\{\bar{n}_{x',y'}, \bar{n}_z\} = \{0.02(2), 0.06(6)\}$, are not more than 1σ from what was observed using the other cooling protocols with square pulse spectroscopy. We, therefore, cannot conclude that the cooling is improved, but this is a rapid pulsed-protocol that works day-to-day and provides much cleaner spectra for thermometry.

Chapter 4

Atomic Hong-Ou-Mandel effect: Two-particle quantum interference in tunnel-coupled optical tweezers

In this chapter, I will present our observation of two-particle interference, revealing the Hong-Ou-Mandel effect with atoms instead of photons. We employ the high-fidelity ground-state laser cooling techniques of the previous chapter in order to control all degrees of freedom of two independently prepared ^{87}Rb atoms. The signatures of indistinguishability we observe – in the form of atomic Hong-Ou-Mandel interference – constitute a direct probe of the purity of the quantum states we independently prepare. Furthermore, to our knowledge, this is the first direct observation of physics strongly influenced by quantum statistics, where the atoms studied are purely laser cooled. The presented results demonstrate a route towards using laser-cooled atoms in optical tweezers to study quantum degenerate systems.

The chapter is long and organized as follows. I first discuss Hong-Ou-Mandel interference generally, and how it fits into the broader set of experimental observations of the quantum statistics of massive particles. I then provide a semi-formal description of entanglement and how it manifests in photonic and atomic Hong-Ou-Mandel interference. With this background, I proceed to describe our experimental implementation of an atomic beam splitter in the form of a tunnel-coupled double-well potential, and experimental characterizations thereof. I then discuss in detail our observation of the Hong-Ou-Mandel effect with atoms, and subsequently our analysis and understanding of these results.

Lastly, this chapter takes considerable material from our work published in Ref. [99], of which

I formulated much of the experiment along with my labmate Brian Lester, and was significantly involved in the theoretically analysis studied by the Rey group. Both the experimental and theoretical conclusions are discussed in detail in this chapter.

4.1 Introduction: interfering indistinguishable single atoms

Quantum interference between possible detection paths for two indistinguishable particles yields information about quantum statistics and correlations [100, 101]. An example is the Hong-Ou-Mandel (HOM) effect, which reveals bosonic quantum statistics through a coalescence effect that causes two indistinguishable photons incident on different ports of a beam splitter to emerge on the same, yet random, output port [1] (see Figure 4.1). The HOM effect has been observed with photons [1, 73, 102] and in an analogous experiment with electrons [103], but has never been observed with independently prepared massive bosons.

Here we demonstrate the HOM effect with bosonic atoms in tunnel-coupled optical tweezers. We attain the requisite, precise control of the single-atom quantum state by laser cooling each atom (see Chapter 3) to its motional ground state in separated, dynamically positionable optical tweezers. The realization of a low-entropy bosonic state by individually placing atoms in their motional ground state has long been a goal in atomic physics [53, 62, 104]. The HOM interference we observe represents a direct observation of quantum indistinguishability with independently prepared, laser-cooled atoms. While the role of quantum statistics in macroscopic ensembles of fermionic and bosonic atoms can be observed via Hanbury Brown and Twiss interference experiments [105, 106, 107, 108, 109, 110, 111], HOM interferometry allows us to study nonclassical few-atom states with single-atom control. Our results lay a foundation for linear quantum computing with atoms [112], interferometric highly sensitive force detection [113], control of neutral atoms in nanoscale optical devices [114, 67], and quantum simulation with laser-cooled atoms in scalable optical tweezer arrays.

In our work, a double-well trapping potential created with optical tweezers realizes a beam splitter for single ^{87}Rb atoms. Analogous to photons incident on separate ports of an HOM beam splitter, when the two bosonic atoms start in separate wells, a tunnel-coupling can result in the

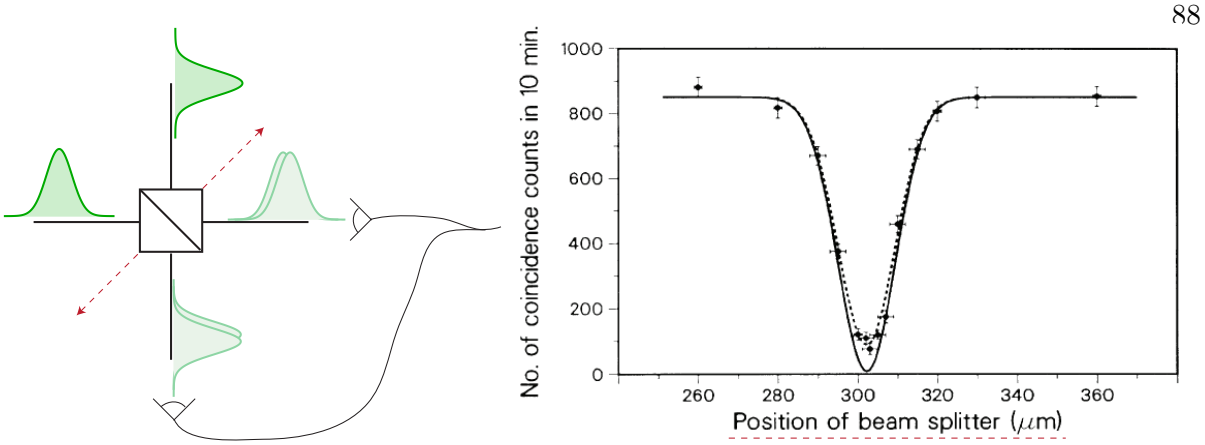

Figure 4.1: Original Hong-Ou-Mandel effect observation. In the experiment, two photons in the same polarization state are incident on separate ports of a balanced beam splitter. The position of the beam splitter is varied so that the overlap of the wave-packets on the beam splitter is tuned. Each output port of the beam splitter is measured on photodetectors, and the likelihood for both detectors to click within a small time-interval, the "coincidence counts", is measured. The data plot on the right is taken directly from Ref. [1]: it shows that for a particular position of the beam splitter, the coincidence counts drastically drop. Even though, classically, we might expect an equal likelihood of the photons coming out the same or different port, there is a coalescence effect induced by the bosonic quantum statistics of the photons. A two particle interference effect, known as the Hong-Ou-Mandel effect, suppresses the quantum amplitude that the photons emerge on different ports, specifically when the photons are overlapped on the beam splitter.

transformation $|1,1\rangle \rightarrow \frac{1}{\sqrt{2}}(|2,0\rangle + |0,2\rangle)$, where $|n_L, n_R\rangle$ is the bosonic state of n_L (n_R) atoms in the left (right) tweezer. To understand the HOM effect in our system, it is helpful to utilize the single-particle states $|L\rangle$ and $|R\rangle$ that correspond to an atom localized in the left or right well. In this notation, the Bose-symmetric state that the atoms initially occupy is $|S\rangle \equiv \frac{1}{\sqrt{2}}(|L\rangle_1|R\rangle_2 + |R\rangle_1|L\rangle_2)$, where the ket subscript is a particle label and $|S\rangle$ is the same as the second-quantized $|1,1\rangle$ state. Introducing a tunnel-coupling between the left and right wells allows for the single-atom transformations $|L\rangle \rightarrow \frac{1}{\sqrt{2}}(|L\rangle + i|R\rangle)$ and $|R\rangle \rightarrow \frac{1}{\sqrt{2}}(|R\rangle + i|L\rangle)$. One might expect that these transformations yield an equal likelihood of finding the atoms in separate wells or the same well. However, when the two atoms are indistinguishable, the paths resulting in a single atom in each well destructively interfere (see Figure 4.2), and hence one finds $|S\rangle \rightarrow \frac{i}{\sqrt{2}}(|L\rangle_1|L\rangle_2 + |R\rangle_1|R\rangle_2)$. The atoms, therefore, only appear in the same, yet random, tweezer.

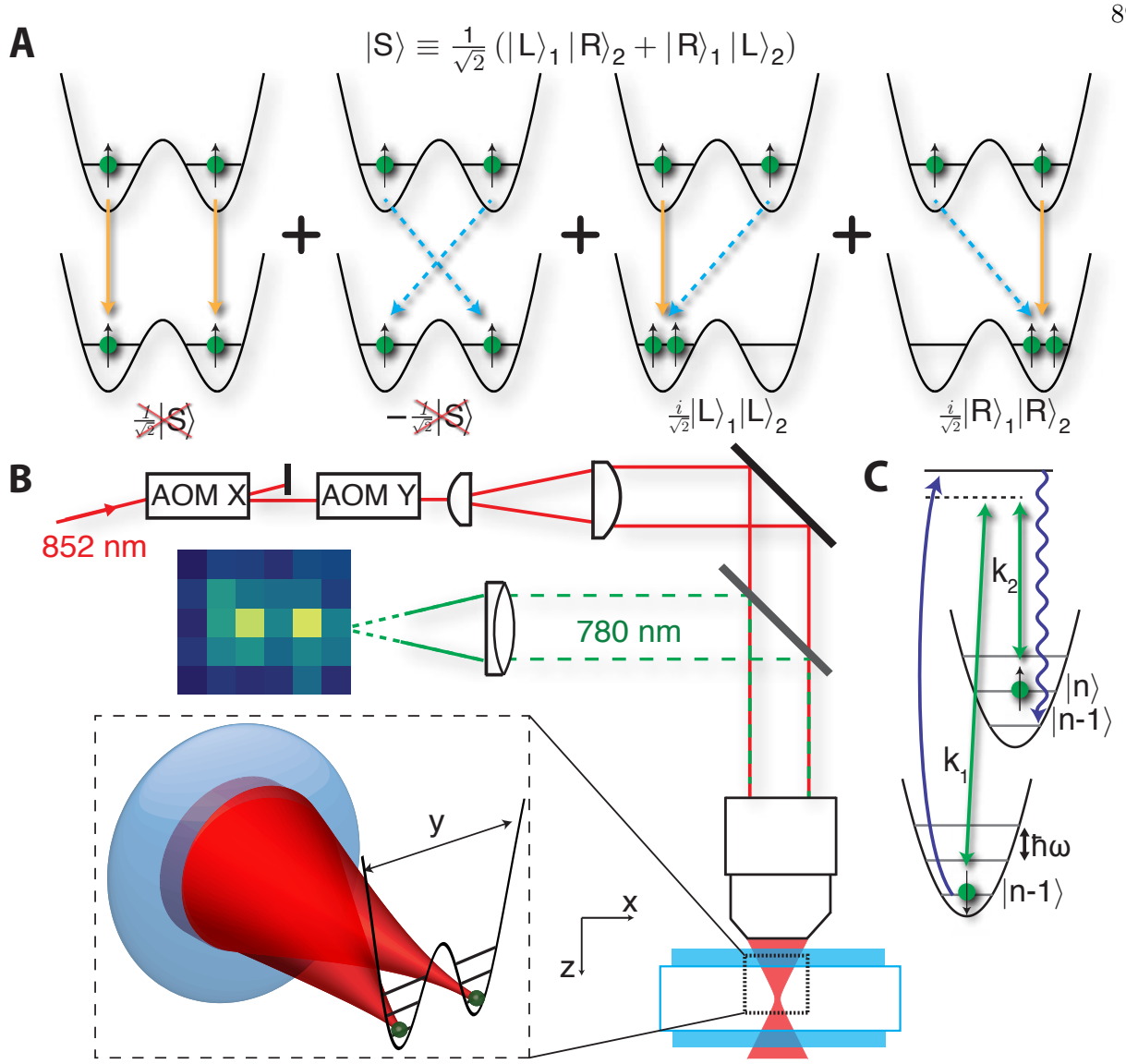

Figure 4.2: Hong-Ou-Mandel effect with atoms and experimental setup. (a) The optical tweezers form a coupled double-well potential. Starting from a state with a ground state spin-up atom in each well, denoted $|S\rangle$, the tunnel-coupling causes the atoms to interfere destructively and results in the state $\frac{i}{\sqrt{2}}(|L\rangle_1|L\rangle_2 + |R\rangle_1|R\rangle_2)$. (b) The apparatus for realizing tunneling between optical tweezers utilizes the high numerical aperture optics and radio frequency signal control of the tweezers' positions and depths discussed in Chapter 2. (c) The sideband cooling (see Chapter 3) is accomplished via lasers driving coherent (green) and spontaneous (blue) Raman transitions that couple to the atomic motion and spin states $|F = 1, m_F = 1\rangle \equiv |\downarrow\rangle$ and $|F = 2, m_F = 2\rangle \equiv |\uparrow\rangle$.

4.2 Entanglement, symmetrization, and distinguishability

At the heart of the HOM effect are three mechanisms central to quantum mechanics: entanglement, symmetrization, and distinguishability. Since these three terms are all related, distinct, and present in the HOM effect, I wanted to define them within the context of this thesis. The ideas gathered in the following section are nearly exclusively from the Refs. [115, 7, 116, 117], which are excellent guides and I hope my summary does them justice. Key concepts that I will attempt to clarify and distinguish are entanglement between particles and entanglement between modes.

4.2.1 Entanglement

There are a number of ways of formulating entanglement, but consistent among them is one feature: the presence of correlated, quantum fluctuations between observable systems that are basis independent. For example, an entangled state of two particles at positions $\{L, R\}$, each with internal spin-states $\{\uparrow, \downarrow\}$ aligned or anti-aligned with a quantization axis, can be written,

$$|bell\rangle = \frac{1}{\sqrt{2}} \left(|\uparrow\rangle_L |\downarrow\rangle_R + |\downarrow\rangle_L |\uparrow\rangle_R \right). \tag{4.1}$$

By application of a $\pi/2$-pulse, we can effectively rotate our basis of measurement, and observe that the anti-correlations in the spins are converted to pure, positive correlations:

$$|cat\rangle \rightarrow |\psi_{\pi/2}\rangle = \frac{1}{\sqrt{2}} \left(|\uparrow\rangle_L |\uparrow\rangle_R + |\downarrow\rangle_L |\downarrow\rangle_R \right). \tag{4.2}$$

In fact, this exact technique is widely used to detect two-particle spin entanglement in ions and neutral atoms, and we employ it in Chapter 5; it is also what is detected by a Bell's inequality [118]. The intrinsic basis independence of the correlations here distinguishes quantum-correlated (entangled) states from classically-correlated states, such as the two-particle spin mixture

$$\rho = \frac{1}{2} \left(|\uparrow\rangle_L |\downarrow\rangle_R \langle\uparrow|_L \langle\downarrow|_R + |\downarrow\rangle_L |\uparrow\rangle_R \langle\downarrow|_L \langle\uparrow|_R \right). \tag{4.3}$$

This state has classical correlations in that the spins are always measured to be anti-aligned. Yet, upon application of a $\pi/2$ pulse the resulting state $\rho_{\pi/2}$ does not exhibit purely positive correlations.

These notions can be formalized by defining entanglement for pure states as the class of states that are not separable, which I will now summarize according to the treatment in Ref. [7]. Suppose we have some state $|\psi\rangle$ living in the bipartite Hilbert space $\mathcal{H} = \mathcal{H}_\mathcal{A} \otimes \mathcal{H}_\mathcal{B}$. Here, $\mathcal{H}_\mathcal{A}$ ($\mathcal{H}_\mathcal{B}$), for example, can correspond to the Hilbert space of a spin-1/2 particle sitting at the position represented by the state $|L\rangle$ ($|R\rangle$). The state $|\psi\rangle$ is separable if it can be written as the product,

$$|\psi\rangle = |\psi\rangle_A \otimes |\psi\rangle_B, \tag{4.4}$$

where states $|\psi\rangle_i$ live in Hilbert space $\mathcal{H}_i$. The ability to write a state in this fashion precludes the presence of the basis-independent, correlated fluctuations previously discussed. This treatment can be extended to mixed states described by density matrices: a density matrix describing a bipartite system is separable provided there exists a decomposition of the total density matrix in which it can be written as,[1]

$$\rho = \sum_j P_j \rho_A^j \otimes \rho_B^j. \tag{4.5}$$

A mixed state that cannot be written in this fashion is entangled. These definitions imply a very useful relation between the purity, $\mathrm{Tr}(\rho^2)$, of the total density matrix in $\mathcal{H}$, and the purity of the reduced density matrix ($\rho_{A(B)} = \mathrm{Tr}_{B(A)}(\rho)$) within one of the subspaces $\mathcal{H}_i$. A separable state satisfies [119, 120],

$$1 \geq \{\mathrm{Tr}(\rho_A^2), \mathrm{Tr}(\rho_B^2)\} \geq \mathrm{Tr}(\rho^2). \tag{4.6}$$

For separable states, this can be understood simply: the states within $\mathcal{H}_A$ and $\mathcal{H}_B$ can only be as mixed as the total density matrix, since the total density matrix necessarily contains the combined mixedness of the states (for example, a product-state has $\mathrm{Tr}(\rho^2) = \mathrm{Tr}(\rho_A^2) * \mathrm{Tr}(\rho_B^2)$). On the other hand, a mixed state that violates Eq. 4.6 is entangled.[2] For example, consider the pure state $\rho = |cat\rangle\langle cat|$. We can trace over the left particle's spin-1/2 Hilbert space, $\mathcal{H}_L$, yielding the mixed

[1] The stipulation that as long as one decomposition exists in which to express the state as separable is important. In this chapter we will consider the NOON states $|\pm\rangle = 1\sqrt{2}\,(|2,0\rangle \pm |0,2\rangle)$, and we will consider entanglement between the modes in their number degree of freedom. The density matrix $\rho = \frac{1}{2}\,(|+\rangle\langle+| + |-\rangle\langle-|)$ might appear entangled since it is the sum of entangled states, but it actually can also be written $\rho = \frac{1}{2}\,(|2,0\rangle\langle 2,0| + |0,2\rangle\langle 0,2|)$, which is separable with respect to the subspaces since it is a sum of product states [116].

[2] Note, however, that not all mixed entangled states violate Eq. 4.6; in other words, it is a witness to entanglement, but not necessary. However, all pure entangled states do violate Eq. 4.6 [116, 95]

state,

$$\rho_R = \frac{1}{2}\left(|\uparrow\rangle_R\langle\uparrow|_R + |\downarrow\rangle_R\langle\downarrow|_R\right), \tag{4.7}$$

where,

$$\frac{1}{2} = \mathrm{Tr}(\rho_R^2) < \mathrm{Tr}(\rho^2) = 1. \tag{4.8}$$

This provides an intuitive description of entanglement, where excluding populated parts of the Hilbert space introduces entropy or loss of information contained in the entangled state. This is also a nice way of visualizing decoherence: when a system of interest becomes entangled with degrees of freedom in the environment that are unmeasured, then the measured sub-space necessarily becomes mixed according to the above treatment. The total state of the system, which includes degrees of freedom in the environment, is of course pure, but the measured subspace is not because it is entangled with these additional degrees of freedom.

Another way of casting the above description (at risk of redundancy) is that local measurements, that is measurements of observables contained within one of the sub-spaces, cannot distinguish a bipartite entangled state from a mixed state contained in one sub-space. For example, by performing operations on just the spin at position $|R\rangle$ in $|cat\rangle$, it is not possible to discern whether the spin at $|R\rangle$ is just in the statistical mixture ρ_R or a participant in the entangled state ρ. However, by performing local operations on both spaces, and measuring the spins at both positions, it is possible to ascertain that there is entanglement and the existence of a pure quantum state occupied by the two-particles via verification of basis-independent correlations.

The importance of the non-local character of the entangled states points to a broader definition of non-entangled and entangled states in terms of equivalence classes. The idea here is that one can define the class of states that are non-entangled or entangled as those states which are connected by "local operations", defined by operators that exist in and measurements[3] on either Hilbert space $\mathcal{H}_A$ or $\mathcal{H}_B$. In other words, it is not possible to start with an unentangled state, and perform a series of local operations that yield an entangled state. For example, consider the "local"

[3] Measurements are a little tricky since one can imagine scenarios where local measurement can allow probabilistic post-selection on entangled states, yielding "detector level entanglement", but the average un-post-selected density matrix describing such a system is still unentangled [7, 117].

operator,

$$\mathcal{O} = o_A \otimes o_B, \tag{4.9}$$

where o_A (o_B) describes the operator for a particle in $\mathcal{H}_A$ ($\mathcal{H}_B$), and, we note, A and B need not necessarily refer to spatially resolved sub-spaces. The operator $\mathcal{O}$ cannot induce or remove entanglement. This is because $\mathcal{O}$ only couples states contained within each Hilbert space, and as such cannot induce or remove correlations between states belonging to different spaces. In the language of Hamiltonians, a Hamiltonian of the form $H = H_A + H_B$ yields a time-evolution operator $U = e^{iH_A t} e^{iH_B t}$ akin to $\mathcal{O}$; therefore, it preserves the class of the initial state. On the other hand, a Hamiltonian with terms that are the product of operators acting in each space, typically how we describe interactions, corresponds to a time evolution operator that cannot be written like $\mathcal{O}$ and can yield entanglement between the spaces.

4.2.2 Symmetrization

The treatment above implicitly treats the particles as distinguishable, in that the existence of two degrees of freedom (e.g. position and spin) means I could always refer to the particle at position L and the one at R each with its own spin degree of freedom. This effectively allows us to neglect the quantum statistics of the particles, which stipulates that the identical particles carrying these physical labels (position and spin) are even or odd symmetric under exchange depending on whether they are bosonic or fermionic, respectively. Since in this thesis we deal with bosons, I will consider the case of two bosonic particles to address this point, which I will refer to as particle 1 and 2, occupying orthonormal states $|a\rangle$ and $|b\rangle$. For the purpose of this discussion, and because I will make reference to this particular case later on, we can take each of these states to describe an internal and external degree of freedom: $|a\rangle = |\uparrow\rangle_L \equiv |L\rangle \otimes |\uparrow\rangle$ and $|b\rangle = |\downarrow\rangle_R \equiv |R\rangle \otimes |\downarrow\rangle$. The symmetrized two-particle state is then written,

$$|\psi_{\text{sym}}\rangle = \frac{1}{\sqrt{2}} \left(|a\rangle_1 |b\rangle_2 + |b\rangle_1 |a\rangle_2 \right), \tag{4.10}$$

which is manifestly symmetric under exchange of the particle labels 1 and 2. Though at first glance this is a somewhat insignificant requirement, it is an immensely important prescription giving rise to physics ranging from Bose-Einstein condensation [29, 121], to the BEC-BCS crossover [33], to HOM interference [1], and to lasers [122]. Notably, these are each phenomena that involve either the coherent mixing of two quantum states (via a beam splitter operation) or the macroscopic occupation of a single quantum state; in other words, they involve operations or phenomena leading to a quantum amplitude for many particles sharing the same single-particle quantum state. Therefore, by way of example, symmetrization tends to influence physical observables when particles can share the same exact quantum state.

4.2.3 Entanglement of identical particles

In the first Section 4.2.1, the discussion centered around entanglement between particles at distinct locations via an internal degree of freedom. Looking at the state in Eq. 4.10, one might conclude that this conforms to the definition of an entangled state provided so far. It appears that if we could trace over one of the particles, we would leave the second particle in a mixed state thereby indicating entanglement; equivalently, the state $|\psi_{\text{sym}}\rangle$ is not separable according to the definitions provided. On the other hand, with this state alone there are no quantum-correlated fluctuations: an observer always measures a particle in state $|a\rangle$ and another particle in state $|b\rangle$, and never fluctuations associated with the particle label; the particle on the left is always spin-up, and the particle on the right is always spin-down. The particle labels 1 and 2 are not truly physical, in the sense that they cannot be measured or identified as the eigenvalues of some observable; likewise, tracing over the particle 1 or particle 2 does not have a physical analog, because, for example, how could we measure just particle 1 but not particle 2 without violating the symmetry of the two-particle quantum state in the first place? In contrast, consider $|cat\rangle$: the subscripts representing $|L\rangle$ and $|R\rangle$, with respect to which there is non-separability, are the eigenstates of some Hermitian, observable operator and we can discern these positions with a microscope. Lastly, there is an even more problematic issue when one considers entanglement as supplying correlated measurements of

uncertain quantities. While quantum mechanics is full of many surprises, the concept that somehow every single identical particle in the universe is entangled is pushing it; surely the measurement of a particle on Mars cannot effect the measurement of an identical particle on earth if they have never interacted or each interacted with the constituents of a Bell pair. Or, to borrow a popular quote on the subject [123, 7]: "No quantum prediction, referring to an atom located in our laboratory, is affected by the mere presence of similar atoms in remote parts of the universe" [124].

With these issues in mind, recent theoretical work has formulated a definition of entanglement between identical particles that addresses this apparent contradiction associated with the non-separability of symmetrized states [7, 117, 115]; we closely follow the treatment of these references here. It is clear that, in formulating a definition of entanglement for identical particles, one must relax this constraint of separability for non-entangled states, but preserve the correlated quantum fluctuations that underlie entanglement. Towards this end, theorists have developed a protocol for discerning entanglement rooted in the following idea: when two particles are unentangled, one can ascribe a "complete set of properties" to each of the particles, irrespective of which particle it is that carries each of these sets. For the state $|\psi_{\rm sym}\rangle$ in Eq. 4.10, it is possible to accurately state that one of the particles is always in state $|a\rangle$ and the other in $|b\rangle$: there are no measurable fluctuations, though formally the unphysical particle label associated with the states ($|a\rangle$ or $|b\rangle$) observed fluctuates. Such a statement is not possible for $|cat\rangle$.

Ref. [115] provides a formalism for identifying the presence of a "complete set of properties" in the quantum state of two identical particles. The formalism relies on the construction of the symmetric operator $\mathcal{E}_P$, with unity expectation value when a symmetrized two-particle state is unentangled. Consider the single-particle Hilbert space spanned by the orthonormal set $\{x_i\}$.[4] If a Bose-symmetrized state $|\psi_{\rm bos}\rangle$ consists of particles with a "complete set of properties", then there is a projector in the single-particle Hilbert space $P = |x_j\rangle\langle x_j|$, satisfying [115, 117],

$$\mathcal{E}_P = P \otimes (\mathbb{I} - P) + (\mathbb{I} - P) \otimes P, \tag{4.11}$$

[4] Note the following argument is not dependent on your exact choice of basis, and rotations on this set can yield appropriate basis sets for the "complete set of properties" of interest.

with,

$$1 = \langle \psi_{\rm bos} | \mathcal{E}_P | \psi_{\rm bos} \rangle, \tag{4.12}$$

where the Kronecker product $\otimes$ is taken with respect to the single particle Hilbert spaces associated with each particle. When these equations are satisfied, one of the particles has a "complete set of properties" associated to the state $|x_j\rangle$, and the fluctuations intrinsic to entanglement cannot be present. The other particle is always in a state $|x\rangle$ (in general, a superposition of states in the orthonormal set excluding $|x_j\rangle$) orthogonal to $|x_j\rangle$, satisfying $1 = \langle x|\mathbb{I} - P|x\rangle = \langle x| \sum_{l\neq j} |x_l\rangle\langle x_l|x\rangle$. However, because two bosons can share the same quantum-state, and yield $0 = \langle \psi_{\rm bos} | \mathcal{E}_P | \psi_{\rm bos} \rangle$, we must provide the additional prescription that a non-entangled state either satisfies Eq. 4.12 or describes two bosons occupying the same quantum state. If neither is true, the particles are entangled. The stipulation can be summarized as follows: two bosons are not entangled when either they share the same quantum state, or are the symmetrized product of two orthogonal quantum states [117, 115, 7].[5] . While the projection operator $\mathcal{E}_P$ exists for the exemplary state $|\psi_{\rm sym}\rangle$ of Eq. 4.10, there is provably[6] no such operator for $|cat\rangle$ and so it exhibits "particle entanglement".

We will now apply these concepts to the HOM effect for the purpose of identifying distinctions in the entanglement created. Importantly, an absence of particle entanglement does not preclude bipartite entanglement between other degrees of freedom in the system: as I will try to show, the HOM effect, and beam splitters, highlight this fact and the existence of so-called "mode entanglement".

4.2.4 First and second quantization in HOM interference

The HOM effect can be understood in first and second quantization, and establishing the connection between the two is useful in understanding the character of the entanglement in the experiment. We will first consider the case of first quantization, and assess the degree of entangle-

[5] The in between case of a symmetrized state of non-orthogonal single-particle states can lead to entanglement according to this prescription [7]. However, a mathematical tool known as the Slater/Schmidt rank along with the reduced density matrix can distinguish these cases [115, 7], which is beyond the scope of this discussion.

[6] This can be shown by assuming the state corresponding to the projector P exists, and then arriving at a contradiction when setting the expectation value of $\mathcal{E}_P$ to one.

ment present before and after HOM interference. We consider two spinful bosons occupying the same internal state (spin or polarization), while occupying distinct spatial modes that could be the bound-state of a harmonic potential or a propagating free-space mode of a photon. We will call these modes $|L^{\text{in}}\rangle$ and $|R^{\text{in}}\rangle$, where the superscript indicates that these are the "input" modes occupied by each particle, which, depending on the experiment, are distinct from the "output" modes $|L^{\text{out}}\rangle$ and $|R^{\text{out}}\rangle$. We will omit the spin state since it is the same for both particles. The initial two-particle state is,

$$|S\rangle = \frac{1}{\sqrt{2}}\left(|L^{\text{in}}\rangle_1|R^{\text{in}}\rangle_2 + |L^{\text{in}}\rangle_2|R^{\text{in}}\rangle_1\right). \tag{4.13}$$

We can now ask whether the particles are entangled according to the metric established in the previous section. We seek the projector P that satisfies Eqs. 4.11 and 4.12. If we take $P = |R\rangle\langle R|$, then $\langle S|\mathcal{E}_P|S\rangle = 1$. The input state $|S\rangle$ describes particles that are not entangled, because it lacks any measurable quantum fluctuations that might support correlations [115].

We now consider the output state after HOM interference. The HOM effect rests on the coherent coupling of the quantum-modes via a particle beam splitter: it erases the which-way information associated with the input states thereby yielding interference, provided the particles themselves carry no distinguishing label that might itself supply which-way information. The beam-splitting could be provided by a literal optical beam splitter or a tunnel-coupling between two bound states: both induce transformations of the form (irrespective of the particle label),

$$\{|L^{\text{in}}\rangle, |R^{\text{in}}\rangle\} \rightarrow \{\frac{1}{\sqrt{2}}\left(|L^{\text{out}}\rangle + i|R^{\text{out}}\rangle\right), \frac{1}{\sqrt{2}}\left(|R^{\text{out}}\rangle + i|L^{\text{out}}\rangle\right)\}, \tag{4.14}$$

which when implemented on $|S\rangle$ yields,

$$\begin{aligned} |S\rangle &\rightarrow \frac{1}{\sqrt{2}}\left(|S\rangle - |S\rangle + i|L^{\text{out}}\rangle_1|L^{\text{out}}\rangle_2 + i|R^{\text{out}}\rangle_1|R^{\text{out}}\rangle_2\right) \\ &= \frac{i}{\sqrt{2}}\left(|L^{\text{out}}\rangle_1|L^{\text{out}}\rangle_2 + |R^{\text{out}}\rangle_1|R^{\text{out}}\rangle_2\right) \\ &\equiv |+\rangle, \end{aligned} \tag{4.15}$$

where in the last line we have introduced a notation for the resulting state, $|+\rangle$, that will be reintroduced later in this chapter. Even though each particle has equal probability of ending up

in either of the output states, the likelihood that they end up in different output states vanishes: this is the signature of HOM interference. We can now analyze whether $|+\rangle$ contains particle entanglement. Again, from the orthonormal space $\{|L\rangle, |R\rangle\}$ we seek the pure-state projector $P = |p\rangle\langle p|$ that satisfies Eqs. 4.11 and 4.12. Interestingly, $|p\rangle = \frac{1}{\sqrt{2}}(|L\rangle + i|R\rangle)$ does the trick, leading to projectors in $\mathcal{E}_p$ that correspond exactly to the beam splitter transformed states. This makes sense because, in analogy to $|\psi_{\text{sym}}\rangle$ in Eq. 4.10, the beam splitter lets $|a\rangle = \frac{1}{\sqrt{2}}\left(|L^{\text{out}}\rangle + i|R^{\text{out}}\rangle\right)$ and $|b\rangle = \frac{1}{\sqrt{2}}\left(|R^{\text{out}}\rangle + i|L^{\text{out}}\rangle\right)$. One of the particles is always in the spatial superposition given by $|a\rangle$, and the other in the superposition given by $|b\rangle$, and the corresponding symmetrized two-particle state equals $|+\rangle$. According to the prescription I have summarized so far the existence of P implies that there is not particle entanglement in the state $|+\rangle$.

Despite the lack of particle entanglement, the state $|+\rangle$ surely exhibits some kind of entanglement: there are correlated, quantum fluctuations associated with the positions of the particles. Yet, given that we have dropped the prescription associated with separability, the formal non-separability of the first-quantized state alone is not sufficient to support this claim. The language of second quantization provides a solution to this conundrum, and properly identifies the entanglement as existing between modes; the key is to no longer attach a quantum state to each particle, but only to the modes which support the particles themselves. We define creation and annihilation operators, a and $a^\dagger$, whose commutation relations encode the quantum statistics of the particles, and, consequently, the matrix elements. Bosonic excitations of a mode, which we interpret as indistinguishable particles (either photonic or massive), transform under these operators as,

$$a_k|n\rangle_k = \sqrt{n}|n-1\rangle_k \tag{4.16}$$

$$a_k^\dagger|n\rangle_k = \sqrt{n+1}|n+1\rangle_k \tag{4.17}$$

where the quantum number in the kets describes the number of excitations within the mode, the subscripts identifies the mode itself, and creation/annhillation operators of different modes commute. We now walk through the beam splitter operation in the second quantized picture. We are interested in the initial state of two particles occupying two distinct input modes, 1 and 2, with

the remaining modes 3 and 4 unoccupied. In the language of second quantization, this corresponds to two modes each with a single excitation,

$$\begin{aligned} |\psi\rangle &= a_1^\dagger a_2^\dagger |0\rangle_1 |0\rangle_2 \\ &= |1\rangle_1 |1\rangle_2, \end{aligned} \tag{4.18}$$

which is equivalent to the state $|S\rangle$ from the viewpoint of first quantization. To connect with the discussion of particles, I like to think of the mode as the external degree of freedom (like the position of a particle) and the mode occupation as the internal degrees of freedom (like the spin of a particle). The state in 4.18 is a product state and hence unentangled with respect to modes. The beam splitter can be modeled as transformations of the operators, coupling the input modes 1 and 2 to pairs of output modes 3 and 4 (see Figure 4.3),

$$\begin{aligned} a_1 &\to \frac{1}{\sqrt{2}} \left(a_3 + i a_4 \right) \\ a_2 &\to \frac{1}{\sqrt{2}} \left(a_4 + i a_3 \right). \end{aligned} \tag{4.19}$$

Substituting these operators in for $a_{1,2}$ in Eq. 4.18, we find

$$\begin{aligned} |\psi\rangle &= \frac{i}{\sqrt{2}} \left(a_3^\dagger a_3^\dagger + a_4^\dagger a_4^\dagger \right) |0\rangle_3 |0\rangle_4 \\ &= \frac{i}{2} \left(|2\rangle_3 |0\rangle_4 + |0\rangle_3 |2\rangle_4 \right) \\ &\equiv |+\rangle. \end{aligned} \tag{4.20}$$

In this notation, there clearly exists "mode entanglement": tracing over either one of the physically distinguishable modes would yield a balanced mixed state of the zero and doubly-excited states. Experimentally, this might be accomplished by sticking a beam block in front of port 4 but not port 3. Furthermore, this view resolves a number of confusions (at least, personally) associated with the beam splitter. It is possible to become confused about the HOM effect because the output state $|+\rangle$ is entangled, but the beam splitter realizes single-particle transformations which themselves should not entangle the particles. This can lead in the direction of concluding the symmetrized state $|S\rangle \equiv |1\rangle_1 |1\rangle_2$ is entangled because if the beam splitter did not add entanglement,

it must have been pre-existing. The initial state however exhibits no correlated fluctuations, and cannot itself, for example, violate a Bell's inequality. The resolution is that there is not particle entanglement, but the beam splitter itself realizes mode entanglement on an initially unentangled state: the beam splitter transformations are not "local" with respect to the final Hilbert spaces that are entangled after HOM interference, because the operator in Eq. 4.20 acting on the two-mode vacuum state cannot be written as $\mathcal{O}$ in Eq. 4.9. The beam splitter, furthermore, preserves the non-separability of the symmetrized states $|S\rangle$ when transformed to $|+\rangle$ with respect to the particle labels, as expected given the single-particle nature of the beam splitter transformations; however, as discussed, this non-separability does not imply particle entanglement. In the language of Hamiltonians, the beam splitter Hamiltonian H_{BS} corresponding to atoms in double-well quite manifestly contains interactions between the bound-state modes (and not the particles), and these interactions periodically realize mode-entanglement,

$$H_{BS} = \frac{1}{\sqrt{2}} \left(a_L^\dagger a_R + a_R^\dagger a_L \right). \tag{4.21}$$

This Hamiltonian couples modes in analogy to a spin-spin Heisenberg Hamiltonian of the form $S_1 \cdot S_2 \propto (S^+S^- + S^-S+) + S_1^z \cdot S_2^z$, in which the parenthetical term yields entanglement between spatially separated particles in their spin degree of freedom (like in $|cat\rangle$).

So, to conclude, the HOM effect yields what I will call mode-entangled states that arise from the mode-coupling of the beam splitter. The beam splitter, however, transforms the non-particle-entangled state $|S\rangle$ into the non-particle-entangled state $|+\rangle$, just as we would expect given that we can write the beam splitter operation in terms of single particle transformations. Nevertheless, the symmetrized structure of the state $|S\rangle$ (or, equivalently, the commutation relations on the creation and annihilation operators), is essential to yielding $|+\rangle$ under the action of the beam splitter. Hence, the HOM effect lives in the space of bosonic particles, yet is facilitated by the mode-entangling nature of the beam splitter

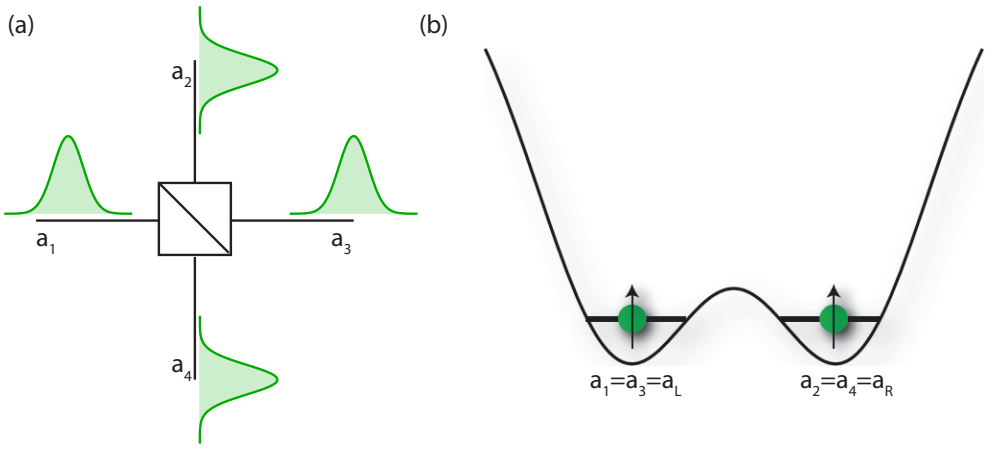

Figure 4.3: Equivalence of second-quantized modes for photonic and atomic beam splitter setups. (a) For a photonic beam splitter, there are two input modes a_1 and a_2, connected via transmission and reflection to a_3 and a_4: the beam splitter transformations in the text (Eq. 4.19) reflect the different phases for each process. (b) For an atomic beam splitter formed from a double-well potential, the creation and annihilation operators refer to the bound-state mode of each well. Since in this case a tunnel-coupling coherently mixes the modes, the transmitted quantum amplitude correspond to the input mode creation operator, while the reflected amplitude yields creation in the other mode; the input and output modes are shared in this way, while preserving the fundamental beam splitter transformations in the text. The transcription between the operators in (a) to those in (b) are indicated in the figure.

4.2.5 Mode entanglement of internal degrees of freedom

Perhaps it is worth discussing in this likely confusing section something that I find very confusing within the context of these different classifications of entanglement. We have mostly been considering experiments in which the particles can occupy two spatial modes. But what about the case of two bosonic particles, each with an internal degree of freedom – one spin-up and the other spin-down – occupying the same ground-state of a harmonic oscillator? They are in a triplet spin-state, $|T\rangle = \frac{1}{\sqrt{2}}\left(|\uparrow\rangle_1|\downarrow\rangle_2 + |\downarrow\rangle_1|\uparrow\rangle_2\right)$, and the state looks formally identical to $|S\rangle$. By the above arguments, this state is definitely not particle-entangled: there are no fluctuations, there is a spin-up particle and a spin-down particle, and that's the whole story. However, now, in analogy to the beam splitter in the HOM effect, if one applies a $\pi/2$ pulse coherently coupling the spin states such that,

$$|\uparrow\rangle \rightarrow \frac{1}{\sqrt{2}}\left(|\uparrow\rangle + i|\downarrow\rangle\right), \tag{4.22}$$

$$|\downarrow\rangle \rightarrow \frac{1}{\sqrt{2}}\left(|\downarrow\rangle + i|\uparrow\rangle\right), \tag{4.23}$$

then we find,

$$|T\rangle \rightarrow \frac{1}{\sqrt{2}}\left(|\uparrow\rangle_1|\uparrow\rangle_2 + |\downarrow\rangle_1|\downarrow\rangle_2\right). \tag{4.24}$$

As with the initial state with respect to $|S\rangle$, this final state is formally identical to $|+\rangle$. Consequently, this state is not particle entangled, as we can identify the analogous projector P as was done for $|+\rangle$ to rule out particle entanglement. On the other hand, formally it is mode-entangled, where the spin states define the modes. Should we conclude then that a $\pi/2$ pulse is mode-entangling? It seems reasonable but many would object to the notion of such a single-particle operation yielding entanglement, yet it is formally identical to the beam splitter except the quantum states coupled are not spatially resolved. Do we then conclude that, in analogy to the mode-entanglement from a single photon on a beam splitter [8, 10, 7] (See Figure 4.4), a single spin in a superposition is mode-entangled? Yes, at least I think so. Furthermore, the spectroscopic enhancement [125, 126] entailed by the correlations in the final two-particle spin-state in Eq. 4.24 can be understood as arising from the combination of the symmetrization and the mode-entanglement induced by the $\pi/2$-pulse, in direct analogy to the interferometric phase sensitivity enhancement associated to the photonic $|+\rangle$ state [127].

4.2.6 Particle and mode entanglement: role of interactions

From this parallel example of the "spin-HOM" effect, it is clear that the distinction between mode and particle entanglement does not pertain to the exact degrees of freedom – internal or external – between which correlated fluctuations exist. By appealing to the general formulation of Ref. [115], and discussion thereof in Ref. [7], it is possible to construct an intuitive partition between how mode and particle entangled states are generated. I will jump to the punch-line now so that it is clear where I am going with this: quite sensibly, mode-entangled states can only result when there are interactions between the modes (Section 4.2.4), and particle-entangled states can only result when there are interactions between the particles.

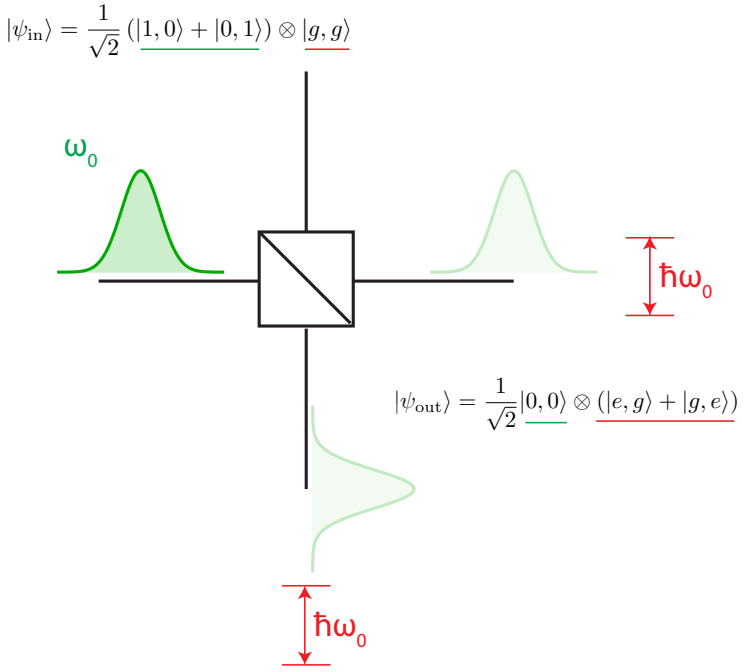

Figure 4.4: Single photon entanglement. While a single quantum particle cannot exhibit particle entanglement, it can create mode-entanglement through the state $\frac{1}{\sqrt{2}}(|1,0\rangle + |0,1\rangle)$. To show that this corresponds to useful entanglement (and can violate a Bell's inequality), we show a procedure (from Ref. [7]) by which local operations connect this photonic state to an atomic $|bell\rangle$ state. For two atoms, each comprised of a two-level system with splitting resonant with the input photon, via the local atom-photon interactions the mode-entanglement is converted into particle entanglement. We show the initial beam-split photonic and atomic states prior to the local atom-photon interactions in the upper-left of the figure, and then the final state after interaction in the bottom-right. To violate a Bell's inequality it is required to measure correlated fluctuations in multiple bases, but the fact that there are not in general unitaries that connect the single excitation state to the zero excitation state within a single mode (this is a so-called "super-selection rule" for the case of massive particles) poses a challenge that is solved by using these additional spins (on which Bell's inequality measurements are routine). There are, however, experimental examples demonstrating the presence of entanglement in the beam-split single photon state without the aid of atomic states [8]; similarly, proposals exist for converting mode-entanglement of massive particles into particle entanglement through the aid of a Bose-Einstein condensate particle reservoir or additional particles supplied to a beam splitter [9, 10].

The general treatment I will now discuss pertains strictly to bosons, but can be modified to the case of fermions and their distinct commutation relations. Though I will not show this here, the general treatment below is shown in Ref. [115] to be equivalent to the rules I gave above in Section 4.2.3. We consider the case of two bosons, 1 and 2, represented in a basis of orthonormal single-particle states $\{|x_j\rangle\}$. Any symmetrized, two-particle state $|\psi_{2\text{p}}\rangle$ of the bosons can be written

in first quantization as,

$$|\psi_{2\mathrm{p}}\rangle = \sum_{i,j} v_{i,j}|x_i\rangle_1|x_j\rangle_2, \tag{4.25}$$

where $v_{i,j}$ is the amplitude associated with particle 1 being in $|x_i\rangle$ while particle 2 is in $|x_j\rangle$. This is the traditional representation used to represent, for example, a pair of particles occupying two orthogonal quantum states. Because these are bosons, symmetrization implies $v_{i,j} = v_{j,i}$. The matrix v (with elements $v_{i,j}$) can be diagonalized [115], such that we can rewrite the two-particle wave function in the diagonal basis $\{|\bar{x_j}\rangle\}$,

$$|\psi_{2\mathrm{p}}\rangle = \sum_{k} \bar{v_k}|\bar{x_k}\rangle_1|\bar{x_k}\rangle_2, \tag{4.26}$$

where $\bar{v_k}$ is the amplitude associated with both particles to occupy the same state $|\bar{x_k}\rangle$. To discriminate the presence of particle entanglement, we introduce the "Schmidt rank", which is the number of terms in the summation with non-zero $\bar{v_k}$. The particles are entangled when the Schmidt rank exceeds two [115, 7]; when the Schmidt rank is two, the state is the symmetrized product of two quantum states (not necessarily orthogonal); when the Schmidt rank is one, the particles are in the same exact quantum state. To highlight the connection between this discussion and the previous discussions, we show the relevant states $|S\rangle$ and $|+\rangle$ in the bases relevant to the present discussion. The state $|+\rangle$, as written in Eq. 4.15, is already in the form of Eq. 4.26 in the $\{|\bar{x_j}\rangle\} = \{|L\rangle, |R\rangle\}$ basis; to write $|+\rangle$ in the form of Eq. 4.25, the two-particle state can be written as the symmetrized product of the orthogonal single-particle quantum states, $\{|x_j\rangle\} = \{\frac{1}{\sqrt{2}}\left(|L\rangle + i|R\rangle\right), \frac{1}{\sqrt{2}}\left(|R\rangle + i|L\rangle\right)\}$. Conversely, the state $|S\rangle$ is in the form of Eq. 4.25 when expressed in the $\{|L\rangle, |R\rangle\}$ basis; it can be represented in the form of Eq. 4.26 when using a basis $\{|\bar{x_j}\rangle\} = \{\frac{1}{\sqrt{2}}\left(|L\rangle + |R\rangle\right), \frac{i}{\sqrt{2}}\left(|L\rangle - |R\rangle\right)\}$. It is clear that both of these states have Schmidt rank of two, and, as such, are not particle entangled. A similar analysis applies to the state $|\psi_{\mathrm{sym}}\rangle$ of Eq. 4.10.

The Schmidt rank treatment provides a natural way of understanding the effect of interactions. If one starts with a pair of non-particle-entangled bosons in two orthogonal quantum states, then the action of a single-particle Hamiltonian (i.e. no interactions) will leave the state in that form, because the unitary Scrodinger evolution preserves the orthogonality of the evolving states.

In other words, the two-particle state remains a symmetrized product of two orthogonal quantum states, and the Schmidt rank of two is invariant with time. If there are interactions between the particles, then the action of the Hamiltonian can promote the Schmidt rank by generating more terms beyond the two that described the initial two-particle state. This introduces particle entanglement. For example, consider again the state $|bell\rangle$, which is routinely produced with ions via their Coulomb interaction [79]. In first quantization, for bosons this state is written,

$$|bell\rangle = \frac{1}{2}\left(|L\rangle_1|R\rangle_2 + |L\rangle_2|R\rangle_1\right)\left(|\uparrow\rangle_1|\downarrow\rangle_2 + |\uparrow\rangle_2|\downarrow\rangle_1\right). \tag{4.27}$$

In the basis $\{|x_j\rangle\} = \{|L,\downarrow\rangle, |L,\uparrow\rangle, |R,\downarrow\rangle, |R,\uparrow\rangle\}$, the associated matrix v is of the form,

$$v = \begin{pmatrix} 0 & 0 & 0 & 1/2 \\ 0 & 0 & 1/2 & 0 \\ 0 & 1/2 & 0 & 0 \\ 1/2 & 0 & 0 & 0 \end{pmatrix}, \tag{4.28}$$

When this matrix is diagonalized to yield $\bar{v}$, the diagonal elements of $\bar{v}$ represent $\bar{v_k}$ associated with Eq. 4.26. Upon diagonalizing, we have that,

$$\bar{v} = \begin{pmatrix} -1/2 & 0 & 0 & 0 \\ 0 & -1/2 & 0 & 0 \\ 0 & 0 & 1/2 & 0 \\ 0 & 0 & 0 & 1/2 \end{pmatrix}, \tag{4.29}$$

and so, $\{\bar{v_k}\} = \{-1/2, -1/2, 1/2, 1/2\}$. The states (which are the eigenvectors of v) attached to these coefficients are $\{|\bar{x_k}\rangle\} = \frac{1}{\sqrt{2}}\{-|L,\downarrow\rangle + |R,\uparrow\rangle, -|L,\uparrow\rangle + |R,\downarrow\rangle, |L,\downarrow\rangle + |R,\uparrow\rangle, |L,\uparrow\rangle + |R,\downarrow\rangle\}$. Plugging these coefficients and states into Eq. 4.26, one finds (with annoying algebra) $|bell\rangle$ represented in first quantization. Because this expansion is unique [115] and there are four terms, the Schmidt rank is four. The Schmidt rank exceeds two, and $|cat\rangle$ is properly identified as particle-entangled.

To conclude, I want to point out that mode and particle entangled states are not mutually exclusive [128]. For example, the Bose-Hubbard Hamiltonian of interacting bosons on a lattice

has tunneling and interactions, which couple the modes and the particles, respectively [39]. Even though the particles may be spinless, and therefore the measurable fluctuations are only in the occupation numbers of the sites, the set of states that can be produced with both the tunneling and interactions is larger than what can be produced with just tunneling. The tunneling produces the number fluctuations among the modes (in this case, these are the lattice sites), but the interactions allow for states that are truly particle entangled: the states exhibit correlated number fluctuations inaccessible to systems exhibiting only tunneling. The distinctions among these states are detected by the framework I just summarized. Crucially, in Hong-Ou-Mandel interference, the particles – whether they be photons or massive atoms – are not interacting: the particles comprise a state possessing only mode entanglement.

4.2.7 Distinguishability

Before moving on to experiment, I want to briefly discuss the concept of distinguishability. In general, I would like to define a two-particle quantum state as consisting of distinguishable particles when there exists two degrees of freedom in each particle, which are uniquely correlated without fluctuations. For example, the second quantized state $|\uparrow\rangle_L|\downarrow\rangle_R$ fulfills this definition, as the particle on the left is always spin-up, and the converse is true of the particle on the right. Even though the particles are still identical in that the state is symmetrized – in first quantization, this state is $|\psi_{\text{sym}}\rangle$ of Eq. 4.10 – one might expect that the effect of the quantum statistics is largely removed because the particles are distinguished through these position and spin labels. Yet, there are substantial counter-examples to this notion. For example, consider the state $|cat\rangle$: one would find HOM interference even though the spin states are fluctuating. The tunnel-coupling yields,

$$|cat\rangle \rightarrow \frac{1}{2}\left(|\uparrow\rangle_L|\uparrow\rangle_L + |\uparrow\rangle_R|\uparrow\rangle_R + |\downarrow\rangle_L|\downarrow\rangle_L + |\downarrow\rangle_R|\downarrow\rangle_R\right). \tag{4.30}$$

The same spins always end up in the same, random mode, due to interference within each spin-aligned component of the state. Alternatively, consider the original example I gave of distinguishable particles in the state $|\uparrow\rangle_L|\downarrow\rangle_R$: instead of coherently mixing the spatial modes occupied by

the particles, one could perform a Raman-assisting tunneling process that couples the positions while concurrently flipping a spin (i.e. realized by the Hamiltonian $H = a_R^\dagger a_L \sigma^- + a_L^\dagger a_R \sigma^+$). This too would exhibit the same signature of HOM interference at certain times,

$$|\uparrow\rangle_L|\downarrow\rangle_R \rightarrow \frac{1}{\sqrt{2}}\left(|\uparrow\rangle_L|\uparrow\rangle_L + |\downarrow\rangle_R|\downarrow\rangle_R\right). \tag{4.31}$$

However, by adding a third degree of freedom distinguishing the particles and invariant with respect to the Hamiltonian, then the interference could be removed. It seems that one must adopt an experimentally dependent notion of distinguishability, wherein the presence of interference due to indistinguishability depends on the exact interference experiment being performed. To be more concrete, an interference experiment between two particles necessarily entails the coherent mixing of two quantum states, such as the modes in the original photonic HOM experiment. When two particles share the same quantum state with respect to all degrees of freedom besides those coherently coupled for the purpose of interference, then they are indistinguishable with respect to that experiment. We will adopt this operational definition through out.

4.3 Intermission

This is an intermission. If you are one of the very few who read this far, remember none of this matters very much.

The prior section comes out of extensive conversations among colleagues in JILA, and a survey of literature on the subject. Though important in their own right, the presented conclusions are also immediately relevant because past and present literature is inconsistent with respect to the notion that symmetrization alone yields entanglement, and the presence of particle entanglement in the Hong-Ou-Mandel effect. Our demonstration of the Hong-Ou-Mandel effect uses initially unentangled, independently prepared atoms, which led to an exploration into understanding how to formulate and distinguish the kinds of entanglement present with identical particles. A subtle, confusing and fascinating effect, Hong-Ou-Mandel interference brings to bear these issues, which is likely the reason for its importance within the quantum optics community. The prior discussion

was an attempt to explain some of the fundamental concepts surrounding it.

I will now transition to our experimental observation of atomic Hong-Ou-Mandel interference, enabled by an atomic beam splitter in the form of a coupled double-well potential.

4.4 Overview of tunneling experiments

Before delving into discussions of our studies of single-particle tunneling, I will give a brief overview of the experiment, including a description of the experiment stepwise, and a summary of our theoretical treatment of the Hamiltonian experienced by the tweezer-trapped atoms.

4.4.1 Experimental sequence and detection

The experimental results in this chapter depend on the mobility of two wavelength-scale optical tweezers and single-site imaging, which are realized via the apparatus illustrated in Fig. 4.2b [3, 69, 89]. For laser cooling to the three-dimensional (3D) ground state (Fig. 4.2c) and imaging in position-resolved potentials, our tweezers are positioned far apart compared to the focused spot radius of 710 nm. For tunneling, the tweezers are brought close together such that there is a small, tunable overlap of the single-particle wavefunctions. The versatility of the tweezers, therefore, enables the simultaneous capabilities of laser-cooling in separated potentials and of coherently overlapping the single-particle wavefunctions with control on a scale much smaller than the size of the atomic wavepackets. Our full experimental sequence consists of the following steps: We image the initial atom positions, laser cool with Raman-sideband cooling, perform tunneling experiments, and then image the atoms again. Hence, we can follow the quantum dynamics between initial and final states that are both known with single-site resolution. This pair of images allows us to form the four sets of probabilities for single particle experiments associated with the atom's origin and final location, and the set of probabilities associated with two particle experiments (see Figure 4.5). For the HOM observation discussed in Sections 4.7 and 4.8, we focus on the two-particle probability P_{11}: this is the likelihood that in the first and second image there is an atom in each optical tweezer.

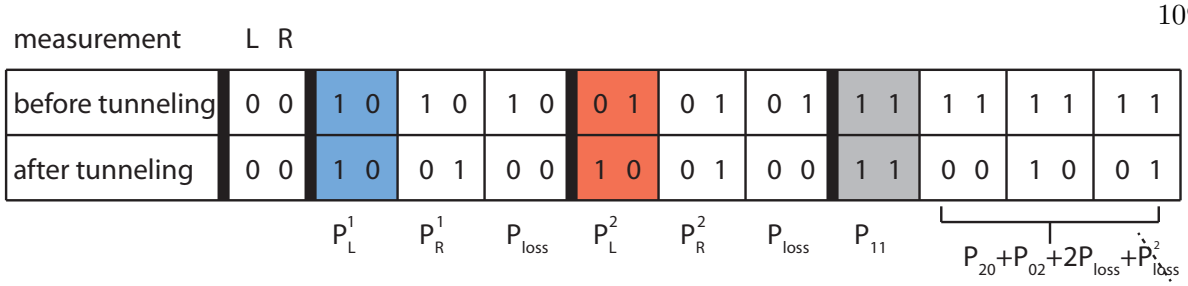

Figure 4.5: A list of the possible outcomes of our imaging protocol. A 0 (1) within a box indicates that on the pixel corresponding to either the left [L] or right [R] wells, the measured counts fell below (exceeded) the threshold for triggering atom detection. The red, blue, and grey regions highlight the signals used to produce the data points in, for example, Fig. 4.14b,e. $P_i^1(P_i^2)$ refers to an atom that started on the left (right), i.e. the first image indicated an atom on the left (right). In our calculation of P_{11} if there is an atom in each well in the second image we count this as 1; if there are zero atoms, we count this as 0; if there is one atom total, we also count this as 0. The latter two cases can occur when atoms end up on the same optical tweezer, with probabilities P_{20} and P_{02} for the left or right tweezer, respectively (see Section 4.7.3). We take the mean over all experimental realizations to extract the single and two-particle probabilities represented. To accurately interpret the measured P_{11} we must take into account particle loss. Hence, in our analysis this loss is independently accounted for by using the value of P_{loss} determined in the parallel single-particle experiments. Specifically, in two-particle experiments the maximum value that P_{11} can reach is $(1-P_{\text{loss}})^2$. P_{loss} ranges in our experiments between 0.03 and 0.05; these values are consistent with variation in vacuum lifetime and experiment length amongst different datasets.

4.4.2 Theory treatment of a double-well formed by (nearly) gaussian optical tweezers

For the HOM studies, it was crucial to gain an accurate understanding of the double-well potential generated experimentally, since there were parameters of the experiment, namely the two-particle interaction energy U, to which we at the time lacked direct experimental access. In the reconfigured trap for quantum-dynamics, the tunnel-coupling is described by $J = -\int \phi_L(\vec{r}) H_{sp} \phi_R(\vec{r}) d^3\vec{r}$, where $\phi_L(\vec{r}) \equiv \langle \vec{r}|L\rangle$ ($\phi_R(\vec{r}) \equiv \langle \vec{r}|R\rangle$) is the lowest energy, localized wavefunction for the left (right) well, and H_{sp} is the single-particle Hamiltonian (see below). We control the bias Δ between the two wells by varying the relative intensity of each tweezer, as discussed in Chapter 2. On the tunneling resonance ($\Delta = 0$), an atom prepared in the left well undergoes the coherent dynamics $|L\rangle \rightarrow \cos(Jt)|L\rangle + i\sin(Jt)|R\rangle$ [129, 16, 130, 2], while the symmetric transformation occurs for an atom starting on the right; the ideal two-particle dynamics are discussed later

in this chapter. After an evolution time t in the presence of tunneling, the depth of the traps is rapidly increased to freeze the atom distribution, the traps are pulled apart, and the single-atom location(s) is (are) imaged.

We devoted significant effort towards understanding the foci that define the double-well potential experienced by the atoms, and the associated single and two-particle Hamiltonians. Based on the measurements discussed in Section 2.8.2 and 2.9.2, we find very good agreement between calculations of the tunneling J and interaction U (see Chapter 5 for direct measurements of the interaction energy) for a double-well potential $V(\mathbf{r})$ of spacing a, waist $w_0 = 0.71$, and $z_R = 2.17\ \mu$m z-length scale,

$$V(\mathbf{r}) = -\frac{V_0}{1+\frac{z^2}{z_0^2}} \exp\left(\frac{-2x^2}{w_0^2\left(1+\frac{z^2}{z_0^2}\right)}\right)\left[\exp\left(-\frac{2\left(y-a/2\right)^2}{w_0^2\left(1+\frac{z^2}{z_0^2}\right)}\right)+\exp\left(-\frac{2\left(y+a/2\right)^2}{w_0^2\left(1+\frac{z^2}{z_0^2}\right)}\right)\right] \tag{4.32}$$

where V_0 is the single tweezer depths when they are separated, $a >> w_0$, and here we have written the potential for a vertically oriented double-well. The depth quoted in subsequent data always refers to this quantity V_0. We exclude gravity in our calculation of double-well parameters since the bias necessary for resonance negligibly perturbs the localized wavefunctions. The single-particle Hamiltonian H_{sp} is the sum of $V(\mathbf{r})$ and the kinetic energy operator in position space. We have performed full 3D calculations using the methods summarized in Ref. [131], which is essential for an accurate description of the two-particle interaction energy (defined in Section 4.6), response of a thermal distribution, and full-description of the spatial wave functions. We have used a 1D calculation by Fourier transforming the symmetric double-well Gaussian system, and diagonalizing the Hamiltonian in a truncated momentum basis. The 1D and 3D tunneling calculations exhibit decent agreement for the ground-state system (see Section 4.5.2.4)

In the modeling of the single-particle dynamics discussed in this chapter, we make use of the solutions to the single-band, single-particle Hamiltonian for the tunnel-coupled double well potential. Provided we operate with small enough biases so that the spatial extent of the wave functions are unaffected, we can model the left and right ground-states as a coupled two-level

system. For a bias Δ and tunneling-coupling J, this Hamiltonian is,

$$H_{eff} = \begin{pmatrix} \Delta/2 & J \\ J & -\Delta/2 \end{pmatrix}. \tag{4.33}$$

We can numerically time-evolve this simple Hamiltonian under the Schrodinger equation in the presence of the ramps of the double-well tweezer depth to understand, for example, the onset of tunneling in the experiment, and, crucially, the dynamics in the final static double-well. When applying this Hamiltonian, we use the measured J where available, and calibrated Δ; in the absence of a measured J, we use the full 3D calculations of the potential unless otherwise noted.

4.5 Tunneling in a double-well potential: characterization and dependences

Here we present data on single-particle tunneling in a double-well potential, by only considering experiments that, after stochastic loading [3], yield a single atom in the left or right well in the first image. We spent a significant amount of time investigating systematics associated with properties of our tunneling observations. These studies help elucidate the origin of the single-particle tunneling contrast and damping, and they verify our understanding of the optical tweezer potential parameters that are important for determining the on-site interaction energy (Section 4.6). Lastly, while we primarily consider single-particle data in this section, the experiments with two particles discussed in subsequent sections are identical except in the outcome of the initial tweezer loading. Hence, many of the conclusions here bear on the two-particle experiments as well.

4.5.1 Initiating tunneling experiments

Once 3D cooling has finished, the tunneling preparation proceeds as follows and is illustrated in Fig. 4.6A.[7] Prior to any of the sweeps, we first set the fractional bias of the optical tweezers that we wish to apply in the final tunneling configuration. While the traps are each still 23(1) MHz deep, the gaussian tweezer spacing is swept from 1570 nm to 808 nm in $T_{\mathrm{pos}} = 10$ ms. Afterward, in

[7] All of the numbers presented here are for the final trap values that realize the smaller value of J presented in Figure 4.14b,e and Figure 4.16,b,c in the context of our HOM observations.

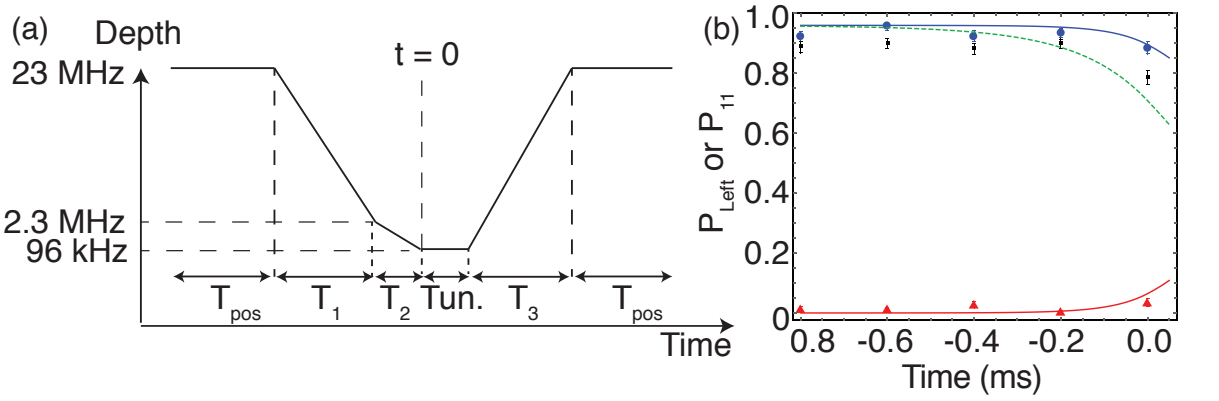

Figure 4.6: Protocol for initiating tunneling. (A) The tunneling sequence as a function of time, illustrated for the 96 kHz final trap depth. (B) For the 96 kHz depth, tunneling at times before $t = 0$ for a single atom starting on the right (red), on the left (blue), and with one atom in each well (black). The solid lines model the single particle dynamics use the Hamiltonian of Eq. 4.33, and using the calculated depth-dependent tunneling shown in Section 4.5.2.4; we also show the expected dynamics of an atom starting in the left well were we to neglect gravity during the ramp down (green).

a $T_1 = 10$ ms linear ramp the traps are dropped to 2.3(1) MHz, and, from there, in a second linear ramp of $T_2 = 5$ ms to a depth of 96(4) kHz. This last ramp initiates the tunneling experiments. After a variable evolve time t, the trap is jumped in 100 μs to 210 kHz (not shown in Fig. 4.6a), and then linearly ramped in $T_3 = 10$ ms back to 23(1) MHz. The traps are then swept apart in $T_{\text{pos}} = 10$ ms to 1570 nm for imaging. The same procedure is used for experiments in which the final tunneling depth is 60 kHz and the well spacing is 805 nm (Fig. 4.14c,f and Fig. 4.16a). For the large spacing and 20 kHz depth double-well experiment displayed in Fig. 4.13, the final depth ramp is increased to 10 ms and performed symmetrically.

The goal of the second ramp T_2 is to minimize tunneling that occurs before $t = 0$, while preserving the ground-state fraction achieved during sideband cooling. The data in Fig. 4.6b affirms that minimal, though measurable, population transfer occurs before our nominal $t = 0$. Based on the data in Fig. 4.14b, we observe that the coherent dynamics are consistent with a small time offset $t_{\text{corr}} = -60\ \mu s$, which informs our calculation of the experimental $t_{\text{HOM}} = 2\pi/8J + t_{\text{corr}} = 0.42$ ms for $2J/2\pi = 524$ Hz used in later sections. With respect to any heating during the ramps, if we do the tunneling initiation procedure forward and then in reverse, we do not observe changes in the

temperature measured via sideband spectroscopy (see Section 4.9). Lastly, we note that the data in Fig. 4.6b validate assumptions made in later sections that interactions during the ramp can be neglected, because very little population transfer occurs in this time.

To model the tunneling dynamics during the ramp, we require knowledge of J and Δ for the Hamiltonian in Eq. 4.33. Using our calculations of J for an arbitrary double-well formed from Gaussian potentials, we compute the dynamic depth dependent tunneling during the ramp where direct measurements of J are not available (since we have not measured the tunneling oscillations at large depths). Other than when scanning the bias for equalization, we typically operate with $\Delta = 0$ resonant tunneling. For a horizontal double-well, the control voltage that we apply via the AOMs to equalize the ground-states in neighboring tweezers is largely independent of the tweezer depth, excluding possible effects associated with optical aberrations. However, for a vertical double-well, gravity causes a shift of the left and right well ground-state to which we are sensitive: for the 808 nm Gaussian spacing between the tweezers, there is a 600 nm spacing between the atoms corresponding to a 1.3 kHz gravitational shift. Since in the final double-well (at the conclusions of the ramps) we must correct for this shift, the total energy bias between the ground-states will change as function of depth since the double-well bias due to the differential AO deflection power scales with the total power in the tweezers.[8] Since we choose a differential AO deflection power such that there is resonant tunneling in the final trap, tunneling during the ramp is suppressed both by a decrease in J and the increase in Δ before the trap reaches its final depth. These effects are modeled in Figure 4.6.

The primary tunneling experiments we perform involve resonant dynamics and bias scans near an evolve time of $t = \pi/(2J)$. As was touched on earlier, the final ramp T_2 is not perfectly diabatic with respect to the tunneling, and as a result some dynamics occur prior to the end of this ramp. This has the effect of modifying the "spectral" response of the system from what is expected from

[8] The control voltage that sets the relative RF power in each tone defining the double-well sets the fractional difference in the deflection efficiency for each tone. The overall total optical power hitting the AOM times this fractional bias determines the absolute energy bias. Since we fix the bias voltage, and hence the fractional bias, this changes as a function of depth.

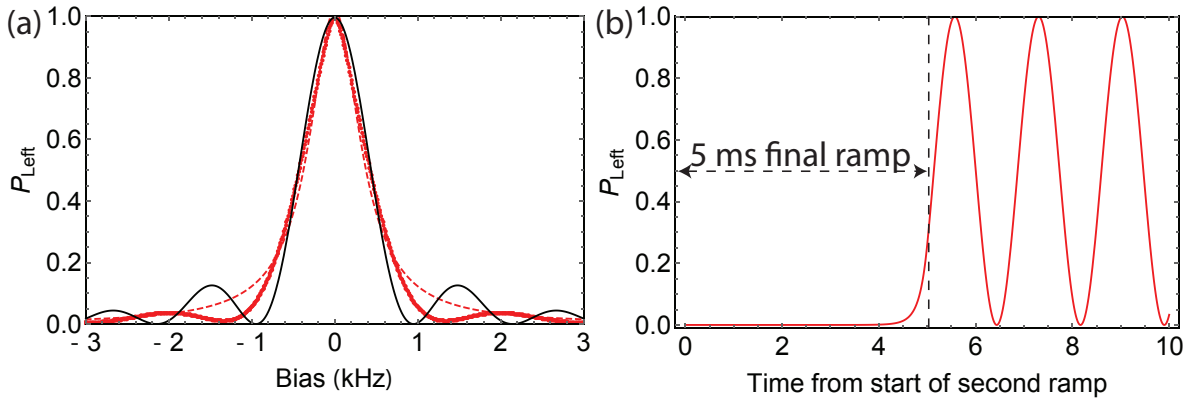

Figure 4.7: Dynamics and bias scan including the ramp dynamics for a horizontal double-well of 96 kHz and 808 nm spacing. (a) The dense, red circles correspond to the numerically computed bias curve for the first half-oscillation. We fit these simulated data to a Lorentzian (dashed red line) with the model from Eq. 4.34; the ramp-dependent fractional disparity between the fitted γ and the $2J$ used in the model is included as a correction when calibrating the bias control. We contrast the expected spectral response of a two-level system driven with a resonant square-pulse and Rabi frequency $2J$ (solid black line). (b) We show the numerically calculated temporal response during and subsequent to the final ramp for a resonant bias. For a vertical double-well there is a small ($< 2\%$) reduction in the single particle contrast due to the off-resonant tunneling prior to the final trap.

a two-level system with detuning Δ driven by a square-pulse, and, furthermore, modifies the phase of tunneling oscillations. These behaviors are illustrated in Figure 4.7 for the case of a horizontal double-well. Importantly, there is relative narrowing of the numerically-computed bias scan profile with respect to a Lorentzian of $2J$, which is a correction we include in our calibration of the bias in the following sections. We experimentally measure the phase shift of the tunneling dynamics with respect to our nominal $t = 0$ at the end of the 5 ms ramp, and this measurement is used when performing comparisons between the single-particle and two-particle oscillations (see Section 4.7); the measured dynamics for a vertical double-well also compare favorably to the simulation in Figure 4.6.

4.5.2 Single particle tunneling characterization

4.5.2.1 Bias spectroscopy

In Fig. 4.8 we display single-particle tunneling data for a double-well trap with a final single-well depth of 96(4) kHz and an $a = 808$ nm gaussian function spacing. In Fig. 4.8a we plot the likelihood of observing the atom in the left well (P_{L}) as a function of the double-well bias Δ for a fixed evolution time of 0.9 ms for the condition of an atom initially imaged on the left (blue) or on the right (red). We will adopt this convention for single particle experiments through-out this thesis, but note that we could produce analogous data for P_{R}. To calibrate the bias control voltage (see Section 2.9.1) to units of energy, we use the measured width of the bias spectrum and compare it to the frequency of the tunneling oscillations. The modeling in the previous section shows that the wings of the expected sinc-function are suppressed, due to the lack of diabaticity in ramping on J. We therefore model the response as simply that of a Lorentzian without the Rabi-wings,

$$P_L = A\frac{(\gamma)^2}{\Delta^2 + (\gamma)^2} \tag{4.34}$$

where γ is the Lorentzian width, and A is a free parameter to account for the finite contrast. We extract a bias calibration by equating γ and the measured frequency $2J$ from the on-resonance tunneling oscillations displayed in Fig. 4.8b, but correcting for the narrowing. We estimate a 15% systematic uncertainty in Δ based on a comparison to a method which directly measures the energy difference Δ through Ramsey-spectroscopy, discussed below. The disparity could be from the weak dependence of the tunnel-coupling on Δ for this double-well configuration. We have also looked at the contrast and frequency of off-resonant tunneling oscillations, which agree at this same level of precision with the calibration.

4.5.2.2 Thermal effects on tunneling

We have performed a number of calculations and experiments to understand the effect of finite temperature on the single particle tunneling. To first order, we verify the necessity of ground-state preparation to our observation of tunneling: we show in Fig. 4.8c a bias scan over a similar range

as in Fig. 4.8a (though at lower statistics) without the sideband cooling. The atoms are essentially completely thermally delocalized between the optical tweezers. This suggests that a thermal occupation can lead to an offset and contrast reduction in the tunneling oscillations, however, later measurements presented here rule out this possibility in our experiment (see Section 4.5.2.3).

In Fig. 4.8b, we plot tunneling oscillations out to times that exhibit damping; in this trap we find a damping $\tau \approx 10$ ms. Our first hypothesis for the damping was that it was due to finite temperature effects. However, a full calculation of the three-dimensional potential and the associated eigenstates reveals that for our 3D temperature we should observe revivals due to the incoherent sum of frequency components from different motional states. Due to the anharmonicities in the shallow double-gaussian potential, we must consider the radially and axially coupled motional eigenstates $|n\rangle$ whose sequential splitting is equal to $2J_n$, the tunnel-coupling in a given motional state for the asymptotically separated wells. In other words, the three-dimensional states form tunnel-coupled doublets (each comprised of states of opposite spatial symmetry), which transform in the large spacing limit to uncoupled motional eigenstates at the same energy. To model the thermal population in a double-well, we consider an initial thermal distribution of $\bar{n} = 0.2$ in the three-dimensional eigenstates of the separated wells, which corresponds to near the center of our spectroscopic estimates of our temperature, and calculate the ensuing dynamics once the tunneling is initiated. This leads to the plot in Fig. 4.8d, illustrating the expected tunneling response of an atom in an initial thermal distribution. We have not observed conclusive evidence of such revivals in our data, and hence we do not believe the dephasing is due to the temperature. If anything, the spectral purity of the tunneling oscillations is suggestive of highly pure 3D ground-state fraction in the final double-well system, at the upper end of our error bars from spectroscopy.

4.5.2.3 Verifying the coherence and ground-state nature of the tunneling oscillations

To verify the quantum nature of the position oscillations we observe, it was necessary to experimentally rule out some pernicious possibilities. One physical process that could mimic our

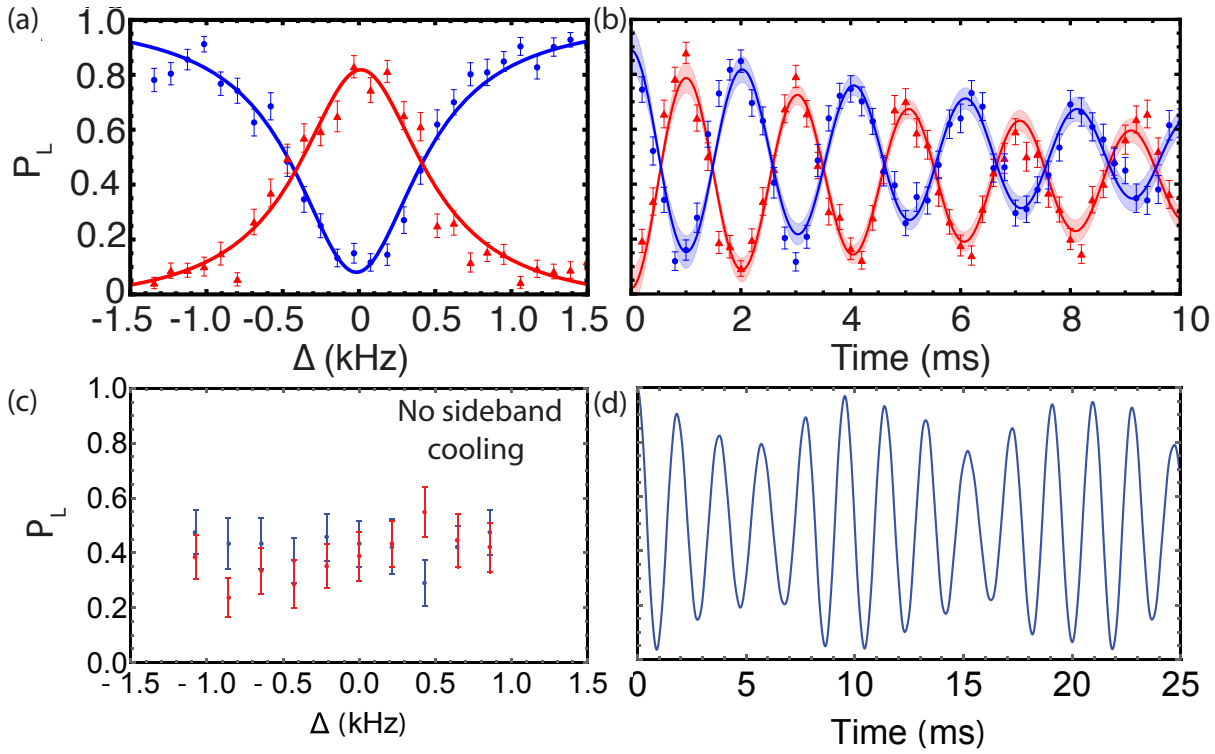

Figure 4.8: Basic characterization of single-particle tunneling in a vertical double-well formed from optical tweezers for a 808 nm spacing and depth of 96 kHz. (a) For a 0.9 ms tunneling time, we scan the relative well bias, Δ, and observe the single particle tunneling resonance, symmetrically for an atom originating from either well. The blue circles (red triangles) correspond to atoms starting in the left (right) well. The evolution time is set for near full coherent swapping of the atomic populations in each well. (b) At $\Delta = 0$, we observe oscillations at $2J$ in the expectation value of an atom's position. For (a,b), for each experimental value (bias or time) the experiment was run 400 times, yielding ~ 140 single particle measurements for each of the red and the blue data points. (c) We perform a first order check on the importance of cooling by omitting the sideband cooling stage while otherwise retaining all the features of the experiment from Figure (a), however, with half the statistics. (d) We theoretically calculate the expected tunneling dynamics for a 3D ground-state fraction of $\bar{n} = 0.2$ in the full dimensionally-coupled space of the Gaussian double-well for a spacing of 808 nm and depth of 96 kHz, mirroring the parameters of the experiment.

observations would be a highly excited motional coherent state oscillating in the double-well, barely aware of the the bump at the bottom of the potential. We would then expect spatial oscillations near the trap frequency, a large superposition of motional states, and increasing oscillation frequency with depth. While the frequency of oscillations was not consistent with any of the motional trap frequencies we expect based on our knowledge of the potential, nor did the oscillation frequency scale with the depth, we performed a set of experiments demonstrating that the tunneling was

occurring in the ground-state doublet of the double-well.

To probe the motional state after tunneling, we apply sideband thermometry after allowing the atom to tunnel for a time near a full spatial swap, i.e. $t = \frac{\pi}{2J}$. We examine the motional state of an atom that started in either the left or right well, and thereby ensure that the process is symmetric: an atom that starts in the right (left) ground-state, should exhibit a large ground-state fraction in the left (right) well after the tunneling. This is precisely what is displayed in Figure 4.9, for both the radial and axial dimensions of the trap. The y-axis of these plots is the product of the probability that the atom tunneled and that it undergoes a spin-flip at a given spectroscopy frequency. For all of the data, it is clear that both the fraction that does and does not tunnel is in the ground-state, which is also evidence that a lack of tunneling near where we expect it to be maximal (determining the contrast) is not due to thermal fraction. We have also measured spectroscopy after setting the bias far off resonance to suppress tunneling, thereby testing if the ramps cause any heating; these measurements are consistent and do not show heating. Therefore, from these data we can conclude that the tunneling process is transferring coherently quantum amplitude between states asymptotically connected to the motional ground-states of the separated optical tweezers, and that process is imperfect (finite contrast, damping) due to effects related to the coherence of the tunneling itself and not the preparation of the motional states.

The tunneling oscillations provide an indicator of the tunneling coherence, but ultimately this is only probing the on-diagonals of the atomic density matrix in the $\{|L\rangle, |R\rangle\}$ basis. We perform a Ramsey interference experiment in this two-dimensional space by applying a pair of "$\pi/2$-pulses" in the tunneling by allowing tunneling for a time $t = \frac{\pi}{4J}$, which places the atomic wavepacket in a superposition of occupying each optical tweezer. Between these resonant tunneling pulses, we quickly increase the bias $|\Delta| >> J$ which serves the dual purpose of suppressing the tunneling during this time t and allowing a relative phase to accrue between the two components of the superposition. The bias thereby causes the evolution of the superposition state $\frac{1}{\sqrt{2}}(|L\rangle + i|R\rangle) \rightarrow \frac{1}{\sqrt{2}}\left(|L\rangle + ie^{i\Delta t}|R\rangle\right)$. Just as in conventional Ramsey spectroscopy, the second $\pi/2$ pulse reads out this evolved phase by mapping it back into the $\{|L\rangle, |R\rangle\}$ populations to yield oscillations such as

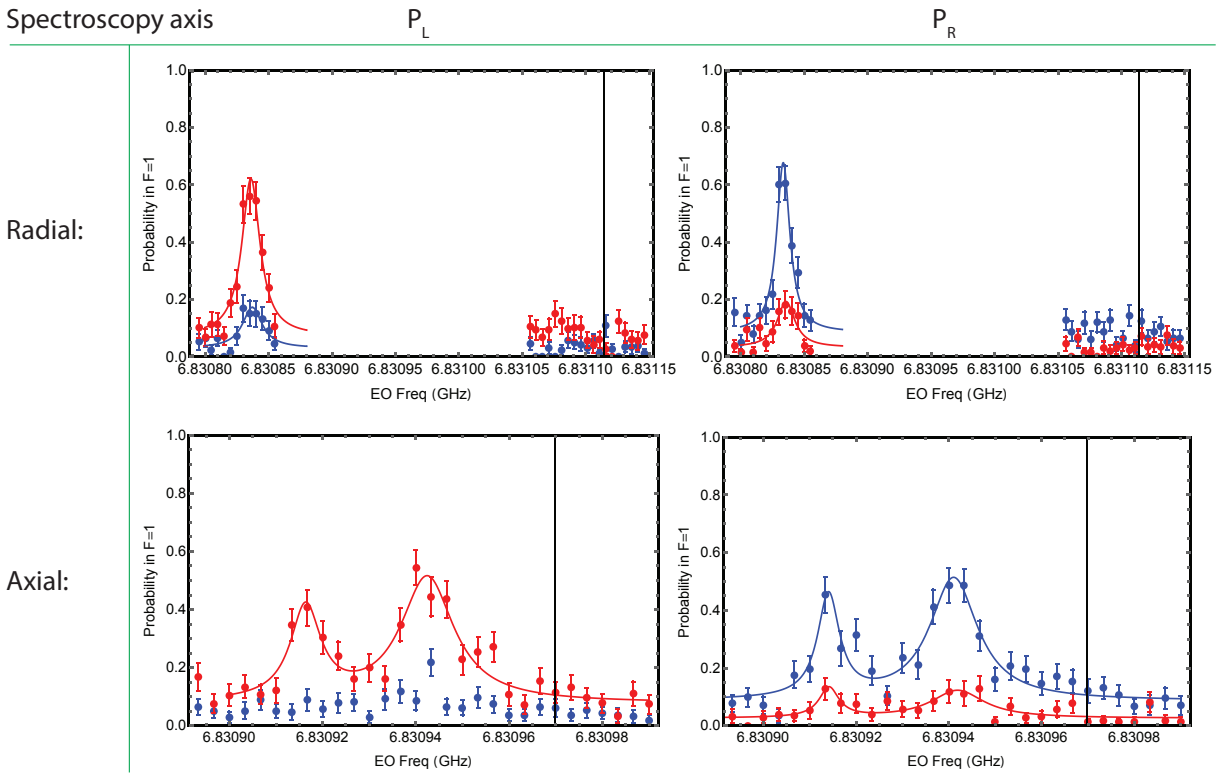

Figure 4.9: Sideband spectroscopy after resonant tunneling for near a full-swapping time of $\pi/2J$, in a horizontal double-well of depth 26 kHz and 918 nm spacing. We perform radial (first row) and axial (second row) spectroscopy after the tunneling procedure, and perform the standard resonant push-out to readout the spin populations. The y-axes on these plots should be interpreted as the product of the final well probability (indicated by the second image atom location) and the probability of being in $F = 1$ (i.e. surviving the resonant push-out). The sum of P_L and P_R for data of the same color corresponds to the overall sideband-specotrscopy transfer at a given frequency, and is consistent with sideband spectroscopy plots without the tunneling occurring prior. The first column (second column) corresponds to the probability of observing the atom on the left P_L (right P_R). For all of the plots, the red (blue) correspond to runs in which the first image showed the atom on the right (left). The flipping of the blue and red peaks between the figures in each row is because if an atom start on the left (right), it is more likely to be on the right (left). The increased offset in the radial data is because we were not using our improved push-out procedure in these data, and the Rabi frequency of the radial spectroscopy Raman beams was slightly too high.

those in Figure 4.10. The oscillation frequency should be equal to the applied bias, and we find agreement at the 15% level with the calibration technique discussed earlier. While the tunneling oscillation damping could result both from fluctuations in J and Δ, the damping observed here can only result from fluctuations in the bias.[9] Furthermore, the relative increase in the damping time

[9] In principle, spontaneous emission could also cause decoherence, but this would effect both tunneling and Ramsey

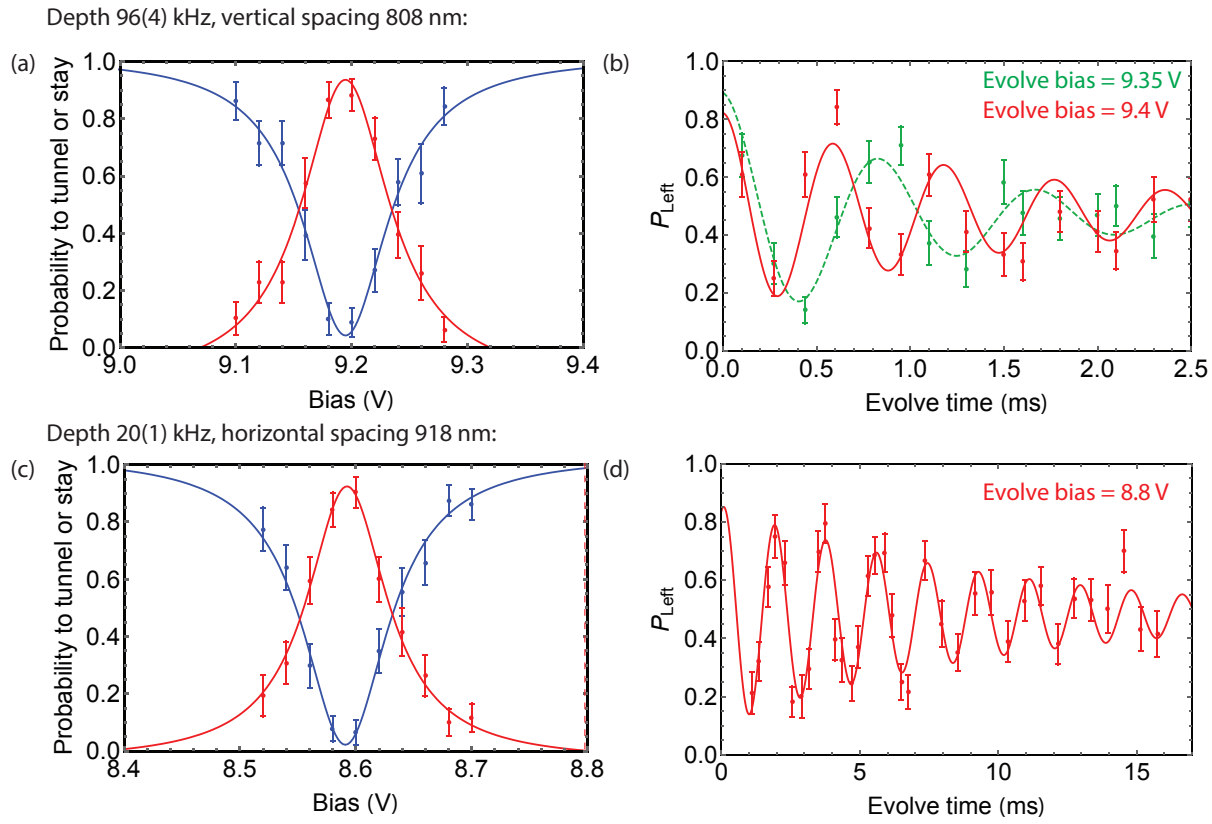

Figure 4.10: Bias spectra and Ramsey spectroscopy. In the first row, we show a bias spectrum (a) and Ramsey dynamics (b) for a vertical double-well of 96 kHz and 808 nm spacing. Using the measured $2J$ of 500 Hz (mean of a number of a measurements) and the bias spectrum width, we compute the expected volts to energy bias calibration. For the 9.35V (9.4V) bias and correcting for the narrowing due to the quasi-adiabaticity, we measure 1.18(3) kHz (1.69(3) kHz) and predict 1.03 kHz (1.4 kHz) according to the calibration. In the second row, we show a bias spectrum (c) and Ramsey dynamics (d) for a horizontal double-well of 20(1) kHz and 808 nm spacing. Using the measured $2J$ of 179(1) Hz and the bias width of (c), we expect for the Ramsey dynamics (d) a frequency of 0.52 kHz and measure 0.55 kHz. The nearness of the widths of the bias spectra here in units of volts is incidental: the bias calibration scales proportionally and inversely with the tunneling and the depth, respectively, and each change by a similar amount.

by going from a deeper to shallower trap double-well indicates a dependence on the tweezer depth, which we explore more thoroughly in next section.

equally. Therefore, the fact that we observe this degree of change in the damping timescale indicates that this is not a dominant effect.

4.5.2.4 Mapping out the contrast and dephasing dependences in vertical and horizontal double wells

We demonstrate in Fig. 4.11a,b the two-dimensional space of spacing a and depth V_0 with which we can tune the measured the tunnel coupling J (half the measured oscillation frequency). In Fig. 4.11a, we observe in accordance with theory that the tunneling changes rapidly with the spacing. The solid line is a 3D calculated expectation for an ideal gaussian beam of waist $w_0 =$ 707 nm and a single-well depth of 96 kHz; the waist used corresponds to the outcome of a least-squares fit, which agrees closely with our independently measured waist of $w_0 = 710(10)$ nm. The depths and spacing used are according to the characterizations in Section 2.8.2 and Section 2.9.2, indicating our absolute knowledge of the trap parameters. The tunneling dependence on depth exhibits disagreement at the 10% level with the theoretical expectation according to both the 1D and 3D calculations, both of which we show to emphasize the similarity between the two calculations. For this parameter range of depth and spacing, these scans exhaust the range over which the atoms are localized (i.e. oscillate between localized states) and there is appreciable tunneling contrast; at the lower end of the spacing and depth range we increasingly observe that the atom position does not oscillate and has split probability between the wells. This is presumably due to the ground-states becoming delocalized. We have also, however, explored vertical and horizontal double-wells at significantly larger spacing and shallower depth, an example of which is shown below.

We have mapped out the contrast and decay of the tunneling oscillations as a function of the trap depth and tunneling magnitude, which we have determined to be the dominant factors that determine the quality of the tunneling. Fluctuations in J or Δ are the primary possible culprits that could influence the tunneling behavior. Our primary hypothesis is that the contrast and damping of the tunneling oscillations in a particular trap come from fluctuations in the energy bias. We assume that we have fixed fractional fluctuations, which could arise, for example, from fluctuations in the relative AO deflection efficiency for the two frequencies that define the double well, or from stray reflections interfering with the main trap. For both of these cases, the magnitude

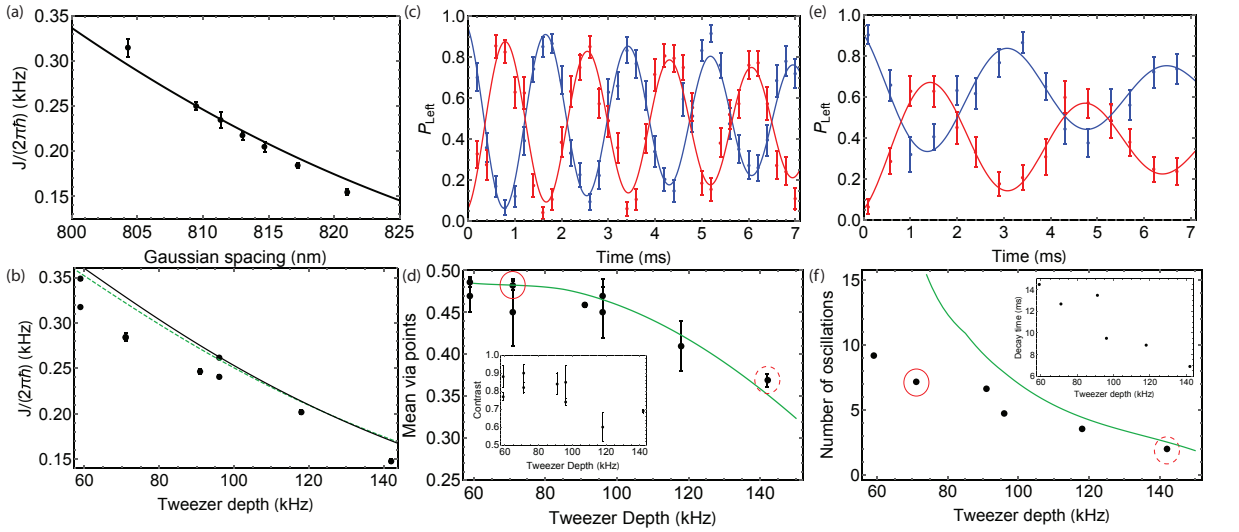

Figure 4.11: Tunneling dependences. (a) Measured tunneling J as a function of the double-well spacing for a vertical double-well of 96(4) kHz. The solid line is a theoretical expectation using the full 3D calculation of the potential (see text). (b) Measured tunneling J as a function for a vertical double-well of 808 nm spacing. The solid line is the full calculated dependence as in (a), while the green dashed line is the 1D calculation by simply Fourier transforming the potential and solving the Schrodinger equation in a truncated momentum basis; these differ by a very small degree, indicating the predominantly separable nature of the potential. (c,e) Tunneling dynamics for a depth of 71(3) kHz and 142(6) kHz, respectively, and a 808 nm spacing. (d) Mean of the oscillation data points as a function of the tweezer depth. The mean gives an indication of the degree to which the tunneling is off-resonant due to the bias fluctuations. The solid-line green line is the model discussed in the text, and we find decent agreement. At sufficiently low depth, the mean of the data approaches the ideal value of 0.5 but corrected for loss, which is 0.48. The inset shows the fitted amplitude, which is influenced by both the preparation and this stability of the bias, and it shows a similar trend to the mean data. (f) Number of oscillations observed in the tunneling dynamics, which is computed to be $2J \cdot \tau$ compared with the theoretical model from the text. We find not amazing model agreement with respect to the dephasing, particularly at small depths; this may indicate other dephasing mechanisms become dominant. Because we took much of the oscillation data on a similar time scale, the error in the fitted τ for the slow J data goes up to 30%, while for the faster J data it is around 10%. I omitted them from the figure for this reason. The inset shows the just the fitted τ. For both (d,f), I have circled the data points that correspond to the oscillation scans (c,e) with a solid and dashed line, respectively.

of the fluctuations in units of energy will scale with the overall tweezer depth V_0. The absolute magnitude of these fluctuations compared to the tunneling energy will determine the damping and mean of the oscillations. This latter symptom is important to our hypothesis of the character of the fluctuations: for fluctuations in J we would only anticipate damping, while fluctuations in Δ bound the peak value of the oscillations (i.e. P_L for an atom starting on the right) such that the

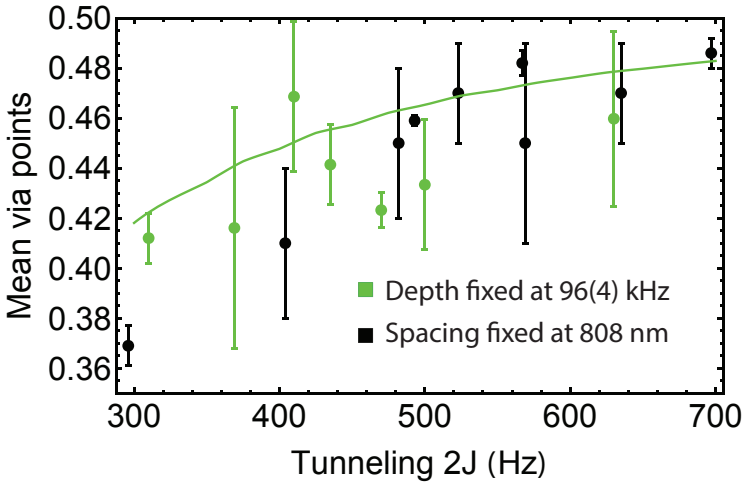

Figure 4.12: Comparing fixed spacing and fixed depth data. We show the variation of the mean of the data from the data in Figure 4.11a plotted against the measured tunneling (green), as well as the Figure 4.11d plotted against the measured tunneling as opposed to the depth (black). Therefore, the green (black) data corresponds to fixed depth and varied spacing (fixed spacing and varied depth) as a function of measured 2J. Though there is scatter, the disparity between the two plots, particularly the faster drop off in the varied depth data, corroborates the hypothesis that both the depth and the tunneling inform the mean of the data. Furthermore, we compare the green data to the model (solid green line) discussed in the text, where here the depth is fixed and the fractional fluctuations are, as above, 0.17%. We find decent agreement.

mean of data, as well as the contrast of the oscillations, is reduced.

We test this hypothesis by constructing a simple noise model to understand the effect of fluctuations. We assume that the experimental fluctuations yield a temporally inhomogeneous, Gaussian distribution in Δ with spread $\sigma = \Delta_{\text{frac}} V_0$. We are interested in extracting Δ_{frac}, which phenomenologically describes the fractional fluctuations. We then model the double-well evolution using the solutions of the simple Hamiltonian H_{eff} in Eq. 4.33 and assuming completely diabatic turn on of J,[10]

$$P_L(t,\Delta) = \frac{1}{2}\frac{(2J_{\text{meas.}})^2}{\Delta^2 + (2J_{\text{meas.}})^2}\left(1 - \cos\left(\sqrt{\Delta^2 + (2J_{\text{meas.}})^2}t\right)\right), \tag{4.35}$$

where $J_{\text{meas.}}$ corresponds to the measured value of J for a given depth, and Δ we average over to simulate the noise in the dynamics for a given V_0 and Δ_{frac}. To extract the modeled quantities

[10] The narrowing due to quasi-diabaticity should inform these dynamics, but for the approximate nature of this modeling we exclude these effects since it would require modeling the narrowing for each ramp.

we wish to compare to experiment, which are primarily the oscillation mean and dephasing, we determine the average dynamics by computing numerically the integral,

$$P_L^{\text{avg.}}(t) = \frac{1}{(2\pi)^{1/2}\sigma} \int_{-\infty}^{\infty} e^{-\frac{\Delta^2}{2\sigma^2}} P_L(t,\Delta) d\Delta. \tag{4.36}$$

Using the result of this noise model, $P_L^{\text{avg.}}(t)$, we fit the simulated data to extract the mean[11] , the dephasing time, and oscillation contrast according with the fit model,

$$P_L(t) = \frac{A}{2}\left(1 - e^{-t/\tau}\cos(2Jt)\right) + k, \tag{4.37}$$

where τ is the dephasing time, A the oscillation contrast, and k an oscillation offset above zero. We use this model to fit the experimental data as well. Including the effect of single particle loss in the experiment, we find favorable agreement between our observed reduction (examples of which are shown in Figure 4.11c,e) in the mean ($k + A/2$) and simulated reduction for a Δ_{frac} of 0.17%, which is displayed in Figure 4.11d. At large depths this model appears to approach the observed dephasing times, though it appears that the damping is limited by other mechanisms as well for smaller depths. In Figure 4.12, we compare the behavior of the mean of the data for fixed spacing (as in Figure 4.11d) versus fixed depth, as a function of the tunneling. For fixed-spacing and varied depth, we expect that the mean drops faster because the tunneling is decreasing while the absolute bias fluctuations are increasing as the depth is increased. Conversely, for fixed depth and varied spacing, we expected that the mean drops only because of the tunneling decreasing since the absolute bias fluctuations are fixed. Indeed, over the range of data shown, the fixed depth data changes more slowly than the spacing-fixed data. Using the same fractional fluctuations of of 0.17% and here a 96 kHz depth for the model, we observe decent agreement with the fixed-depth, varied-spacing data although the experimental error bars leave something to be desired. Lastly, if we fit the Ramsey oscillation data from Figure 4.10b to a sinusoid with Gaussian decay (the expected decay response for Gaussian frequency fluctuations)[12] , we extract frequency fluctuations

[11] For the measured data, we use the mean of the data points.

[12] For historical reasons, we used the decay model of Eq. 4.39, but for Gaussian frequency distributions, the Fourier transform has Gaussian temporal decay.

$\sigma = 150(30)$ Hz, implying a consistent $\Delta_{\text{frac}} = 0.15(3)\%$ with the tunneling data from Figure 4.11 and Figure 4.12.

Focusing back on varied depth data, while the saturation of the mean near the ideal value suggests that the fluctuations in the final trap are no longer relevant for depths below 100 kHz, we do observe nevertheless that the contrast is still between 0.75-0.85, as indicated by the oscillation the data in Figure 4.11c and the inset of Figure 4.11d. This implies that the fluctuations in the final trap are not limiting the final contrast once we are at traps depths below 100 kHz for this spacing and hence range of tunneling (see Figure 4.13). One possible mechanism for this behavior is dephasing during the tunneling before $t = 0$, which occurs in the deeper traps for which we already know decoherence occurs according to the measurements presented here. If the tunneling that occurs before $t = 0$ dephases, it will contribute the offset k to the data, thereby limiting the oscillation contrast to $C = 1 - 2k < 1$. We do observe an offset in the data in shallower traps that appears to decrease in the deeper traps, as would be expected for this mechanism since less tunneling occurs before $t = 0$ when the trap is deeper. Our error bars on these fitted values of the offset, however, are too large (fractionally greater than 50%) to draw any conclusions. A possible test of whether this is indeed determining the final contrast would be to measure the tunneling contrast by initiating the tunneling via sweeping the traps together as opposed to dropping the depth; we avoided this approach since we were concerned that thermal effects in the AO are enhanced close to when these ramps occur. Nevertheless, it could reduce the amount of tunneling that occurs before the final trap since the tunneling changes so rapidly with the spacing, and, furthermore, the fraction of tunneling that does occur would occur in the final trap depth in which contrast reduction is diminished. Initial attempts of this did not show an improvement, but these were conducted before we had optimized the setup and therefore it is worth revisiting.

In conclusion, we have some instabilities in our double-well that in certain respects are consistent with bias fluctuations at the $\sim 0.2\%$ level. A short-term goal is to incorporate incoherent light for the tweezer light, which could mitigate fluctuating interferences from weak reflections in the setup. In particular, reflections at the 10^{-6} level could interfere with the main spot to produce

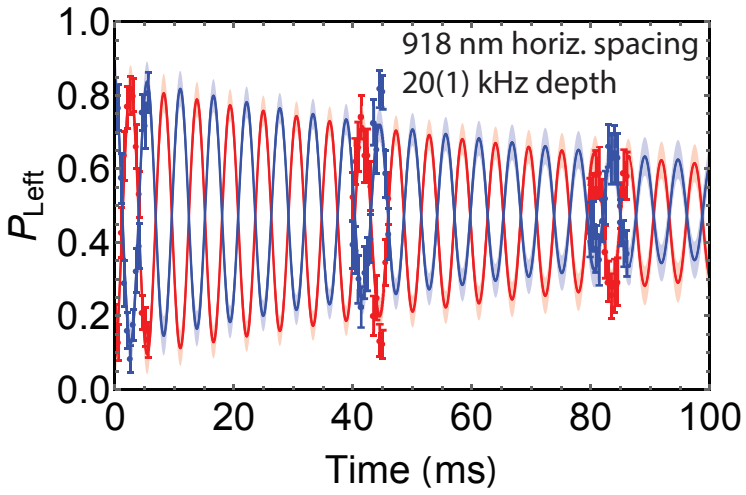

Figure 4.13: Large-spacing, shallow trap tunneling. We have explored a large range of double-well potentials, and, as expected given the model, we observe that the damping drastically improves as we go to very shallow depths, even though the tunneling rate has been reduced significantly. The fit gives a $\tau = 110(20)$ ms, while from the model in the text we would expect a damping time of 125 ms using the measured $2J$ and depth of 20 kHz. The fitted amplitude, however, is 0.75(5) while we would expect from the model 0.99. This points to other mechanisms limiting the contrast as well, which are discussed in the text.

the magnitude of fluctuations (10^{-3}) indicated by the characterization in this section. In any case, further investigation of the origin of the fluctuations is still necessary, but these have not precluded the HOM effect investigations I will discuss shortly.

4.6 On-site interaction energy

The prior sections describe our characterization of single atoms tunneling in the double-well potential. The other important parameter is the interaction energy U between two particles in the same well, to which we lacked direct experimental access in these experiments. In our experiment we determine the on-site interaction energy by using independent knowledge of our trap parameters (well depths, Gaussian center spacing, and the effective Gaussian waist) as inputs to the theoretical calculations for the full 3D potential, our understanding of which is corroborated by the theoretical agreement with our tunneling observations. For the contact interactions experienced by ^{87}Rb atoms

in the HOM experiments, the interaction U can be expressed,

$$U = \frac{4\pi\hbar^2 a_s}{m} \int d\vec{r} |\psi_L(\vec{r})|^4, \tag{4.38}$$

where a_s is the background atomic scattering length, and ψ_L is the ground-state localized wave function in the left optical tweezer, which is formed from the even or odd superposition of the states comprising the tunnel-coupled doublet. We chose the left-well wave function simply for explanatory purposes, and the right-well localized wave-function yields the same U. Propagating the uncertainties in the trap parameters, as described in Sec. 2.8.2 and Sec. 2.9.2, we find the uncertainty in the predicted U. Due to the extreme sensitivity of J to trap parameters we can predict U with less uncertainty than an equivalent prediction of J. The values of U/J presented use the measured J (and associated statistical uncertainty from the oscillation measurement) and calculated U to generate our best determination of U/J in each of the double-well traps studied. Later measurements of spin-exchange oscillations, presented in Chapter 5, experimentally demonstrate the accuracy of these calculations, and affirm theoretically that the interactions present between the atoms do not inform the HOM interference we observe.

4.7 Dynamical Hong-Ou-Mandel interference of two atoms

In Figure 4.14, we display our observation of dynamical Hong-Ou-Mandel interference of single atoms. For these experiments we use two different double-well configurations in order to verify the invariance of our observations to the exact values of J and U. For each configuration, we scan the evolve time and run the experiment for 400 repetitions at each time. Each repetition yields randomly an experiment with an atom starting on the left, the right, an atom in each well, or no atoms. The first two cases correspond to the data in Figure 4.14b,c, and the two particle experiments correspond to the data in Figure 4.14e,f. While the two-particle data contain our observation of HOM interference, the single particle data benchmark our conclusions. For the characterization of the tunneling oscillations, the single-particle tunneling data are fit with the

model,

$$P(t) = \frac{A}{2}\left(1 - \cos(2Jt - \phi)\right) + k. \tag{4.39}$$

For the case of fitting the two-particle data, the only difference is that $2J$ is replaced with $4J$. This modeling is akin to the earlier fits discussed in this chapter except we exclude the dephasing term since over the time scales explored here we do not observe significant dephasing.

4.7.1 Single atom beam splitter formed by optical tweezers

We first assess the resonant single-particle tunneling, yielding the tunable beam splitter dynamics evidenced in Figure 4.14b,c with which we can observe two-particle interference. A fit to the data in Figure 4.14b reveals $J/2\pi = 262(4)$ Hz; Figure 4.14c shows data in which J is increased to 348(4) Hz. Along with the systematics discussed in prior sections, part of the finite contrast of the oscillations is due to atom loss from background collisions; in the atomic HOM data the loss probability (P_{loss}) ranges from 0.03 to 0.05 and is known precisely for each experiment by taking the sum of P_{L}^{i} and P_{R}^{i} (Figs. 4.14b,c gray regions). Within a given experiment, these loss numbers vary fractionally by less than 10% (i.e. absolute less than 0.5%). As will be discussed, primarily significant are the times indicated by the dashed green lines, at which an atom that has started in either well has been placed in an equal superposition of being in each tweezer.

4.7.2 Ideal two-atom quantum interference via tunneling dynamics

Before examining the two-particle data, we first consider the theoretical expectation for an equivalent dynamical experiment starting with two particles, one atom in each well. For perfect cooling and spin preparation of the isolated atoms, all degrees of freedom besides their position (left or right) will have been made the same, i.e. we know there is a particle in the left well and there is a particle in the right well, but we cannot associate any additional label to the particles. The bosonic atoms will then, necessarily, occupy the spatially symmetric $|S\rangle$ state, comprised of orthogonal spatial wave-functions that are coupled by the tunneling. For poor cooling or spin preparation, the atoms can be distinguished by a degree of freedom other than their position; hence,

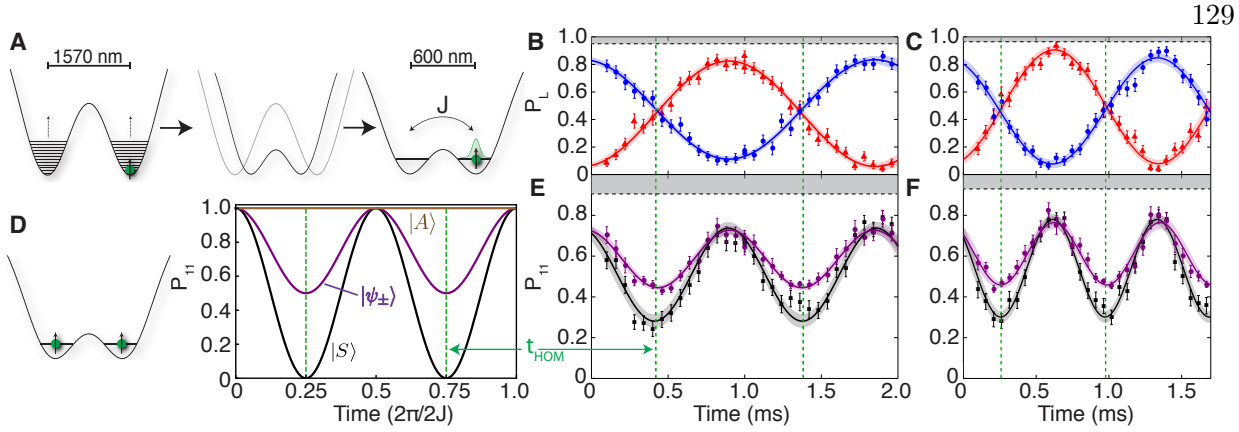

Figure 4.14: Single and two-particle tunneling. (a) Experimental overview. While the tweezers are 23(1) MHz deep, the atom is imaged, cooled and optically pumped to $|\uparrow\rangle$. For tunneling experiments, the tweezers are swept together such that the two gaussian functions are defined with an offset of ≈ 800 nm (resulting in double-well minima spaced by ≈ 600 nm), and the total trap intensity is dropped by a large factor, resulting in a single-well depth of either 96 kHz or 60 kHz. (b) Resonant tunneling oscillations at $2J$ for a 808 nm gaussian function spacing and a 96 kHz depth. Blue circles (red triangles) are the expectation value $P_{\mathrm{L}}^{1(2)}$ for finding an atom in the left well given an initial single atom in the left (right) well. The gray shaded region indicates the contribution from atom loss P_{loss}. (c) Same as [b] except with a 805 nm gaussian function spacing and a depth of 60 kHz. (d) Idealized two-particle tunneling dynamics. Expectation for $P_{11}(t)$ for dynamics initiated at $t = 0$ and in the symmetric spatial state $|S\rangle$, the distinguishable states $|\psi_\pm\rangle$, and the anti-symmetric state $|A\rangle$. The dashed green lines mark the locations of t_{HOM}. (e) Measured two-particle dynamics during the same experimental sequence as [b]. Likelihood to measure exactly one atom in each well (P_{11}) for the initial condition in which an atom is prepared in each well (black squares). Distinguishable expectation P_{dist} as determined from the single-particle data in [b] (purple circles). The gray shaded region above the dashed black line indicates the expected reduction from atom loss. (f) Same as [e] except here we realize a larger value of J and smaller value of U (see text) using the double-well parameters of [c]. t_{HOM} for the experimental data is affected by a phase shift due to a small amount of tunneling before the nominal final trap is reached; this effect is larger for faster tunneling. In all plots, the shaded regions are the 95% confidence interval for a sinusoidal fit. The error bars are the standard error in the measurement; each black data point is the mean of ≈ 140 measurements, and each red or blue data point is the mean of ≈ 100 measurements.

the atoms can anti-symmetrize in the additional degree of freedom, motional state or spin, and in turn have a projection onto the anti-symmetric spatial state $|A\rangle \equiv \frac{1}{\sqrt{2}}(|L\rangle_1|R\rangle_2 - |R\rangle_1|L\rangle_2)$. The bosonic state can then be written as a mixture of the states $|\psi_\pm\rangle = \frac{1}{\sqrt{2}}(|S\rangle|\chi_+\rangle \pm |A\rangle|\chi_-\rangle)$, where $|\chi_\pm\rangle = \frac{1}{\sqrt{2}}(|\chi\rangle_1|\bar{\chi}\rangle_2 \pm |\bar{\chi}\rangle_1|\chi\rangle_2)$ and $\{\chi, \bar{\chi}\}$ describe the other degree of freedom such as motional state $\{n, n'\}$ or spin $\{\uparrow, \downarrow\}$. Two atoms in either of the $|\psi_\pm\rangle$ states are distinguishable according to the discussion in Section 4.2.7 because the additional degree of freedom $\{\chi, \bar{\chi}\}$ is uniquely

correlated with the atoms' positions and invariant[13] with respect to the Hamiltonian: For the $|\psi_+\rangle$ ($|\psi_-\rangle$) state, the atom on the left is in state $|\chi\rangle$ ($|\bar{\chi}\rangle$) and the atom on the right is in state $|\bar{\chi}\rangle$ ($|\chi\rangle$). The ability to measure two-atom indistinguishability arises from the different dynamics exhibited in the symmetric and anti-symmetric cases. The symmetric spatial state dynamically evolves as $|S\rangle \rightarrow |S\rangle\cos(2Jt) + \frac{i}{\sqrt{2}}(|L\rangle_1|L\rangle_2 + |R\rangle_1|R\rangle_2)\sin(2Jt)$. The anti-symmetric state $|A\rangle$ undergoes destructive interference that prevents the two bosons from being in the same well, and hence displays no tunneling dynamics. This is precisely the wave function occupied by identical fermions, and hence the destructive interference could be equivalently interpreted as a consequence of the Pauli-exclusion principle.

In Figure 4.14d we show the expected *ideal* dynamics for the distinguishable (purple) and indistinguishable (black) cases; we emphasize that t is the time the atom spends tunneling. We consider the observable $P_{11}(t)$, which is the likelihood to measure the atoms in separate wells as a function of time spent tunneling, and is directly analogous to looking at coincidence counts on a pair of photon detectors. The symmetric state $|S\rangle$ yields unity contrast oscillations of $P_{11}(t)$, whereas $|A\rangle$ yields a time-independent $P_{11}(t) = 1$. Hence, the distinguishable states $|\psi_\pm\rangle$ result in a $P_{11}(t)$ that is the average of these dynamics, and as such does not attain a value below 0.5. The tunneling between the wells yields an effective atom beam splitter where t varies the reflection and transmission coefficients. Of particular importance are the times $t_{\mathrm{HOM}} = 2\pi/8J$ and odd multiples thereof (green dashed lines). At $t = t_{\mathrm{HOM}}$, the tunneling realizes a balanced atom beam splitter according to the transformations $|L\rangle \rightarrow \frac{1}{\sqrt{2}}(|L\rangle + i|R\rangle)$ and $|R\rangle \rightarrow \frac{1}{\sqrt{2}}(|R\rangle + i|L\rangle)$. Accordingly, for the $|S\rangle$ state, $P_{11}(t_{\mathrm{HOM}})$ vanishes equivalent to indistinguishable photons incident on separate ports of a balanced beam splitter in the original HOM experiment: at these times, experimentally we have the mode-entangled two-particle state $|+\rangle = \frac{i}{\sqrt{2}}(|L\rangle_1|L\rangle_2 + |R\rangle_1|R\rangle_2))$. However, distinguishable atoms, like distinguishable photons, will yield $P_{11} = 0.5$ when equally beamsplit, and only partial amplitude in the state $|+\rangle$ when tracing over the distinguishing degree of freedom. As will be

[13] Invariant in the sense that the quantum numbers associated with $\{\chi, \bar{\chi}\}$, whether they be the spin state or the axial motional state, are unchanged during evolution under the tunneling Hamiltonian.

discussed, because we cannot directly detect two-particles in the same optical tweezer, which is dictated by $|+\rangle$, we will focus on the measurable P_{11} in discerning indistinguishability driven HOM intererence.

4.7.3 Observation of the atomic HOM effect via two-particle tunneling dynamics

In Figure 4.14e, we experimentally investigate the population dynamics observed with two particles. We plot $P_{11}(t)$ for cases in which the stochastic loading results in two atoms, one in each well (black squares). During the 25 ms to 50 ms imaging time, due to light-assisted atomic collisions we observe signal corresponding to either zero or one atom [3, 11, 2] as discussed in Section 2.7.3. P_{11} is determined by the distinct experimental signature in which the final image indicates one atom in each tweezer. However, we expect that when $P_{11}(t)$ is minimal, the likelihood of the atoms being on the same tweezer, P_{20} or P_{02}, is maximized. If the experiment yields two atoms in one well, the experimental signature is *not* unique: this is manifest by final images that yield zero atoms, or in some cases one atom in a single well. These latter "two-to-one" events are illustrated in Figure 4.15. Since we cannot distinguish two-to-one events, which inform our observation of HOM interference, from single-particle loss during a two-particle experiment, we keep such events in our analysis of P_{11}. To accurately interpret P_{11}, therefore, we take into account signal depletion due to the single-particle loss described earlier (P_{loss}). This effect reduces the maximum value that can be achieved by the measured P_{11} to $(1 - P_{\text{loss}})^2$ (gray region above the black dashed line in Figure 4.14e,f indicates the loss contribution), and correspondingly modifies the distinguishable lower bound on $P_{11}(t) \geq (1 - P_{\text{loss}})^2/2$ in analogy to the ideal 0.5 from above. Nevertheless, if one were to throw out the (meaningful) data associated with two-to-one events, the HOM interference that I will now discuss is statistically significant to 4.1σ; including these data, therefore, is not essential to our observations.[14]

[14] The apparent reduction in the statistical significance is because we are throwing out data associated with the HOM interference events, namely, times when we have created a relative preponderance of the $\frac{1}{\sqrt{2}}(|2,0\rangle + |0,2\rangle)$. And, as expected, the degree to which the statistical significance is reduced (1/3) corresponds closely to the fraction with which these two-to-one events occur.

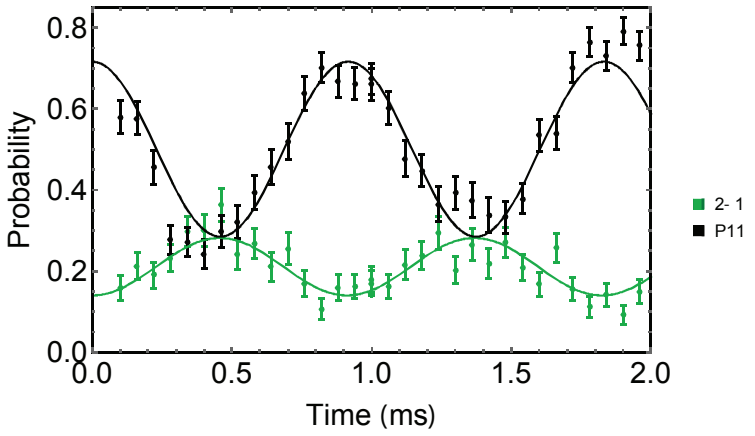

Figure 4.15: Two-to-one events during imaging. P_{11} is defined by the case in which both images indicate one atom in each well. We can study the two-to-one events we observe and confirm that they are a signature of two atoms on a single well, by looking at the anti-correlated nature of these events with respect to $P_{11}(t)$. As shown (note, this is the data from Figure 4.14e), we find that in our experiments we see an increase in two-to-one events (green) when $P_{11}(t)$ (black) is minimal, i.e. when the likelihood of finding two atoms on the same tweezer is maximal. Using the calibrated single atom loss, we conclude from these data that 29(4)% of the time a two-to-one event occurs when the data is analyzed at t_{HOM} (minimum of P_{11}) and a consistent value of 22(5)% when the data is analyzed at the maximum of P_{11}. We also can directly measure two-to-one events by carrying out a separate experiment in which we combine two traps each with a single atom to deterministically start with two atoms in a single trap. In this experiment we find 26(2)% of the time a two-to-one event occurs. While these findings are in contrast to many optical lattice experiments in which pure parity imaging is observed [11, 2], other optical tweezers experiments have observed similar phenomena [12].

We extract the presence of indistinguishability in the data in Figure 4.14e,f through the size of the oscillation contrast of the two-particle tunneling. Our goal is to compare $P_{11}(t)$ from our two-particle measurement to that of a theoretical expectation for distinguishable atoms in an uncorrelated state, which we refer to as $P_{\mathrm{dist}}(t)$. P_{dist} at any time can be calculated directly from corresponding single-particle data via $P_{\mathrm{dist}} = P_{\mathrm{L}}^{1} P_{\mathrm{R}}^{2} + P_{\mathrm{R}}^{1} P_{\mathrm{L}}^{2}$ (purple circles in Fig. 4.14e). To reiterate, $P_{\mathrm{L}}^{1(2)}$ corresponds to measuring an atom in the left well when an atom starts in the left (right) well, i.e. the blue (red) data of Fig. 4.14b, and $P_{\mathrm{R}}^{1(2)}$ is the corresponding information for measuring an atom in the right well. For distinguishable particles in an unentangled state, we expect at any given time the two-particle behavior to be equivalent to flipping two-independent coins representing each atom, each weighted by the measured single-particle data; this description

is formalized in Section A.1.1.1. A calculation of P_{dist}, furthermore, directly from the single-particle points inherently contains both loss and finite single-particle contrast. For example, $P_{\mathrm{dist}}(t_{\mathrm{HOM}})$ reaches a value consistent with $(1 - P_{\mathrm{loss}})^2/2$, and the amplitude of $P_{\mathrm{dist}}(t)$ is consistent with the expectation of one half the product of the single-particle contrasts (see Appendix, Section A.1.1.1). We can compare the amplitude of oscillation for the distinguishable expectation (purple circles) to our two-particle measurement (black squares). We find these values differ by 6σ (see Appendix, Section B for discussion of statistical analysis): $A_{P_{\mathrm{dist}}} = 0.282(12)$ and $A_{P_{11}} = 0.46(2)$.

A full treatment of the observed $P_{11}(t)$ must also consider potential effects of interactions between the atoms. In many experiments with atoms in optical lattices the on-site interaction energy U is the dominant scale [129, 132]; however, we intentionally operate in a regime where U is smaller than J. For the data shown in Fig. 4.14e, $U = 0.44(4)J$. In Figure 4.14f we demonstrate a similar HOM signature for experimental conditions of even smaller relative interaction $U = 0.22(2)J$, with measurements $A_{P_{11}} = 0.48(2)$ and $A_{P_{\mathrm{dist}}} = 0.306(18)$. The similarity of these results to those in Figure 4.14e suggests that interactions are not a relevant scale in either experiment. Nevertheless, we also theoretically analyze whether interactions between distinguishable atoms could mimic the HOM signal. For the two-particle initial conditions expected in our experiment, the interaction energy shift suppresses two-particle tunneling regardless of distinguishability, and hence the theoretical expectation for $A_{P_{\mathrm{dist}}}$ decreases with increasing interactions. In the implausible case that the particles initially have specific coherences (see Appendix, Section A.1.1.2 and Figure A.2), $A_{P_{\mathrm{dist}}}$ can be larger and $P_{\mathrm{dist}}(t)$ can reach a lower minimum value. Even in this unlikely circumstance our data are statistically different from this interacting distinguishable case (see Figure A.2 and surrounding discussion). Another independent piece of evidence that the HOM interference we observe arises due to quantum statistics and not atom interactions comes from the studies presented below. In these experiments we vary the two-particle spin state and observe the HOM interference vanish, while this variation of the two-particle spin state only changes the interactions by at most 5% [133]. Therefore, the behavior we observe cannot be attributed to interactions between the particles influencing $P_{11}(t)$.

Lastly, we have observed the same violations in $P_{11}(t)$ of the expectation for distinguishable particles for double-wells oriented horizontally, and for a depth (spacing) five times shallower ($\sim$ 10% larger). This implies that these observations are independent of the details of the double-well and dynamics during the ramp. The latter is changed due to the relative shallowness and spacing of the final traps, the time scale of the final ramp (10 ms instead of 5 ms), and the absence of a gravitational shift. After making assumptions about the character of the initial single particle density matrices, we can also conjecture an expression for the two-particle oscillation contrast that includes the effect of finite tunneling contrast and temperature. We find good agreement with this expression: see appendix A for this discussion as well a table summarizing our observations (Table A.1).

4.8 Tuning the distinguishability

We now focus on experiments in which we fix the tunneling time at t_{HOM}, where P_{11} reaches a value that we refer to as P_{HOM}. While so far we have focused on comparisons of the oscillation contrast of $P_{11}(t)$ and $P_{\mathrm{dist}}(t)$, our observation of HOM interference can also be discussed in terms of the disparity between these two quantities at times near t_{HOM} (see Section A.1.1.1). The agreement between $P_{11}(t)$ and $P_{\mathrm{dist}}(t)$ at times far away from t_{HOM} affirm that classical effects associated with single-particle loss and finite-single particle tunneling contrast are manifest as expected in $P_{11}(t)$. Their disparity, however, near t_{HOM} affirms the non-classicality of the physics, the influence of quantum-mechanical indistinguishability in our data. The observations so far, therefore, can be summarized as tuning the reflection and transmission ports of an atom-beam splitter between being balanced and imbalanced, and thereby adjusting the degree of quantum interference experimentally produced. However, by now studying the behavior of P_{HOM}, we explore specifically the times at which we have produced a balanced beam splitter, and can more closely reproduce the original photonic HOM experiment. In that case, the two-photon interference was manifest as the distinguishability of the photons was tuned via their wave packet overlap on the beam splitter, as discussed in Section 4.1. Accordingly, we can observe an atomic "HOM dip" as the indistin-

guishability of the atoms is varied. In particular, we vary the two-particle spin state and the 3D motional ground-state fraction to introduce distinguishing spin or motional degrees of freedom, and observe the non-classical behavior vanish and be restored as we modulate the presence of atomic indistinguishability.

The three experimental methods we employ to vary the two-atom distinguishability are displayed in Figure 4.16. For each measurement, we plot both our observed $P_{11}(t_{\mathrm{HOM}})$ (black) as well as $P_{\mathrm{dist}}(t_{\mathrm{HOM}})$ (purple) from the single particle measurements. On each plot, we also have a dashed black line at the calibrated position $(1 - P_{\mathrm{loss}})^2/2$, where P_{loss} is also measured from the single particle data for each data plot. For distinguishable particles, the minimum value of $P_{11}(t)$ should occur at t_{HOM} and reach this value of $(1 - P_{\mathrm{loss}})^2/2$. The correspondence between this latter quantity and $P_{\mathrm{dist}}(t_{\mathrm{HOM}})$ for the entirety of all three of these sets affirms that the manner by which we introduce distinguishability in each experiment does not disturb the single-particle tunneling; the beam splitter operation is sound and it is only the two-particle distinguishability that influences the observed $P_{11}(t_{\mathrm{HOM}})$. This statement, however, is contingent on the tunneling being symmetric[15] between the wells ($P_L^i, P_R^i \sim (1 - P_{\mathrm{loss}})/2 = 0.48$), which indeed we observe from the single particle data in all of the measurements at the ± 0.05 level (see Table 4.1), with the exception of the range of data noted in the axial cooling variation.

4.8.1 Varying the two-particle distinguishability via the spin degree of freedom

We start by studying the dependence of P_{HOM} on the relative spin state of the two atoms using two distinct methods. In the first method, after cooling the atoms, we apply a variable-length microwave pulse that couples the $|\uparrow\rangle$ and $|\downarrow\rangle$ spin states in only the right well (see Section 2.12.2). This is accomplished by shifting the transition in the left well out of resonance using a circularly-polarized, tightly focused laser spot. Upon π rotation of this spin, the atoms become distinguishable, and we expect the HOM dip to disappear. The observed dependence on the microwave pulse area

[15] For example, if the tunneling is not symmetric, one could imagine a situation in which an atom that starts on the left has split probability between each well, while an atom which starts on the right has unity likelihood of remaining in the right well. This yields a $P_{\mathrm{dist}} = (1 - P_{\mathrm{loss}})^2/2$, even though the tunneling is clearly not realizing a balanced beam splitter.

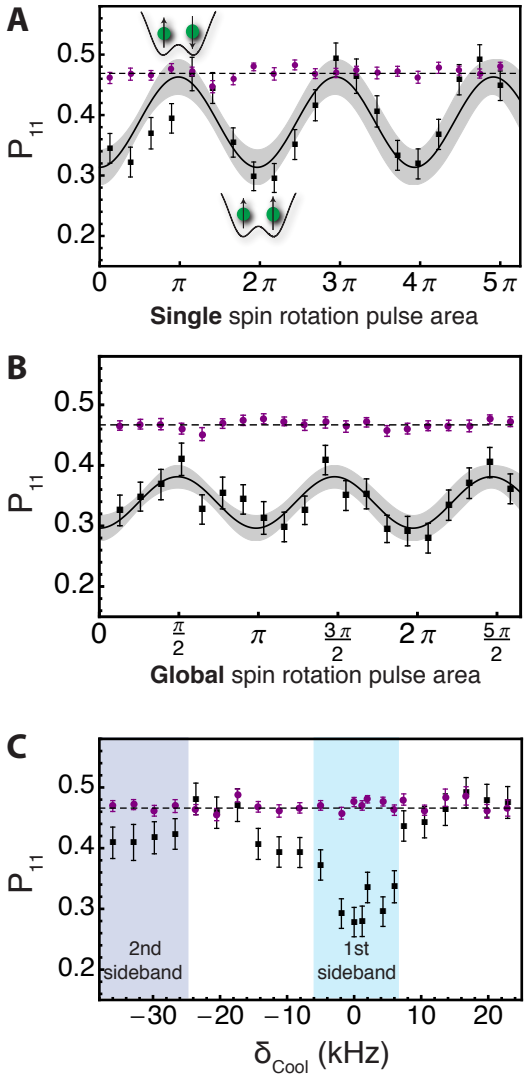

Figure 4.16: The HOM effect observed by varying atom distinguishability. In all plots the black squares are $P_{11}(t_{\mathrm{HOM}})$=P_{HOM}, the purple circles are the expectation for distinguishable particles calculated directly from the single-atom tunneling ($P_{\mathrm{dist}}(t_{\mathrm{HOM}})$), and the dashed black line marks $(1-P_{\mathrm{loss}})^2/2$. (a) Before tunneling we apply a microwave drive that couples $|\uparrow\rangle$ and $|\downarrow\rangle$ for one of the atoms in a two-particle experiment. In the trap where $J/2\pi = 348$ Hz the tunneling time is fixed at $t = 0.99$ ms (second realization of t_{HOM}). (b) Before tunneling we apply a global coherent drive of varied pulse area to couple $|\uparrow\rangle$ and $|\downarrow\rangle$ and then allow for decoherence. In the trap where $J/2\pi = 262$ Hz the tunneling time is fixed at $t = 0.45$ ms. In (a) and (b) the solid line and shaded band are sinusoidal fits and the associated 95% confidence interval. (c) HOM dip dependence on cooling. We vary the detuning (δ_{Cool}) of the cooling beams of motion along the z-axis. In the trap where $J = 262$ Hz the tunneling time is fixed at $t = 0.45$ ms. The two shaded regions correspond to frequency ranges of efficient (1st sideband) and less efficient (2nd sideband) cooling. For all plots, each black data point is the average of ≈ 360 measurements, and each set of measurements corresponding to a purple point is the average of ≈ 240 measurements. All error bars are the standard error in the measurement.

is shown in Figure 4.16a; for comparison we show that P_{dist}, from the single-particle measurements, remains constant (purple circles).[16] We study multiple spin rotations to show that the HOM effect is recovered after a 2π rotation, indicating that the light-shifting procedure is not heating the atoms or introducing distinguishability independent of the microwave pulses. We find the frequency of oscillation of P_{HOM} is 32.6(6) kHz, which is in agreement with the measured microwave Rabi frequency of 32.05(18) kHz. The displayed fit to the data determines $P_{\mathrm{HOM}}^{\mathrm{min}} = 0.314(14)$, and the amplitude of the variation in P_{HOM} is 0.15(2). Taking into account the spin rotation fidelity (for a square pulse) we expect an amplitude of $0.84((1-P_{\mathrm{loss}})^2/2-P_{\mathrm{HOM}}^{\mathrm{min}}) = 0.130(13)$, which is consistent with the measured value.

In the second spin study (Figure 4.16b), we simultaneously couple the $|\uparrow\rangle$ and $|\downarrow\rangle$ spin states of atoms in both wells using a pair of Raman beams. This global rotation avoids any systematic effects that might be introduced by single-site addressing, ensuring the inherently asymmetric process does not itself introduce a history that distinguishes the atoms. During the time (25 ms) between the Raman pulse and the tunneling, the atoms lose their spin coherence, and hence the spin state of each atom is in an incoherent mixture. For common mode magnetic field fluctuations, we would expect the HOM interference to be unaffected since the indistinguishability of the spins would be retained, even though each run of the experiment the phase of their superposition would vary. The primary contributors to their relative decoherence are differential fluctuations and a finite bias of the optical tweezers during the ramps to the tunneling trap. At the largest depth during the ramps (1.1 mK), which persists for 10 ms while the traps are swept together, each tweezer induces a measured ~ 10 kHz shift on the energy splitting of the spin-states. Any fractional depth difference f in the traps causes relative phase winding of the superpositions at $\sim f \cdot 10$ kHz; we apply a 1.3% bias to the 1.1 mK tweezers prior to the sweeps in order to have a tunneling resonance in the final trap, and the tunneling dephasing we observe supports the presence of relative fluctuations of the traps. While we have strong evidence for these effects, it would be ideal to be able to measure

[16] If we perform a microwave π-pulse without the light-shift beam on, thereby flipping both spins, the HOM dip is unaffected.

the relative spin decoherence directly. However, the single particle spin coherence (with spin echo, < 1 ms) is much shorter than the amount of time between when we apply the global-pulse and the two-particle beam splitter; the HOM interference, therefore, is the best tool we have for actually identifying the equality of the superposition phase. Lastly, spontaneous emission from the trap ($\Gamma = 30$ s^{-1} for 1.1 mK) which preserves the spin state due to the large detuning could in principle matter, but for the large detuning at 852 nm the near equality of the scattering amplitudes from the two spin-states suppresses this decoherence mechanism [134].

Ideally, we expect odd multiples of a global $\pi/2$-pulse to yield an equal mixture of all possible two-atom spin states, and hence the likelihood for the atoms to have opposite spin is $1/2$ and the magnitude of the HOM dip should be reduced by $1/2$. The observed dependence on the Raman pulse area is shown in Fig. 4.16b. We find the frequency of oscillation is 65.5 ± 1.2 kHz, which, as expected, is *twice* the measured Raman Rabi frequency of 32.3(3) kHz. The displayed fit to the data determines $P_{\mathrm{HOM}}^{\mathrm{min}} = 0.296(10)$, and the amplitude of the variation in P_{HOM} is 0.085(15). Taking into account the relative spin rotation fidelity of 0.90(3), we expect a half amplitude of $(0.90^2/2)((1 - P_{\mathrm{loss}})^2/2 - P_{\mathrm{HOM}}^{\mathrm{min}}) = 0.069(6)$, which is consistent with the measured amplitude.

4.8.2 Variation of the HOM interference with temperature

Lastly, we study the dependence of P_{HOM} on the motional state of the atoms in Fig. 4.16c by deliberatively compromising our cooling performance. There are 100 Raman-sideband cooling cycles, and within each cycle we alternate between the axial and then radial trap dimensions. For the first 75 cycles, we cool on the first (second) sideband for the radial (axial) direction, while for the last 25 cycles we cool on the first sideband for both dimensions. The first 75 cycles realize a measured axial ground-state fraction of $P_{\mathrm{axial}}^{\mathrm{GS}} \approx 50\%$, the final ground-state fraction depends on the last 25 cycles of first sideband cooling. During this second stage of our cooling we vary the frequency δ_{Cool} of one Raman beam that controls the cooling along the weak axis (z) of both tweezer wells. Based on spectroscopy taken directly after the data in Fig. 4.14b,e, we conclude an axial ground-state fraction of of $P_{\mathrm{axial}}^{\mathrm{GS}} = 85^{+12}_{-10}\%$ when $\delta_{\mathrm{Cool}} = 0$.

The key challenge of this measurement, in contrast to the previous two, is assessing the degree to which distinguishability versus atom beam splitter performance affects our observation of P_{11}. For a separable potential, motional excitation along the axial axis would leave the single-particle tunneling unaffected. For our non-separable tweezer potential, we expect and observe some variation in the tunneling, but near t_{HOM} the single-particle tunneling still results in a relatively constant P_{dist} (purple circles), which is consistent with the distinguishable expectation $(1-P_{\mathrm{loss}})^2/2 = 0.4660(14)$. We have observed, however, that as we approach the carrier (in particular, $\delta_{\mathrm{Cool}} > 12$ kHz), the single-particle tunneling data is increasingly affected likely due to optical pumping heating of the radial axes as well. In particular, we see the tunneling in the right well droop compared to the left well ($P_L^2 \approx 0.3, P_R^2 \approx 0.65$ while $P_L^1 \approx P_R^1 \approx (1 - P_{\mathrm{loss}})/2$), this implies that in these frequency ranges the symmetry of the beam splitter is compromised, though P_{dist} is largely unaffected because $P_{L,R}^1$ are close to 0.5. I would like to stress that the four data points where $\delta_{\mathrm{Cool}} > 12$ kHz are the only data in all three plots in Figure 4.16 where we observe this asymmetric single-particle behavior, and this is not surprising since this is the only time we significantly depart from the regime of optimal cooling. The consistency in symmetry is why I opted to not put all the single particle data on each plot, since P_{dist} was sufficient given the measured symmetry of the tunneling. To this end, Table 4.1 provides a summary of the single particle numbers as evidence of this symmetry for all of the data in this section. In the region of interest about the primary sideband cooling resonance ($\delta_{\mathrm{Cool}} = 0$), we observe a dip to $P_{\mathrm{HOM}}^{\mathrm{min}} = 0.28(2)$, which is a value below the distinguishable expectation. In the frequency range about this resonance (and below the regime in which we observe evidence of heating), the measured P_{11} interpolates between the dip to the expectation for distinguishable particles while the single-particle data remains constant.

Single particle data in distinguishability measurements

Measurement	P_L^1	P_L^2
Single spin flip	0.45(4)	0.49(3)
Global spin flip	0.48(4)	0.47(3)
Axial cooling vary	0.50(3)	0.45(3)

Table 4.1: For the three data plots in Figure 4.16 we tabulate the mean of the single-particle data over the entire datasets to evidence the symmetry of the beam splitter; the error is the standard deviation for these numbers, as opposed to the standard error which is significantly smaller (by a factor ~ 5). For the axial cooling variation data, however, we show the single particle means for the data around the main resonance, $\delta_{\mathrm{Cool}} = \pm 12$ kHz.

Chapter 5

Entangling transportable atoms via local spin-exchange

In this chapter, I will discuss our most recent results exploiting local spin-exchange dynamics to create verifiable non-local entanglement. The spin-exchange we observe is mediated by the contact interaction between two atoms when they are situated in the same optical tweezer. While in the HOM studies it was crucial to prepare the two separated atoms in the same spin-state and motional-state to observe the studied behavior, here we prepare two atoms in the same optical tweezer but in different spin states and different motional states. By deliberately creating these two degrees of freedom and introducing distinguishability,[1] one might expect that the effect of quantum statistics is negated. This, however, is not so: it is in fact the quantum statistics of the atoms that gives rise to the spin-exchange effect we study for the purpose of creating two-particle entanglement.

The past decade has seen significant advances in the field of quantum control of single, a few, and many quantum bits (qubits) formed by ultracold atoms [16, 135, 15, 46, 2, 38, 136], with a focus on single and two-qubit manipulations [79, 45, 66, 76, 137, 138]. Robust two-qubit entanglement with neutral atoms and ions is typically achieved by strong, long-range interactions in the form of Coulomb or Rydberg dipolar interactions [79, 45, 66, 76]. While such an approach allows fast gates, atoms subject to these interactions must combat the associated coupling to the environment and overcome cross-talk among qubits [50, 77, 46, 78]. Local interactions, interactions which require wave-function overlap, offer an alternative that avoids these decoherence and cross-talk effects yet

[1] There are no couplings that would allow for indistinguishability here, in the sense discussed in Section 4.2.7

presents a new challenge: to distribute entanglement in a large system, qubits must be transported amongst each other, merged for interaction, and then isolated for storage and subsequent operations. In this work, we show how via a mobile optical tweezer, it is possible to prepare, entangle, and then separate two neutral atoms whose two-particle coherence is retained. The entanglement operation is achieved via ultracold spin-exchange collisions [139, 16, 140], while the controlled combining and separating is realized by quantum tunneling between transportable optical tweezers. We developed and apply a new protocol for verifying the entanglement generated once the atoms are separated through the application of a magnetic field gradient and parity measurements [79]. Our work provides a framework for dynamically entangling arbitrary qubits via local operations for large scale quantum operations.

5.1 Theory of spin-exchange for neutrals atoms interacting via a contact potential

Spin exchange is a vital resource for realizing controlled entanglement [13, 139, 16, 140] (Figure 5.1), and its underlying mechanism relies on the quantum statistics of identical particles. When two spin-1/2 particles interact, their interaction energy depends on the spatial symmetry of the two-particle wave function, which in turn depends on the symmetry of the two-particle spin state. For positive contact interactions, two bosons (fermions) of opposite spin in a triplet configuration experience enhanced (vanishing) contact interactions, while the converse occurs for the singlet spin state. This implies that by preparing a superposition of triplet and singlet configurations, a dynamical effect results known as spin exchange, which entangles the spatial and spin degrees of freedom of the two particles. We will discuss the origin of these dynamics in more detail in this section.

5.1.1 Basics of spin-exchange

The state from which spin-exchange occurs in our experiment is illustrated in Figure 5.2. For the purpose of the discussion in this section, we will neglect the effect of non-separability of the atomic potential, and later discuss the effect of this feature of our system. Through a sequence

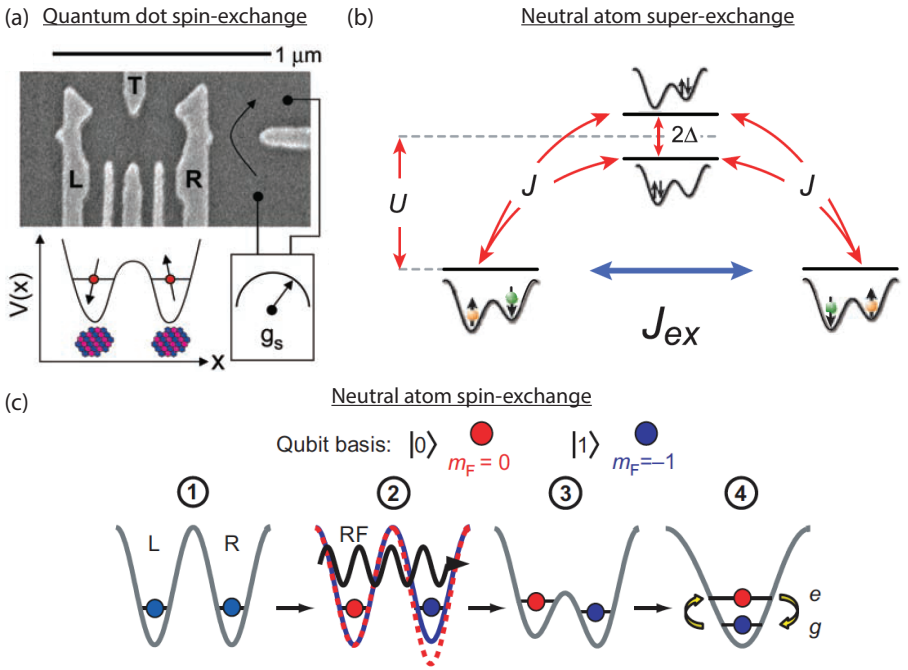

Figure 5.1: Forms of spin-exchange. (a) Picture from Ref. [13]. Electrons trapped in double quantum-dots exhibit a tunable spin-spin coupling. The spin-1/2 electrons exhibit a strong-Coulomb repulsion that, in conjunction with their fermionic statistics, creates an exchange interaction. This platform has been considered theoretically as a strong candidate for a universal quantum computer [14]. (b) Picture from Ref. [15]. Neutral atoms trapped in an optical lattice can exhibit a nearest-neighbor exchange interaction that is contingent on virtual wave-function overlap. Here strong on-site interactions lead to a second-order effect where anti-aligned spins on neighboring sites can coherently swap sites, which can be formally cast as a Heisenberg exchange interaction. Here too the underlying physics is dependent on strong interactions and the quantum statistics of the particles. (c) Picture from Ref. [16]. When two neutral atoms are prepared in opposing spin-states and in different motional states, the interactions realize a first-order exchange interaction. The spatial symmetry of the two-particle wave functions depends on the spin-states, which in turn causes a splitting between the triplet and singlet two-particle spin states. This splitting causes dynamics at a multiple of the contact interaction energy. This chapter is concerned with this kind of exchange interaction.

of steps involving single spin addressing and vertical tunneling (see Section 5.2.1), we prepare a spin-up particle in the first excited state of the y-direction ("e"), and a spin-down particle in the y-direction ground-state ("g). Each particle we take to be in the ground-state of the motional degrees of freedom not otherwise specified, and we will omit these from the notation below. We can write this symmetrized two-particle state in second quantization as,

$$|\psi_{\text{in}}\rangle = |e,\uparrow\rangle|g,\downarrow\rangle. \tag{5.1}$$

This notation is useful for writing down a simple Hamiltonian to model the dynamics, however, it is less useful in explaining the origin of the spin-exchange interaction. We use first quantization to elucidate the spin-exchange: we will use the general symmetrized two-particle states for a particular degree of freedom,

$$|\pm\rangle_j = \frac{1}{\sqrt{2}}\left(|\chi\rangle_1|\bar{\chi}\rangle_2 \pm |\chi\rangle_2|\bar{\chi}\rangle_1\right), \tag{5.2}$$

where $\{\chi,\bar{\chi}\} = \{e,g\}$ ($\{\chi,\bar{\chi}\} = \{\uparrow,\downarrow\}$) if $j =$ "y" ($j =$ "s"). In this notation, $|+\rangle_s$ and $|-\rangle_s$ are the triplet and singlet spin states, respectively; these are labeled $|T\rangle$ and $|S\rangle$ in Figure 5.2b. We write the states in this general (and slightly less transparent) fashion because in later sections we will include the effect of an axial degree of freedom induced by finite temperature, which necessitates using $j =$ "z". We can write $|\psi_i\rangle$ in terms of $|\pm\rangle_y$ and $|\pm\rangle_s$,

$$|\psi_{\text{in}}\rangle = \frac{1}{\sqrt{2}}\left(|+\rangle_y|+\rangle_s + |-\rangle_y|-\rangle_s\right), \tag{5.3}$$

which is a superposition of the two possible bosonic states given the number of degrees of freedom per particle. To show the connection to the initial state in Eq. 5.1, we can expand Eq. 5.3 in terms of the expressions in Eq. 5.2: after simplifying one finds,

$$|\psi_{\text{in}}\rangle = \frac{1}{\sqrt{2}}\left(|e\rangle_1|\uparrow\rangle_1|g\rangle_2|\downarrow\rangle_2 + |g\rangle_1|\downarrow\rangle_1|e\rangle_2|\uparrow\rangle_2\right), \tag{5.4}$$

which, as expected, is the symmetrized two-particle state of having a spin-up particle in $|e\rangle$, and a spin-down particle in $|g\rangle$.[2] This state is a symmetrized state that exhibits no particle-entanglement, in reference to the discussions in Section 4.2.3. The effect of the contact interactions, however, is to dynamically induce particle entanglement through spin-exchange.

5.1.2 Interaction energy for the triplet and singlet channels

For atoms colliding via contact interactions, the spatial symmetry of the wave-function is crucial in determining the interaction energy. In what follows, we will consider interaction energies

[2] If in Eq. 5.3 we had taken the difference as opposed to the sum of the two-particle states, this would correspond to the symmetrized two-particle state of having a particle spin-down in the first y-excited state, and a particle spin-up in the ground-state

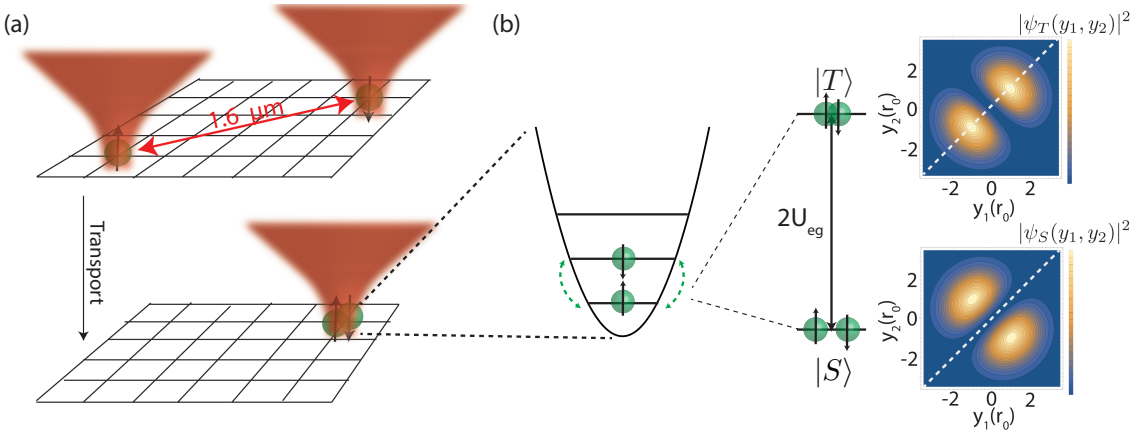

Figure 5.2: Initial two-particle state from which exchange occurs. (a) Through a sequence of ground-state cooling, single-spin addressing, tweezer transport, and biased tunneling we are able to prepare a single spin in the first motional excited state of the y-axis of motion, and spin-down particle in the 3D-ground state, all in the same optical tweezer. (b) In this configuration we expect spin-exchange dynamics between the atoms occupying different motional states. Enforced by the quantum-statistics, this arises due to the difference in the contact interaction energy for the spatially symmetric ($\psi_T(y_1, y_2)$) and anti-symmetric ($\psi_S(y_1, y_2)$) wave functions associated with the states $|+\rangle_y$ and $|-\rangle_y$, respectively. The anti-symmetric wave-function $\psi_S(y_1, y_2)$ is non-interacting since the particles (defined to be at y_1 and y_2 along one-dimension, in units of the oscillator length r_0) are never found in the same place (red-dashed line in bottom wave-function plot, which corresponds to the spatial wave-function for the spin singlet).

much smaller than any motional energy scale. Hence, we can consider the contact interaction as simply a first-order pertubative energy shift of the two-particle eigenstates represented in the basis of the single-particle eigenstates. In general, for atoms in the two-particle spatial wave function $\psi(\mathbf{r_1}, \mathbf{r_2}) = \langle \mathbf{r_1}, \mathbf{r_2}|\psi\rangle$, the contact interaction energy is,

$$U = \frac{4\pi\hbar^2 a_s}{m} \int_{-\infty}^{\infty} \psi(\mathbf{r_1}, \mathbf{r_2})^* \delta(\mathbf{r_1} - \mathbf{r_2}) \psi(\mathbf{r_1}, \mathbf{r_2}) d^3r_1 d^3r_2, \tag{5.5}$$

where a_s is the atomic scattering length and m is the mass of ^{87}Rb. We now seek to calculate the interaction energies $U_\pm$ for the two spatial states $|\pm\rangle_y$ comprising $|\psi_{\text{in}}\rangle$; to emphasize the link to the spin-states, the one-dimensional wave functions in Figure 5.2 associated with $|+\rangle_y$ and $|-\rangle_y$ are called $\psi_T(y_1, y_2)$ and $\psi_S(y_1, y_2)$, respectively. For representing the three-dimensional wave-functions, we use the notation that $\psi_e(\mathbf{r})$ ($\psi_g(\mathbf{r})$) corresponds to the three-dimensional motional state of $\{n_x, n_y, n_z\} = \{0, 1, 0\}$ ($\{n_x, n_y, n_z\} = \{0, 0, 0\}$) where n_i are the motional quantum num-

bers for the i-axis. First solving for U_+, we have,

$$U_+ = 2U_{eg}, \tag{5.6}$$

where,

$$U_{eg} = \frac{4\pi\hbar^2 a_s}{m} \int |\psi_e(\mathbf{r})|^2 |\psi_g(\mathbf{r})|^2 d^3\mathbf{r}. \tag{5.7}$$

For a simple harmonic oscillator with trap frequencies $\{\omega_x, \omega_y, \omega_z\}$, the interaction energy scales like $(\omega_x\omega_y\omega_z)^{1/2}$ indicating the role of the confinement in determining the size of the interactions; this is relevant to later measurements in which we study this exact scaling. Furthermore, I would like to highlight this factor of 2 in U_+, which arises from the symmetrization of the two-particle wave function. If both particles were in the same motional state, the interaction energy would be $U = U_{gg}$ without this factor of 2.[3] . If we now consider $|-\rangle_y$, it is clear that the anti-symmetrization causes the two-particle wavefunction to vanish when $\mathbf{r_1} = \mathbf{r_2}$, and therefore,

$$U_- = 0. \tag{5.8}$$

These distinctions between the wave functions are summarized in Figure 5.2. We will now use these results to explain the exchange dynamics expected experimentally from the state $|\psi_{\text{in}}\rangle$.

5.1.3 Spin exchange dynamics

From the above discussion, we can understand the exchange dynamics as arising from the coherent beating of the two-components with interactions energies U_+ and U_-. For $|\psi(0)\rangle = |\psi_{\text{in}}\rangle$, the time-evolved wave-function $|\psi(t)\rangle$ can be expressed,

$$|\psi(t)\rangle = \frac{1}{\sqrt{2}} \left(e^{iU_+ t/\hbar} |+\rangle_y |+\rangle_s + e^{iU_- t/\hbar} |-\rangle_y |-\rangle_s \right). \tag{5.9}$$

Since $U_- = 0$, we expect coherent dynamics at the frequency $U_+ = 2U_{eg}$. After expanding the above equation, we can express the dynamics compactly in second-quantization as,

$$|\psi(t)\rangle = |e,\uparrow\rangle|g,\downarrow\rangle \cos(\frac{1}{2} J_{ex} t/\hbar) + i|e,\downarrow\rangle|g,\uparrow\rangle \sin(\frac{1}{2} J_{ex} t/\hbar), \tag{5.10}$$

[3] U_{gg} is computed by substituting $\psi_g(\mathbf{r})$ for $\psi_e(\mathbf{r})$ in Eq. 5.7

where we have defined the quantity $J_{\rm ex} = U_+$. The exchange dynamics, therefore, yield anti-correlated oscillations in the probabilities to measure $|e,\uparrow\rangle|g,\downarrow\rangle$ and $|e,\downarrow\rangle|g,\uparrow\rangle$, at a frequency $J_{\rm ex}$. These are the dynamics expected for the effective Hamiltonian,

$$H_{\rm eff} = J_{ex}\vec{S}_e \cdot \vec{S}_g, \tag{5.11}$$

where $\vec{S}_g$ ($\vec{S}_e$) are the spin-operators for the atom in $|g\rangle$ ($|e\rangle$), and I have neglected a constant term. This Hamiltonian more explicitly displays the spin-exchange interaction achieved by the contact interactions and quantum statistics. Crucially, these dynamics periodically create the maximally entangled state,

$$|\psi(t_{\rm ent})\rangle = \frac{1}{\sqrt{2}}\left(|e,\uparrow\rangle|g,\downarrow\rangle \pm i|e,\downarrow\rangle|g,\uparrow\rangle\right), \tag{5.12}$$

where $t_{\rm ent} = \frac{N_{\rm odd}\pi}{2J_{ex}}$ and $N_{\rm odd}$ is an odd integer. In what follows, we will discuss our observation of the dynamics encapsulated in Eq. 5.10, and the creation of entanglement between spatially separated particles via the local entangling collisions.

5.2 Observation of spin-exchange dynamics

Starting from two thermal atoms, our goal is to prepare the two-particle state $|\psi_{\rm in}\rangle$. As with the HOM studies, the experiment begins by loading, imaging, and detecting two thermal atoms in separated optical tweezer potentials, each of optical waist 710 nm and of 1.6 μm centroid separation. Each atom is then separately laser cooled to the 3D ground-state via Raman-sideband cooling leaving a 3D ground state fraction of 90(8)% [50, 89, 99], using either the continuous (see Section 3.4.6) or Gaussian-pulsed cooling (see Section 3.4.7). We subsequently prepare the desired two-particle spin state using an additional beam to change the local effective magnetic field at one tweezer with respect to the other, allowing resonant spin flipping of an atom in just one optical tweezer (see Section 2.12.2). At this point, the two atoms are each prepared in the motional ground-state of their respective optical tweezer, and the right (left) spin is in the $|F,m_F\rangle = |1,1\rangle \equiv |\downarrow\rangle$ ($|F,m_F\rangle = |2,2\rangle \equiv |\uparrow\rangle$) state. After these initial steps, the traps are reconfigured to use coherent

tunneling to prepare the spins in well-defined motional states of a single tweezer for spin-exchange, namely in the configuration given by $|\psi_{\text{in}}\rangle$.

5.2.1 Generating and detecting two-particle spin-configurations in a single tweezer

To generate $|\psi_{\text{in}}\rangle$, one optical tweezer is swept close to the other to realize a tunnel-coupling, with similar ramps to those of the HOM studies. However, there are a number of distinctions in the rest of the experiment. We tune the bias to an assymetric configuration such that the the ground-state of the left optical tweezer is near resonant with the first radial excited of the right optical tweezer (Figure 5.3), while we set the spacing and depth to 854 nm and 91(4) kHz, respectively. These double-well parameters were chosen for several reasons. Firstly, for this spacing and depth, the left-well ground-state and right-well excited state along the tunneling direction (y) were ~ 3 kHz below the peak of the biased double-well bump, which was similar to the ground-states in the 96 kHz deep and 808 nm spaced symmetric double-well from the previous chapter. This ensured that we were not near an unstable regime such that the atoms are unbound, which, for example, we observe at the edge of the scans of depth and spacing from Section 4.5.2.4. Secondly, we wanted to maximize J to maintain robustness against the fluctuations discussed in Section 4.5.2.4, while (thirdly) maintaining a large depth to keep the interactions large. In this configuration (including the effect of the bias), we expect an interaction energy of approximately $U_{\text{eg}} = 2\pi \cdot 60$ Hz for two atoms in the right optical tweezer, and consequently spin-exchange oscillations at a frequency of 120 Hz.

In the described double-well configuration, we regularly perform calibration measurements to ascertain the position of the tunneling resonance between the left-well ground state and right-well first excited-state (along the tunneling direction, y). Exemplary bias scans are shown in Figure 5.4a,b, where the asymmetric nature of the tunneling resonance is manifest. The initial left-well data (blue, P_i^1) shows a clear resonance feature in each plot, indicating that an initially left-well atom tunnels to the right well while an initial right well atom (red) stays put as a function of bias; this is significantly different from the symmetric tunneling seen in the dynamical HOM

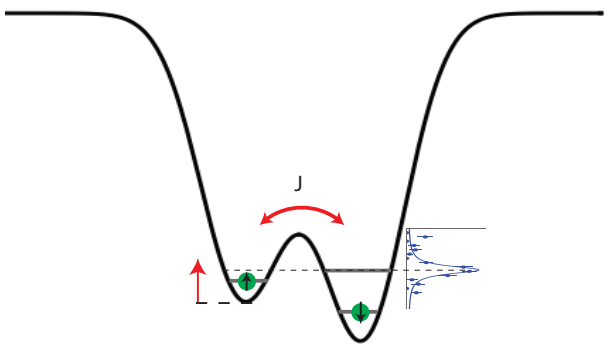

Figure 5.3: Adiabatic passage through the ground-excited tunneling resonance. In order to consistently prepare the configuration for exchange, $|\psi_{\text{in}}\rangle$, we use adiabatic passage. The ground-state of the left well is adiabatically swept across the tunneling resonance with the excited state, shown in the figure with actual data from a typical bias scan. This procedure relaxes constraints on the absolute bias stability. Experimentally, the ARP occurs in a trap spacing of 854 nm and 91(4) kHz, with a ramp range of 4.4 kHz in a time of 12 ms symmetrically about the position of the resonance (which is calibrated daily).

interference. The tunneling time of 1.6 ms is set to near a full spatial swap for the measured $J/(2\pi) = 165(6)$ Hz. As an additional confirmation, we observe that P_{11} nearly perfectly parallels the behavior of the P_L^1, because for the two particle experiments we are primarily preparing two atoms in the same tweezer when on the tunneling-resonance. We do observe a slight shift between the resonance positions of the dips in Figure 5.4a, which could be due to the interactions shifting the resonance for two-particle tunneling. While in many scans we observe such a shift, the resolution is not sufficiently high to perform a comparison with the expected shift, though the measurement is the correct order of magnitude (in experimental units, .002 V, corresponding to a 50 Hz shift).

Frequent recalibration of the position of the bias resonance was not sufficient for consistently transferring the population from the left-ground state into the first excited state of the right well. Small shifts in the resonance position on an hourly time-scale caused inconsistent transfer between the tweezers that varied over the course of data sets, and sometimes drifted completely off resonance. Borrowing a common technique from microwave and RF spectroscopy, we instead perform an adiabatic rapid passage (ARP), by slowly ramping the bias through the ground-excited tunneling resonance. Here the tunnel-coupling plays the role of the Rabi frequency (over two). As the bias is slowly swept through the resonance, the tunneling atom remains in the instantaneous tunnel-

dressed state, which is adiabatically converted from the left-ground state to the right excited state. Crucially, the adiabatic transfer is much less sensitive to the exact position of the resonance provided the end points of the bias ramp are each sufficiently far away from resonance, and the ramp itself is sufficiently slow so as to avoid Landau-Zener transitions.

Though in later sections we model the effect of this process on the spin-exchange, here I will only discuss the experimental calibration of this technique. Each day, we measure the position of the bias resonance, and then fix the ramp end points at $\pm 0.1V$ about the resonance position, which corresponds to ± 2.2 kHz. To calibrate the adiabatic passage, we plot the transfer probabilities as a function of the ramp time when ramping the bias from below to above the resonance (Figure 5.4c,d). This ramp time sets the adiabaticity of the ramp. As with the bias scans, we observe the same asymmetry in the single-particle experiments and the correspondence between P_i^1 and P_{11}. Using the Landua-Zener formula, we fit the data (solid lines) and extract a $J/2\pi = 220(10)$ Hz. There is approximately 30% disagreement between the measured value 165 Hz, but this formula is likely not accounting for a number of effects. For the fastest ramp rates (ARP times < 2 ms), we could be causing motional heating and thermally delocalizing an atom initially on the left, which is more loosely bound compared to the atom in the ground state of the right-well. Secondly, as we scan the bias through the resonance, there is a variation in the tunneling because the left-bound state becomes closer to the double-well bump. Though we have not explicitly modeled these effects, we choose an ARP time of 12 ms, which is adiabatic with respect to all the motional time scales[4] and well into the regime where the transfer probability saturates. Interestingly, the fact that the transfer probability does not reach unity suggests that the timescale of the fluctuations that effect the tunneling is likely fast and occurring within an experimental cycle, as opposed to shot-to-shot.

After performing the ARP, we have prepared the atoms in the target state $|\psi_{\text{in}}\rangle$ in which we expect spin-exchange dynamics. Observing the spin-exchange dynamics entails a measurement of the spin-state of the atoms in each motional state, which cannot be imaged directly using

[4] Necessarily so, since the tunneling is much slower than any of the trap frequencies, the lowest of which is the ~ 2 kHz axial trap frequency

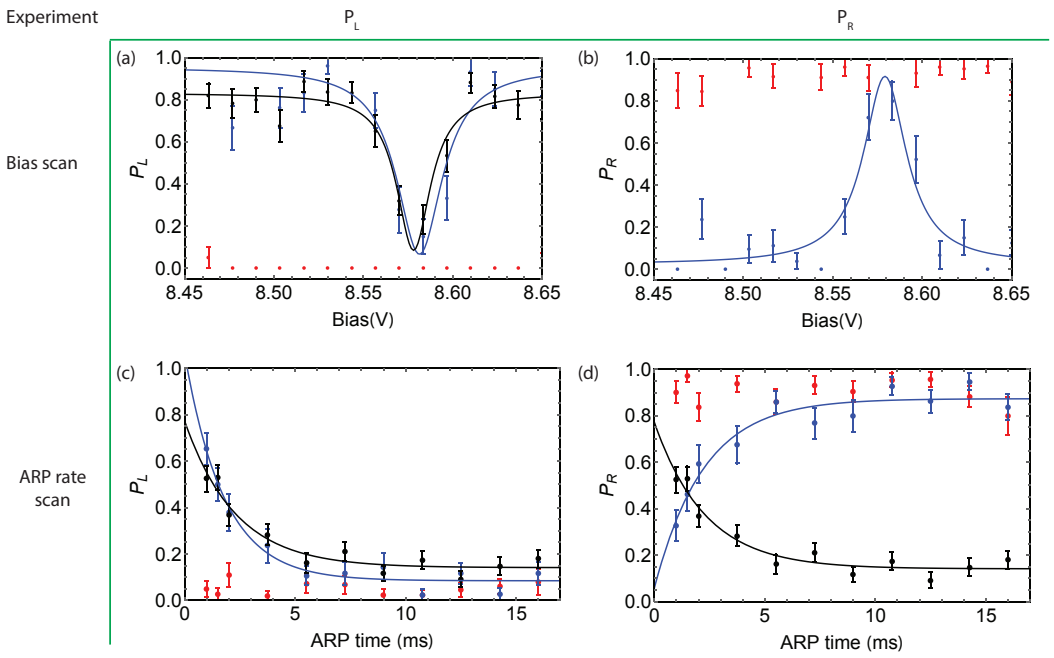

Figure 5.4: Experimental data of bias scans and ARPs across the excited-ground tunneling resonance. For all plots, blue (red) corresponds to data in which the atomic origin well is the left (right) well; the black data is P_{11}, which is slightly inconsistent with the y-axis labels. (a,b) For a fixed tunneling time of 1.6 ms, we scan the bias across the ground-excited tunneling resonance, which is 9.0(1.5) kHz from the ground-ground resonance. To emphasize the asymmetry of the resonance, we plot both P_L^i (a) and P_R^i (b), indicating the presence (absence) of population transfer from the left-well (right-well). The statistics for these data is fairly low (25 single particle runs per well), and causes some scatter. (c,d) We show show ARP data using the parameters indicated in Figure 5.3. Here we also plot both P_L^i (c) and P_R^i (d), showing the same asymmetry in the tunneling. These data are used to extract the ARP fidelities quoted in the text. In the ARP data, we observe a small amount of transfer from the right well to the left well, which we observe increases when we deliberately compromise our radial cooling. This is consistent with an increase in excited fraction in the right well tunneling to the left well. For optimal cooling, this on average is about 3%, which is consistent with the ground-state temperature extract from spectroscopy.

fluorescence imaging. While we have considered alternative approaches,[5] we simply perform the adiabatic passage in reverse, mapping the atom in the first-excited state of the right well back into the left-ground state. After this second ARP, we apply resonant push-out light to detect the spin-states of the atom in each tweezer. The time between the end of the first ARP and the beginning of the second ARP we define as the "exchange time".

[5] In principle, we could use sideband-spectroscopy to probe the spin population in each motional state, but this would require ramping the traps up to reach the LDR and consequently a large speed up of the exchange dynamics.

Before moving on to the exchange dynamics, I wanted to briefly discuss an important check on these tunneling techniques. The resonance we observe occurs at a bias of 9.0(1.5) kHz, according to the calibration technique discussed in Section 4.5.2.1. However, this calibration technique is not tested for biases far away from the main tunneling resonance used for the calibration, and so it is not clear how reliable this 9.0 kHz number is. Based on the three-dimensional modeling of the potential, we expect a 8 kHz bias for the excited-ground tunneling resonance, which is set by the y-axis trap frequency as well as the relative change in this quantity in each tweezer as the bias is varied.[6] To confirm that we are indeed creating a radial excitation in the right well for an atom tunneling from the left, we perform sideband-spectroscopy as in Section 4.5.2.3 after tunneling.

We perform two sets of experiments in this regard. In the first (first row of Figure 5.5), we perform spectroscopy after allowing for resonant ground-excited tunneling as in Figure 5.4a,b. From these data, it is clear that when an atom that originates on the left is probed on the right, a large red-sideband is evident, indicating that the atom is not in the radial ground-state. Since the spectroscopy is performed after the traps are swept apart, we cannot determine from these data whether the radial excitation is added specifically to the axis along which tunneling occurs, but the alternative possibility (tunneling coupling to the x-direction) is greatly suppressed due to energy conservation and symmetry. We also observe that an atom on the right is spectroscopically indicated to be in the ground-state, as expected. In the second set of spectroscopy measurements (second row of Figure 5.5), we perform spectroscopy after applying the ARP procedure in both directions with 15 ms time between. Here we observe that an initial left atom is in the ground-state provided it ends up in the left well, while as in the prior measurement an initial right-well atom is in the ground-state. The combination of these two measurements (both rows) is strong evidence that the tunneling is mapping the initial left well particle into the first excited of the right well, and mapping it back to the ground-state of the left well for detection.

[6] This latter effect means that the bias applied is not strictly equal to the trap-frequency in order to hit this resonance, since the trap frequency in each well changes as a function of bias. As the left-well is made shallower and the right-well is made deeper, the bound-state in the left (right) well moves down (up) in energy implying that the resonant bias is larger than the oscillator splitting when the trap is symmetric (unbiased).

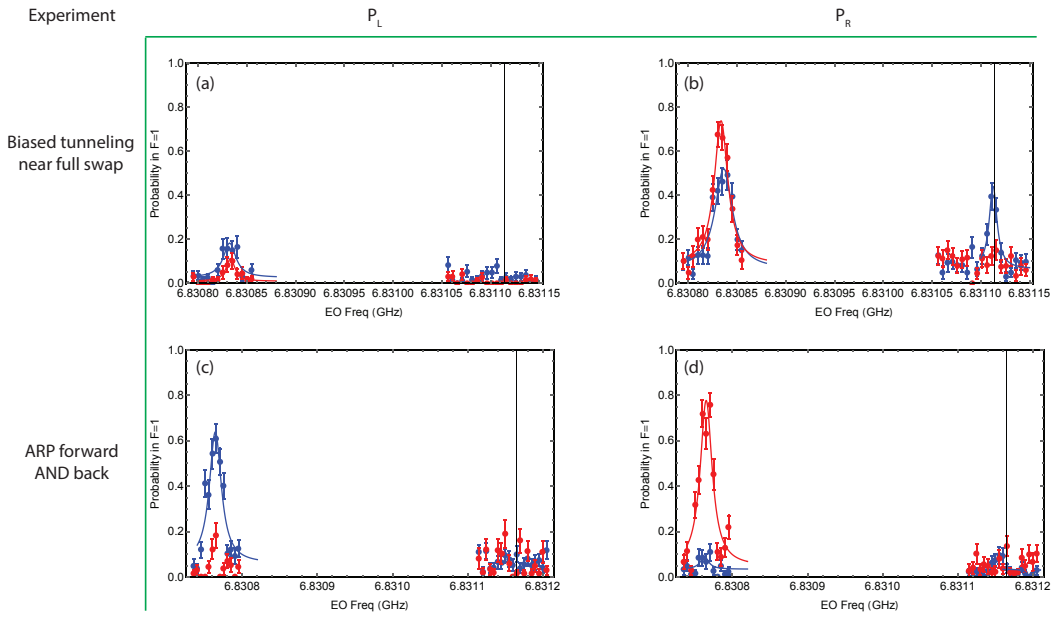

Figure 5.5: Sideband spectroscopy after ground-excited tunneling. (a,b) We perform sideband spectroscopy after allowing for 1.6 ms of tunneling, correspond to a near full transfer of the left-well ground-state population to the right tweezer excited-state. We apply push-out light after applying radial Raman beams (top plus EO). As with the analogous data from the previous chapter, the y-axis should be interpreted as the product of the spin-flip probability and the transfer probability (P_L in (a) and P_R in (b)) to the indicated well.(c,d) We apply sideband-spectroscopy after performing the ARPs in both directions with a 15 ms delay in between. As expected, the left-well population (blue) that ends up back in the left-well implies a large ground-state fraction. The fraction ($\sim 10\%$) with which right-to-left tunneling occurs is anomalously higher than indicated in other data we have, which suggests that perhaps for this data the radial cooling was worse. Note for these data we do not spin-flip the right atom or rotate the quantization axis to along z, but the light-shift beam does come on in order to retain as much of the experiment as possible in performing the thermometry.

5.2.2 Spin-exchange oscillations

The previous sections have discussed in detail the preparation and detection procedure for spin-exchange, and the entire sequence we summarize in Figure 5.6. After applying this procedure, we seek to detect the spin configurations indicated in Figure 5.6f. To do so, we apply the same push-out used in all of our spin-sensitive spectroscopy, however, we ramp to a 60 μK trap to maximize the sensitivity of the atoms to the resonant push-out.[7] This leads to the detection outcomes indicated in Figure 5.7a. We can analyze these two-particle data in two ways: we can keep all the

[7] For the Gaussian cooled spectrum of Section 3.4.7, this procedure was also applied

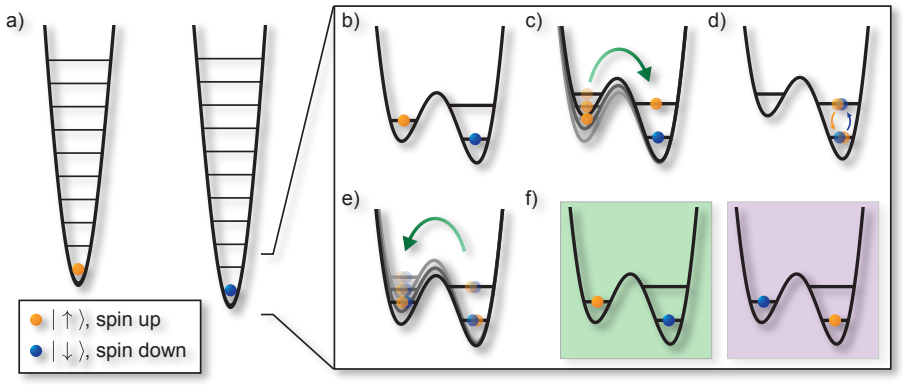

Figure 5.6: Experimental protocol for spin-exchange dynamics. We perform the illustrated sequence in order to observe spin-exchange dynamics. Panel (d) is where exchange occurs, and we vary the time in this configuration by varying the time between the end of the first ARP and the beginning of the second ARP.

experimental runs, or we can throw out those runs in which the second image indicates a failure of our spin preparation. The latter is discriminated on the basis of whether the second image shows a single atom, since if there are no atoms or an atom in each well, we can be certain that the spin-preparation failed and/or there was atom loss. This allows us to negate the effect of imperfect spin-preparation (discussed in detail below), which is $80-90\%$ depending on the experiment, at a small expense to the statistics. Lastly, an important experimental discovery that bears on this post-selection was that if one of the ARPs fails, leaving two atoms in the right tweezer, the push-out technique does not cause both atoms to leave due to light-assisted collisions. We tested this by performing the ARP in one direction and performing push-out: only the spin-up atom was kicked out, leaving one atom for imaging. Therefore, the post-selection technique does not allow us to post-select on the ARP success as well.

In Figure 5.7b, we show an exemplary scan of the time between the ARPs and the resulting oscillations in the final measurement probabilities. We only observe these oscillations in the measured probabilities in the two-atom experiments (see Figure 5.8), indicating the two-particle nature of the oscillations. The fitted contrast of the oscillations is 0.29(2) using the post-selection procedure; if we do not post-select on the spin-preparation the contrasts are $A_{\uparrow,\downarrow} = 0.24(2)$ (green) and $A_{\downarrow,\uparrow} = 0.23(2)$ (purple). These contrasts are informed by a number of systematics we analyze

below, but the equality of $A_{\uparrow,\downarrow}$ and $A_{\downarrow,\uparrow}$ affirms the anti-correlated nature of the oscillations and that the spin-interaction preserves the two-particle S_z, as expected for an exchange interaction. The exchange frequency observed of 106(1) Hz implies an interaction of $U_{eg}/(2\pi) = 53.0(5)$ Hz. As a first order check on this interaction energy, we can Fourier transform the double-well along the y-direction to determine the trap-frequency along the y-axis[8] ; for ω_x and ω_z, we can scale from the measured trap-frequencies in the 23 MHz deep trap ($\omega_r/(2\pi) = 140$ kHz, $\omega_z/(2\pi) = 29$ kHz) to the tweezer in which the atoms interact. The depth of the tweezer holding the atoms is informed by the double-well bias, which is 2.2 kHz above the ground-excited resonance at $\Delta = 9$ kHz, leading to a depth for this tweezer of 97(4) kHz during the exchange time. We find then that $\{\omega_x, \omega_y, \omega_y\} = (2\pi)^{-1}\{9.0, 5.4, 1.9\}$ kHz; approximating the atomic wave-functions as eigenstates of harmonic oscillators with these frequencies along each axis, we find from Eq. 5.7 that $U_{\mathrm{eg}} = 59(2)$. This is decent agreement using a simple model for the potential.

In Figure 5.7c, we compare the measured exchange frequency to the full 3D calculation (again, including the bias and calibrated features of the potential) as a function of the tweezer depth. In this figure, though we vary the tweezer depth, we apply the ARPs always in the same 91(4) kHz deep trap. After the first ARP we ramp the intensity in the optical tweezers adiabatically in 5 ms to a new depth (x-axis in Figure 5.7c), wait for a varied time Δt, ramp the trap symmetrically in reverse, and perform the detection ARP. Though the depth ramps add a phase shift to the oscillations, the frequency of the exchange dynamics is purely determined by the trap in which we vary Δt. The consistency between the oscillation frequency and our calculation of the depth dependent interactions is strong evidence that we are preparing the intended two-particle state, and that the dynamics are governed by the symmetry-mediated exchange interaction.

[8] This is accomplished by finding the splitting of the lowest eigenstates (which are bound below the bump) of the unbiased symmetric double-well for the 854 nm spacing

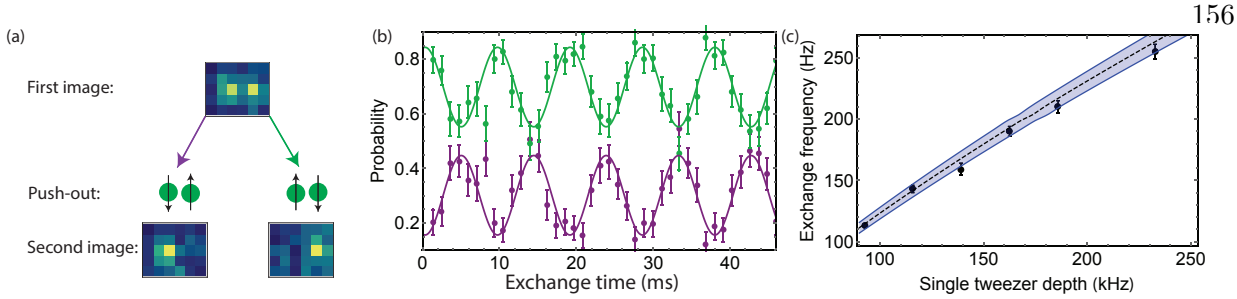

Figure 5.7: Observation of spin-exchange dynamics. (a) After applying the protocol of Figure 5.6, we analyze the data according to the rubric indicated, keeping only those two-atom experiments in which we end up with a single atom after the resonant push-out (this is the post-selection routine discussed in the text). The location of the atom in the second image indicates the final spin-configuration prior to the push-out. (b) According to the coloring in (a), we plot the probabilities to measure each of the associated outcomes. We observe anti-correlated oscillations of equal amplitude, at a frequency consistent with twice the onsite interactions U_{eg}. (c) We observe the variation of the exchange frequency with the tweezer depth: as expected, the interaction energy increases with the two-particle density. The center dashed line corresponds to a no-free-parameter theory line from 3D calculations of the potential by Michael Wall and the experimental characterizations of the double-well parameters. The blue swath comes from our uncertainty in the bias, because this influences the depth of the tweezer in which exchange occurs, as well as the tweezer depth.

5.2.3 Analysis of the exchange contrast

As alluded to above, a number of factors inform the observed spin-exchange oscillation contrast. First, to understand the difference in the post-selected and non-post-selected data, we show in Figure 5.8 the single-particle data from the exchange oscillations in Figure 5.7b. As noted, these do not exhibit any spin-oscillations, and also provide a calibration of the spin preparation. Including the effect of single-particle loss, the two-particle preparation of the atoms in the state $|\uparrow\rangle_L|\downarrow\rangle_R$ prior to the ARPs (the atom in the left well spin-up, and the atom in the right-well spin down) is 0.835(10). When the spin-preparation fails, the most likely outcome is that both atoms are spin-up or both spin-down[9] , both of which are configurations we have experimentally verified lead to no spin-dynamics. Therefore, from the post-selected contrast of 0.29(2) and the calibrated spin-preparation of 0.835(10), we expect from the un-post-selected data an oscillation contrast of $0.29 \cdot 0.835 = 0.24(2)$, which is consistent with the measurement. [10]

[9] The likelihood to improperly spin flip both atoms is $\sim .01$.

[10] The post-selection also eliminates the case in which we successfully prepare the spins, but lose the spin-down atom due to background collisions. But this is also accounted for in the single-particle data.

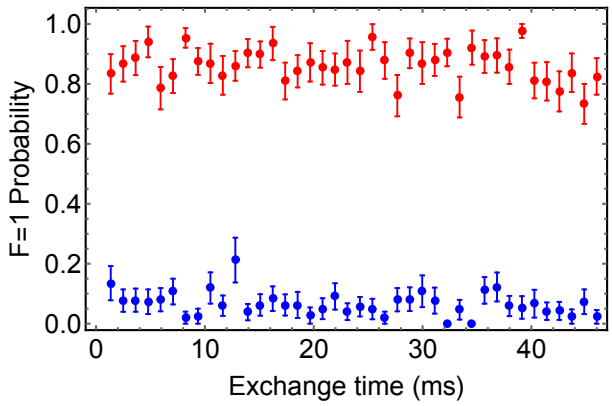

Figure 5.8: Single particle data from exchange dynamics. We show the single particle data from data displayed in Figure 5.7b. We do not observe the same oscillations in the spin probabilities for either the left (blue) or right (left) origin well: the left well is primarily spin-up, while the right well is primarily spin-down (in F=1). We use these data to calibrate the spin-preparation for the two-particle experiments.

Another straightforward systematic is the fidelity of the ARPs. If we fail to either produce the initial desired state in the first ARP, or to detect the final state in the final ARP, then we will not detect spin-exchange. According to the single-particle (two-particle) first ARP data in Figure 5.4, we expect a total ARP preparation and detection success probability of 0.82(6) (0.79(5)); furthermore, directly prior to the measurement in Figure 5.7b, we performed the ARP forward and backward with a 15 ms delay between, and measured a success probability of 0.81(4). We note however that the ARP success probability did fluctuate by about 10% over the course of two months for unknown reasons: we always measure the forward and back efficiency for this reason and use this measurement for calibration purposes.

The above systematics suggest an expected contrast of 0.68(4). Clearly these alone do not explain the contrast we observe, and I will now discuss in more detail the effects of temperature and spin-dependence in the potential.

5.2.3.1 Effect of finite temperature on exchange dynamics

In analogy to the HOM section, the motional state of the particles can influence how the quantum-statistics of the particles is manifest. For the spin-exchange experiments we have per-

formed, we have tried both the continuous cooling and Gaussian pulsed cooling methods, and observed spin-exchange contrasts that are fractionally similar at the 10% level, implying that the single-particle ground-state fractions were similar at the 5% level. This suggests that the two cooling methods achieve similar final ground-state fractions, and the Gaussian spectroscopy merely provides a more precise measurement of this temperature. Therefore, we use the Gaussian spectroscopy data from Figure 3.15 for thermometry.[11]

We will consider here the most likely scenario of one of the atoms having a single axial excitation. The treatment below, however, is general to the case of a radial excitation, but in practice this situation is less likely and filtered by the tunneling, because the tunneling is influenced more directly by this temperature. We consider the scenario in which the initial state of the two particle system is (in second quantization),

$$|\psi_{\rm in}^{\rm exc}\rangle = |e, e, \uparrow\rangle|g, g, \downarrow\rangle, \tag{5.13}$$

where the second entry of the kets indicates the axial motional state, ground ("g") or excited ("e").[12] . In first quantization, we can write out this state using the notation of Eq. 5.2,

$$|\psi_{\rm in}^{\rm exc}\rangle = \frac{1}{2}\left(|+\rangle_y|+\rangle_z|+\rangle_s + |-\rangle_y|-\rangle_z|+\rangle_s + |-\rangle_y|+\rangle_z|-\rangle_s + |+\rangle_y|-\rangle_z|-\rangle_s\right). \tag{5.14}$$

By inspection, all of the terms except for the first are non-interacting, because these contain anti-symmetric spatial wave-functions along at least one of the axes. The interaction energy for the first term we will define as $U_{\rm exc}$. The full-state then evolves as,

$$|\psi^{\rm exc}(t)\rangle = \frac{1}{2}\left(e^{iU_{\rm exc}t/\hbar}|+\rangle_y|+\rangle_z|+\rangle_s + |-\rangle_y|-\rangle_z|+\rangle_s + |-\rangle_y|+\rangle_z|-\rangle_s + |+\rangle_y|-\rangle_z|-\rangle_s\right). \tag{5.15}$$

In analogy to the vanilla spin-exchange discussed earlier, this state gives rise to three coherent and simultaneous exchange processes. There is "axial exchange" (1), where the quantum numbers in the y-dimension and the spin remain while the axial excitation exchanges. There is spin exchange (2),

[11] These thermometry data were taken the same day as a spin-exchange measurement that yielded a consistent contrast to the data in Figure 5.7b

[12] Note that in what follows, the exact quantum number for the axial motional excitation is somewhat irrelevant, because all that matters is that it distinguishes the particles in an additional degree of freedom. It is only relevant in determining the frequency components of the final dynamics since it determines the two-particle interaction energy.

where the quantum numbers in the y and z dimension remain while the spin exchanges. And there is exchange of the "radial" excitation (3), while the z and spin quantum numbers are unchanged. We can schematically write these three exchange processes as follows,

$$|e,e,\uparrow\rangle|g,g,\downarrow,\rangle \leftrightarrow |e,g,\uparrow\rangle|g,e,\downarrow\rangle, \tag{5.16}$$

$$|e,e,\uparrow\rangle|g,g,\downarrow,\rangle \leftrightarrow |e,e,\downarrow\rangle|g,g,\uparrow\rangle, \tag{5.17}$$

$$|e,e,\uparrow\rangle|g,g,\downarrow,\rangle \leftrightarrow |g,e,\uparrow\rangle|e,g,\downarrow\rangle, \tag{5.18}$$

each of which occur coherently from the initial state. Interestingly, the spin- exchange and radial exchange processes would each be detected as spin-exchange in our experiment. Bizarrely, and purely coincidently, for a harmonic potential $U_{\text{exc}} = J_{ex} = U_+$ due to a conspiracy of cancellation of several factors of 2. This means that, in the presence of an axial excitation, we would expect to detect in this purely harmonic case the same exchange frequency. Furthermore, from these states one can show that we would detect an spin-exchange oscillation contrast of $1/2$.[13] If we then took the harmonic assumption to be valid, this would imply a single-atom 3D ground-state fraction of less 50%, which is completely inconsistent with thermometry measurements taken prior and after the tunneling.

Fortunately, our potential makes the harmonic description inappropriate to this situation. Because the anharmonicity is on the scale of the interaction energy, two of the exchange processes become off-resonant. A full calculation of these effects performed by Michael Wall shows that we would expect multiple frequency components (Figure 5.9),[14] while the amplitude of the main frequency component is determined by the two-particle 3D ground-state probability (among other things). Since we do not detect significant additional frequency components, we can be fairly confident that the temperature is not limiting our contrast. However, for the purpose of including

[13] This can be calculated from computing the dynamics and then converting to second quantization while tracing over the axial degree of freedom.

[14] While the harmonic and separable approximation used to predict the interaction energy was accurate, small changes in the energy of the oscillator states due to anharmonicities change the states at the level of the interaction energy. Therefore, while the interaction energy is largely unaffected, the motional states are shifted on a scale comparable to this interaction energy.

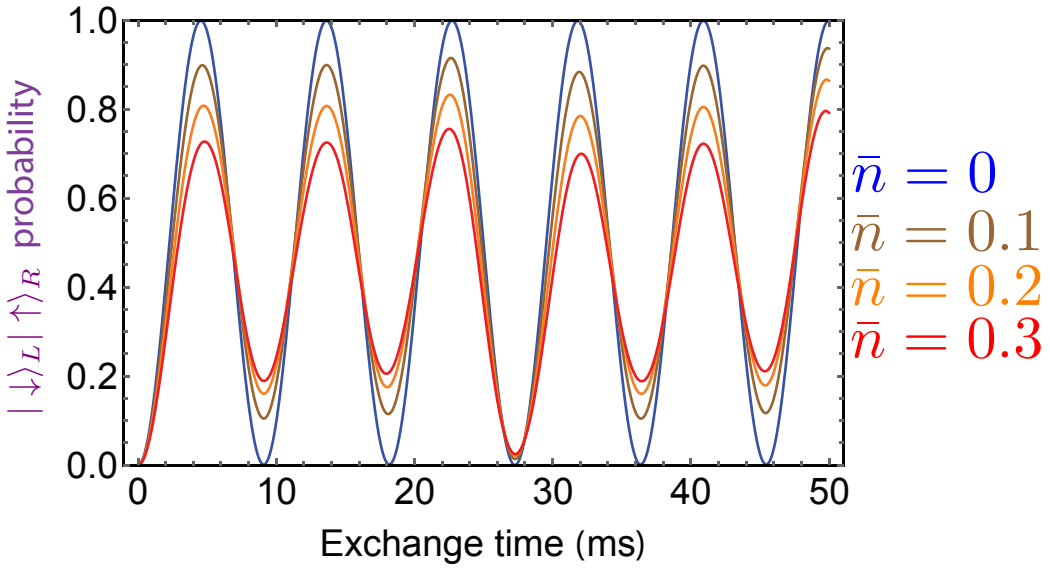

Figure 5.9: Temperature effects on spin-exchange. Here we show calculations indicating the expected dynamics in the presence of a thermal distribution of varying temperature, indicated by the legend on the right. We show just the probability to measure the state $|\downarrow\rangle_L|\uparrow\rangle_R$, which corresponds to the purple data in Figure 5.7. The effect of this systematic, frequency beating, does not correlate well with what we see in the experiment.

the effect of temperature, we expect that the single-atom 3D ground-state temperature of $P_{\mathrm{GS}} = 0.90(7)$ reduces to the peak exchange contrast to $P_{\mathrm{GS}}^2 = 0.81(12)$. This includes both radial and axial temperature, which in principle means we could be double-counting the effect of the radial temperature since it influences the ARP fidelity. However, the ARP fidelity is below unity by an amount much greater than the radial excited state fraction, so this double-counting is not significant, and it is not obvious how else to include this temperature.

5.2.3.2 Modeling the full exchange dynamics with the preparation ARPs and spin-dependence

Due to the very small energy scales in play here, a number of systematics related to the optical tweezers can effect the spin-exchange. For example, if there is any spin-dependence to the optical tweezer that changes the y-trap frequency of spin-up compared to spin-down, then the exchange coupled states $|e,\uparrow\rangle|g,\downarrow\rangle$ and $|e,\downarrow\rangle|g,\uparrow\rangle$ are no longer degenerate. If the the spin-up (spin-down) y

trap frequency is $\omega_y^{\uparrow}$ ($\omega_y^{\downarrow}$), then the exchange is off-resonant by an amount $\delta_\omega = \omega_y^{\uparrow} - \omega_y^{\downarrow}$. In the language of two-level systems, $J_{\mathrm{ex}} = 2U_{\mathrm{eg}}$ is the Rabi-frequency and this δ_ω is the detuning between the coupled states $|e,\uparrow\rangle|g,\downarrow\rangle$ and $|e,\downarrow\rangle|g,\uparrow\rangle$: as δ_i approaches J_{ex}, the exchange oscillations are suppressed by an amount $J_{ex}^2/(J_{\mathrm{ex}}^2+\delta_i^2)$. We model this effect and the full preparation and detection scheme to understand the expected exchange contrast. In the basis of $|L,\uparrow\rangle|R,\downarrow\rangle$, $|L,\downarrow\rangle|R,\uparrow\rangle$, $|e,\uparrow\rangle|g,\downarrow\rangle$, and $|e,\downarrow\rangle|g,\uparrow\rangle$, the Hamiltonian for the dynamics is,[15]

$$H = \begin{pmatrix} \delta_G/2 & 0 & -J & 0 \\ 0 & -\delta_G/2 & 0 & -J \\ -J & 0 & \Delta_{eg} + \delta_\omega/2 + U_{\mathrm{eg}} & U_{\mathrm{eg}} \\ 0 & -J & U_{\mathrm{eg}} & \Delta_{eg} - \delta_\omega/2 + U_{\mathrm{eg}} \end{pmatrix}, \tag{5.19}$$

where Δ_{eg} is the bias detuning from the tunneling resonance, $J = 2\pi$ 165 Hz is the excited-ground tunneling, and δ_G is the energy difference between $|L,\uparrow\rangle|R,\downarrow\rangle$ and $|L,\downarrow\rangle|R,\uparrow\rangle$ due to an effective magnetic field gradient. This gradient is created due to a combination of the spin-dependence of the potential and the bias applied to the wells. To quantify the spin-dependence of the potential, we measure with microwave spectroscopy the $|\uparrow\rangle \leftrightarrow |\downarrow\rangle$ transition with the quantization axis parallel to the optical tweezer (which is its orientation after we perform single-spin addressing, and how it remains during spin-exchange experiments). The spectroscopy is performed in the 1.15 mK and the 91 kHz deep tweezers, between which we observe a +129(2) kHz shift of the transition. If the quantization is along x, the shift between these two depths is only 8 kHz, which is near the expected scalar shift of 6.5 kHz. This pair of measurements indicates residual σ^+ circular polarization in the optical tweezers at the focus that creates an effective magnetic field. In the 91 kHz tunneling trap, and at the resonant excited-ground tunneling bias, this corresponds to a $\delta_G = 2\pi \cdot 50$ Hz. The spin-dependence also modifies the relative depth (and associated confinement) of the optical tweezer when both atoms are in the same tweezer, yielding a $\delta_\omega = 2\pi \cdot 22$ Hz.[16]

[15] Note I have switched my notation here to be consistent with the $|e,\uparrow\rangle|g,\downarrow\rangle$, and $|e,\downarrow\rangle|g,\uparrow\rangle$ notation. The states $|L,\uparrow\rangle|R,\downarrow\rangle$ and $|L,\downarrow\rangle|R,\uparrow\rangle$ are the same as $|\uparrow\rangle_L|\downarrow\rangle_R$ and $|\downarrow\rangle_L|\uparrow\rangle_R$, respectively.

[16] This was calculated using the three-dimensional modeling of the potential performed by Michael Wall in conjunction with the measured spin-dependence. Assuming a purely harmonic potential, we calculate a smaller $\delta_\omega = 2\pi \cdot 15$ Hz

In Figure 5.10, we show the expected dynamics using the Hamiltonian in Eq. 5.19 with the parameter values discussed, and I will address the effect of these parameters here. In time-evolving the Schrodinger equation, I have included the time-dependence of Δ_{eg}. The simulation includes the ARPs with their associated parameters in both directions, and the x-axis of the plot corresponds to the time between the end of the first ARP and the beginning of the second ARP. The y-axis corresponds to the state probabilities at the end of the second ARP. In total then this is an attempt at a faithful representation of the experiment. Despite the saturation in the ARP transfer fidelity displayed in Figure 5.4, the simulation indicates that we are not perfectly adiabatic, which gives rise to the high-frequency Stuckleberg oscillations on most of the probabilities and a reduction by 11% in the detected exchange amplitude due to imperfect preparation and detection. Though at much slower time-scales, δ_G can cause the adiabatic loading of the interacting ground-state in one well (i.e. only the singlet, as opposed to the singlet and the triplet, which together allow for exchange oscillations) and thereby reduce the amplitude of the spin-exchange oscillations, on the present ARP time-scale of 12 ms this effect occurs only at the 5% level. Because δ_ω is much less than U_{eg}, it also only reduces the contrast by 5%. The final oscillation amplitude including all of these effects is then 0.79, which is indicated by the purple and green data in the figure. Since we account for the ARP fidelity experimentally, I will only include the spin-dependent effects from this calculation in the subsequent analysis: with and without the spin-dependence, the exchange contrast in the purple and green data is reduced by a factor of 0.89.[17]

5.2.3.3 Summing all of the contributions to the contrast

In Table 5.1, we list all of the known systematics that influence the exchange contrast. The significant disagreement between the expected and measured contrast suggests that we are missing some aspect of the physics. We do observe an unexplained offset in the exchange data; specifically, the minima of the measured purple data have an offset from zero of 0.12. We have verified that

[17] The contrast reductions stated in this paragraph are determined from fitting the simulated purple data (with the indicated parameters) with a sine-wave.

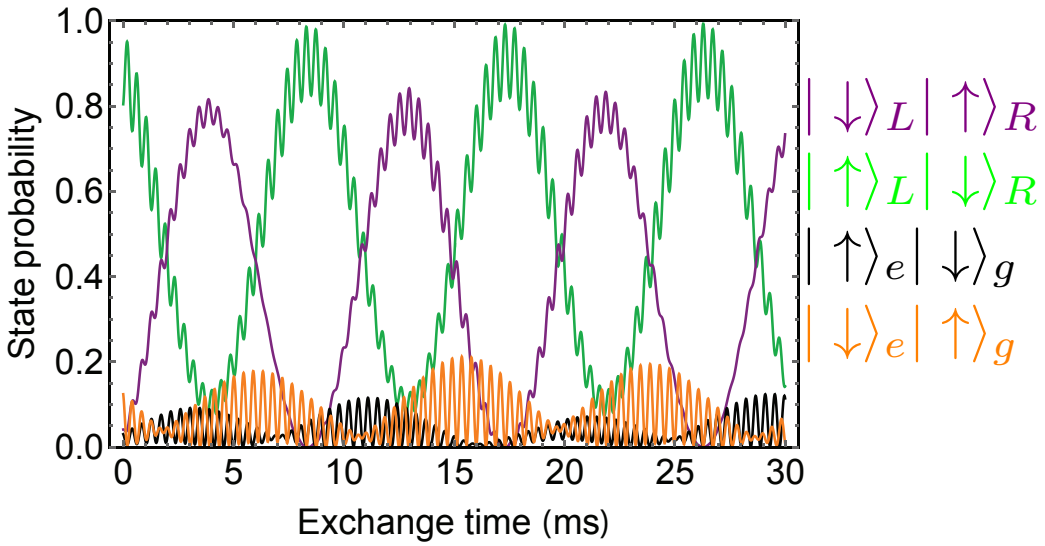

Figure 5.10: Simulation of exchange dynamics including the ARP preparation and detection protocol. We plot the expected measurement probabilities for the states in the Hilbert space, indicated on the right, at the end of the experimental protocol indicated in Figure 5.6. The dynamics are simulated by numerically evolving the Schrodinger equation for the Hamiltonian in Eq. 5.19, including the bias ramps from both of the ARPs. The ARP parameters are indicated in the text and Figure 5.3. For the simulation, we use the parameters $U_{eg}/(2\pi) = 50$ Hz, $\delta_\omega/(2\pi) = 22$ Hz, and $\delta_g/(2\pi) = 50$ Hz; the x-axis is the time between the ARPs, as in the experimental data of Figure 5.7b.

the presence of this offset is contingent on overlapping the atoms (i.e. performing the ARPs), and therefore not a feature of the preparation prior to the exchange. While the unexplained disparity will require further investigation in hopes of improving the contrast, we were able to work with the system as is to show that we could propagate the entanglement generated locally to the situation of the atoms separated.

5.3 Verifying non-local entanglement

The spin-exchange results so far rely on detection of the exchange oscillations through a motional-state position mapping achieved by the second ARP. We map the excited state spin onto the left-optical tweezer, which is subsequently imaged. The observed oscillations in the spin populations imply that the exchange dynamics are realizing entangled states between the particles occupying different motional states, but do not indicate whether this entanglement is preserved after

Spin exchange contrast systematics

Quantity	Multiplicative factor from unity contrast
Single-atom loss	0.92(2)
Spin preparation	0.835(10)
ARP fidelity (both ways)	0.81(4)
Single-atom ground-state fraction	0.81(12)
Spin-dependence	0.89
Expected contrast	**0.45(7)**
Measured contrast	**0.24(2)**

Table 5.1: Here we list all of the expected contributions to the sub-unity contrast. In the final two lines we show the expected and measured contrast.

we perform the mapping of the excited atom into the left optical tweezer. For quantum information applications where distributing entanglement is crucial, verifying that the entanglement is preserved upon separating the atoms is essential. After we allow an exchange time for t_{ent} (henceforth called "entangling exchange"), defined in Section 5.1.3, and perform the mapping for detection, we have the state,

$$|\psi_{\text{ent}}\rangle = \frac{1}{\sqrt{2}}\left(|\uparrow\rangle_L|\downarrow\rangle_R + e^{i\phi}|\downarrow\rangle_L|\uparrow\rangle_R\right), \tag{5.20}$$

where ideally $\phi = \pm\pi/2$. In the experiment, the main cause of decoherence is noise in this phase angle ϕ, because there is not dissipation that changes the spin-states of the atoms on a time-scale relevant to the spin-exchange and detection ARP. This means that in order to understand whether we are creating an entangled state between spatially separated particles, we must determine that we are reproducing the same ϕ each run of the experiment. If ϕ is randomized from run to run of the experiment, then the final state prior to imaging is merely the unentangled statistical mixture $\rho = \frac{1}{2}\left(|\downarrow\rangle_L|\uparrow\rangle_R\langle\downarrow|_L\langle\uparrow|_R + |\uparrow\rangle_L|\downarrow\rangle_R\langle\uparrow|_L\langle\downarrow|_R\right)$. Furthermore, as I will discuss, the imperfections in our spin-preparation stipulate certain requirements in how we assess the presence of two-particle entanglement.

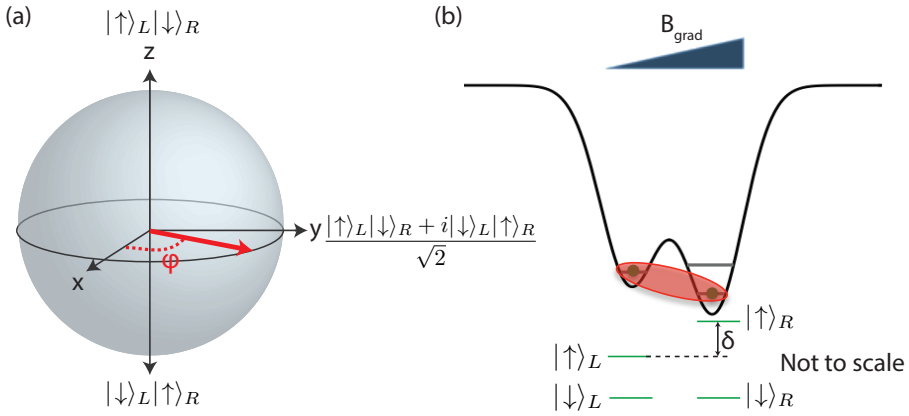

Figure 5.11: Measuring entanglement: Bloch-sphere picture and experimental tools. (a) Bloch sphere in the effective spin-1/2 Hilbert space of $|\uparrow\rangle_L|\downarrow\rangle_R$ and $|\downarrow\rangle_L|\uparrow\rangle_R$. By measuring the coherence between these states in a two-particle Ramsey experiment, it is possible to detect the presence of entanglement. The initial two-particle preparation (prior to the ARPs and exchange) yields a state along positive z. After the first ARP, entangling exchange, and then the detection ARP, we ideally have a state pointing along the Bloch-sphere y-axis. The parity measurements discussed in this section are sensitive to states pointing along x, hence necessitating rotating the state off the y axis. (b) We rotate the state in the equatorial plane of the Bloch-sphere by applying a magnetic field gradient, which changes the energy splitting between the spin-states in each tweezer by an amount δ. This relative difference in the splitting leads to rotation of the two-particle state in the Bloch-sphere equatorial plane.

5.3.1 Detecting entanglement via the spin-parity

To explain the technique we use to verify that the final state is entangled, it is helpful to use the Bloch sphere (Figure 5.11a) for the effective two-level system of $|\downarrow\rangle_L|\uparrow\rangle_R$ and $|\uparrow\rangle_L|\downarrow\rangle_R$. After entangling exchange and the detection ARP, we have the state $|\psi_{\text{ent}}\rangle$ that resides in the equatorial plane of the Bloch sphere and points at an angle ϕ with respect to the x-axis; in the ideal case of no disturbance to the state, the Bloch vector points along the y-axis. In analogy to Ramsey interferometry, we now wish to vary and measure the angle ϕ so that way can determine the length of the two-particle Bloch vector. We vary ϕ by applying a magnetic field gradient which changes the energy-splitting between $|\uparrow\rangle$ and $|\downarrow\rangle$ in the two optical tweezers, by an amount which I will define as δ (Figure 5.11b). After applying this gradient for a time t_{grad}, we have achieved the

transformation,

$$|\psi_{\rm ent}\rangle \rightarrow |\psi_{\rm ent}(t_{\rm grad})\rangle = \frac{1}{\sqrt{2}}\left(|\uparrow\rangle_L|\downarrow\rangle_R + e^{i(\phi+\delta\cdot t_{\rm grad})}|\downarrow\rangle_L|\uparrow\rangle_R\right). \tag{5.21}$$

The gradient, as desired, rotates the state in the equatorial place of the Bloch sphere by mapping $\phi \rightarrow \phi + \delta \cdot t_{\rm grad}$. We now require a way to detect this advancement of the superposition phase, because our measurement only specifies the z-projection on the Bloch sphere. This is accomplished by applying an "analysis" global (i.e. applied concurrently to both atoms) microwave $\pi/2$-pulse. To understand the effect of this, we consider two special cases of $\phi + \delta \cdot t_{\rm grad} = N_{\rm even}\pi$ and $\phi + \delta \cdot t_{\rm grad} = N_{\rm odd}\pi$, where $N_{\rm even}$ ($N_{\rm odd}$) is an even (odd) integer, each of which is periodically created as a function of $t_{\rm grad}$. Consider first the even case: here we have the state $|cat\rangle$, with a Bloch vector pointing along the positive x-axis. The $\pi/2$-pulse achieves transformation,

$$\frac{1}{\sqrt{2}}\left(|\uparrow\rangle_L|\downarrow\rangle_R + |\downarrow\rangle_L|\uparrow\rangle_R\right) \rightarrow \frac{1}{\sqrt{2}}\left(|\uparrow\rangle_L|\uparrow\rangle + |\downarrow\rangle_L|\downarrow\rangle_R\right), \tag{5.22}$$

converting the anti-correlations into positive correlations in the spin-states. This is identical to the discussion in the previous chapter in Section 4.2.1: by rotating the spins and the effective measurement basis, we can verify the entanglement by observing the persistence of correlations. Consider now the odd case: we now have the spatially non-local singlet state, with corresponding Bloch vector pointing along the negative x-axis. Here, the $\pi/2$-pulse achieves transformation,

$$\frac{1}{\sqrt{2}}\left(|\uparrow\rangle_L|\downarrow\rangle_R - |\downarrow\rangle_L|\uparrow\rangle_R\right) \rightarrow \frac{1}{\sqrt{2}}\left(|\uparrow\rangle_L|\downarrow\rangle - |\downarrow\rangle_L|\uparrow\rangle_R\right), \tag{5.23}$$

mapping the initial state back to itself: in this case the anti-correlations are mapped to anti-correlations. Therefore, we can measure the advancement of the superposition phase angle by observing how likely the spins are to be aligned or anti-aligned as a function of $t_{\rm grad}$. With the twist of using the gradient as opposed to a Raman light phase, this is directly analogous to the spin-parity measurements performed with ions and neutral atoms [79, 66, 76] to verify the presence of entanglement. The nature of the correlations, aligned or anti-aligned, can be quantified by the spin-parity [79],

$$\Pi = (P_{\uparrow,\uparrow} + P_{\downarrow,\downarrow}) - (P_{\uparrow,\downarrow} + P_{\downarrow,\uparrow}), \tag{5.24}$$

which is 1 (-1) when the spins are completely aligned (anti-aligned). We seek to then measure oscillations in Π as a function of t_{grad}. Given the correspondence with the Bloch vector direction between the odd and even case, the spin-parity can be related to the Bloch-vector as $\Pi = \langle\sigma_x\rangle$ prior to the $\pi/2$ pulse, where σ_x is the associated Pauli-operator within this effective spin-1/2 space. Therefore, in analogy to Ramsey interferometry, by observing oscillations in $\langle\sigma_x\rangle$, we are measuring the length of the Bloch-vector and coherence between the two states comprising the two-level system: in this case, $|\downarrow\rangle_L|\uparrow\rangle_R$ and $|\uparrow\rangle_L|\downarrow\rangle_R$.

Lastly, I would like to point out why, in contrast to entanglement via Rydberg blockade, it is necessary to apply this gradient to verify entanglement. Prior to applying the gradient, ideally the Bloch vector points along the $\pm y$-axis. This is because the spin-exchange conserves the populations in the singlet and triplet sectors (which are equal, see Eq. 5.9) and only changes the relative phase of their superposition (again, see Eq. 5.9). This leads to a coherence of $\pm i = e^{\pm i\pi/2}$ between $|\downarrow\rangle_L|\uparrow\rangle_R$ and $|\uparrow\rangle_L|\downarrow\rangle_R$. This is why it is necessary to apply a gradient to readout the parity, because the spin-parity of this initial state is zero. If on the other hand, the resulting entangling state after exchange were $|cat\rangle$, seeing a sufficiently large parity after just a $\pi/2$-pulse (no gradient), would be sufficient to verify entanglement: this is precisely what is done in Refs. [66, 76]. In our case, however, it is only with the gradient that we can rotate to states with non-zero spin-parity, and, hence, read-out the underlying entanglement.

5.3.2 Creating a bound on parity oscillations for separable density matrices

The above treatment assumed that the space of two-particle states was restricted to the two-particle $S_z = 0$ sub-space spanned by $|\uparrow\rangle_L|\downarrow\rangle_R$ and $|\downarrow\rangle_L|\uparrow\rangle_R$. Indeed, if all of the probability were confined to the $S_z = 0$ sector then any parity oscillation would verify entanglement. However, because our spin-preparation is imperfect, it is necessary to understand how large a parity oscillation contrast certifies entanglement in the presence of these imperfections.[18] Unfortunately,

[18] The following comes out of our collaboration with Ana Maria Rey's group, and, in particular, between me and Michael Foss-Feig.

by expanding the space to include $|\uparrow\rangle_L|\uparrow\rangle_R$ and $|\downarrow\rangle_L|\downarrow\rangle_R$, there are many unentangled states that yield a non-zero parity oscillation signal. For example, if we simply had two spins each in a balanced superposition, it is straightforward to see that there would be a parity oscillation signal at frequency δ with parity oscillation amplitude of 1 between -0.5 and 0.5. Even more perniciously, if these spins were subject to spatially-homogeneous magnetic field noise, it can be shown that this parity signal persists due to the insensitivity of the $S_z = 0$ sector to magnetic fields. Importantly, with or without the magnetic field dephasing, the state has the crucial feature that prior to the $\pi/2$ analysis pulse, there is equal population in each of the four possible two-particle states. As we will show, by experimentally bounding the population outside the two-particle $S_z = 0$ sector (i.e. by bounding the total population in $|\uparrow\rangle_L|\uparrow\rangle_R$ and $|\downarrow\rangle_L|\downarrow\rangle_R$), we can form a bound on the parity oscillation contrast for unentangled two-particle states.

We will now write a general expression for the two-atom state after entangling exchange and the detection ARP. The measured spin coherence time in the experiment is much less than the time between when we prepare the initial spin-state after sideband-cooling and when we perform parity detection (greater than 50 ms): therefore, any coherences between two-atom states of differing S_z are zero. Including the effect of imperfect spin-preparation, the general density matrix in the basis $|\uparrow\rangle_L|\uparrow\rangle_R$, $|\uparrow\rangle_L|\downarrow\rangle_R$,$|\downarrow\rangle_L|\uparrow\rangle_R$, and $|\downarrow\rangle_L|\downarrow\rangle_R$ is,

$$\rho = \begin{pmatrix} p_{\uparrow,\uparrow} & 0 & 0 & 0 \\ 0 & p_{\uparrow,\downarrow} & \epsilon & 0 \\ 0 & \epsilon^* & p_{\downarrow,\uparrow} & 0 \\ 0 & 0 & 0 & p_{\downarrow,\downarrow} \end{pmatrix}. \tag{5.25}$$

In the experiment, we can measure every quantity in this density matrix. The on-diagonals are straight-forwardly measured via the push-out detection of the spin states after calibrating for single-particle loss. The coherence ϵ between $|\uparrow\rangle_L|\downarrow\rangle_R$ and $|\downarrow\rangle_L|\uparrow\rangle_R$ can be measured via the parity detection as discussed in the prior Section 5.3.1: After applying the gradient and $\pi/2$-pulse, the parity is related to ϵ by,

$$\Pi = 2\mathrm{Re}(\epsilon e^{i(\phi+\delta\cdot t_{\mathrm{grad}})}). \tag{5.26}$$

This implies that the parity oscillation contrast $\mathcal{C} = 4\epsilon$. Using something very fancy sounding called the "Peres-Horodecki" criterion [141, 142] that has to do with partial transposes and negative eigenvalues (see Appendix C), it can be shown that ρ is not entangled when,

$$\epsilon^2 < p_{\uparrow,\uparrow} p_{\downarrow,\downarrow}, \tag{5.27}$$

and, otherwise, this state ρ is entangled.[19] Equivalently, for the oscillation contrast $\mathcal{C}$ of the parity, the bound on separable states is,

$$\mathcal{C} < 4(p_{\uparrow,\uparrow} p_{\downarrow,\downarrow})^{1/2} \equiv \mathcal{C}_{\text{bnd}}. \tag{5.28}$$

Experimentally then our goal is to measure a contrast $\mathcal{C} > \mathcal{C}_{\text{bnd}}$ to certify entanglement. While the criterion used to get here is somewhat opaque, the bound is very sensible based on the example I gave above about separated particles each in a superposition. Simply put, if there is population outside $S_z = 0$ that is equally divided between $|\uparrow\rangle_L|\uparrow\rangle_R$ and $|\downarrow\rangle_L|\downarrow\rangle_R$, then it is possible to measure parity as large as this population. Any parity measurement using this gradient plus analysis pulse procedure that exceeds this population certifies entanglement; the expression above is further generalized to account for the case of $p_{\uparrow,\uparrow} \neq p_{\downarrow,\downarrow}$.

In the subsequent sections, we focus on the oscillation contrast of the parity as opposed to the exact value of the parity, even though the latter can also certify entanglement as can be seen from Eq. 5.26 and Eq. 5.27. Both the loss and the ARP fidelity[20] can contribute a small constant offset to the parity, but these effects cannot contribute an oscillation signal in the parity.

5.3.3 Experimentally verifying entanglement

Applying the above procedure, we are able to verify that we produce non-local entanglement via the local spin-exchange. We prove the presence of entanglement using the procedure schematically represented in Figure 5.12, important features of which I will now discuss.

[19] The extent to which this bound is violated is related to the concurrence. In particular, the quantity $\frac{1}{2}|\mathcal{C} - 4\left(p^{\uparrow,\uparrow}p^{\downarrow,\downarrow}\right)^{1/2}| > 0$, is a lower bound on the concurrence in the density matrix ρ_0 [80].

[20] The ARPs can do this via the two-to-one collisions discussed in the context of the HOM studies.

5.3.3.1 Experimental procedure

After applying entangling exchange and performing the detection ARP (a-c), we have two atoms in separate optical tweezers. The spacing of the atoms at this time is approximately ten atomic wave-packets along the spatial y-direction. We then apply a magnetic field gradient via the MOT coils, which creates a quadrupole field with symmetry axis along the z-direction, while we also maintain our quantization axis along z. The goal of this quadrupole field is to create a difference in the total local magnetic field experienced by each atom, because this difference sets δ from the previous section (shown in Figure 5.11). This arrangement of magnetic fields is actually bad for several reasons. Because the atoms are separated along the y direction, this is not an optimal geometric configuration for maximizing the gradient experienced by the atoms since the gradient is maximal along the z-direction. This configuration is made worse because our quantization axis is along the z-direction, which has the effect of reducing the variation of the total quantization axis along the y-direction. And, lastly, the variation in the local magnetic field experienced by each atom, and hence δ, is coupled to the atoms exact position in the total field. We could improve this last issue by changing our quantization to along y, but this is precisely the direction for which effective magnetic fields from the optical tweezer become problematic (see Section 2.11.2). We are therefore somewhat stuck with this setup. We do increase the sensitivity to the gradient by reducing the size of the quantization axis from 3 G to 750 mG, which is sufficiently large to avoid any issues associated with the effective magnetic fields in the 91 kHz trap. The gradient is applied as follows: it is switched on, there is a 3 ms delay to allow for settling, a varied wait time, the gradient is switched off, and there is an additional 3 ms delay for field settling. This varied wait time corresponds to t_{grad}, or equivalently what I will call the "gradient time", from Eq. 5.21: it tunes the superposition phase of the entangled state.

After the second 3 ms delay for field settling, we apply a resonant microwave $\pi/2$-pulse. This so-called analysis pulse allows read-out of the two-particle spin-parity. The tweezer depths are then ramped up to 23 MHz adiabatically, and swept apart to 1.6 μm. We then drop the traps

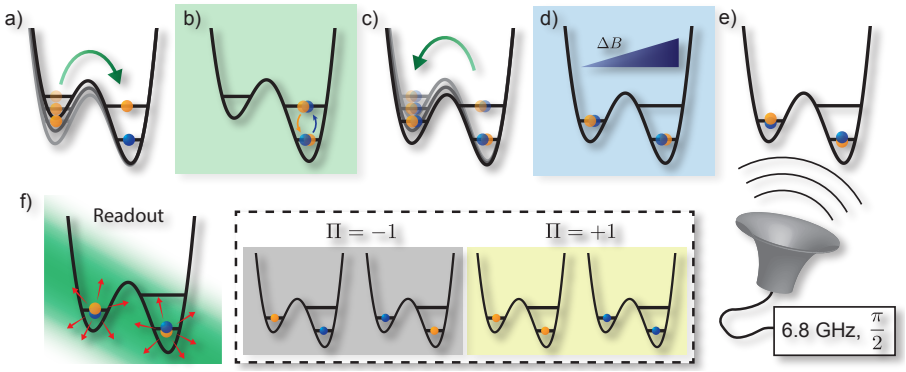

Figure 5.12: Experimental protocol for verifying the two-particle entanglement. The read-out stage of panel (f) corresponds to the push-out spin-sensitive detection.

back down to 1.2 MHz, and apply resonant $2 - 3'$ push-out light to map spin-down or spin-up onto the presence or absence of an atom in each trap, respectively.[21] The tweezers are then ramped back up and their contents imaged. Because we cannot distinguish background loss from an atom that is spin-up, we separately calibrate this quantity by running the experiment without the push-out 1000 times: in the subsequent discussion, the quoted values of the spin populations to ascertain $\mathcal{C}_{\mathrm{bnd}}$ are corrected for this loss, which is approximately 4%. Furthermore, because we care about measuring all possible two-particle spin combinations for the parity measurements, there is necessarily no post-selection applied to parity data. Lastly, I want to stress that the loss correction to the spin-preparation in order to determine $\mathcal{C}_{\mathrm{bnd}}$ is the only loss correction applied: the parity measurements below are not corrected in any fashion.

5.3.3.2 Verifying entanglement

In Figure 5.13a, we show our primary measurement verifying entanglement. For these data, we apply a gradient of 9.1 G/cm, and observe a 263(4) Hz oscillation in the parity. The contrast of the parity oscillations observed $\mathcal{C} = 0.49(4)$ (to which no corrections are applied) violates the bound on unentangled particles by 7.6σ (see Table 5.2). If instead we apply the fidelity criterion of

[21] This mapping occurs in all of our spectroscopy, but since it is so relevant to the present procedure I was explicit.

Ref. [79] adapted to the entangled states we produce in the $S_z = 0$ sector, we achieve a fidelity of,

$$\mathcal{F} \;=\; (p_{\uparrow,\downarrow} + p_{\downarrow,\uparrow})/2 + \mathcal{C}/4 = 0.580(12). \tag{5.29}$$

This fidelity also exceeds the bound of 0.5 sufficient to certify entanglement [79]; this bound is less tight compared to the Peres-Horodecki criterion, and as a result less significantly violated (6.6σ). The Pere-Horodecki criterion represents the tightest possible bound because it gives a necessary and sufficient condition on the parity contrast of entangled states. The probabilities to prepare $p_{\uparrow,\uparrow}$ and $p_{\downarrow,\downarrow}$ were measured by conducting the experiment up to the point prior to when we would ramp for the tunneling, and measuring at high statistics (1000 runs of the experiment) the probabilities to measure each of the particles in spin up or down; after the parity oscillation measurement, we redid this measurement to confirm that the light-shift beam did not drift and compromise the spin-preparation. In order to push down on $\mathcal{C}_{\mathrm{bnd}}$ as much as possible, it was vital to use the Gaussian shaped microwave pulses. These pulses greatly mitigated off-resonant excitation and hence $p_{\downarrow,\downarrow}$. Using square-pulses in conjunction with our light shifting technique increased the bound to the point where the violation was closer to $1-3\sigma$ depending on the measurement: in fact, we originally used this technique for the spin-exchange data, which is why the implied spin-preparation fidelity in the Table 5.2 is better than what is discussed in Section 5.2.3.

We can perform helpful consistency checks on the parity oscillations by comparing them to the exchange data. We expect that half of the parity contrast (or, equivalently, the peak absolute value of the parity) should correspond to the contrast of the spin-exchange oscillations from Section 5.2.2, because the contrast of the exchange oscillations indicates the degree of coherence in the entangled state. The non-spin-preparation-post-selected exchange data yielded a contrast of 0.24(2), and here with the parity we measure a consistent $\mathcal{C}/2 = 0.25(2)$. We have observed fluctuations in the parity contrast, which we attribute to phase drift in the exchange oscillations that compromise how well we set the exchange time to be entangling. We have regularly observed these fluctuations in the phase, which we have identified as arising from the bias resonance position fluctuating: variations in the resonance position change the time during the ARP where exchange effectively begins, thereby

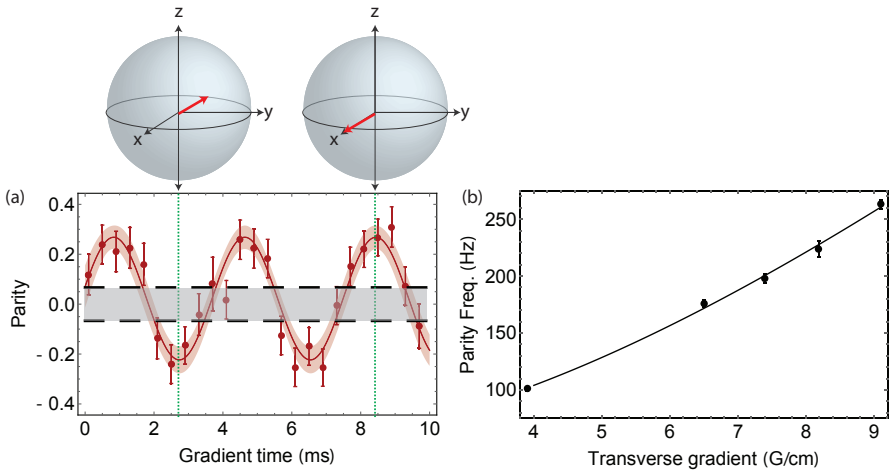

Figure 5.13: Entanglement verification data. (a) Applying the protocol outlined in the text and Figure 5.12, we observe the displayed parity oscillations. From the detected parity, we illustrate the implied direction of the Bloch vector (for the coherent part of the density matrix) prior to applying the $\pi/2$ analysis pulse. The horizontal lines and gray region correspond to the bounds on the parity below which the density matrix could be separable (see Table 5.2). The parity oscillations we observe significantly exceed these bounds. (b) We show the frequency of the observed parity oscillations as a function of the gradient applied. The x-axis indicates the size of the gradient along z, which is the coil axis of symmetry but also transverse to the displacement of the optical tweezers. The solid line corresponds to a fit from the magnetic field model discussed in the text, Eq. 5.30.

changing the appropriate times for realizing entanglement.

We also study the dependence of the parity oscillation frequency on the magnitude of the gradient, displayed in Figure 5.13b. This dependence confirms that δ is controlling the phase evolution of the superposition. Despite the coupling of δ to the exact position of the optical tweezers in the magnetic field formed by the quadrupole field and the quantizing field, we can model the expected dependence of δ on the size of the quadrupole gradient leaving the position of the tweezers as a free parameter. The modeling is accomplished by the function,

$$\delta = \delta_G + (2.1 \text{ MHz/G}) \left(|B_{\text{QP}}(\vec{r}) + B_{\text{QA}}| - |B_{\text{QP}}(\vec{r} + \Delta y \hat{y}) + B_{\text{QA}}| \right), \tag{5.30}$$

where $\Delta y = 715$ nm corresponds to the spacing of the atoms along the y-direction, $\vec{r}$ is the position of the lower atom that we leave as a free parameter, $B_{QA} = 750$ mG is the quantization axis pointing along z, and B_{QP} corresponds to the quadrupole magnetic field for the current we apply to the coils. The first term δ_G is the residual spin-dependence of the potential from Section 5.2.3.2: since the

wells are biased during the parity measurement, and there is the measured spin-dependence already discussed, there is an effective-gradient from the tweezers. This implies that if we simply did not apply a gradient, we would expect to observe parity oscillations at δ_G; I only realized the importance of this term in modeling the gradient, and the possibility of such a measurement, after we completed these experiments. This would be a nice additional check. Lastly, because of the orientation of the fields, the x position of the tweezers is not relevant for small displacements from zero (we know we are less than 2 mm from the center of the coils due to geometric constraints), so we set $x = 0$ in fitting $\vec{r} = \{0, y, z\}$ to gain precision in y and z. Fitting the data to this model[22] , we find nice agreement: the fit suggests $y = 0.8(4)$ mm, $z \sim 0$, and the $\delta_G/(2\pi) = 54(15)$ Hz. Based on the microwave spectroscopy numbers mentioned above, the bias applied during the parity measurement (7(1) kHz), and the tweezer depth of 91(4) kHz, we expect a consistent $\delta_G/(2\pi) = 43(6)$ Hz.

Entanglement verification numbers

Quantity	Value
$p_{\uparrow,\uparrow}$	0.071(14)
$p_{\downarrow,\downarrow}$	0.016(5)
$\mathcal{C}_{bnd}$	0.133(25)
$\mathcal{C}$	0.49(4)

Table 5.2: Here we list the experimental numbers that inform our claim of entanglement.

5.3.3.3 Dependence of measured parity on exchange dynamics

Lastly, we can examine the relationship between the parity measurement and the generation of entanglement from the exchange dynamics. The exchange dynamics periodically realize the two entangled states (alternating each t_{ent}),

$$|\psi_+\rangle = \frac{1}{\sqrt{2}} \left(|\uparrow\rangle_L |\downarrow\rangle_R + i |\downarrow\rangle_L |\uparrow\rangle_R \right), \tag{5.31}$$

$$|\psi_-\rangle = \frac{1}{\sqrt{2}} \left(|\uparrow\rangle_L |\downarrow\rangle_R - i |\downarrow\rangle_L |\uparrow\rangle_R \right). \tag{5.32}$$

[22] Note we use the current applied to the coils as an independent parameter when fitting, but I plot the x-axis of the plot in terms of the gradient to which this current corresponds.

In the Bloch sphere picture of Figure 5.11a, these states point in opposite directions along the y-axis. Consequently, the gradient time $t_{\rm grad}$ that rotates $|\psi_+\rangle$ to maximal positive parity, rotates $|\psi_-\rangle$ to maximal negative parity. This means that if we fix $t_{\rm grad}$ to such a time, and vary the exchange dynamics prior the parity detection, we will observe the associated parity oscillations as each of these states is created. We perform this exact experiment (Figure 5.14) by fixing $t_{\rm grad}$ at the time of peak parity for the initial entangled state $|\psi_+\rangle$, and then vary the exchange time prior to the motional state mapping and full parity measurement.[23] From the above discussion, one expects that at the minima and maxima of the exchange oscillations (purple, green) the parity vanishes since these are times at which the atoms are unentangled; at the linear points of the exchange oscillations, one expects maximal entanglement and peaking of the parity. Quantitatively this is manifest as a $\pi/2$ phase shift between the data sets: we observe a nearly consistent phase shift of 2.0(3) radians. This is additional evidence that the entangling exchange interaction is realizing the non-zero parity, as opposed to some perverse separable density matrix.

There is an important point to be made regarding the near expected correspondence between these parity and exchange data shown here. The agreement suggests that the onsite spin-dependence (δ_ω) is likely not larger than we think, because if the spin-exchange dynamics were off-resonant we would not expect the full-swap times ($t = N_{odd} \cdot \pi/J_{ex}$) of the exchange to be unentangling (i.e. to show zero parity); in analogy to Rabi oscillations, when the coupling drive is detuned the peaking of the oscillations corresponds to a superposition and not a full spin-flip. There is a small +2.2(1.4)% offset in the parity oscillations, which could indicate the presence of this effect; given the expected 5% reduction in the exchange contrast from δ_ω, we would expect a +2.5% offset. Though not very precise, the measurement is consistent, at least suggesting that δ_ω is not significantly larger than other measurements from microwave spectroscopy indicate.

[23] In other words, while for the data of Figure 5.13 we fix the parameters of panel (b) in Figure 5.12 and vary the gradient time of panel (d), here we fix the parameters of panel (d) and vary the exchange time parameter of panel (b).

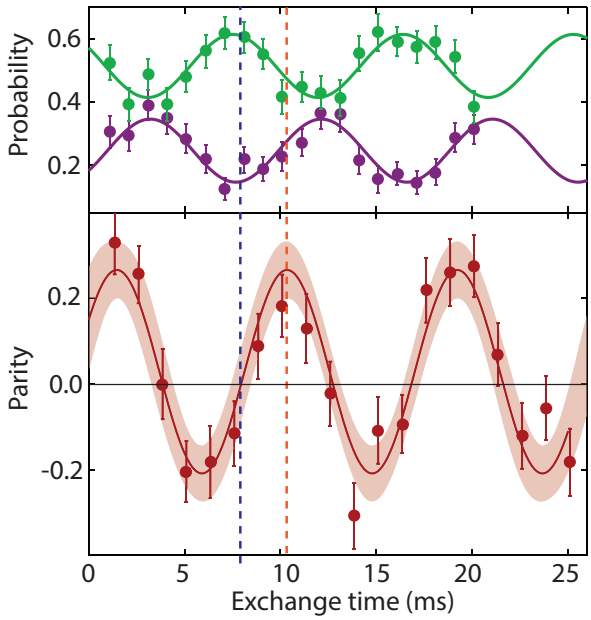

Figure 5.14: Parity dependence on exchange dynamics. Here we vary the exchange time prior to the parity detection. We set the gradient time such that the parity is peaked when we create the $|\psi_+\rangle$ via the exchange dynamics prior. We then vary the exchange time to observe its influence on the measured parity. We can compare the parity to spin-exchange oscillation data, which indicates near the expected $\pi/2$ phase shift in the oscillations. When the spin-exchange dynamics are in a peak or a trough, corresponding to full exchange or no exchange, the resulting state is unentangled. Conversely, where the exchange dynamics are linear, the state is entangled and we see maximizing/minimizing of the parity. The dashed orange (blue) line indicate an example time where the entangling (unentangling) behavior is manifest in both data sets.

Chapter 6

Conclusion

Laser cooled atoms in optical tweezers offer a variety of novel experimental avenues, the promise of which is supported by what we have already been able to do. The Hong-Ou-Mandel interference of atoms had been an experimental goal in the community for some time, and our experimental platform provided the ideal toolset for its realization. The spin-exchange studies exploit the full spectrum of capabilities enabled by the tweezer platform, which solves some of the key challenges associated with particle transport when using spin-exchange. Combined with the near-term improvements presently being applied to the experiment, a number of exciting projects are on the horizon.

The first huge improvement recently implemented in the experiment is the incorporation of deterministic single atom loading. Given the $\sim 0.5^n$ scaling of loading single atoms into n independent optical tweezers, the experiment quickly becomes time-consuming as the particle number is increased. Using the techniques of Ref. [17], we are able to load a single ^{87}Rb atom into an optical tweezer with 90% probability (see Figure 6.1). We applied the technique to the case of a two-by-two array, and observed the same performance. However, the loading was strongly dependent on the spacing between the traps, indicating that at least a micron separation was necessary before the loading saturated on the 90% single-tweezer performance. While the spacing dependence limits the number of traps to which we can apply this technique presently, this is a technical limitation with respect to the rail optics and the success of the technique immediately increases the realistic number of particles with which we can perform experiments. For example, we can now perform

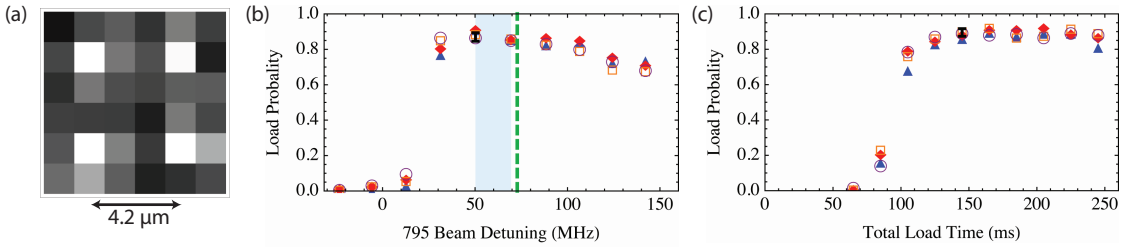

Figure 6.1: Deterministic loading of a square array using blue-detuned light on the D1 line [17]. (a) We create a square array of optical tweezer via the AOMs in our optical rail. We apply blue-detuned loading in conjunction with relevant depumping beams during the MOT loading stage of the experiment. (b) We measure the single atom load probability as a function of the detuning of the 795 nm light on the D1 line from the tweezer-light-shifted trap. The blue swath is the range over which we find consistent optimal loading, and the green line is the location where the detuning equals the tweezer trap depth. (c) Parking the D1 laser in the blue swath, we vary the MOT load time and observe the single atom load fidelity. We observe saturation in the loading probability on short time-scales. In (a,b), the blue triangles are the top-left tweezer; the red diamonds are the top-right tweezer; orange squares are the bottom-left tweezer; the purple circles are the bottom-right tweezer. The black error bar is an example of the typical error bar in each measurement.

a four-particle experiment in the same time as a single-particle experiment in the absence of the enhanced loading, or an 8 particle experiment in the same time as the two particle experiments in Chapters 4 and 5. With these improvements in mind, I will discuss small and large experiments possible in the future.

6.1 Measurement-induced entanglement of atoms

While generally we think of interactions as a prerequisite for entanglement, this is actually only true for non-identical particles. It is possible to generate probabilistic entanglement between identical particles through a process known as measurement-induced entanglement [7]. The idea here is as follows. Suppose we prepare two atoms in the state $|\uparrow\rangle_L|\downarrow\rangle_R$ in a pair of tunnel-coupled optical tweezers. From the discussions in Section 4.7.2 regarding distinguishable states, we know that this state is a superposition of the symmetric and anti-symmetric spatial wave-functions, each paired with the triplet and singlet spin-states, respectively. If we allow tunneling for t_{HOM}, we expect a superposition of bosonic HOM interference and "fermionic" HOM interference, where in the former the atoms always end up in the same tweezer while in the latter they always end up in differ-

ent tweezers. Because of the correspondence between each of these outcomes with the symmetrized spin-states, we can probabilistically post-select on a particle-entangled state. If we measure at the end of the experiment that the atoms are in different optical tweezers, the atoms are projected onto the spin-singlet. This idea of measurement-induced probabilistic entanglement underlies linear quantum computing protocols with photons [143, 112], because it allows non-interacting photons to become entangled. Experimentally we could observe the measurement-induced entanglement protocol described here through spin-sensitive imaging and the parity measurements we employ in Chapter 5. This would be an interesting realization, and could pave the way for doing linear quantum computing applications with neutral atoms.

6.2 Microscopic Kondo model

Understanding condensed-matter systems that do not conform to Fermi-liquid theory [144, 145] is an on-going endeavor. Heavy fermion materials [27] are one such example, which exhibit anomalously large specific heats as their temperature is reduced. While this behavior is inconsistent with predictions of Fermi-liquid theory, Fermi-liquid theory is still applied to draw conclusions about the mass of the quasi-particles in the system. A key prediction of Fermi-liquid theory is that the mass of the quasi-particles is proportional to the specific heat of the sample, which implies that the large enhancement in the specific heat is associated with a 1000-fold (in some cases) increase in the quasi-particle mass. The Kondo model is a simple paradigm that is used to explain the physics exhibited in heavy fermion materials. The model includes two bands, one of which contains effectively localized particles while the other contains mobile particles; these two bands could, for example, correspond to the ground and excited band of an optical lattice, since the associated tunnelings differ drastically. A key prediction of the Kondo model is that as the interactions between the localized and mobile particles is turned up, there is a phase transition between a material with magnetic properties to one with reduced tunneling of the mobile particles, the latter of which is equivalent to mass enhancement [146, 147]. Loosely speaking, these phases can be described as follows. In the weak interactions phase, the atoms in the mobile band can tunnel from

site to site resonantly, and they experience an onsite spin-exchange interaction (identical to the one in Chapter 5) with the localized atoms. To second-order, the tunneling atoms then mediate a magnetic interaction between the localized spins known as the RKKY interaction, which, in turn, induces magnetic properties. When the interactions are large compared to the tunneling energy in the mobile band, the symmetry of the many-body spatial wavefunctions, which is coupled to the localized spins, determines the interaction energy: this has the effect of slowing down the rate at which the atoms can tunnel due to the interaction shifts, which consequently mimics heavy-mass behavior. These key behaviors are readily realizable at the microscopic level in a double well consisting of a tunneling single atom in the excited motional state, and a localized spin in each ground-state of the double-well. Spin-exchange dynamics between the ground spins could reveal the RKKY interaction, while particle tunneling at half the excited band tunneling rate would show the heavy-mass behavior in this system. Applying the techniques developed in the previous chapters, the preparation and detection of these dynamics is accessible. Furthermore, the ability to prepare a single atom in the motional excited state, which is more challenging in a lattice setup, circumvents collisional instabilities associated with higher bands that might mitigate the experimental signal [148].

6.3 Observing superfluid behavior in a system of known particle number

When we think about lasers from a quantum optics perspective, we generally think of the complete uncertainty in the photon number as supplying certainty in the phase. Bose-Einstein condensates retain significant parallels with lasers [121], and, given their large particle number, they too are often considered in the contexts of coherent states. However, the particle number is of course completely conserved, so understanding the actual equivalence between BECs and lasers is of particular interest. Specifically, it would be interesting to measure a macroscopic phase when the particle number is constrained [149]. Our experiment provides the exact tool to perform such studies, because we always know the particle number prior to performing an experiment. One could imagine preparing two 1D chains of single atoms in optical tweezers, ground-state cooling

each atom, and then ramping on a tunneling within the chains. This should be equivalent to a small superfluid-Mott transition, starting from the Mott side. We could study the character of the many-body state by looking at the number statistics on each site, which should exhibit a coherent-state-like dependence in the number distribution when on the superfluid side of the transition. If each 1D "superfluid" has a phase, by allowing tunneling between the 1D chains we should be able to discern an interference signal written in the density distribution of the particles.

6.4 Measuring entanglement entropy and thermalization in finite-sized systems

While the atomic Hong-Ou-Mandel effect is interesting in its own right, it also shows the promise of scaling to larger system sizes. What are the kinds of things one could explore with such a system? After all, when we think about traditional many-body physics, often we are considering systems in the thermodynamic limit with 10^{23} particles, and here limitations on single-particle preparation fidelities will always be a challenge as the atom number is increased. Yet, a key feature of quantum mechanics, both interesting and theoretically challenging, is the way the Hilbert space of a quantum system scales with the number of degrees of freedom. As we add more particles, each with its own quantum degrees of freedoms, the Hilbert space grows exponentially. And because many of the features of many-body physics depend on this Hilbert space size, even upon reaching a handful of atoms interesting things can happen. For example, a recent theoretical prediction constrained how the entanglement in a quantum system scales with the system size under various experimental conditions. For deep reasons, something as complicated as entanglement in a one-dimensional Bose-Hubbard chain can be reduced to a logarithmic [150] or linear scaling [151] depending on the Hamiltonian parameters and quantum states explored. Untested experimentally, these so-called "area laws" or "volume laws" arise theoretically in the limit of infinite particles, but even for a handful particles, they are evidenced in numerics (Figure 6.2c). From this example, we see that a finite-sized system can probe the many-body physics sought in quantum simulation experiments [152], and, in particular, as the particle number surpasses fifty and dimensionality

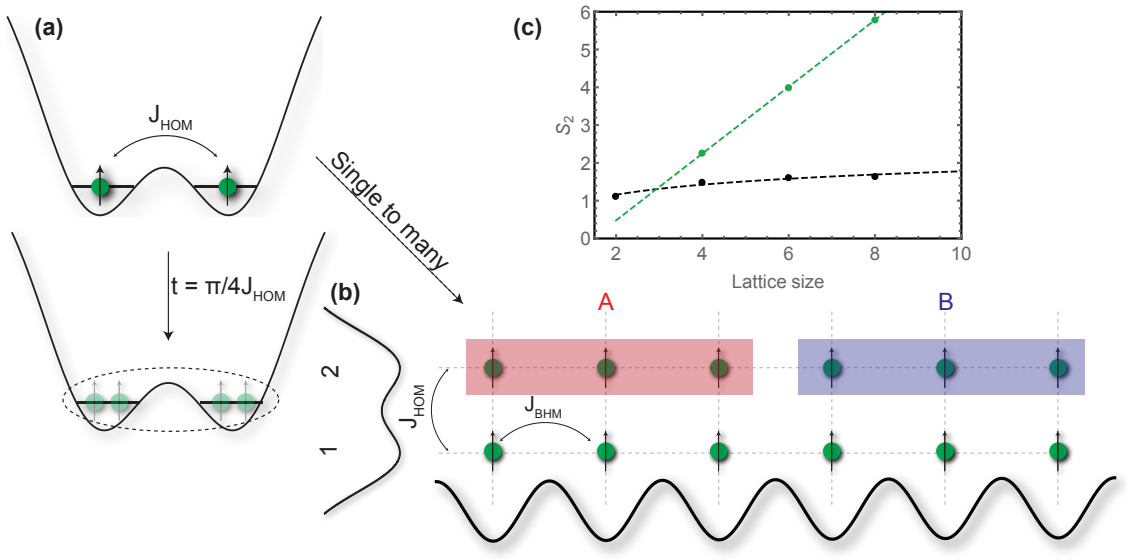

Figure 6.2: Hong-Ou-Mandel to many-particle interference. (a) Realization of the HOM effect with two atoms in a double well. By preparing indistinguishable bosons and interfering them in a tunnel-coupled double well, the mode-entangled state of $\frac{1}{\sqrt{2}}(|2,0\rangle + |0,2\rangle)$ is created after allowing tunneling. (b) Extension to many particles for a pair of copies (1 and 2) of a Bose-Hubbard chain. After applying tunneling between the copies, the odd or even particle number within the copies encodes the many-body purity of the quantum states as well as the mode entanglement contained. (c) Using the setup in (b), comparison of the bipartite entanglement entropy S_2 as a function system size for a quench (green) versus the ground-state (black) in an interacting Bose-Hubbard chain near the phase transition. The dashed lines are a linear (logarithmic) fit for quenched (ground state) calculations, indicating the presence of "volume" and "area" law-like physics in finite-sized systems.

grows the comparative computational challenges become immense. And, for the example at hand, additional proposals have indicated just how one might directly measure spatial-entanglement [153], and the protocol is precisely the many-body extension of the Hong-Ou-Mandel interference we observe with two bosonic atoms (Figure 6.2a,b).

In addition to the entanglement entropy scaling experiments already proposed, studying how closed many-body systems locally thermalize is a near-term possibility. The dynamics of the entanglement entropy after a quench of the Hamiltonian exhibits steady-state-like saturation, even though the entire many-body system is in a pure state. The linear/volume law scaling that I calculated in Figure 6.2c was of this near steady-state value. This saturation of the dynamics is related to

the question of thermalization in closed many-body systems: how does a closed pure system evolve to one which locally has a thermal distribution as prescribed by statistical mechanics [154, 155]? The steady-state behavior is akin to equilibration of the many-body system [154], where one can think of sub-sets of the Hubbard chain as thermalizing with the larger many-body system, which is itself closed. Key experimental work so far has shown how density ordering evolves under a quench [156], yet microscopic characterization of the many-body states to which the system converges remains experimentally unexplored. By detecting this saturation, and then studying local quantities like the particle number on a site, it may be possible to observe a correspondence between the quench distance (loosely speaking, the magnitude of the diabatic change in the Hamiltonian) and the local temperature on the site. An experiment that demonstrates a clear correspondence between the equilibrated, pure many-body state and the thermal behavior of its constituents would be ground-breaking.

Bibliography

[1] C. K. Hong, Z. Y. Ou, and L. Mandel, "Measurement of subpicosecond time intervals between two photons by interference," Phys. Rev. Lett. **59**, 2044 (1987), URL http://link.aps.org/doi/10.1103/PhysRevLett.59.2044.

[2] C. Weitenberg, M. Endres, J. F. Sherson, M. Cheneau, P. Schauß, T. Fukuhara, I. Bloch, and S. Kuhr, "Single-spin Addressing in an Atomic Mott Insulator," Nature **471**, 319 (2011).

[3] N. Schlosser, G. Reymond, I. Protsenko, and P. Grangier, "Sub-poissonian Loading of Single Atoms in a Microscopic Dipole Trap," Nature **411**, 1024 (2001).

[4] D. Steck, "Rubidium 87 D Line Data," .

[5] N. Schlosser, G. Reymond, and P. Grangier, "Collisional Blockade in Microscopic Optical Dipole Traps," Phys. Rev. Lett. **89**, 023005 (2002).

[6] J. D. Thompson, T. G. Tiecke, A. S. Zibrov, V. Vuletić, and M. D. Lukin, "Coherence and Raman Sideband Cooling of a Single Atom in an Optical Tweezer," Phys. Rev. Lett. **110**, 133001 (2013), URL http://link.aps.org/doi/10.1103/PhysRevLett.110.133001.

[7] M. C. Tichy, F. Mintert, and A. Buchleitner, "Essential entanglement for atomic and molecular physics," Journal of Physics B: Atomic, Molecular and Optical Physics **44**, 192001 (2011), URL http://stacks.iop.org/0953-4075/44/i=19/a=192001.

[8] B. Hessmo, P. Usachev, H. Heydari, and G. Björk, "Experimental Demonstration of Single Photon Nonlocality," Phys. Rev. Lett. **92**, 180401 (2004), URL http://link.aps.org/doi/10.1103/PhysRevLett.92.180401.

[9] S. Ashhab, K. Maruyama, and F. Nori, "Observing quantum nonlocality in the entanglement between modes of massive particles," Phys. Rev. A **75**, 022108 (2007), URL http://link.aps.org/doi/10.1103/PhysRevA.75.022108.

[10] L. Heaney, S.-W. Lee, and D. Jaksch, "Bell inequality for pairs of particle-number-superselection-rule restricted states," Phys. Rev. A **82**, 042116 (2010), URL http://link.aps.org/doi/10.1103/PhysRevA.82.042116.

[11] W. S. Bakr, J. I. Gillen, A. Peng, S. Fölling, and M. Greiner, "A Quantum Gas Microscope for Detecting Single Atoms in a Hubbard-regime Optical Lattice," Nature **462**, 74 (2009).

[12] P. Sompet, A. V. Carpentier, Y. H. Fung, M. McGovern, and M. F. Andersen, "Dynamics of two atoms undergoing light-assisted collisions in an optical microtrap," Phys. Rev. A **88**, 051401 (2013), URL http://link.aps.org/doi/10.1103/PhysRevA.88.051401.

[13] J. R. Petta, A. C. Johnson, J. M. Taylor, E. A. Laird, A. Yacoby, M. D. Lukin, C. M. Marcus, M. P. Hanson, and A. C. Gossard, "Coherent Manipulation of Coupled Electron Spins in Semiconductor Quantum Dots," Science **309**, 2180 (2005), http://www.sciencemag.org/content/309/5744/2180.full.pdf, URL http://www.sciencemag.org/content/309/5744/2180.abstract.

[14] D. P. DiVincenzo, D. Bacon, J. Kempe, G. Burkard, and K. B. Whaley, "Universal quantum computation with the exchange interaction," Nature **408**, 339 (2000), URL http://dx.doi.org/10.1038/35042541.

[15] S. Trotzky, P. Cheinet, S. Fölling, M. Feld, U. Schnorrberger, A. M. Rey, A. Polkovnikov, E. A. Demler, M. D. Lukin, and I. Bloch, "Time-resolved Observation and Control of Superexchange Interactions with Ultracold Atoms in Optical Lattices," Science **319**, 295 (2008).

[16] M. Anderlini, P. J. Lee, B. L. Brown, J. Sebby-Strabley, W. D. Phillips, and J. V. Porto, "Controlled Exchange Interaction Between Pairs of Neutral Atoms in an Optical Lattice," Nature **448**, 452 (2007).

[17] T. Grunzweig, A. Hilliard, M. McGovern, and M. F. Andersen, "Near-deterministic Preparation of a Single Atom in an Optical Microtrap," Nat. Phys. **6**, 951 (2010).

[18] P. Kapitza, "Viscosity of Liquid Helium below the λ-point," Nature **141**, 74 (1938).

[19] J. F. Allen and D. Misener, "Flow Phenomena in Liquid Helium II," Nature **142**, 643 (1938).

[20] J. Bardeen, L. N. Cooper, and J. R. Schrieffer, "Theory of Superconductivity," Phys. Rev. **108**, 1175 (1957), URL http://link.aps.org/doi/10.1103/PhysRev.108.1175.

[21] B. T. Matthias, T. H. Geballe, and V. B. Compton, "Superconductivity," Rev. Mod. Phys. **35**, 1 (1963), URL http://link.aps.org/doi/10.1103/RevModPhys.35.1.

[22] K. v. Klitzing, G. Dorda, and M. Pepper, "New Method for High-Accuracy Determination of the Fine-Structure Constant Based on Quantized Hall Resistance," Phys. Rev. Lett. **45**, 494 (1980).

[23] D. Thouless, M. Kohmoto, M. Nightingale, and M. D. Nijs, "Quantized Hall Conductance in a Two-Dimensional Periodic Potential," Physical review letters **49**, 405 (1982).

[24] B. Halperin, "The quantized Hall effect," Scientific American **254**, 52 (1986).

[25] M. Z. Hasan and C. Kane, "Topological insulators," arxiv.org/pdf/1002.3895v2 (2010), URL http://arxiv.org/pdf/1002.3895v2.

[26] D. C. Tsui, H. L. Stormer, and A. C. Gossard, "Two-Dimensional Magnetotransport in the Extreme Quantum Limit," Phys. Rev. Lett. **48**, 1559 (1982), URL http://link.aps.org/doi/10.1103/PhysRevLett.48.1559.

[27] G. R. Stewart, "Heavy-fermion systems," Rev. Mod. Phys. **56**, 755 (1984), URL http://link.aps.org/doi/10.1103/RevModPhys.56.755.

[28] R. B. Laughlin, "Anomalous Quantum Hall Effect: An Incompressible Quantum Fluid with Fractionally Charged Excitations," Phys. Rev. Lett. **50**, 1395 (1983), URL http://link.aps.org/doi/10.1103/PhysRevLett.50.1395.

[29] M. H. Anderson, J. R. Ensher, M. R. Matthews, C. E. Wieman, and E. A. Cornell, "Observation of Bose-Einstein Condensation in a Dilute Atomic Vapor," Science **269**, 198 (1995), http://www.sciencemag.org/content/269/5221/198.full.pdf, URL http://www.sciencemag.org/content/269/5221/198.abstract.

[30] B. DeMarco and D. S. Jin, "Onset of Fermi Degeneracy in a Trapped Atomic Gas," Science **285**, 1703 (1999), http://www.sciencemag.org/content/285/5434/1703.full.pdf, URL http://www.sciencemag.org/content/285/5434/1703.abstract.

[31] S. Inouye, M. R. Andrews, J. Stenger, H. J. Miesner, D. M. Stamper-Kurn, and W. Ketterle, "Observation of Feshbach resonances in a Bose-Einstein condensate," Nature **392**, 151 (1998), URL http://dx.doi.org/10.1038/32354.

[32] M. Greiner, O. Mandel, T. Esslinger, T. W. Hansch, and I. Bloch, "Quantum phase transition from a superfluid to a Mott insulator in a gas of ultracold atoms," Nature **415**, 39 (2002), URL http://dx.doi.org/10.1038/415039a.

[33] C. A. Regal, M. Greiner, and D. S. Jin, "Observation of Resonance Condensation of Fermionic Atom Pairs," Phys. Rev. Lett. **92**, 040403 (2004), URL http://link.aps.org/doi/10.1103/PhysRevLett.92.040403.

[34] K. M. Lang, V. Madhavan, J. E. Hoffman, E. W. Hudson, H. Eisaki, S. Uchida, and J. C. Davis, "Imaging the granular structure of high-Tc superconductivity in underdoped Bi2Sr2CaCu2O8+[delta]," Nature **415**, 412 (2002), URL http://dx.doi.org/10.1038/415412a.

[35] J. T. Stewart, J. P. Gaebler, and D. S. Jin, "Using photoemission spectroscopy to probe a strongly interacting Fermi gas," Nature **454**, 744 (2008), URL http://dx.doi.org/10.1038/nature07172.

[36] W. S. Bakr, A. Peng, M. E. Tai, R. Ma, J. Simon, J. I. Gillen, S. Flling, L. Pollet, and M. Greiner, "Probing the Superfluid-to-Mott Insulator Transition at the Single-Atom Level," Science **329**, 547 (2010), http://www.sciencemag.org/content/329/5991/547.full.pdf, URL http://www.sciencemag.org/content/329/5991/547.abstract.

[37] J. F. Sherson, C. Weitenberg, M. Endres, M. Cheneau, I. Bloch, and S. Kuhr, "Single-atom-resolved fluorescence imaging of an atomic Mott insulator," Nature **467**, 68 (2010), URL http://dx.doi.org/10.1038/nature09378.

[38] J. Simon, W. S. Bakr, R. Ma, M. E. Tai, P. M. Preiss, and M. Greiner, "Quantum simulation of antiferromagnetic spin chains in an optical lattice," Nature **472**, 307 (2011), URL http://dx.doi.org/10.1038/nature09994.

[39] P. M. Preiss, R. Ma, M. E. Tai, A. Lukin, M. Rispoli, P. Zupancic, Y. Lahini, R. Islam, and M. Greiner, "Strongly correlated quantum walks in optical lattices," Science **347**, 1229 (2015), http://www.sciencemag.org/content/347/6227/1229.full.pdf, URL http://www.sciencemag.org/content/347/6227/1229.abstract.

[40] M. Cheneau, P. Barmettler, D. Poletti, M. Endres, P. Schausz, T. Fukuhara, C. Gross, I. Bloch, C. Kollath, and S. Kuhr, "Light-cone-like spreading of correlations in a quantum many-body system," Nature **481**, 484 (2012), URL http://dx.doi.org/10.1038/nature10748.

[41] T. Fukuhara, P. Schausz, M. Endres, S. Hild, M. Cheneau, I. Bloch, and C. Gross, "Microscopic observation of magnon bound states and their dynamics," Nature **502**, 76 (2013), URL http://dx.doi.org/10.1038/nature12541.

[42] T. Fukuhara, A. Kantian, M. Endres, M. Cheneau, P. Schausz, S. Hild, D. Bellem, U. Schollwock, T. Giamarchi, C. Gross, I. Bloch, and S. Kuhr, "Quantum dynamics of a mobile spin impurity," Nat Phys **9**, 235 (2013), URL http://dx.doi.org/10.1038/nphys2561.

[43] D. Greif, T. Uehlinger, G. Jotzu, L. Tarruell, and T. Esslinger, "Short-Range Quantum Magnetism of Ultracold Fermions in an Optical Lattice," Science **340**, 1307 (2013), http://www.sciencemag.org/content/340/6138/1307.full.pdf, URL http://www.sciencemag.org/content/340/6138/1307.abstract.

[44] R. A. Hart, P. M. Duarte, T.-L. Yang, X. Liu, T. Paiva, E. Khatami, R. T. Scalettar, N. Trivedi, D. A. Huse, and R. G. Hulet, "Observation of antiferromagnetic correlations in the Hubbard model with ultracold atoms," Nature **519**, 211 (2015), URL http://dx.doi.org/10.1038/nature14223.

[45] D. Leibfried, B. DeMarco, V. Meyer, D. Lucas, M. Barrett, J. Britton, W. M. Itano, B. Jelenkovic, C. Langer, T. Rosenband, and D. J. Wineland, "Experimental demonstration of a robust, high-fidelity geometric two ion-qubit phase gate," Nature **422**, 412 (2003), URL http://dx.doi.org/10.1038/nature01492.

[46] J. P. Home, D. Hanneke, J. D. Jost, J. M. Amini, D. Leibfried, and D. J. Wineland, "Complete methods set for scalable ion trap quantum information processing," Science **325**, 1227 (2009).

[47] M. A. Rowe, D. Kielpinski, V. Meyer, C. A. Sackett, W. M. Itano, C. Monroe, and D. J. Wineland, "Experimental violation of a Bell's inequality with efficient detection," Nature **409**, 791 (2001), URL http://dx.doi.org/10.1038/35057215.

[48] K. Kim, M. S. Chang, S. Korenblit, R. Islam, E. E. Edwards, J. K. Freericks, G. D. Lin, L. M. Duan, and C. Monroe, "Quantum simulation of frustrated Ising spins with trapped ions," Nature **465**, 590 (2010), URL http://dx.doi.org/10.1038/nature09071.

[49] J. W. Britton, B. C. Sawyer, A. C. Keith, C. C. J. Wang, J. K. Freericks, H. Uys, M. J. Biercuk, and J. J. Bollinger, "Engineered two-dimensional Ising interactions in a trapped-ion quantum simulator with hundreds of spins," Nature **484**, 489 (2012), URL http://dx.doi.org/10.1038/nature10981.

[50] C. Monroe, D. M. Meekhof, B. E. King, S. R. Jefferts, W. M. Itano, D. J. Wineland, and P. Gould, "Resolved-Sideband Raman Cooling of a Bound Atom to the 3D Zero-Point Energy," Phys. Rev. Lett. **75**, 4011 (1995).

[51] S. E. Hamann, D. L. Haycock, G. Klose, P. H. Pax, I. H. Deutsch, and P. S. Jessen, "Resolved-Sideband Raman Cooling to the Ground State of an Optical Lattice," Phys. Rev. Lett. **80**, 4149 (1997).

[52] H. Perrin, A. Kuhn, I. Bouchoule, and C. Salomon, "Sideband Cooling of Neutral atoms in a Far-detuned Optical lLttice," Europhys. Lett. **42**, 395 (1998).

[53] V. Vuletic, C. Chin, A. J. Kerman, and S. Chu, "Degenerate Raman Sideband Cooling of Trapped Cesium Atoms at Very High Atomic Densities," Phys. Rev. Lett. **81**, 5768 (1998).

[54] D.-J. Han, S. Wolf, S. Oliver, C. McCormick, M. T. DePue, and D. S. Weiss, "3D Raman Sideband Cooling of Cesium Atoms at High Density," Phys. Rev. Lett. **85**, 724 (2000).

[55] S. Stellmer, B. Pasquiou, R. Grimm, and F. Schreck, "Laser Cooling to Quantum Degeneracy," Phys. Rev. Lett. **110**, 263003 (2013), URL `http://link.aps.org/doi/10.1103/PhysRevLett.110.263003`.

[56] A. J. Kerman, Raman sideband cooling and cold atomic collisions in optical lattices, Ph.D. thesis, Stanford University (2002).

[57] S. Wolf, S. J. Oliver, and D. S. Weiss, "Suppression of Recoil Heating by an Optical Lattice," Phys. Rev. Lett. **85**, 4249 (2000), URL `http://link.aps.org/doi/10.1103/PhysRevLett.85.4249`.

[58] P. Maunz, T. Puppe, I. Schuster, N. Syassen, P. W. H. Pinkse, and G. Rempe, "Cavity Cooling of a Single Atom," Nature **428**, 50 (2004).

[59] A. D. Boozer, A. Boca, R. Miller, T. E. Northup, and H. J. Kimble, "Cooling to the Ground State of Axial Motion for One Atom Strongly Coupled to an Optical Cavity," Phys. Rev. Lett. **97**, 083602 (2006).

[60] L. Forster, M. Karski, J.-M. Choi, A. Steffen, W. Alt, D. Meschede, and A. Widera, "Microwave Control of Atomic Motion in Optical Lattices," Phys. Rev. Lett. **103**, 233001 (2009).

[61] X. Li, T. A. Corcovilos, Y. Wang, and D. S. Weiss, "3D Projection Sideband Cooling," Phys. Rev. Lett. **108**, 103001 (2012).

[62] D. S. Weiss, J. Vala, A. V. Thapliyal, S. Myrgren, U. Vazirani, and K. B. Whaley, "Another Way to Approach Zero Entropy for a Finite System of Atoms," Phys. Rev. A **70**, 040302(R) (2004).

[63] B. Darque, M. P. A. Jones, J. Dingjan, J. Beugnon, S. Bergamini, Y. Sortais, G. Messin, A. Browaeys, and P. Grangier, "Controlled Single-Photon Emission from a Single Trapped Two-Level Atoms," Science **309**, 454 (2005).

[64] M. K. Tey, Z. Chen, S. Abdullah-Aljunid, B. Chng, F. Huber, G. Maslennikov, and C. Kurtsiefer, "Strong Interaction Between Light and a Single Trapped Atom Without the Need for a Cavity," Nature Phys. **4**, 924 (2008).

[65] X. L. Zhang, L. Isenhower, A. T. Gill, T. G. Walker, and M. Saffman, "Deterministic Entanglement of Two Neutral Atoms via Rydberg Blockade," Phys. Rev. A **82**, 030306(R) (2010).

[66] T. Wilk, A. Gaetan, C. Evellin, J. Wolters, Y. Miroshnychenko, P. Grangier, and A. Browaeys, "Entanglement of Two Individual Neutral Atoms Using Rydberg Blockade," Phys. Rev. Lett. **104**, 101502 (2010).

[67] J. D. Thompson, T. G. Tiecke, N. P. de Leon, J. Feist, A. V. Akimov, M. Gullans, A. S. Zibrov, V. Vuletic, and M. D. Lukin, "Coupling a Single Trapped Atom to a Nanoscale Optical Cavity," Science **340**, 1202 (2013).

[68] T. G. Tiecke, J. D. Thompson, N. P. de Leon, L. R. Liu, V. Vuletic, and M. D. Lukin, "Nanophotonic quantum phase switch with a single atom," Nature **508**, 241 (2014), URL http://dx.doi.org/10.1038/nature13188.

[69] F. Serwane, G. Zurn, T. Lompe, T. Ottenstein, A. N. Wenz, and S. Jochim, "Deterministic Preparation of a Tunable Few-Fermion System," Science **332**, 336 (2011).

[70] B. Zimmermann, T. Müller, J. Meineke, T. Esslinger, and H. Moritz, "High-resolution Imaging of Ultracold Fermions in Microscopically Tailored Optical Potentials," New Journal of Physics **13**, 043007 (2011).

[71] S. Murmann, A. Bergschneider, V. M. Klinkhamer, G. Zürn, T. Lompe, and S. Jochim, "Two Fermions in a Double Well: Exploring a Fundamental Building Block of the Hubbard Model," Phys. Rev. Lett. **114**, 080402 (2015), URL http://link.aps.org/doi/10.1103/PhysRevLett.114.080402.

[72] K.-K. Ni, S. Ospelkaus, M. H. G. de Miranda, A. Pe'er, B. Neyenhuis, J. J. Zirbel, S. Kotochigova, P. S. Julienne, D. S. Jin, and J. Ye, "A High Phase-space-density Gas of Polar Molecules," Science **322**, 231 (2008).

[73] J. Beugnon, M. P. A. Jones, J. Dingjan, B. Darquié, G. Messin, A. Browaeys, and P. Grangier, "Quantum interference between two single photons emitted by independently trapped atoms," Nature **440**, 779 (2006), URL http://dx.doi.org/10.1038/nature04628.

[74] R. Lopes, A. Imanaliev, A. Aspect, M. Cheneau, D. Boiron, and C. I. Westbrook, "Atomic Hong-Ou-Mandel experiment," Nature **520**, 66 (2015), URL http://dx.doi.org/10.1038/nature14331.

[75] P. Richerme, Z.-X. Gong, A. Lee, C. Senko, J. Smith, M. Foss-Feig, S. Michalakis, A. V. Gorshkov, and C. Monroe, "Non-local propagation of correlations in quantum systems with long-range interactions," Nature **511**, 198 (2014), URL http://dx.doi.org/10.1038/nature13450.

[76] L. Isenhower, E. Urban, X. Zhang, A. Gill, T. Henage, T. Johnson, T. Walker, and M. Saffman, "Demonstration of a Neutral Atom Controlled-NOT Quantum Gate," Phys. Rev. Lett. **104**, 010503 (2010), URL http://link.aps.org/doi/10.1103/PhysRevLett.104.010503.

[77] R. Blakestad, C. Ospelkaus, A. VanDevender, J. Amini, J. Britton, D. Leibfried, and D. Wineland, "High-Fidelity Transport of Trapped-Ion Qubits through an **X**-Junction Trap Array," Phys. Rev. Lett. **102**, 153002 (2009), URL http://link.aps.org/doi/10.1103/PhysRevLett.102.153002.

[78] L. Béguin, A. Vernier, R. Chicireanu, T. Lahaye, and A. Browaeys, "Direct Measurement of the van der Waals Interaction between Two Rydberg Atoms," Phys. Rev. Lett. **110**, 263201 (2013), URL http://link.aps.org/doi/10.1103/PhysRevLett.110.263201.

[79] C. A. Sackett, D. Kielpinski, B. E. King, C. Langer, V. Meyer, C. J. Myatt, M. Rowe, Q. A. Turchette, W. M. Itano, D. J. Wineland, and C. Monroe, "Experimental entanglement of four particles," Nature **404**, 256 (2000), URL http://dx.doi.org/10.1038/35005011.

[80] L. Mazza, D. Rossini, R. Fazio, and M. Endres, "Detecting two-site spin-entanglement in many-body systems with local particle-number fluctuations," New Journal of Physics **17**, 013015 (2015), URL http://stacks.iop.org/1367-2630/17/i=1/a=013015.

[81] T. Fukuhara, S. Hild, J. Zeiher, P. Schauss, I. Bloch, M. Endres, and C. Gross, "Spatially resolved detection of a spin-entanglement wave in a Bose-Hubbard chain," arXiv:1504.02582 (2015).

[82] S. Papp, Experiments with a two-species Bose-Einstein condensate utilizing widely tunable interparticle interactions, Ph.D. thesis, University of Colorado at Boulder (2001).

[83] Y. R. P. Sortais, H. Marion, C. Tuchendler, A. M. Lance, M. Lamare, P. Fournet, C. Armellin, R. Mercier, G. Messin, A. Browaeys, and P. Grangier, "Diffraction-limited Optics for Single-atom Manipulation," Phys. Rev. A **75**, 013406 (2007).

[84] C.-Y. Shih and M. S. Chapman, "Nondestructive light-shift measurements of single atoms in optical dipole traps," Phys. Rev. A **87**, 063408 (2013), URL http://link.aps.org/doi/10.1103/PhysRevA.87.063408.

[85] F. Le Kien, P. Schneeweiss, and A. Rauschenbeutel, "Dynamical polarizability of atoms in arbitrary light fields: general theory and application to cesium," The European Physical Journal D **67**, 92 (2013), ISSN 1434-6060, URL http://dx.doi.org/10.1140/epjd/e2013-30729-x.

[86] T. G. Walker and M. Saffron, "Entanglement of Two Atoms Using Rydberg Blockade," arXiv:1202.5328 (2012).

[87] B. Richards and E. Wolf, "Electromagnetic Diffraction in Optical Systems. II. Structure of the Image Field in an Aplanatic System," Proc. R. Soc. A **253**, 358 (1959).

[88] S. Blatt, J. W. Thomsen, G. K. Campbell, A. D. Ludlow, M. D. Swallows, M. J. Martin, M. M. Boyd, and J. Ye, "Rabi Spectroscopy and Excitation Inhomogeneity in a One-dimensional Optical Lattice Clock," Phys. Rev. A **80**, 052703 (2009).

[89] A. M. Kaufman, B. J. Lester, and C. A. Regal, "Cooling a Single Atom in an Optical Tweezer to Its Quantum Ground State," Phys. Rev. X **2**, 041014 (2012), URL http://link.aps.org/doi/10.1103/PhysRevX.2.041014.

[90] D. Leibfried, R. Blatt, C. Monroe, and D. Wineland, "Quantum Dynamics of Single Trapped Ions," Rev. Modern Phys. **75**, 281 (2003).

[91] D. M. Meekhof, C. Monroe, B. E. King, W. M. Itano, and D. J. Wineland, "Generation of Nonclassical Motional States of a Trapped Atom," Phys. Rev. Lett. **76**, 1796 (1996).

[92] I. Dotsenko, Raman spectroscopy of single atoms, Ph.D. thesis, University of Bonn, Germany (2002).

[93] D. Wineland, M. Barret, J. Britton, J. Chiaverini, B. DeMarco, W. M. Itano, B. Jelenkovic, C. Langer, D. Leibfried, V. Meyer, T. Rosenband, and T. Schatz, "Quantum information processing with trapped ions," arXiv:quant-ph/0212079 (2003).

[94] D. M. Meekhof, C. Monroe, B. E. King, W. M. Itano, and D. J. Wineland, "Generation of Nonclassical Motional States of a Trapped Atom," Phys. Rev. Lett. **76**, 1796 (1996).

[95] Private communication Michael Foss-Feig.

[96] Q. A. Turchette, Kielpinski, B. E. King, D. Leibfried, D. M. Meekhof, C. J. Myatt, M. A. Rowe, C. A. Sackett, C. S. Wood, W. M. Itano, C. Monroe, and D. J. Wineland, "Heating of trapped ions from the quantum ground state," Phys. Rev. A **61**, 063418 (2000), URL http://link.aps.org/doi/10.1103/PhysRevA.61.063418.

[97] C. Tuchendler, A. M. Lance, A. Browaeys, Y. R. P. Sortais, and P. Grangier, "Energy Distribution and Cooling of a Single Atom in an Optical Tweezer," Phys. Rev. A **78**, 033425 (2008).

[98] L. Foroster, Microwave control of atomic motion in a spin dependent optical lattice, Ph.D. thesis, University of Bonn, Germany (2010).

[99] A. M. Kaufman, B. J. Lester, C. M. Reynolds, M. L. Wall, M. Foss-Feig, K. R. A. Hazzard, A. M. Rey, and C. A. Regal, "Two-particle quantum interference in tunnel-coupled optical tweezers," Science **345**, 306 (2014), http://www.sciencemag.org/content/345/6194/306.full.pdf, URL http://www.sciencemag.org/content/345/6194/306.abstract.

[100] R. J. Glauber, "The Quantum Theory of Optical Coherence," Phys. Rev. **130**, 2529 (1963).

[101] R. Hanbury Brown and R. Q. Twiss, "Correlation between Photons in two Coherent Beams of Light," Nature **177**, 27 (1956), URL http://dx.doi.org/10.1038/177027a0.

[102] C. Lang, C. Eichler, L. Steffen, J. M. Fink, M. J. Woolley, A. Blais, and A. Wallraff, "Correlations, indistinguishability and entanglement in Hong-Ou-Mandel experiments at microwave frequencies," Nat. Phys. **9**, 345 (2013), URL http://dx.doi.org/10.1038/nphys2612.

[103] E. Bocquillon, V. Freulon, J.-M. Berroir, P. Degiovanni, B. Plaçais, A. Cavanna, Y. Jin, and G. Fève, "Coherence and Indistinguishability of Single Electrons Emitted by Independent Sources," Science **339**, 1054 (2013), http://www.sciencemag.org/content/339/6123/1054.full.pdf, URL http://www.sciencemag.org/content/339/6123/1054.abstract.

[104] A. Steffen, A. Alberti, W. Alt, N. Belmechri, S. Hild, M. Karski, A. Widera, and D. Meschede, "Digital atom interferometer with single particle control on a discretized space-time geometry," Proceedings of the National Academy of Sciences **109**, 9770 (2012), http://www.pnas.org/content/109/25/9770.full.pdf+html, URL http://www.pnas.org/content/109/25/9770.abstract.

[105] M. Yasuda and F. Shimizu, "Observation of Two-Atom Correlation of an Ultracold Neon Atomic Beam," Phys. Rev. Lett. **77**, 3090 (1996).

[106] S. Fölling, F. Gerbier, A. Widera, O. Mandel, T. Gericke, and I. Bloch, "Spatial quantum noise interferometry in expanding ultracold atom clouds," Nature **434**, 481 (2005), URL http://dx.doi.org/10.1038/nature03500.

[107] M. Schellekens, R. Hoppeler, A. Perrin, J. V. Gomes, D. Boiron, A. Aspect, and C. I. Westbrook, "Hanbury Brown Twiss effect for ultracold quantum gases," Science **310**, 648 (2005).

[108] A. Ottl, S. Ritter, M. Kohl, and T. Esslinger, "Correlations and Counting Statistics of an Atom Laser," Phys. Rev. Lett. **95**, 090404 (2005).

[109] T. Rom, T. Best, D. van Oosten, U. Schneider, S. Folling, B. Paredes, and I. Bloch, "Free fermion antibunching in a degenerate atomic Fermi gas released from an optical lattice," Nature **444**, 733 (2006).

[110] T. Jeltes, J. M. McNamara, W. Hogervorst, W. Vassen, V. Krachmalnicoff, M. Schellekens, A. Perrin, H. Chang, D. Boiron, A. Aspect, and C. I. Westbrook, "Comparison of the Hanbury Brown–Twiss effect for bosons and fermions," Nature **445**, 402 (2007).

[111] S. S. Hodgman, R. G. Dall, A. G. Manning, K. G. H. Baldwin, and A. G. Truscott, "Direct measurement of long-range third-order coherence in Bose–Einstein condensates," Science **331**, 1046 (2011).

[112] P. Kok, W. J. Munro, K. Nemoto, T. C. Ralph, J. P. Dowling, and G. J. Milburn, "Linear optical quantum computing with photonic qubits," Rev. Mod. Phys. **79**, 135 (2007), URL http://link.aps.org/doi/10.1103/RevModPhys.79.135.

[113] V. Giovannetti, S. Lloyd, and L. Maccone, "Quantum-Enhanced Measurements: Beating the Standard Quantum Limit," Science **306**, 1330 (2004), http://www.sciencemag.org/content/306/5700/1330.full.pdf, URL http://www.sciencemag.org/content/306/5700/1330.abstract.

[114] E. Vetsch, D. Reitz, G. Sagué, R. Schmidt, S. T. Dawkins, and A. Rauschenbeutel, "Optical Interface Created by Laser-Cooled Atoms Trapped in the Evanescent Field Surrounding an Optical Nanofiber," Phys. Rev. Lett. **104**, 203603 (2010).

[115] G. Ghirardi and L. Marinatto, "General criterion for the entanglement of two indistinguishable particles," Phys. Rev. A **70**, 012109 (2004), URL http://link.aps.org/doi/10.1103/PhysRevA.70.012109.

[116] J. I. Cirac, "Entanglement in many-body quantum systems," arXiv:1205.3742v1 (2012).

[117] M. C. Tichy, Entanglement and interference of identical particles, Ph.D. thesis, Physikalisches Institut (2011).

[118] R. Horodecki, P. Horodecki, M. Horodecki, and K. Horodecki, "Quantum entanglement," Rev. Mod. Phys. **81**, 865 (2009), URL http://link.aps.org/doi/10.1103/RevModPhys.81.865.

[119] R. Horodecki and M. Horodecki, "Information-theoretic aspects of inseparability of mixed states," Phys. Rev. A **54**, 1838 (1996), URL http://link.aps.org/doi/10.1103/PhysRevA.54.1838.

[120] R. N. Palmer, C. Moura Alves, and D. Jaksch, "Detection and characterization of multipartite entanglement in optical lattices," Phys. Rev. A **72**, 042335 (2005), URL http://link.aps.org/doi/10.1103/PhysRevA.72.042335.

[121] M. R. Andrews, C. G. Townsend, H.-J. Miesner, D. S. Durfee, D. M. Kurn, and W. Ketterle, "Observation of Interference Between Two Bose Condensates," Science **275**, 637 (1997), http://www.sciencemag.org/content/275/5300/637.full.pdf, URL http://www.sciencemag.org/content/275/5300/637.abstract.

[122] A. E. Siegman, Lasers (University Science Books, 1986).

[123] J. Schliemann, J. I. Cirac, M. Kuś, M. Lewenstein, and D. Loss, "Quantum correlations in two-fermion systems," Phys. Rev. A **64**, 022303 (2001), URL http://link.aps.org/doi/10.1103/PhysRevA.64.022303.

[124] A. Peres, Quantum Theory: Concepts and Methods (Kluwer, New York, NY, 1993).

[125] D. J. Wineland, J. J. Bollinger, W. M. Itano, and D. J. Heinzen, "Squeezed atomic states and projection noise in spectroscopy," Phys. Rev. A **50**, 67 (1994), URL http://link.aps.org/doi/10.1103/PhysRevA.50.67.

[126] B. Lcke, M. Scherer, J. Kruse, L. Pezz, F. Deuretzbacher, P. Hyllus, O. Topic, J. Peise, W. Ertmer, J. Arlt, L. Santos, A. Smerzi, et al., "Twin Matter Waves for Interferometry Beyond the Classical Limit," Science **334**, 773 (2011), http://www.sciencemag.org/content/334/6057/773.full.pdf, URL http://www.sciencemag.org/content/334/6057/773.abstract.

[127] M. J. Holland and K. Burnett, "Interferometric detection of optical phase shifts at the Heisenberg limit," Phys. Rev. Lett. **71**, 1355 (1993), URL http://link.aps.org/doi/10.1103/PhysRevLett.71.1355.

[128] Private communication Malte Tichy.

[129] S. Fölling, S. Trotzky, P. Cheinet, M. Feld, R. Saers, A. Widera, T. Muller, and I. Bloch, "Direct observation of second-order atom tunnelling," Nature **448**, 1029 (2007), URL http://dx.doi.org/10.1038/nature06112.

[130] J. Sebby-Strabley, B. L. Brown, M. Anderlini, P. J. Lee, W. D. Phillips, J. V. Porto, and P. R. Johnson, "Preparing and probing atomic number states with an atom interferometer," Phys. Rev. Lett. **98**, 200405 (2007), ISSN 0031-9007.

[131] Manuscript in preparation, "Microscopic analysis of non-separable optical potentials with Gaussian curvature.

[132] R. Ma, M. E. Tai, P. M. Preiss, W. S. Bakr, J. Simon, and M. Greiner, "Photon-Assisted Tunneling in a Biased Strongly Correlated Bose Gas," Phys. Rev. Lett. **107**, 095301 (2011), URL http://link.aps.org/doi/10.1103/PhysRevLett.107.095301.

[133] M. Egorov, B. Opanchuk, P. Drummond, B. V. Hall, P. Hannaford, and A. I. Sidorov, "Precision measurements of s-wave scattering lengths in a two-component Bose-Einstein condensate," Phys. Rev. A **87**, 053614 (2013).

[134] H. Uys, M. J. Biercuk, A. P. VanDevender, C. Ospelkaus, D. Meiser, R. Ozeri, and J. J. Bollinger, "Decoherence due to Elastic Rayleigh Scattering," Phys. Rev. Lett. **105**, 200401 (2010), URL http://link.aps.org/doi/10.1103/PhysRevLett.105.200401.

[135] S. Fölling, S. Trotzky, P. Cheinet, M. Feld, R. Saers, A. Widera, T. Muller, and I. Bloch, "Direct observation of second-order atom tunnelling," Nature **448**, 1029 (2007), URL http://dx.doi.org/10.1038/nature06112.

[136] J. W. Britton, B. C. Sawyer, A. C. Keith, C. C. J. Wang, J. K. Freericks, H. Uys, M. J. Biercuk, and J. J. Bollinger, "Engineered two-dimensional Ising interactions in a trapped-ion quantum simulator with hundreds of spins," Nature **484**, 489 (2012), URL http://dx.doi.org/10.1038/nature10981.

[137] K. Brown, A. Wilson, Y. Colombe, C. Ospelkaus, A. Meier, E. Knill, D. Leibfried, and D. Wineland, "Single-qubit-gate error below 10^{-4} in a trapped ion," Phys. Rev. A **84**, 030303 (2011), URL http://link.aps.org/doi/10.1103/PhysRevA.84.030303.

[138] J. H. Lee, E. Montano, I. H. Deutsch, and P. S. Jessen, "Robust site-resolvable quantum gates in an optical lattice via inhomogeneous control," Nat Commun **4** (2013), URL http://dx.doi.org/10.1038/ncomms3027.

[139] D. Hayes, P. Julienne, and I. Deutsch, "Quantum Logic via the Exchange Blockade in Ultracold Collisions," Phys. Rev. Lett. **98**, 070501 (2007), URL http://link.aps.org/doi/10.1103/PhysRevLett.98.070501.

[140] C. Weitenberg, S. Kuhr, K. Mølmer, and J. Sherson, "Quantum computation architecture using optical tweezers," Phys. Rev. A **84**, 032322 (2011), URL http://link.aps.org/doi/10.1103/PhysRevA.84.032322.

[141] A. Peres, "Separability Criterion for Density Matrices," Phys. Rev. Lett. **77**, 1413 (1996), URL http://link.aps.org/doi/10.1103/PhysRevLett.77.1413.

[142] M. Horodecki, P. Horodecki, and R. Horodecki, "Separability of Mixed States: Necessary and Sufficient Conditions," arXiv:quant-ph/9605038 (1996).

[143] E. Knill, R. Laflamme, and G. J. Milburn, "A Scheme For Efficient Quantum Computing With Linear Optics," Nature **409**, 46 (2010).

[144] L. D. Landau, "The theory of a Fermi liquid," Sov. Phys. JETP **3**, 920 (1957).

[145] E. Lifshitz and L. P. Pitaevskii, Statistical Physics, Part 2, vol. 9 of Landau and Lifshitz Course of Theoretical Physics (Butterworth-Heinemann, 1980).

[146] M. Foss-Feig, M. Hermele, and A. M. Rey, "Probing the Kondo lattice model with alkaline-earth-metal atoms," Phys. Rev. A **81**, 051603 (2010), URL http://link.aps.org/doi/10.1103/PhysRevA.81.051603.

[147] M. Foss-Feig, M. Hermele, V. Gurarie, and A. M. Rey, "Heavy fermions in an optical lattice," Phys. Rev. A **82**, 053624 (2010), URL http://link.aps.org/doi/10.1103/PhysRevA.82.053624.

[148] T. Müller, S. Fölling, A. Widera, and I. Bloch, "State Preparation and Dynamics of Ultracold Atoms in Higher Lattice Orbitals," Phys. Rev. Lett. **99**, 200405 (2007), URL http://link.aps.org/doi/10.1103/PhysRevLett.99.200405.

[149] Y. Castin and J. Dalibard, "Relative phase of two Bose-Einstein condensates," Phys. Rev. A **55**, 4330 (1997), URL http://link.aps.org/doi/10.1103/PhysRevA.55.4330.

[150] P. Calabrese and J. Cardy, "Entanglement entropy and quantum field theory," Journal of Statistical Mechanics: Theory and Experiment **2004**, P06002 (2004), URL http://stacks.iop.org/1742-5468/2004/i=06/a=P06002.

[151] P. Calabrese and J. Cardy, "Evolution of entanglement entropy in one-dimensional systems," Journal of Statistical Mechanics: Theory and Experiment **2005**, P04010 (2005), URL http://stacks.iop.org/1742-5468/2005/i=04/a=P04010.

[152] A. N. Wenz, G. Zrn, S. Murmann, I. Brouzos, T. Lompe, and S. Jochim, "From Few to Many: Observing the Formation of a Fermi Sea One Atom at a Time," Science **342**, 457 (2013), http://www.sciencemag.org/content/342/6157/457.full.pdf, URL http://www.sciencemag.org/content/342/6157/457.abstract.

[153] A. J. Daley, H. Pichler, J. Schachenmayer, and P. Zoller, "Measuring Entanglement Growth in Quench Dynamics of Bosons in an Optical Lattice," Phys. Rev. Lett. **109**, 020505 (2012), URL http://link.aps.org/doi/10.1103/PhysRevLett.109.020505.

[154] M. Rigol, V. Dunjko, and M. Olshanii, "Thermalization and its mechanism for generic isolated quantum systems," Nature **452**, 854 (2008), URL http://dx.doi.org/10.1038/nature06838.

[155] M. Cramer, A. Flesch, I. P. McCulloch, U. Schollwöck, and J. Eisert, "Exploring Local Quantum Many-Body Relaxation by Atoms in Optical Superlattices," Phys. Rev. Lett. **101**, 063001 (2008), URL http://link.aps.org/doi/10.1103/PhysRevLett.101.063001.

[156] S. Trotzky, Y.-A. Chen, A. Flesch, I. P. McCulloch, U. Schollwock, J. Eisert, and I. Bloch, "Probing the relaxation towards equilibrium in an isolated strongly correlated one-dimensional Bose gas," Nat Phys **8**, 325 (2012), URL http://dx.doi.org/10.1038/nphys2232.

[157] M. C. Tichy, "Interference of identical particles from entanglement to boson-sampling," Journal of Physics B: Atomic, Molecular and Optical Physics **47**, 103001 (2014), URL http://stacks.iop.org/0953-4075/47/i=10/a=103001.

[158] Private communication Kaden Hazzard.

Appendix A

Derivation of bounds for distinguishable particles and further analysis of the two-particle tunneling contrast

A.1 Creation of bounds and analysis of the HOM oscillations

In this section, our goals are two-fold. We first derive bounds on the behavior of distinguishable particles, experimental violations of which support our claims of indistinguishability. Secondly, we show that with a reasonable set of assumptions, the observed HOM contrast $A_{P_{11}}$ and dip $P_{11}(t_{\mathrm{HOM}}) = P_{\mathrm{HOM}}^{\mathrm{min}}$ are consistent with our thermometry and single-particle tunneling characterization. A crucial aspect of both of these goals is the availability of the single-particle data, without which the claims made in this section would be more difficult to support. Therefore, the ability to post-select our data on single and two particle experiments with known initial and final conditions permits a level of analysis that is not typically available, and is experimentally empowering for understanding systems of increasing system size.

A.1.1 Constructing two-particle tunneling oscillation bounds on distinguishable particles

A.1.1.1 Non-interacting distinguishable particles

Here we will use the single-particle data to construct an expectation for the two-particle experiments, assuming the particles are distinguishable and non-interacting.[1] We make no spec-

[1] Note that this is a summary of calculations originally formulated and performed by Michael Foss-Feig and Michael Wall.

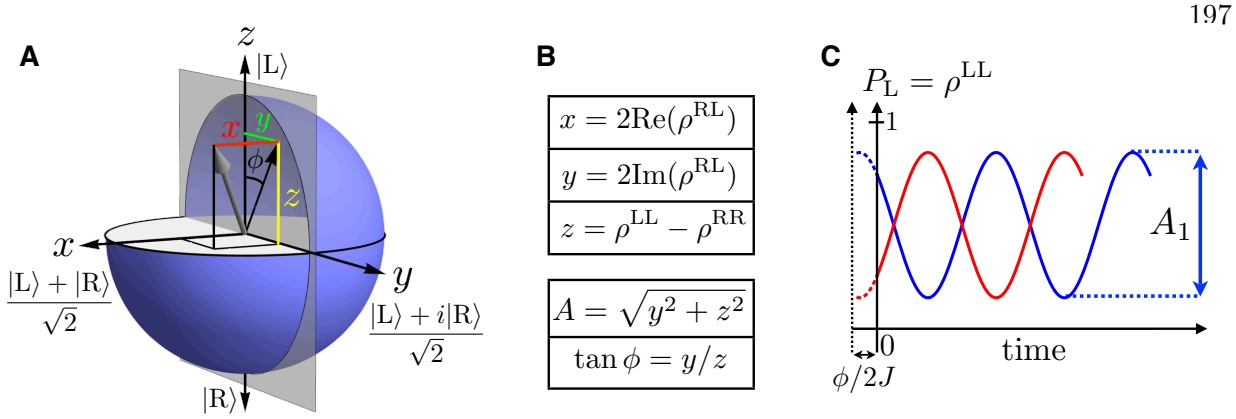

Figure A.1: (a) Bloch sphere used to describe the single-atom density matrices. (b) Two tables: The top one summarizes the connection between Cartesian coordinates of the Bloch vector and populations/coherences in the $|\mathrm{L}\rangle$,$|\mathrm{R}\rangle$ basis, while the bottom one connects the Cartesian coordinates to experimentally measured phase and contrast. (c) Schematic of the single-particle dynamics and the meaning of $\phi_{1(2)}$ and $A_{1(2)}$.

ification of the source of distinguishabilty, but this must exist in an observable degree of freedom independent of the spatial degree of freedom that is coherently-coupled by the tunneling. The additional label manifest, for example, in the particle's spin, allows us to treat the two-particle experiments as follows: we call "atom 1" ("atom 2") the particle the initially starts on the left (right). Using the time origin of $t = 0$ defined in Section 4.5.1, we can define density matrices $\rho_i(t)$,

$$\rho_1(0) = \overbrace{\begin{pmatrix} \rho_1^{\mathrm{LL}}(0) & \rho_1^{\mathrm{LR}}(0) \\ \rho_1^{\mathrm{RL}}(0) & \rho_1^{\mathrm{RR}}(0) \end{pmatrix}}^{\text{originally in left well}}, \qquad \rho_2(0) = \overbrace{\begin{pmatrix} \rho_2^{\mathrm{LL}}(0) & \rho_2^{\mathrm{LR}}(0) \\ \rho_2^{\mathrm{RL}}(0) & \rho_2^{\mathrm{RR}}(0) \end{pmatrix}}^{\text{originally in right well}}.$$

Since we are assuming distinguishability and an absence of interactions, we can construct the expected two-particle dynamics via the separable two-particle density matrix in the combined Hilbert space of the two particles. An understanding of these two-particle dynamics is aided by parsing the single-particle density matrices as follows,

$$\rho_1(0) = \frac{1}{2}\begin{pmatrix} 1+z_1 & x_1 - iy_1 \\ x_1 + iy_1 & 1 - z_1 \end{pmatrix}, \qquad \rho_2(0) = \frac{1}{2}\begin{pmatrix} 1+z_2 & x_2 - iy_2 \\ x_2 + iy_2 & 1 - z_2 \end{pmatrix}.$$

where the complex off-diagonals encode the single-particle coherences in the $\{|L\rangle, |R\rangle\}$ basis of the double-well. The effective spin-1/2 space can be represented on the Bloch-sphere, as shown

in Figure A.1a: this picture helps explain the extent to which experimental observables can constrain a theoretical expectation of distinguishable particles. In this picture, the eigenstates of our measurement observable, $\{|L\rangle, |R\rangle\}$, correspond to the z-axis, and the angle of the Bloch-sphere projection in the $x-y$ plane is defined by the angle $\theta_i = \tan^{-1}(y_i/x_i)$ of the coherences. Therefore, for the single particle i, the Bloch-vector has components $\{x_i, y_i, z_i\}$ and the tunneling realizes the single-particle Hamiltonian,

$$H_{BS}^{SP} = J\sigma_x + \frac{\Delta}{2}\sigma_z. \tag{A.1}$$

Therefore, on-resonance tunneling realizes rotations of the Bloch sphere about the x-axis in direct analogy to resonant Rabi-oscillations at $\Omega = 2J$. Since at $t = 0$, we have experimentally observed prior onset of tunneling, there can be a phase shift of the dynamics encoded in the y-component of the Bloch vector. We can express the measured oscillation contrast of subsequent single-particle tunneling oscillations for each atom, A_1 and A_2, in terms of the density matrix components as follows,

$$A_1 = \sqrt{y_1^2 + z_1^2} \qquad A_2 = \sqrt{y_2^2 + z_2^2}, \tag{A.2}$$

and the measured phases, ϕ_1 and ϕ_2, of these oscillations,

$$\tan\phi_1 = y_1/z_1 \qquad \tan\phi_2 = y_2/z_2. \tag{A.3}$$

These phases are just the initial tilt of Bloch vectors off the z-axis into the $y-z$ plane. Since each atom has two independent equations involving y_i, z_i and measured quantities, we can constrain experimentally the projection of the Bloch-vector along the y and z axes. However, the projection of the vector along x is not experimentally constrained. This is because our tunneling measurements cannot distinguish whether the quantum state of the single particles is impure (yielding $(x_i^2 + y_i^2 + z_i^2)^{1/2} < 1$), or if the state is pure but with finite projection onto the x-axis at $t = 0$. This latter case is invariant with respect to H_{BS}^{SP} when $\Delta = 0$, and hence is experimentally manifest as $A_i < 1$ just like an impure single-particle density matrix.[2] Nevertheless, we can still express the observed

[2] In conjunction with Ramsey spectroscopy, we could however experimentally constrain the x component.

dynamics for atom 1 and 2 in terms of these quantities as,

$$P_L^1 = \rho_1^{\mathrm{LL}}(t) = \frac{1}{2} + \frac{A_1}{2}\cos(2Jt - \phi_1), \tag{A.4}$$

$$P_L^2 = \rho_2^{\mathrm{LL}}(t) = \frac{1}{2} - \frac{A_2}{2}\cos(2Jt - \phi_2), \tag{A.5}$$

where we have invoked the notation from measurement sections in order to concretely establish the connection between the measurements and this theoretical treatment.

Our goal is now to use our parameterization of the single-particle density matrices to construct the $P_{\mathrm{dist}}(t)$ used in our analysis. In the absence of interactions and by assumption of distinguishability, the two-particle density matrix is the separable Kronecker product of the single particle density matrices,

$$\rho_{\mathrm{dist}}(0) = \rho_1(0) \otimes \rho_2(0). \tag{A.6}$$

For the two-particle experiments, we measure $P_{11}(t)$ corresponding to the operator O_{11}. It can be written,

$$O_{11} = |L_1\rangle\langle L_1| \otimes |R_2\rangle\langle R_2| + |L_2\rangle\langle L_2| \otimes |R_1\rangle\langle R_1|, \tag{A.7}$$

which is simply a detector of the two possible ways of observing a particle in each well. For distinguishable particles, we expect for $P_{11}(t)$,

$$P_{\mathrm{dist}}(t) = Tr(O_{11}\rho_{\mathrm{dist}}(t)). \tag{A.8}$$

This expression can is then easily simplified to,

$$\begin{aligned} P_{\mathrm{dist}}(t) &\equiv \mathrm{Tr}\left[\rho(t)|\mathrm{L}\rangle_1\langle L|_1 \otimes |\mathrm{R}\rangle_2\langle \mathrm{R}|_2\right] + \mathrm{Tr}\left[\rho(t)|\mathrm{R}\rangle_1\langle R|_1 \otimes |\mathrm{L}\rangle_2\langle \mathrm{L}|_2\right] \\ &= \rho_1^{\mathrm{LL}}(t)\rho_2^{\mathrm{RR}}(t) + \rho_1^{\mathrm{RR}}(t)\rho_2^{\mathrm{LL}}(t) \\ &= P_1^{\mathrm{L}}(t)P_2^{\mathrm{R}}(t) + P_1^{\mathrm{R}}(t)P_2^{\mathrm{L}}(t), \end{aligned} \tag{A.9}$$

corresponding to the equation used in the Section 4.7 to define the purple points in Figures 4.14 and 4.16. As expected, it is the incoherent sum of the probabilities associated with the two paths leading to the atoms in different wells, namely, both atoms tunneling or both atoms remaining where they

started. This equation can be expressed in terms of the measured single-particle quantities as,

$$P_{\text{dist}}(t) = \frac{1}{2} + \frac{A_1 A_2}{2} \cos(2Jt - \phi_1) \cos(2Jt - \phi_2). \tag{A.10}$$

This implies that the expected contrast of the purple points in Figure 4.14 should be $A_1 A_2/2$, which is indeed the case as can be checked via Table A.1. Furthermore, our observation that the oscillation contrast of $P_{11}(t)$ significantly exceeds this quantity corroborates our claims of indistinguishability when assuming the particles are non-interacting. Conveniently, this bound includes the effect of loss and finite single-particle contrast; though the former quantity was not included in the calculations in these sections, it corresponds to probability outside the Hilbert space and reduces the contrast proportionately regardless of whether there is additional contrast reduction from impurity or Bloch vector tilting along x.

Lastly, we can use these equations to also constrain $P_{\text{HOM}}^{\text{min}}$ for non-interacting, distinguishable particles. The expression in Eq. A.10 reaches a minimum at $t_{\text{HOM}} = 2\pi/8J + t_{corr}$, where the single-particle tunneling trajectories intersect at a value of 0.5 since the tunneling is symmetric (neglecting single particle loss). As was discussed in the ramp section, $t_{corr} = \phi_{1,2}/2J$ defines the temporal shift in the tunneling from $t = 0$. At t_{HOM} it follows then that the cosine terms vanish, leaving $P_{\text{dist}}(t_{\text{HOM}}) = 0.5$; this is just the expected outcome of two equally-weighted, flipped coins landing differently. Therefore, we have a second bound that an observation of $P_{11}(t_{\text{HOM}}) < P_{\text{dist}} = 0.5$ proves indistinguishability for non-interacting distinguishable particles. Since we have some likelihood of one of the atoms being lost due to our vacuum lifetime and thereby leading to a 0 event in P_{11}, this bound of 0.5 is reduced to $0.5(1 - P_{\text{loss}})^2$.

A.1.1.2 Interacting distinguishable particles

The above treatment excludes the effect of interactions, which can induce spatial correlations between the distinguishable particles. However, we can use the treatment above to form bounds including the effect of interactions. Since minimal tunneling occurs prior to the end of the ramp, we will neglect the effect of any spatial correlations adiabatically introduced that could arise during

the ramp down itself, and treat U and J as static quantities appropriate to the final trap in which tunneling occurs[3] . Furthermore, this assumption allows us to use the uncorrelated/separable density matrix of Eq. A.7 as our initial state. The static Hamiltonian for the interacting two-particle system is,

$$\hat{H} = \begin{pmatrix} U & -2J & 0 & 0 \\ -2J & 0 & 0 & 0 \\ 0 & 0 & U & 0 \\ 0 & 0 & 0 & 0 \end{pmatrix}, \tag{A.11}$$

where the two-particle basis is,

$$\langle \mathbf{r}_1, \mathbf{r}_2 | + \rangle = \frac{1}{\sqrt{2}} \left(\psi_L(\mathbf{r}_1) \psi_L(\mathbf{r}_2) + \psi_R(\mathbf{r}_1) \psi_R(\mathbf{r}_2) \right) \tag{A.12}$$

$$\langle \mathbf{r}_1, \mathbf{r}_2 | S \rangle = \frac{1}{\sqrt{2}} \left(\psi_L(\mathbf{r}_1) \psi_R(\mathbf{r}_2) + \psi_R(\mathbf{r}_1) \psi_L(\mathbf{r}_2) \right) \tag{A.13}$$

$$\langle \mathbf{r}_1, \mathbf{r}_2 | - \rangle = \frac{1}{\sqrt{2}} \left(\psi_L(\mathbf{r}_1) \psi_L(\mathbf{r}_2) - \psi_R(\mathbf{r}_1) \psi_R(\mathbf{r}_2) \right) \tag{A.14}$$

$$\langle \mathbf{r}_1, \mathbf{r}_2 | A \rangle = \frac{1}{\sqrt{2}} \left(\psi_L(\mathbf{r}_1) \psi_R(\mathbf{r}_2) - \psi_R(\mathbf{r}_1) \psi_L(\mathbf{r}_2) \right) . \tag{A.15}$$

Expressed in first quantization, these are the symmetrized states that are used to represented an arbitrary distinguishable two-particle state. To translate the treatment from above for non-interacting distinguishable particles into this symmetry respecting basis, we need only equally weight the two-particle states in the spatially symmetric and anti-symmetric sectors to reflect the observability of the labels 1 and 2. For example, the state $|L_1\rangle|R_2\rangle$ equally projects onto the second and fourth basis states above. In practice, this basis transformation is realized by acting on the two-particle density matrix of Eq. A.7 with the appropriate rotation matrix.

We now seek an expression for $P_{11}(t)$ for an arbitrary initial two-particle density matrix in

[3] Note, however, that were we to include ramp down effects, it would only further increase the lower bound on the observed P_{11}, since this inclusion would cause some quantum amplitude for occupation of the interacting ground-state. For non-zero positive interactions, the ground-state increases the likelihood that the atoms occupy different wells.

the above basis. For the completely general initial density matrix,

$$\rho(0) = \begin{pmatrix} a & \alpha & \beta & \gamma \\ \alpha^\star & b & \epsilon & \zeta \\ \beta^\star & \epsilon^\star & c & \eta \\ \gamma^\star & \zeta^\star & \eta^\star & 1-a-b-c \end{pmatrix}, \tag{A.16}$$

it can be shown that

$$P_{11}(t) = 1 - a - c + \frac{4J\left(2J(a-b) + U\mathcal{R}(\alpha)\right)}{\omega_{JU}^2} - \frac{4J\left(2J(a-b) + U\mathcal{R}(\alpha)\right)}{\omega_{JU}^2}\cos(\omega_{JU}t) \tag{A.17}$$

$$- \frac{4J\mathcal{I}(\alpha)}{\omega_{JU}}\sin(\omega_{JU}t)\ . \tag{A.18}$$

Here $\omega_{JU}^2 = 16J^2 + U^2$, and $\mathcal{R}(\bullet)$ and $\mathcal{I}(\bullet)$ denote real and imaginary parts. This is computed by taking this density matrix, evolving it in the von-Neumann equation under the Hamiltonian in Eq. A.11, and computing $\mathrm{Tr}(O_{11}\rho(t))$. Mathemagica does some simplification afterward.

Transforming the density matrix of Eq. A.7 into the basis shown in Eq. A.15, and applying Eq. A.17, it can be shown that the minimum value of $P_{\mathrm{dist}}(t)$ is,

$$\begin{aligned}\mathcal{P}(x) =& \frac{2 + A_1A_2}{4} + \frac{U(Jx + UA_1A_2\cos(2\phi)/4)}{16J^2 + U^2} \\ & - \frac{J\sqrt{(Ux - 4JA_1A_2\cos 2\phi)^2 + 64J^2A_1^2A_2^2\cos^2\phi\sin^2\phi + U^2A_1^2A_2^2\sin^2(2\phi)}}{16J^2 + U^2},\end{aligned} \tag{A.19}$$

while the oscillation contrast is given by,

$$\mathcal{A}(x) = \frac{2J\sqrt{(Ux - 4JA_1A_2\cos 2\phi)^2 + 64J^2A_1^2A_2^2\cos^2\phi\sin^2\phi + U^2A_1^2A_2^2\sin^2(2\phi)}}{16J^2 + U^2}, \tag{A.20}$$

where we have set $\phi_1 = \phi_2 = \phi$ (since the equality of these phases is confirmed experimentally). We can now apply the constraints imposed by the single particle density matrices, namely,

$$x_1 \leq (1 - A_1^2)^{1/2} \quad \text{and} \quad x_2 \leq (1 - A_2^2)^{1/2}. \tag{A.21}$$

When x_i is maximal, this corresponds to unity length single-particle Bloch vectors and maximal coherences along x. $P(x)$ and $A(x)$ are separately minimized and maximized, respectively, within

the space constrained by the experimental measurements in Table A.1 and the inequalities in Eq A.21. This occurs for both at a value,

$$x_0 = -(1 - A_1^2)^{1/2} - (1 - A_2^2)^{1/2}. \tag{A.22}$$

In Figure A.2, we show the outcome of the above procedure for the evil and unlikely case of $x = x_0$ and the excessively likely case of $x = 0$. These "$x_0$ist" statements are made for the following reasons. The initial single-particle Bloch vectors that correspond to x_0 are those which each have the same projection along x, i.e. $r_1 = r_2$ and $\theta_1 = \theta_2$. If the x-projection of the single particle Bloch vectors is non-zero (i.e. $\theta_i \neq Z_{odd}\pi/2$, where Z_{odd} is an odd integer), then according to Eq. A.1, this is necessarily due to the presence of a bias at the end of the ramp when a small amount of tunneling occurs. For a fixed bias this would yield $\theta_1 = -\theta_2$ since σ_z causes precession in opposing directions for Bloch vectors on opposites sides of the equator: near $t = 0$, $z_1 > 0$ and $z_2 < 0$ with $|z_1| = |z_2|$, yielding $x = 0$. A fluctuating bias, on the other hand, dephases the coherences to yield $x_i = x = 0$ and a shortened Bloch vector. Experimentally, therefore, it is very difficult (basically impossible) to produce non-zero x, and so we compare our observed HOM oscillation contrast $A_{P_{11}}$ and dip $P_{\text{HOM}}^{\text{min}}$ to the more experimentally appropriate case of $A(0)$ and $P(0)$ as well. For this case, the expected reduction (increase) of $A(0)$ ($P(0)$) due to the suppression of two-particle tunneling from the interactions is manifest. But either way, even when including the evil x_0 case, our measurements violate the behavior of interacting distinguishable particles.

A.2 Analysis of observed HOM interference: understanding indistinguishability with imperfect beam splitters

While the violation of the bounds above support the presence of indistinguishability and HOM interference in our experiment, we can also borrow elements of the analysis to try to understand whether the contrast we observe makes sense given the experimental information available. An important feature of the Hamiltonian in Eq. A.11 is that the second two basis states, $|A\rangle$ and $|-\rangle$ completely decouple from the resonant tunneling dynamics, each contributing a static $P_{11} = 1$

Important numbers from tunneling dynamics plots

Measurement	P_{loss}	$A_{P_{11}}$	$A_{P_{\text{dist}}}$	U/J	A_1	A_2	ϕ
Fig. 4.14b, e	0.049(2)	0.46(2)	0.282(12)	0.44(4)	0.722(15)	0.765(16)	−0.20(7)
Fig. 4.14 c,f	0.034(2)	0.48(2)	0.306(18)	0.22(2)	0.77(2)	0.83(2)	−0.45(7)

Important numbers from t_{HOM} plots

Measurement	P_{loss}	$(1-P_{\text{loss}})^2/2$	P_{HOM}^{min}
Fig. 4.16a	0.032(2)	0.4689(19)	0.314(14)
Fig. 4.16b	0.0337(17)	0.4669(16)	0.296(10)
Fig. 4.16c	0.0346(15)	0.4660(14)	0.28(2)

Table A.1: Summary of the important parameters for understanding the experimentally observed two-particle interference. The experimental signature of the HOM effect is reflected in the difference between our measurements and the expectation for distinguishable atoms: In the top table the values to compare are $A_{P_{11}}$ and $A_{P_{\text{dist}}}$. In the bottom table the values to compare are $(1-P_{\text{loss}})^2/2$ and $P_{\text{HOM}}^{\text{min}}$. Each value of P_{loss} is computed by taking the mean over all single atom data in the specified set. The values tabulated here are used to produce the distinguishable limits shown in Fig. A.2.

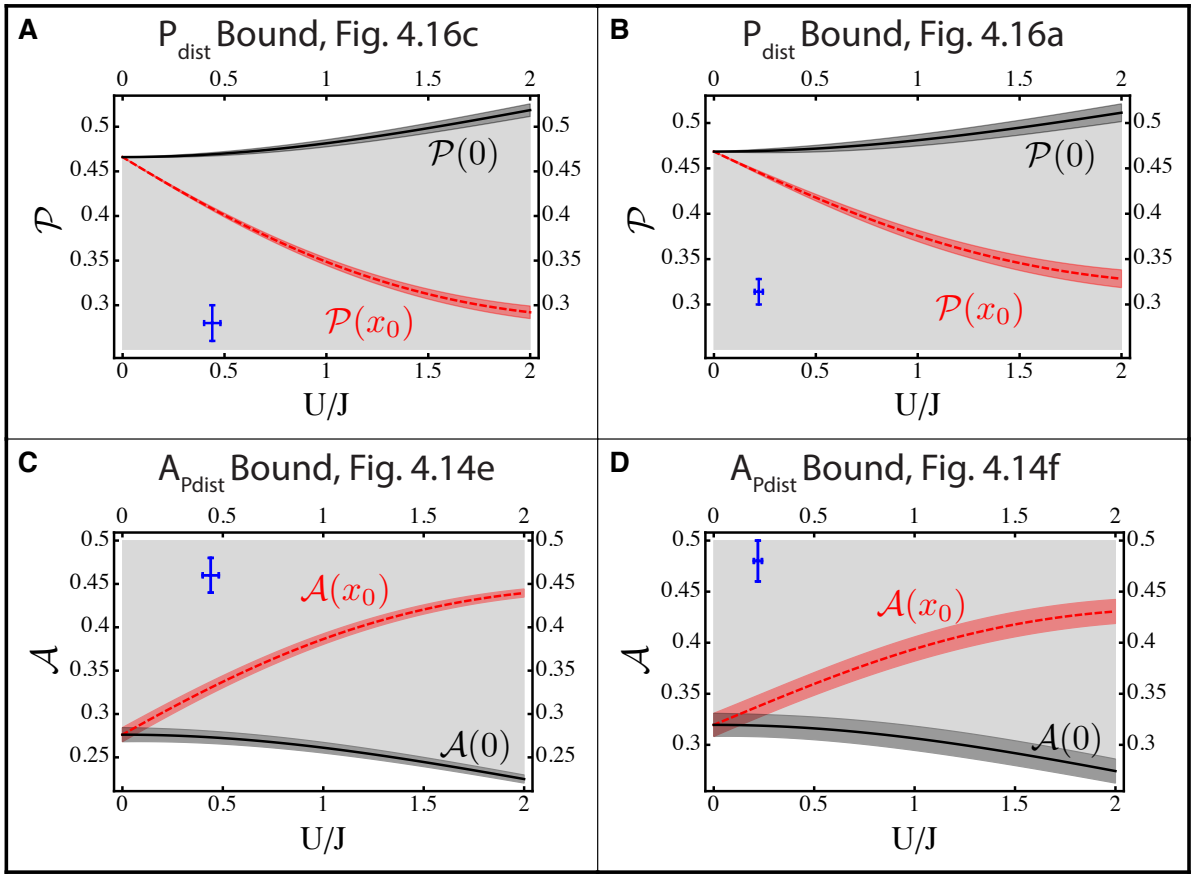

Figure A.2: Bounds on $P_{\text{dist}}(t_{\text{HOM}})$ (a,b) and $A_{P_{\text{dist}}}$ (c,d): The two left panels (a,c) are for experiments with $U/J = 0.44(4)$, while the two right panels (b,d) are for experiments with $U/J = 0.22(2)$. In all plots, the figure in the main text to which the presented data corresponds is given in the plot label. In panels a and b, the black curve is $\mathcal{P}(x = 0)$, which is a lower bound on the HOM dip for distinguishable particles assuming no initial coherences along the x-direction of the Bloch sphere. The dark shaded uncertainty region of the curve is obtained by propagating uncertainties in the experimentally measured single-particle amplitudes (A_1,A_2) and phases (ϕ_1,ϕ_2) through Eq. (A.19). The light shaded region below the black curve is therefore classically forbidden, i.e. inaccessible to distinguishable particles. The red dashed curve is $\mathcal{P}(x_0)$, which is the evil and unlikely case scenario that could, in principle, be saturated by distinguishable particles (the red shaded region is obtained in the same way). The measured minimum of the HOM dip ($P_{\text{HOM}}^{\text{min}}$, blue point) sits in the classically forbidden region. Panels c and d are similar to the top panels, except now we plot the contrast bound ($\mathcal{A}$) and the blue points are measured values of $A_{P_{11}}$. The numbers used to create this plot are tabulated in Table A.1.

and $P_{11} = 0$, respectively. The former case was noted earlier as well in our discussion of distinguishability for the observed two-particle oscillations. The first two basis states, on the other hand, are coupled, and as such each oscillate out of phase by π. This means that the imbalance between

the probabilities of being in the $|S\rangle$ and $|+\rangle$ states determines the oscillation contrast of $P_{11}(t)$, as is also illustrated by Eq A.17.

Using these simple observations, we wish to now use the single particle contrasts, in conjunction with an assumption about the character of the initial density matrix, to form an expectation for the HOM dip $P_{11}(t_{\mathrm{HOM}}) = P_{\mathrm{HOM}}^{\mathrm{min}}$. Ideally, we could predict the expected HOM dip if we knew the full density matrix at any given time. However, our observations of P_{11} only supply us with information about the probabilities of the particles being found in the $|A\rangle$ and $|S\rangle$ versus $|+\rangle$ and $|-\rangle$ sectors, but not the breakdown within each sector. Given our observations of a depth-dependent contrast, and the resulting evidence for bias fluctuations, we will make the following assumption: at $t = 0$, two-particle states of different **total** S_z on the composite Bloch sphere of two particles (in the basis of $\{L, R\}$) are incoherent.[4] This assumption is justified because fluctuations in Δ should dephase the states $|A\rangle$ and $|S\rangle$ with respect to $|2,0\rangle = \frac{1}{\sqrt{2}}(|+\rangle + |-\rangle)$ and $|0,2\rangle = \frac{1}{\sqrt{2}}(|+\rangle - |-\rangle)$, since the first two states have $S_z = 0$ while the latter two have $S_z = \pm 1$. Similarly, for the single particle experiments, the finite contrast we take to be due to shortening of the single particle Bloch vector, as opposed to coherences. In other words, we assume $x_i = 0$ in the language of the previous section. I will call all of this the "incoherence assumption".

Using the above assumption, along with our thermometry, we can conjecture an expression for the expected HOM oscillation contrast $A_{P_{11}}^{\mathrm{exp}}$ and dip $P_{\mathrm{HOM}}^{\mathrm{exp}}$. We will first consider the effect of temperature in the absence of the effects of single-particle contrasts. Assuming the radial ground-state fraction is effectively unity, the single particle axial ground-state fraction[5] of $P_{\mathrm{GS}} = 0.85(11)$ defines the distinguishability introduced by motional degrees of freedom. It implies that the likelihood that the atoms are indistinguishable is $P^{\mathrm{ind}} = 0.85^2 + 0.13^2 = 0.74(18)$, where the second term comes from the thermal probability that the atoms both occupy the first axial excited state

[4] I am loosely referring to $t = 0$ here in that I am not including the phase shift. Specifically, I mean any amplitude outside that which participates in the P_{11} oscillations we will assume to be strictly incoherent

[5] For the error bar of 0.11 quoted, I took the mean of the upper and lower value to simplify the analysis. They differ by 2%.

(higher order terms we neglect). Therefore, from this effect alone we would expect [157],

$$P_{\mathrm{HOM}}^{\mathrm{min}} = 0 \cdot P^{\mathrm{ind}} + (1 - P_{\mathrm{loss}})^2/2 \cdot (1 - P^{\mathrm{ind}}) = 0.12(5). \tag{A.23}$$

But, as said, this excludes any effects associated with the atom beam splitter itself, and clearly underestimates the imperfections of the experiment.

To understand the effect of the beam splitter, we will first neglect the presence of distinguishability in the experiment and consider indistinguishable atoms on an imperfect beam splitter. This means we seek to understand how to include the impurity of the single particle density matrices in the $\{L, R\}$ basis. Including these effects is tricky because our goal is to construct a symmetrized two-particle density matrix of impure single particle density matrices. For example, suppose both single particle density matrices were completely mixed: $\rho_i = \frac{1}{2}(|L\rangle\langle L| + |R\rangle\langle R|)$. If we seek to compute,

$$\rho = \rho_1 \otimes \rho_2, \tag{A.24}$$

then how do we choose which pairs of spatial states in each single particle mixture to symmetrize in order to respect the quantum statistics of the atoms? The problem can be recast as follows: each run of our experiment produces a two-particle state that respects the quantum statistics of the atoms, but that state may vary shot-to-shot. Can we use the single particle density matrices that we understand to construct the distribution of these two-particle states about which we have less information? To approach this problem, we use second quantization to build up the final two-particle density matrix from the single-particle density matrices, while retaining the symmetry of the two-particle states comprising the mixed density matrix.

Consider first the case of our single particle measurements where we deduce oscillation contrasts A_i. By our incoherence assumption, and given the closeness of the mean of the oscillations of $P_{L,R}$ to 0.48 (which is the ideal 0.5 corrected for loss, see Section 4.5.2.4), we can write the initial $t = 0$ single particle density matrix,

$$\rho_i = \frac{1 - A_i}{2}\left(|L\rangle\langle L| + |R\rangle\langle R|\right) + A_i|p\rangle\langle p|, \tag{A.25}$$

where $p = L$ ($p = R$) if $i = 1$ ($i = 2$). This density matrix yields oscillation contrast A_i because the initial probability imbalance in the $\{L, R\}$ basis determines the single-particle oscillation contrast in the absence of coherences. We can rewrite this in second quantization as,

$$\rho_i = \frac{1 - A_i}{2} \left(a_L^\dagger |0\rangle\langle 0| a_L + a_R^\dagger |0\rangle\langle 0| a_R \right) + A_i a_p^\dagger |0\rangle\langle 0| a_p \tag{A.26}$$

Using this equation we can iterate to create the two-particle density matrix $\rho_{\rm com}$ at $t = 0$ as follows. In the absence of any knowledge about the specifics of the noise that create ρ_i, we make the assumption that the noise does not introduce any correlations between the particles. This is a simplifying assumption, which need not be true. Indeed, if during the ramp there are fluctuations in the bias as we suspect, this will induce $x_1 = -x_2$ on any given run of the experiment. However, given that we do not know the exact process by which we end up with ρ_i, it is a necessary step in attempting to form a basic expectation for the two-particle oscillation contrast in terms of the single particle oscillation contrasts. We conjecture then [158],

$$\rho_{\rm com} = \frac{1 - A_2}{2} \left(a_L^\dagger \rho_1 a_L + a_R^\dagger \rho_1 a_R \right) + A_2 a_R^\dagger \rho_1 a_R, \tag{A.27}$$

which we note is symmetric under exchange of 1 and 2. This resulting density matrix must be normalized since the iterating operation does not preserve probability. Our goal is to now expand this density matrix and determine the probability imbalance in the $|S\rangle$ and $|+\rangle$ sectors. Expanding Eq. A.27 and performing some simplification we find,

$$\begin{aligned}
\rho_{\rm com}^N = & \frac{1}{2N}(1 - A_1)(1 - A_2) \left(|S\rangle\langle S| + |+\rangle\langle +| + |-\rangle\langle -| \right) \\
& + \frac{1}{2N}(1 - A_2)(A_1) \left(|S\rangle\langle S| + 2|2, 0\rangle\langle 2, 0| \right) \\
& + \frac{1}{2N}(1 - A_1)(A_2) \left(|S\rangle\langle S| + 2|0, 2\rangle\langle 0, 2| \right) \\
& + \frac{A_1 A_2}{N} |S\rangle\langle S|.
\end{aligned} \tag{A.28}$$

where I have used the notation $|n_L, n_R\rangle$ of n_L (n_R) in the left (right) well, and included the renormalization constant of $N = \frac{1}{2}(3 - A_1 A_2)$. We now want to assess the imbalance between the $|S\rangle$ and $|+\rangle$ sectors. The first line is manifestly symmetric with respect to $|S\rangle$ and $|+\rangle$ and therefore

does not contribute any oscillation. After some algebra, it can be shown that the sum of the first and third term also yield zero imbalance between these two sectors. Therefore, the only imbalance is in the last term. Hence, we expect an oscillation contrast $A_{P_{11}}^{\text{ind.}}$ for indistinguishable particles on an imperfect beam splitter,

$$A_{P_{11}}^{\text{ind.}} = \frac{2A_1A_2}{3 - A_1A_2}. \tag{A.29}$$

It is clear that this expression yields unity contrast oscillations for $A_1 = A_2 = 1$, while for either of $A_i = 0$ there is zero oscillation contrast, as expected.

With Eq. A.29 we can now include the effect of distinguishability. For distinguishable particles, the expected oscillation contrast is $A_{P_{11}}^{\text{dist.}} = A_1A_2/2$ (See section A.1.1.1) while for indistinguishable particles we have our new expression for $A_{P_{11}}^{\text{ind.}}$. Given the probability P^{ind} that the atoms are indistinguishable, we have that the expected contrast $A_{P_{11}}^{\text{exp}}$ is,

$$A_{P_{11}}^{\text{exp}} = P^{\text{ind}} \cdot A_{P_{11}}^{\text{ind.}} + (1 - P^{\text{ind}})A_{P_{11}}^{\text{dist.}}, \tag{A.30}$$

while the expected dip $P_{\text{min}}^{\text{exp}}$ is,

$$P_{\text{min}}^{\text{exp}} = \left(\frac{(1 - P_{\text{loss}})^2}{2} + \frac{A_1A_2}{2}\right) - A_{P_{11}}^{\text{exp}}. \tag{A.31}$$

In the second equation, the term in the parentheses corresponds to the expected peak of the oscillations in $P_{11}(t)$ and agrees to 1% with both of the oscillation measurements in Figure 4.14. By subtracting from the peak the total amplitude of oscillation, which includes both contributions from the distinguishable and indistinguishable cases, we can determine the expected dip. Table A.2 lists the measured and expected amplitudes and dips, and Figure A.3 diagrammatically illustrates our expectation for the data in Figure 4.14f; we find decent agreement.

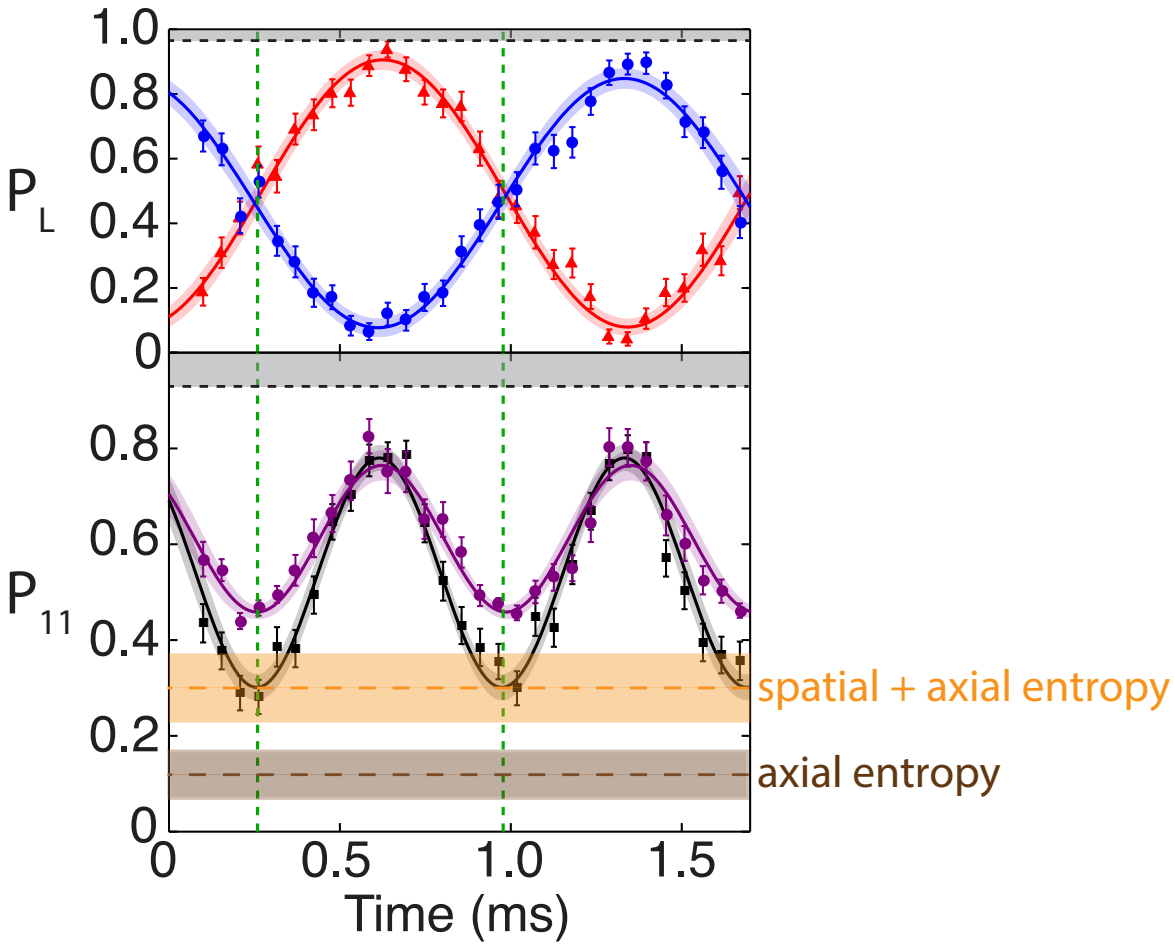

Figure A.3: Expected HOM oscillation behavior. Using the calculated values from Table A.2, we put lines at the expected HOM dip value including just the effect of axial temperature (brown), and the effect of both the temperature and finite tunneling contrast (orange). The density matrix impurity due to temperature gives rise to probability that the atoms are distinguishable in their motional degree of freedom, while the single-particle oscillation contrasts effects the coherence of the two-particle beam splitter. We find decent agreement for these data of Fig. 4.14c,f as well as that of Fig. 4.14b,e (not shown, but tabulated in Table A.2).

Comparison of expected and measured amplitudes and HOM dips

Oscillation data	$A_{P_{11}}^{\mathrm{exp}}\{A_{P_{11}}\}$	$P_{\mathrm{min}}^{\mathrm{exp}}\{P_{\mathrm{HOM}}^{\mathrm{min}}\}$
Fig. 4.14b,e	0.41(5){0.46(2)}	0.32(5){0.28(2)}
Fig. 4.14c,f	0.48(7){0.48(2)}	0.30(7){0.30(1)}

Table A.2: Here we list the expected two-particle oscillation contrasts and HOM dip (minimum measured value of $P_11(t)$) according to Eqs. A.30 and A.31, using the tabulated single particle contrasts in Table A.1. We use the axial temperature (axial ground-state fraction of 0.85) to determine the two-particle indistinguishability, including the probability of indistinguishability in the excited state: $P_i = 0.74(18)$

Appendix B

Summary of HOM measurements and associated statements about statistical siginificance

We present five distinct measurements, each of which contains a statistically-significant measurement of the HOM effect. Table A.1 summarizes these experimental measurements and their uncertainties. The quantities and their uncertainties are determined as follows: P_{loss} is given by an average over all single-particle data in the relevant measurement, and is equal to the mean of $P_L^i(x) + P_R^i(x)$ for $i = i, 2$ and x is the independent variable from the experiment (e.g. time, pulse area, etc.); the uncertainty is the standard error determined from this set of points. $A_{P_{11}}$, $A_{P_{\text{dist}}}$, A_1, A_2, ϕ, and $P_{\text{HOM}}^{\text{min}}$ are determined from weighted fits to the data, where each data point is weighted based on the statistical uncertainty associated with the measured value ($w_i = \frac{1}{\sigma_i^2}$), and the uncertainty in the final fit parameters are then calculated from the weighted average variance of the data. U/J and its uncertainty is determined from the procedure described in Sec. 4.6. $P_{\text{HOM}}^{\text{min}}$ in Fig. 4.16c is determined from the data point at $\delta_{\text{cool}} = 0$, and the associated uncertainty indicated by the error bar on this point, namely the standard error from the average over the experimental realizations (of which there are ≈ 360).

The purple circles shown in the figures in the main text represent P_{dist} as calculated from the expression $P_{\text{L}}^1 P_{\text{R}}^2 + P_{\text{R}}^1 P_{\text{L}}^2$. The error bars on these points are determined by propagating the uncertainty from each single-particle data point $P_L^1, P_R^1, P_L^2, P_R^2$, taking into account correlations between these quantities. Note that near the crossing point of the single-particle datasets the uncertainty in the calculated P_{dist} values decreases since P_{dist} is the sum of two nearly anti-correlated

variables and because the quantity reaches a minimum at this point. The degree to which they are not perfectly anti-correlated comes from the uncorrelated single-particle loss for an atom starting on the left or right.

In our analysis of the results presented in Figs. 4.14e,f we must determine from our measurements of the amplitude of the $P_{\mathrm{dist}}(t)$ and $P_{11}(t)$ oscillations our confidence that these amplitudes are statistically different. To do this we employ a modified Student's t-test called the Welch's t-test, which can be applied to samples with possibly unequal uncertainty and degrees of freedom, such as the number of data points. Using this procedure and the standard errors from the fits (Table A.1), we find for the $J/2\pi = 262$ Hz experiment ($J/2\pi = 348$ Hz experiment) a 6.1σ (5.5σ) deviation between the $P_{\mathrm{dist}}(t)$ data and $P_{11}(t)$ oscillation amplitudes. Note that these are quite close to what one would calculate from a simple analysis of the standard errors quoted in Table A.1, but this method accounts for the finite number of data points.

Appendix C

Derivation of parity oscillation bound for a separable density matrix

In Section 5.3.2, we exploited a bound, C_{bnd}, on the parity oscillation contrast. Here we show that when this bound is violated by a density matrix, that density matrix is necessarily entangled.

As noted in the main text, we construct this bound according to the Peres-Horodecki criterion [141, 142], henceforth called the PHC. We are interested in detecting entanglement between the spin-1/2 Hilbert space $\mathcal{H}_A$ and $\mathcal{H}_B$ for a particle at a position x_i and x_j, respectively; the total Hilbert space is $\mathcal{H} = \mathcal{H}_A \otimes \mathcal{H}_B$. The PHC makes stipulations on separable density matrices, which in general can be written,

$$\rho = \sum_i P_i \rho_i^A \otimes \rho_i^B, \tag{C.1}$$

where P_i are the positive (normalized) weights associated with each product state $\rho_i^A \otimes \rho_i^B$. The key requirement of PHC is that upon performing the transformation,

$$\rho' = \sum_i P_i (\rho_i^A)^\dagger \otimes \rho_i^B, \tag{C.2}$$

it is the case that ρ' has positive eigenvalues. Demonstrating that a density matrix is entangled, therefore, amounts to showing that upon performing this transformation the density matrix has at least one eigenvalue that is negative.

Prior to the parity detection, our experiment produces the density matrix,

$$\rho_{\rm exp} = \begin{pmatrix} p_{\uparrow,\uparrow} & 0 & 0 & 0 \\ 0 & p_{\uparrow,\downarrow} & \epsilon & 0 \\ 0 & \epsilon^* & p_{\downarrow,\uparrow} & 0 \\ 0 & 0 & 0 & p_{\downarrow,\downarrow} \end{pmatrix}. \tag{C.3}$$

By applying the partial transpose step of Eq. C.2, we have the density matrix (this transformation is easily deduced in Mathematica...if you are like me and not so facile with matrix manipulations),

$$\rho'_{\rm exp} = \begin{pmatrix} p_{\uparrow,\uparrow} & 0 & 0 & \epsilon^* \\ 0 & p_{\uparrow,\downarrow} & 0 & 0 \\ 0 & 0 & p_{\downarrow,\uparrow} & 0 \\ \epsilon & 0 & 0 & p_{\downarrow,\downarrow} \end{pmatrix}. \tag{C.4}$$

We now seek the eigenvalues of this density matrix in terms of the matrix elements, which are all determined experimentally. After diagonalizing ρ', we focus on the smallest eigenvalue in order to determine a relation among the matrix elements that yields a negative eigenvalue. The smallest eigenvalue is,

$$h = \frac{1}{2}\left(p_{\uparrow,\uparrow} + p_{\downarrow,\downarrow} - \sqrt{p_{\downarrow,\downarrow}^2 + p_{\uparrow,\uparrow}^2 + 2p_{\uparrow,\uparrow}p_{\downarrow,\downarrow} + 4\epsilon^2}\right). \tag{C.5}$$

After some simple algebra, we find that $h < 0$ when,

$$\epsilon^2 < p_{\uparrow,\uparrow}p_{\downarrow,\downarrow}, \tag{C.6}$$

As discussed in the main text, the measured parity contrast is related to the coherence by $\mathcal{C} = 4\epsilon$. We then arrive at the desired result,

$$\mathcal{C} < 4(p_{\uparrow,\uparrow}p_{\downarrow,\downarrow})^{1/2} \equiv \mathcal{C}_{\rm bnd}. \tag{C.7}$$

Because we measure a parity oscillation contrast in excess of $\mathcal{C}_{\rm bnd}$, we know that the final state cannot be described by a separable density matrix.